

Harnessing Narrow and Stable Luminescence
from Silicon Quantum Dots

by

I Teng Cheong

A thesis submitted in partial fulfillment of the requirements for the degree of

Doctor of Philosophy

Department of Chemistry

University of Alberta

© I Teng Cheong, 2023

Abstract

Luminescent silicon quantum dots (SiQDs) are attractive nanoparticles due to the utilization of non-toxic and earth-abundant silicon. Despite these advantages, challenges in optimizing their optical properties, particularly broad luminescence bandwidths and photostability, persist. This thesis embarks on a comprehensive exploration employing a multidisciplinary approach to overcome these obstacles and unlock the full potential of SiQDs for optical applications.

SiQD-based Fabry-Pérot (FP) optical cavities were first explored to narrow the emission bandwidths. Chapter 2 introduces optically driven FP resonators of SiQD-polymer hybrids. This strategy remarkably reduced the photoluminescence (PL) linewidths and demonstrated tunability through variations in nanoparticle size, polymer matrix, and active layer thickness. Furthermore, a significant milestone has been reached with the fabrication of a flexible device. Building on this foundation, Chapter 3 expands the exploration into electrically driven systems and presents SiQD-based cavity light-emitting diodes (SiQD-cLEDs). Beyond developing external structure, Chapter 4 explored the impact of materials' internal structure. The study employed a combination of techniques to investigate the influence of an amorphous silicon (a-Si) layer on SiQD PL under prolonged UV irradiation. A comparison between SiQDs with thick a-Si shells, and those without, reveals nuanced differences in photoluminescence quantum yield (PLQY) after extended exposure.

In conclusion, this thesis represents a significant multidisciplinary effort to address challenges in harnessing the SiQDs luminescence. Through the exploration of external and internal structures, these contributions push the boundaries of SiQDs and pave the way for future advancements in light-emitting technologies.

Preface

This thesis is an original work by I Teng Cheong. The research was conducted under the co-supervision of Professor Jonathan G. C. Veinot at the Department of Chemistry, University of Alberta, and PD Dr.-Ing. habil. Markus Becherer at the Department of Electrical Engineering, Technical University of Munich.

Chapter 2 of this thesis has been published as Cheong, I.T.; Morrish, W.; Sheard, W.; Yu, H.; Tavares Luppi, B.; Milburn, L.; Meldrum, A.; Veinot, J. G. C. Silicon Quantum Dot–Polymer Fabry–Pérot Resonators with Narrowed and Tunable Emissions. *ACS Appl. Mater. & Inter.* **2021** *13*(23), 27149–27158. I was responsible for experimental design, synthesizing the SiQDs-polymer hybrids, fabricating the FP resonators, data collection and analysis, as well as manuscript preparation. Morrish, W. assisted with the physical deposition of the mirrors, optical response collection and analysis, as well as manuscript edits. Sheard, W. assisted with materials synthesis and spin-coating parameters development. Yu, H. assisted with the SEM image collection and preparation of cover page artwork. Tavares Luppi, B. assisted with GPC data collection and analysis. Milburn, L. assisted with materials preparation. Meldrum, A. assisted with data collection, analyses, and manuscript edits. Veinot J. G. C. was the supervisory author and contributed to concept formation, data analysis, and manuscript preparation.

Chapter 3 of this thesis has been published as Cheong, I T.; Mock, J.; Kallergi, M.; Groß, E.; Meldrum, A.; Rieger, B.; Becherer, M.; Veinot, J. G. C. Colloidal Silicon Quantum Dot-Based Cavity Light-Emitting Diodes with Narrowed and Tunable Electroluminescence. *Adv. Optical Mater.* **2023**, *11*, 2201834. This study is a collaboration with Dr. Markus Becherer’s group in the Department of Electrical Engineering at the Technical University of Munich, where the experiments were conducted. Mock, J. and I contributed equally to this work. We both took part in experimental design, LED fabrication and testing, as well as data analysis. I am responsible for preparing the SiQDs, simulating the cavity spectra, and manuscript preparation. Mock, J. performed preliminary experiments for the fabrication of the LEDs, work function and profilometry measurement of the ITO layers, AFM image collection and analysis, and manuscript edits. Kallergi, M. assisted with the preliminary experiments of device fabrication and testing. Groß, E. assisted with the preparation of SiQDs and manuscript edits. Meldrum, A. assisted with data analysis and manuscript edits. Rieger, B. provided equipment and chemicals for material

synthesis. Becherer, M. and Veinot, J. G. C. were the supervisory authors and contributed to concept formation, data analysis, and manuscript preparation.

Chapter 4 is an original work. I was responsible for experimental design, SiQDs synthesis, data collection and analysis, and manuscript preparation. LiYifan Yang Szepesvari assisted with SiQDs synthesis, conducting PL degradation experiments, and PLQY data collection. Chuyi Ni collected the TEM images. Cole Butler acquired the XP spectra. Kevin M. O'Connor assisted with HF etching and manuscript editing. Riley Hooper assisted with EPR acquisition and manuscript editing. Alkiviathes Meldrum assisted with data interpretation and manuscript edits. Veinot, J. G. C. was the supervisory author and contributed to concept formation, data analysis, and manuscript preparation.

Chapter 5 presents preliminary results and original work. I was responsible for concept formation, material preparation, as well as data collection and analysis.

“走不以手，縛手不能疾；飛不以尾，屈尾不能遠” – 淮南子

“大智若愚，大成若缺” – 老子

“不忘初心，放得始終；初心易得，始終難守” – <<華嚴經>>

常思己過

Acknowledgments

“Why am I studying chemistry?”, I asked myself after my first year of undergraduate study in 2014. This question brought me to the Veinot lab as a CHEM 299 undergraduate researcher and eventually reached the journey of studying Ph.D. Needless to say, this thesis wouldn’t have happened without my supervisor, Dr. Jonathan G. C. Veinot. Thank you for your utmost enthusiasm when you first showed me those beautiful glowing silicon nanoparticles. Your guidance encourages me to play, to explore, and to push beyond. I appreciate your patience and tolerance for my writing. The rounds of manuscript edits were painful, but also taught me how to communicate more effectively. I would also like to thank my co-supervisor Dr. Markus Becherer for accepting me without question, hosting the successful Germany exchange with the ZEIT lab, and connecting me with other great researchers in TUM. A special thanks is dedicated to Dr. Glen Loppnow who has supervised me in chemical education research and shown me the colors of a successful educator. All your mentorships will be always appreciated and remembered.

I would like to acknowledge my past and current committee members, Drs. Jillian M. Buriak and Arthur Mar, for their time and invaluable comments. Thank you, Drs. Vladimir Michaelis, Matthew Macauley, and Joe Takats for your time in participating my candidacy exam. Dr. Eva Hemmer, thank you, for being an external reader for my thesis. In addition, I would like to thank Dr. John Washington for your time in editing this thesis and the valuable conversations.

Throughout this journey, I was fortunate to have a vast opportunity to work with amazing people in different fields. A huge thank you to Drs. Alkiviathes Meldrum, Xihua Wang, Josef (Sepp) Mock, William Morrish, Elisabeth Groß, Bruno Luppi, and Parth Vashishtha for the enlightening times as we worked together. I also like to thank all who were involved in the ATUMS program for building a supportive research community. Specifically, I would like to acknowledge Professor Bernhard Rieger, Dr. Sergei Vagin, Mortiz Kleybolte, and Amelie Mühlbach for hosting my Germany research exchange. Eli, Amelie, Sepp, and Moritz, thank you for showing me Munich. Nevertheless, a special thanks goes to Leah Veinot who made all the ATUMS events happen, even in the middle of COVID when international collaborations seemed impossible.

I would like to acknowledge all the support staff in the Chemistry Department and the Nanofab. Thank you, Wayne Moffat, Jennifer Jones, Ryan Lewis, Dirk Kelm, Paul Crothers,

Michael Barteski, Andrew Yeung, Greg Popowich, Anita Weiler, Connor Part, Laura Pham, Peng Li, Aaron Hryciw, Shihong Xu, and Xuehai Tan for your support and assistance. I would also like to thank Drs. Yoram Apelblat and Hayley Wan for organizing my teaching assistantship. You are heroes behind the scenes, and I enjoyed working with you all. I would also like to acknowledge ATUMS and the Alberta government for their financial support through scholarships and awards.

Veinot group members, past and present, thank you very much for supporting me since 2014. The inclusiveness and kindness that you have all shown me not only taught me how to do research but also how great work depends on a united team. To my first mentor, Maryam Aghajamali, you will always be remembered and appreciated for your patience, guidance, and positiveness. You have made my first-ever research experience wonderful. To the students that I have supervised, thank you for teaching me how to mentor and bringing energy into the lab. A special thanks is dedicated to Liyifan Yang. The last research chapter would not have been completed without your help. Drs. Haoyang Yu, Alyx Thiessen, and Sarah Milliken thank you all for being good mentors and friends of mine. Kevin M. O'Connor and Riley Hooper, thank you for your help and fun times within and outside the lab. To my other friends whom we 'suffer' through the Ph.D. study together, thank you and I wish us all the best in our future endeavors.

I would like to acknowledge my family and my second 'family' in Canada who would probably never read this thesis. Your unconditional love and support are more important than you will ever know. Dr. Qiwei Xu, thank you for bringing colors into my last few years at the UofA. You taught me important lessons in both research and in life... After all, it is hard to believe my Ph.D. study is almost to the end. The past five years have been challenging academically, personally, and worldwide. To all who contributed to my time in Edmonton, thank you. To all who have helped us to survive the pandemic, thank you.

"Why am I studying chemistry?" – I still don't know the full answer to this question... it is not easy, but it has been fun...thank you for making this happen...

Table of Contents

CHAPTER 1 : INTRODUCTION.....	1
1.1 Quantum Dots	2
1.2 Silicon Quantum Dots.....	7
1.3 Luminescence of Silicon Quantum Dots	12
1.4 Applications of Luminescent Silicon Quantum Dots	18
1.5 Interacting Silicon Nanomaterials with Optical Cavities.....	22
1.6 Thesis Outline	30
1.7 References.....	31
CHAPTER 2 : SILICON QUANTUM DOT-POLYMER FABRY-PÉROT RESONATORS WITH NARROWED AND TUNABLE EMISSIONS.....	42
2.1 Introduction.....	43
2.2 Experimental Details.....	46
2.3 Result and Discussion	51
2.4 Conclusion	71
2.5 References.....	72
CHAPTER 3 : COLLOIDAL SILICON QUANTUM DOT-BASED CAVITY LIGHT- EMITTING DIODES WITH NARROWED AND TUNABLE ELECTROLUMINESCENCE	76
3.1 Introduction.....	77
3.2 Experimental Details.....	79
3.3 Result and Discussion	86
3.4 Conclusion	111
3.5 References.....	111
CHAPTER 4 : PHOTOSTABILITY OF SILICON QUANTUM DOTS WITH AND WITHOUT A THICK AMORPHOUS SHELL	116
4.1 Introduction.....	117
4.2 Experimental Details.....	119
4.3 Result and Discussion	125
4.4 Conclusions.....	147
4.5 References.....	148
CHAPTER 5 : CONCLUSIONS AND FUTURE DIRECTION	153
5.1 Conclusions.....	154
5.2 Future Directions	156
5.3 References.....	161
BIBLIOGRAPHY	164
APPENDICES.....	184

List of Tables

Table 1.1. A summary of the methods used to prepare SiQDs and their associate properties. ⁵⁵	9
Table 2.1. Spin-coating conditions for fabricating the SiQD-polymer active layers.....	61
Table 2.2. Q-factors of rSi-PS resonators	62
Table 2.3. Spin-coating conditions for fabricating the oSi-PMMA active layers.....	67
Table 3.1. Comparing surface coverage of SiQD functionalized via different methods.	88
Table 3.2. Analysis of the SiQD-LED EL spectra at different voltage.	97
Table 3.3. Reflectance spectra analysis of SiQD-cLEDs with 40 nm Ag output coupler.....	100
Table 3.4. Electroluminescence analysis of SiQD-cLEDs with 40 nm Ag output coupler.....	101
Table 3.5. Reflectance spectra analysis of SiQD-cLEDs with 500 nm SiO ₂	107
Table 3.6. Electroluminescence analysis of SiQD-cLEDs with 500 nm SiO ₂ spacer at + 4.0 V.	107
Table 3.7. Simulated reflectance spectra analysis of SiQD-cLED cavities with 500 nm SiO ₂ . .	107
Table 4.1. Summary of Optical Properties for the As-produced SiQDs	130
Table 4.2. Summary of Optical Properties for N-SiQDs Throughout Photo-degradation	136
Table 4.3. Summary of Optical Properties for O-SiQDs Throughout Photo-degradation	137
Table 4.4. Summary of Linear Fit for SiQDs Recombination Rate.....	140

List of Figures

Figure 1.1. Evolution of the energy structure from an atom to a bulk semiconductor.	3
Figure 1.2. Representation of band edge alignment for different types of core-shell QDs.	5
Figure 1.3. The trend in the application of QDs in 2018 and forecast for 2030. (Reprint with permission from ref. 24. Copyright 2022 The Royal Society of Chemistry)	6
Figure 1.4. Simplified band structure diagram of (a) c-Si and (b) nanoscale Si. The broadened wavefunction in nanoscale Si induces a “quasi-direct” like band gap.	8
Figure 1.5. Preparing free-standing H-SiQDs from thermally processed solid-oxide precursors. Inset is an illustration depicting the graded structure of the QD.	10
Figure 1.6. Schematic representation of radical abstraction and propagation along the silicon surface during hydrosilylation.	11
Figure 1.7. Scheme showing organolithium reagent-mediated functionalization on a silicon nanoparticle.	12
Figure 1.8. A summary of SiQDs PL correlating to (a) particle sizes (Reprinted with permission from ref. 40, Copyright 2020 The Royal Society of Chemistry) and (b) surface-species (Adapted with permission from ref. 87, Copyright 2014 American Chemical Society).	13
Figure 1.9. (a) An illustration of full-width-at-half-maximum (FWHM) of an emission peak. (b) Representative photoluminescence spectra of H-SiQDs prepared from thermally processed HSQ. (Reprint with permission from ref. 82, Copyright 2006 American Chemical Society)14	
Figure 1.10. (a) Dodecyl-SiQDs in toluene showing PLQY (open circles) reduction under 365 nm UV light exposure under inert atmosphere. Minor decrease (< 20 nm) in peak wavelength (solid squares) was observed (Reprinted with permission from ref. 146. Copyright 2015 The Royal Society of Chemistry) (b) Scanning tunneling spectroscopic measurement of a H-SiQD with different applied voltages. Left is the topographic image of the QD showing the different measuring points. Right is the localized density of states spectra measured at points A to F under forward (from 1.6 to -1.1 V; blue line) and backward (from -1.1 to 1.6 V; red line) bias. (Reprinted with permission from ref. 86. Copyright 2018 American Chemical Society).....	18
Figure 1.11. (a) Schematic representation of a luminescent solar concentrator of SiQDs. (b) Overlapped spectrum of solar energy (grey line), absorption (black line), and PL (red line) of 4.3 nm SiQDs. The transparency window is indicated by grey shading. (Adapted by permission from ref. 166. Copyright 2017 Springer Nature.)	20

Figure 1.12. A schematic representation of (a) the multilayered structure and (b) an energy diagram showing the working principle of a SiQD-LED. (Reprint with permission from ref. 180. Copyright 2023 Wiley-VCH)	22
Figure 1.13. Illustration depicting the propagation of light within a Fabry-Pérot optical cavity (left) and the resulted spectrum (right).	23
Figure 1.14. (a) Schematic representation and (b) the optical response of free-standing SiQDs inside a distributed Bragg reflector cavity. (Reprint with permission from ref. 197. Copyright 2004 AIP Publishing).....	25
Figure 1.15. (a) Scanning electron microscopic images showing the structure of a distributed feedback grating of thermally processed HSQ. A digital photo of the device is attached on the right side. (b) Edge emission spectrum of the cavity pumped by a 400 nm pulsed laser with a pulse duration of 120 fs. (Reprint with permission from ref. 201. Copyright 2021 American Chemical Society).....	26
Figure 1.16. (a) Fluorescence image of 5 μm silica microspheres coated with 100 nm of thermally processed SRO. (b) Ensemble PL spectra showing whispering gallery modes from the microspheres at different sizes. (Reprint with permission from ref. 205. Copyright 2007 Elsevier).....	27
Figure 1.17. (a) Cross-sectional transmission electron microscopic image of a representative Fabry-Pérot cavity structure. This sample consists of the SiO_2 substrate, a thick silver mirror, an SRO active layer, an output coupler or a thinner silver mirror (OC), and a protective coating (PC). (b) Luminescence spectra representing the range achievable in the graded samples. (Reprint with permission from ref. 212. Copyright 2005 Wiley-VCH)	28
Figure 2.1. Illustration of (a) SiQD-polymer Fabry-Pérot microresonator and (b) a secondary electron SEM image of a representative device cross-section.	44
Figure 2.2. FT-IR spectra of red-emitting SiQD-polystyrene (rSi-PS, green), yellow-emitting SiQD-polystyrene (ySi-PS, pink), and orange-emitting SiQD-poly(methyl methacrylate) (oSi-PMMA, blue) hybrid; as well as styrene-functionalized (Sty-rSi, red), and dodecyl-functionalized (dodecyl-oSi, black) colloidal SiQDs.	54

Figure 2.3. High-resolution C 1s XP spectra of (a) rSi-PS, (c) ySi-PS, (e) oSi-PMMA, (g) Dodecyl-oSi, and (i) Sty-rSi. High-resolution Si 2p XP spectra of (b) rSi-PS, (d) ySi-PS, (f) oSi-PMMA, (h) Dodecyl-oSi, and (j) Sty-rSi.	55
Figure 2.4. Gel permeation chromatogram of (a) rSi-PS and (b) ySi-PS hybrid.....	56
Figure 2.5. Simulated reflectivity spectrum of 40 nm thick silver output coupler.	57
Figure 2.6. (a) Photoluminescence spectra ($\lambda_{ex} = 351$ nm) of rSi-PS. Inset is a photo of the solid hybrid. (b) Luminescence spectra of rSi-PS when incorporated into a half- and a full-cavity (bottom) and reflectance spectrum confirming the resonance modes (top). (c) Tuning the PL spectra of rSi-PS FP microresonator by varying the measured active layer thicknesses through different spin-coating speeds. Inset is a photo of the resonator with a nominally 1.76 μm thick active layer. (d) PL spectrum of rSi-PS FP resonator with sub-micron active layer one major emission. The inset is a photo of the resonator.	59
Figure 2.7. (a) Index of refraction and extinction coefficient of rSi-PS. (b) Angle-dependent PL spectra of rSi-PS Fabry-Perot resonator ($T = 1.76$ μm).	60
Figure 2.8. Photoluminescence spectra of (a) ySi-PS in toluene, (b) solid state thin film (dotted line), and cavity with an active layer thickness of 1.32 μm (solid line). Inset of (a) is a photograph of the solid hybrid upon UV illumination. A photograph of the ySi-PS FP resonator is shown at inset of (b).....	64
Figure 2.9. PL spectra measured from a blank Ag mirror (solid), PS on a Si wafer (dashed), and a PS cavity indicate presence of background PL signals from the FPR.....	64
Figure 2.10. Non-normalized PL spectra of rSi-PS (a), ySi-PS (b), and rSi/PS (c) show qualitative enhancement emission intensities in cavity (solid) compared to solid thin film (dashed). ...	65
Figure 2.11. Photoluminescence spectra of (a) oSi-PMMA in toluene and (b) FP resonators of the material with various active layer thicknesses. Inset of (a) is a photo of the solid hybrid. Photographs of the $T = 2.52$, 0.60, and 0.50 μm FP resonators are shown inside (b).	67
Figure 2.12. Three-dimensional models of representative rSi-PS (left) and oSi-PMMA (right) FPR obtained from optical profilometry.....	68
Figure 2.13. CIE 1931 plot of the fabricated oSi-PMMA FP cavity spectra (a) and a simulated diagram of the cavities after removing the SiO ₂ -related emissions (b).	68
Figure 2.14. PL spectra of (a) ‘red’-emitting SiQDs blended with commercial PS, rSi/PS, thin film (dashed) and the corresponding FP resonator (solid line). (b) Tuning the cavity response of	

‘orange’-emitting SiQDs mixed with PMMA by varying the active layer thickness (solid line) and the material’s original PL response (dashed line). Inset of (a) and (b) are the photographs of rSi/PS and oSi/PMMA ($T = 1.52 \mu\text{m}$) resonators.	70
Figure 2.15. (a) CIE chromaticity diagram and (b) representative digital photos showed that the SiQD-polymer hybrid/blend Fabry-Pérot structure. (c) PL spectra of the narrowed emissions from the first bendable SiQD-based FP resonators when it was bent to two different curvatures. Insets are photographs of the bent device under ambient light (top) and being excited by an Ar ion laser in dark (bottom).	71
Figure 3.1. (a) FT-IR spectrum and (b) TGA of Hex-SiQDs.	87
Figure 3.2. (a) Survey XP spectrum of Hex-SiQDs. High resolution XP spectra showing the (b) C 1s and (c) Si 2p features.	89
Figure 3.3. (a) BF-TEM image of Hex-SiQDs (Inset: Average shifted histogram presenting the size distribution of a representative sample of Hex-SiQDs.). (b) Photoluminescence spectrum ($\lambda_{\text{ex}} = 365 \text{ nm}$) of Hex-SiQDs in benzene (Inset: A photograph of the solution upon exposure to a standard transilluminator UV lamp.).	90
Figure 3.4. Schematic of the (a) cavity-free SiQD-LED, (b) SiQD-cLED device structure, and (c) associated energy level alignment. The thickness of the FP cavity can be tuned by defining the thickness of the SiO_2 layer.	91
Figure 3.5. (a) Profilometry measurement of Ag thin films at 40, 45, 50, and 100 nm. (b) Reflectance spectra (solid line) and transmission spectra (dash line) of Ag thin films. The reflectance spectra were measured against a reference Thorlabs Ag mirror, and the transmission spectra were simulated using TFCalc software.	92
Figure 3.6. (a) Work function and (b) profilometry measurement of the as-deposited ITO layer.	93
Figure 3.7. Refractive indices of the active layers in the SiQD-LED obtained by ellipsometry.	94
Figure 3.8. EL spectra of (a) cavity-free SiQD-LED and (b) cLED with 350 nm SiO_2 spacer (cLED-1) at different applied voltages. (c) Simulated reflectance spectrum (top) and EL spectra (bottom) of two different cLEDs with 350 nm SiO_2 spacer under +4 V. (d) Digital photographs comparing cavity-free LED and cLED-2 at different applied voltages. Inset scale bars are 2 mm.	96

Figure 3.9. (a) Absolute current density, (b) irradiance, and (c) EQE of control SiQD-LED at different voltages.	97
Figure 3.10. Simulated reflectance spectra of SiQD-cLED with 40 nm Ag output coupler and different SiO ₂ thicknesses.....	98
Figure 3.11. Correlation between cLED-1 EL spectrum (right) and simulated reflectance spectrum (left) with 40 nm Ag output coupler and 319 nm SiO ₂	99
Figure 3.12. Reflectance spectra of SiQD-cLED with 40 nm Ag output coupler and different SiO ₂ thicknesses.	100
Figure 3.13. Correlation between cLED-2 EL spectrum (right) and simulated reflectance spectrum (left) with 40 nm Ag output coupler and 355 nm SiO ₂	103
Figure 3.14. (a) EL spectra of SiQD-cLEDs with different SiO ₂ thicknesses showing tunable emission ranging from red/orange to NIR. The grey spectrum corresponds to the EL of the control LED. (b) EL spectra of cLEDs with different Ag output coupler thickness; all devices were deposited with 500 nm SiO ₂	104
Figure 3.15. Smooth surface profile of SiQD-cLED with 40 nm Ag and 500 nm SiO ₂ spacer revealed by (a) three-dimensional and (b) two-dimensional AFM images. Inset scale bars are 2 μm.	105
Figure 3.16. Experimental (a) and simulated (b) reflectance spectra of SiQD-cLED with 500 nm SiO ₂ spacers and different Ag.....	106
Figure 3.17. Angle-dependent EL spectra of SiQD-cLED with 500 nm SiO ₂ spacers and 50 nm Ag.	108
Figure 3.18. EL spectra of SiQD-cLED with 500 nm SiO ₂ spacers and 50 nm Ag at different applied voltages.	109
Figure 3.19. (a) Absolute current density, (b) irradiance, and (c) EQE of SiQD-cLED with 500 SiO ₂ nm and 50 nm Ag at different voltages.	110
Figure 4.1. Preparation of ‘normal’ and ‘over-etched’ dodecyl-functionalized SiQDs. Freestanding H-SiQDs were liberated from HF-etching of thermally-processed HSQ, followed by radical-initiated hydrosilylation with 1-dodecene.	126
Figure 4.2. Transmission electron microscopic (TEM) images of the dodecyl-SiQDs used in this study. Bright-field TEM images show equivalent physical dimensions of (a) N-SiQDs (5.1 +	

1.2 nm) and (b) O-SiQDs (5.3 + 1.1 nm). The respective size distributions, (c) and (d), are presented as average-shifted histograms. Dark-field TEM images show equivalent physical dimensions of (e) N-SiQDs (5.2 + 1.4 nm) and (f) O-SiQDs (5.3 + 1.2 nm). The respective size distributions, (g) and (h), are presented as average-shifted histograms. 128

Figure 4.3. Structural and compositional analyses of the as-produced dodecyl-SiQDs. (a) XRD patterns and (b) Raman spectra show evidence of greater long-range order in O-SiQDs. (c) FT-IR spectra and (d) TGA of the SiQDs. (e) Survey and (f) high-resolution Si 2p XP spectra of the as-produced nanoparticles. 129

Figure 4.4. Boxplots comparing the (a) PL max, (b) mean PL lifetime, (c) PLQY, and (d) k_r/k_{nr} of the as-produced N-SiQDs and O-SiQDs. Mean and median of the distributions are represented by dash and solid lines in the boxes, respectively. 130

Figure 4.5. UV-vis absorption (dotted) and PL (solid) spectra of N-SiQDs. The numbering corresponds to Table 4.2. 133

Figure 4.6. UV-vis absorption (dotted) and PL (solid) spectra of O-SiQDs. The numbering corresponds to Table 4.3. 134

Figure 4.7. A summary of the optical properties of N-SiQDs (red circles) and O-SiQDs (black squares). (a) PL maxima, (b) PLQY, (c) PL lifetime, and (d) recombination rate ratio as a function of time over a period of 72 h of UV irradiation. Error bars represent the 95% limit of measurement. Representative PL and UV-vis absorption spectra of each sample are plotted in Figure 4.5 - Figure 4.6 and summarized in Table 4.2 - Table 4.3. 135

Figure 4.8. Linear fit of k_r , k_{nr} , and k_r/k_{nr} of SiQDs (a-c for N-SiQDs and c-d for O-SiQDs). .. 139

Figure 4.9. High-resolution Si 2p XP spectra of (a) N-SiQDs and (b) O-SiQDs with (top) and without (bottom) 72 h of UV irradiation. 142

Figure 4.10. FT-IR spectra of (a) N-SiQDs and (b) O-SiQDs with (top) and without (bottom) 72 h of UV irradiation showing similar surface species. The Si-H_x stretches are deconvoluted in spectra (c) and (d) for N-SiQDs and O-SiQDs, respectively. 142

Figure 4.11. Summary of possible bond breakages in SiQDs upon 365 nm UV irradiation 144

Figure 4.12. Bright-field (a) and dark-field (c) TEM images showing preservation of spheroidal shape and sizes of N-SiQDs after 72 h irradiation. The respective size distributions, (b) and (d), were plotted as average-shifted histograms. 145

Figure 4.13. Bright-field (a) and dark-field (c) TEM images showing preservation of spheroidal shape and sizes of O-SiQDs after 72 h irradiation. The respective size distributions, (b) and (d), were plotted as average-shifted histograms. 145

Figure 4.14. Structural analyses comparing N-SiQDs (top) and O-SiQDs (bottom) before and after 72 h of irradiation. (a) Raman spectra showing negligible changes in structural orderliness for both classes of nanoparticles. More intense EPR signal (b) of N-SiQDs is observed in comparison to O-SiQDs after exposure to UV. Black solid lines and red dotted lines indicate data obtained from nanoparticles before and after irradiation, respectively..... 147

Figure 5.1. Workflow in developing nanotechnology..... 156

Figure 5.2. FT-IR spectra of H-SiQDs obtained from different HF etching time. The evolution of Si-H_x stretches is presented in (a) and Si-H_x bends are highlighted in (b). Left are H-SiQDs obtained from HSQ processed at 1100 °C for 1 h under 5% H₂. Right are H-SiQDs obtained from HSQ processed at 1200 °C for 1 h under 5% H₂. 161

List of Schemes

- Scheme 2.1. (a) Preparation of hydride-terminated SiQDs. (b) Synthesis of SiQD-polymer hybrids via i) thermal- or ii) radical-initiated copolymerization of H-SiQDs with the monomer of choice. Synthesis of colloidal SiQDs via iii) PCl_5 initiated hydrosilylation. 52
- Scheme 3.1. Schematic representation of the synthesis of Hex-SiQDs used in the present investigation. (a) Preparation of H-SiQDs from thermally processed hydrogen silsesquioxane. (b) Functionalization of H-SiQDs upon reaction with 1-hexyllithium to yield Hex-SiQDs. 87
- Scheme 5.1. Schematic representation of growing well-defined polystyrene onto SiQDs. (a) A living polymer anion is first prepared from n-butyllithium and styrene, of which will then be (b) quenched and terminated by vinyl-SiQDs. 158

List of Symbols, Nomenclature, and Abbreviations

AFM	Atomic force microscopy
a-Si	Amorphous silicon
a-Si:H	Hydrogenated amorphous silicon
a-SiQDs	Amorphous silicon quantum dots
B.E.	Bond energy
CB	Conduction band
CIE	Commission Internationale de l'éclairage
c-LED	Cavity light-emitting diode
c-Si	Crystalline silicon
Da	Dalton or gram per mole
DB	Dangling bond
dB	Magnetic field
DBR	Distributed Bragg reflector
DFB	Distributed feedback cavities
DOS	Electronic density of states
E_g	Band gap (energy)
EL	Electroluminescence
EMA	Effective mass approximation
EPR	Electron paramagnetic resonance
EQE	External quantum efficiency
FP	Fabry-Pérot cavity
FSR	Free spectral range
FT-IR	Fourier transform infrared spectroscopy
FWHM	Full-width-at-half-maximum
G	Gauss for magnetic field
GHz	Gigahertz
GPC	Gel-permeation chromatography
HS	Hydrosilylation
H-SiQDs	Hydride-terminated silicon quantum dots
HSQ	Hydrogen silsesquioxane
J	Current density or ampere per square meter
K	Kelvin
mmol	Millimole(s)
MO	Molecular orbital
Mw	Molecular weight
NCs	Nanocrystals
nc-Si	Nanocrystalline silicon
neV	Nanoelectron volt(s)
NIR	Near-infrared
nm	Nanometer(s)
NP	Nanoparticle
N-SiQD	Normal silicon quantum dot with thick amorphous shell
OLED	Organic light-emitting diodes
OLR	Organolithium reagent
O-SiQD	Over-etched silicon quantum dot with thin amorphous shell

PL	Photoluminescence
PMMA	poly(methyl methacrylate)
PSi	Porous Si
PTFE	Polytetrafluoroethylene
QC	Quantum confinement
QD	Quantum dot
Q-factor	Quality factor
QY	Quantum efficiency
RMS	Root mean square
RoHS	European Union Restriction of Hazardous Substances
rpm	Revolutions per minute
SI unit	International system of units
SiNPs	Silicon nanoparticles
SiQD-LED	Silicon quantum dot-hybrid light-emitting diode
SiQDs	Silicon quantum dots
SRO	Silicon-rich oxide
STM	Scanning tunneling microscope
SWE	Staebler-Wronski effect
T	Thickness(es)
TEM	Transmission electron microscopy
TGA	Thermogravimetric analysis
THz	Terahertz
UV	Ultraviolet
V	Voltage
VB	Valence band
W	Watt(s)
WGM	Whispering gallery mode
XPS	X-ray photoelectron spectroscopy
XRD	X-ray diffraction
°	Degree
°C	Degree Celsius
λ_{ex}	Excitation wavelength
μL	Microliter
$\mu\text{W}/\text{cm}^2$	Irradiance or microwatts per square centimeter
ν	Frequency or wavenumber
τ	Photoluminescence lifetime
Ω/sq	Sheet resistance or ohm per square
I	Intensity
R	Radius
c	Speed of light
d	Physical thickness
e	Electron
l	Optical pathlength
m	Resonance mode
α	Detection angle
η	Index of refraction / refractive index
ϵ	Dielectric constant

Chapter 1

Introduction

1.1 Quantum Dots

The exploration of material properties dependent on the dimensions of small particles dates back to the early 20th century, when groundbreaking theories began to unravel the unique behaviors of matter at the nanoscale.¹ Quantum dots emerged as a remarkable manifestation of these principles. These nanomaterials offer size-tunable properties for precise control over electronic and optical characteristics that have transformative impact in various fields. As the 2023 Nobel Prize in Chemistry underscored, quantum dots "have planted an important seed for nanotechnology".²

1.1.1 Nanomaterials

Nano – linguistically derived from the Latin (*nānus*) or Greek (*νᾶνος*) word for “dwarf” – represents “10⁻⁹” in the International System of Units (SI unit).³ Nanomaterials are materials with sizes in the nanoscale bridging between molecules and condensed matters.⁴ In this small size regime, unique chemical and physical properties emerge that are not observed in the molecular or bulk system.⁵ In particular, structure (i.e., size and shape) and surface morphology become critical in defining the materials characteristics.⁵ Among all, luminescent semiconductor NPs possess tunable size-dependent optoelectronic properties that are of interests for future optical and energy technologies.⁶

1.1.2 Semiconductor

An essential part of investigating semiconductor nanomaterials is a basic understanding about their electronic structure.⁷ A bulk semiconductor is an extended solid formed by the overlap of electronic orbitals of many atoms.⁸ Increasing the number of atoms leads to the formation of more molecular orbitals (MOs) at slightly different energies and shrinks the intervals between the MOs. In a solid-state semiconductor with numerous atoms, the closely packed energy levels can be approximated

as continuous bands as shown in **Figure 1.1**.⁹ The lower-energy valence band (VB) and higher-energy conduction band (CB) are separated by an energy region where no electron states exist which is known as the band gap (E_g). The magnitude of E_g defines the energy needed to excite an electron from the VB edge into the empty CB. The resulting electron-hole pair is electrically bound and known as an exciton, which influences the electronic characteristics of the materials.⁹

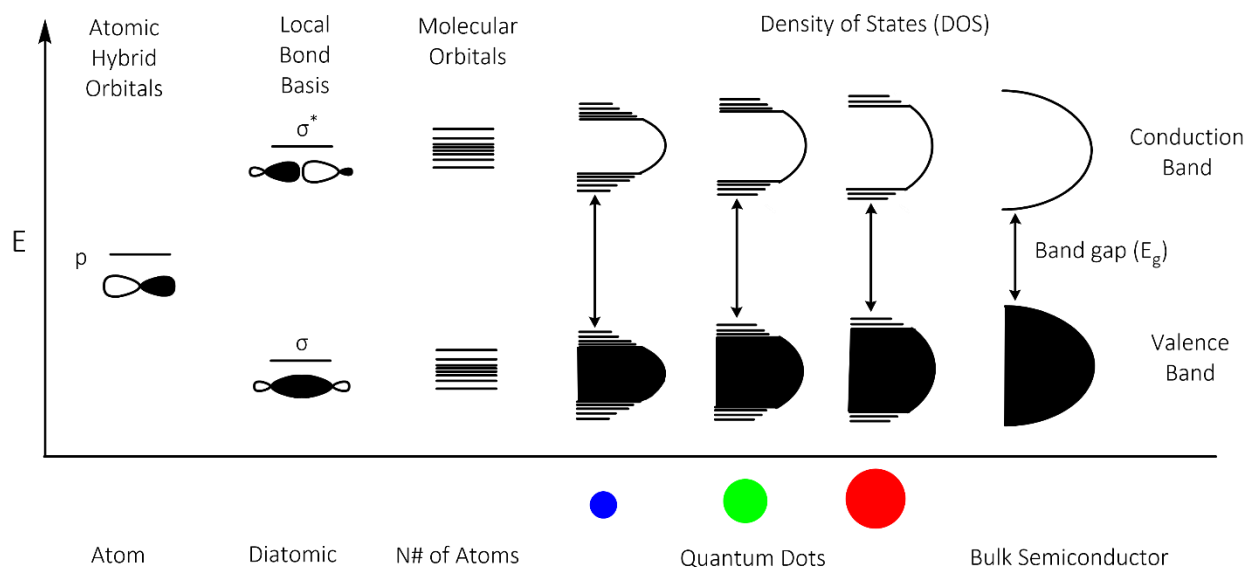


Figure 1.1. Evolution of the energy structure from an atom to a bulk semiconductor.

1.1.3 Quantum Confinement Effect

The quantum confinement (QC) effect is one of the most important phenomena that gives rise to the size-dependent optical and electronic properties of semiconductor nanomaterials.¹⁰ As the dimensions of the materials decrease, the exciton pair is spatially confined; the resulting quantization of energy levels is referred to as QC.⁹ The size at which the QC effect manifests is material dependent and related to the distance between the electron and hole in the electron-hole pair namely the exciton Bohr radius.¹² As the material's dimensions approach its exciton Bohr radius, QC effect becomes prominent and disrupts the electronic density of states (DOS). Upon

the removal of atoms (i.e., reducing the size of a material) and subsequently orbitals, the band edge becomes discrete, while the band center remains continuous.¹⁰ The band gap consequently widens, shifting the optical spectra to higher energy as the material reduces its dimensions.¹⁰

Nanomaterials that exhibit spatial confinement along a single dimension are categorized as two-dimensional nanomaterials, such as quantum well and nanosheets, where carriers can freely move in two dimensions.¹¹ By further restricting the exciton in an additional dimension, we obtain one-dimensional nanomaterials like nanowires. Zero-dimensional nanomaterials, in particular, confine excitons along all three physical dimensions and exhibit discrete band structures that lie between those of bulk materials and molecules.¹¹

1.1.4 Quantum Dots

Quantum dots (QDs) are zero-dimensional colloidal semiconductor nanoparticles that exemplify the QC effect. This was first reported in the early 1980s by Ekimov, A. I. and Brus, L. E. et al. which showed optical spectra increasing in energy as particles size decreased.^{13, 14} This correlation between the QD size and E_g can be accounted by the removal of orbitals at the band edges (**Figure 1.1**). Drawing on the solution of the “particle-in-a-box” problem and assuming the charged carriers have effective masses different than the free carriers, the effective mass approximation (EMA) model is developed to estimate the band gap energy.¹⁵ With consideration of the Coulombic interaction of the electrons and holes, the energy can be predicted by the following equation:^{10, 16}

$$E_{g(QD)} = E_{g(bulk)} + \frac{h^2}{8R^2} \left(\frac{1}{m_e} + \frac{1}{m_H} \right) - \frac{1.8e^2}{\epsilon R} \quad (1.1)$$

where E_g is the band gap of QD or bulk semiconductor, h is Planck’s constant, R is the QD radius, m is the effective mass of each charge carrier, ϵ is the dielectric constant. As shown by the relationship, the band gap energy increases with smaller sizes and dependent on the materials.

Although this model can generally predict the E_g of QDs and hence the corresponding luminescence, other factors such as surfaces, composition, and structure can also affect the optical properties of the nanoparticles as discussed below.

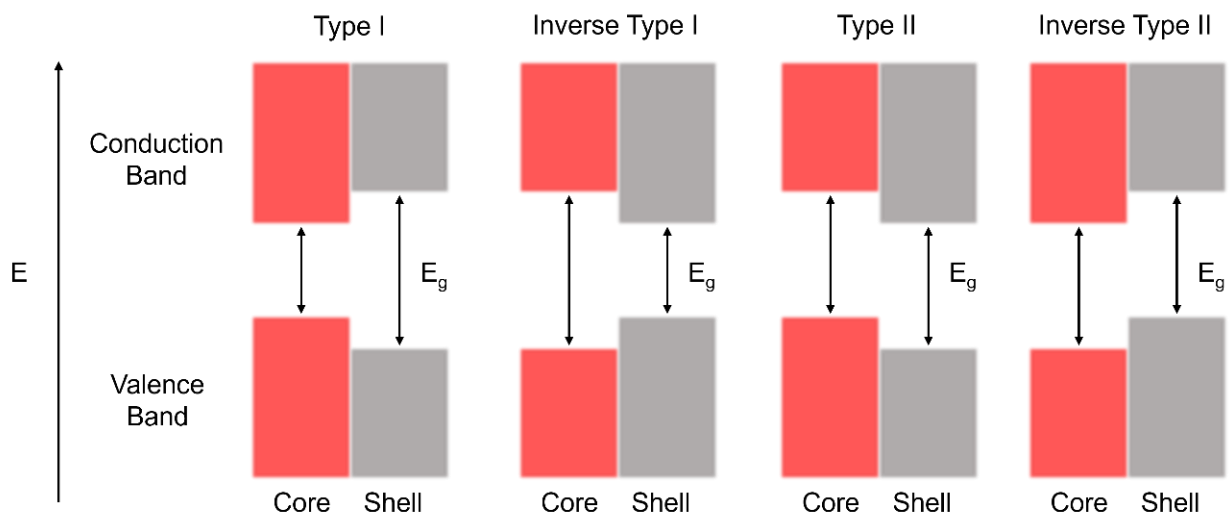


Figure 1.2. Representation of band edge alignment for different types of core-shell QDs.

Epitaxial surface passivation of a QD with a different material forms a core-shell QD.¹⁷ This strategy controls the confinement of carriers based on the relative band positions of the core and shell materials. Four categories of core-shell QDs exist, as shown in **Figure 1.2** : Type I, inverse Type I, Type II, and inverse Type II.¹⁸ When the band gap of the core lies within the band gap of the shell, a Type I QD forms. This system, such as CdSe/CdS, is commonly employed to improve the QD emission quantum efficiency by confining the exciton within the core and passivating non-radiative recombination sites.^{19, 20} In contrast, the reversed alignment of bands in inverse Type I QDs (i.e., CdS/CdSe) confines the carriers at the shell facilitating electron and hole transfer out of the QDs.²¹ Type II (e.g., CdTe/CdSe) and inverse Type II (e.g., CdSe/ZnTe) QDs are characterized by positioning the energy levels of the core's CB and VB above or below the bands of the shell, correspondingly.²² These band offsets effectively delocalize one of the carriers

in the core and the other in the shell. Separation of the carriers promotes charge extraction and can result in an effective band gap smaller than the original materials.^{22, 23} With their tunability and versatility, QDs are appealing for various optical applications, as summarized in **Figure 1.3**.²⁴ Notably, the majority of QD interest lies in light-emitting devices, with a projected 90% of QD applications focusing on displays and light-emitting diodes (LEDs) by 2030.

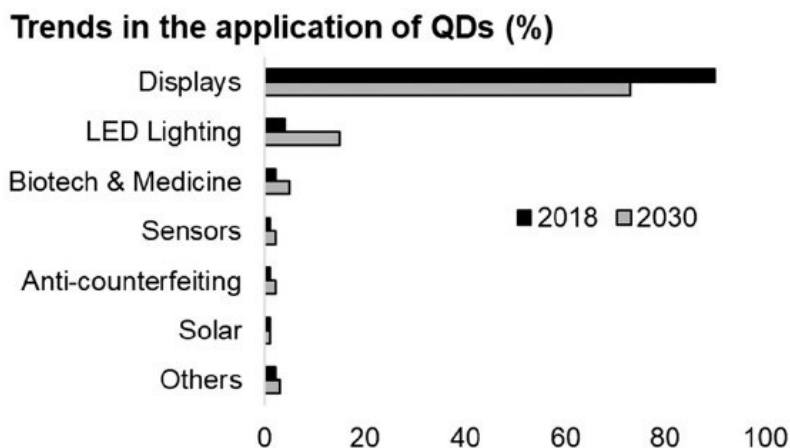


Figure 1.3. The trend in the application of QDs in 2018 and forecast for 2030. (Reprint with permission from *ref. 24*. Copyright 2022 The Royal Society of Chemistry)

1.2 Silicon Quantum Dots

Despite their intriguing properties, heavy-metal-based quantum dots (e.g., II-VI Cd-based,^{25,26} III-V In-based,^{27, 28} or Pb-based^{29, 30} QDs) raise toxicity and sustainability concerns.^{24, 31} Silicon quantum dots (SiQDs) are obvious and attractive alternatives. Si is an intrinsic semiconductor with advantages due to its low toxicity,^{32, 33} silicate abundance in the earth crust,³⁴ and compatibility with electronic technology³⁵.

1.2.1 Luminescence In Silicon

Silicon is a Group 14 element first isolated in the early 1800s.³⁶ Crystalline silicon (c-Si) adopts the cubic diamond structure with eight tetrahedrally bonded atoms per unit cell. The indirect band gap ($E_g \sim 1.1$ eV at 300 K)³⁷ for c-Si indicates the minimum of CB and the maximum of VB are not aligned in k -space (**Figure 1.4a**).³⁸ The direct excitation or relaxation of electrons across the band gap is only possible when the electron undergoes changes in its momentum from lattice vibration (i.e., phonon) coupling. Due to the low probability of such phonon-assisted transition, c-Si exhibits a long excited lifetime in the range of milliseconds.³⁹ Consequently, the electrons and holes are more susceptible to defects and deactivation through non-radiative decay processes resulting in low-to-none c-Si emission at standard conditions.⁴¹

A disordered form of Si, known as amorphous Si (a-Si), is commonly studied in the form of hydrogenated a-Si (a-Si:H). This a-Si:H is generally considered a continuous random network of tetrahedrally bonded atoms that contains localized ordering, defects with undercoordinated Si atoms, and bond distortions.⁴¹⁻⁴⁴ The E_g of a-Si:H can range from ~ 1.5 to 2.0 eV increasing with level of hydrogen content and structural ordering.^{45, 46} The larger band gap a-Si:H has shown successes in passivating c-Si surfaces for improving photovoltaic performances, resulting in a

heterojunction solar cell with 25% conversion efficiency.⁴⁷ Similar to c-Si, a-Si emission is not observable at ambient conditions.⁴⁸

Ambient luminescence from Si was first observed in 1990. The luminescence originates from nanocrystalline Si domains in pillars known as porous Si (PSi) or embedded in silicon oxide matrix.^{49,50} As the Si approaches the size of the exciton Bohr radius (~ 4 nm),⁵¹ the spatial confinement of excitons introduces uncertainty in their momentum. The charge carrier wavefunctions consequently broaden, which increases the probability of wavefunction overlap in k -space (**Figure 1.4b**).⁵²⁻⁵⁴ This allows non-phonon-assisted transitions to occur, which increases radiative recombination and enables the visible luminescence at room temperature. Consequently, the quasi-direct bandgap of Si nanoparticles (SiNPs) also shortens the radiative lifetime to microseconds.⁵⁵ Although these theories explain the visible luminescence of Si nanomaterials, the nature of the emission is complex and will be discussed in later sessions.

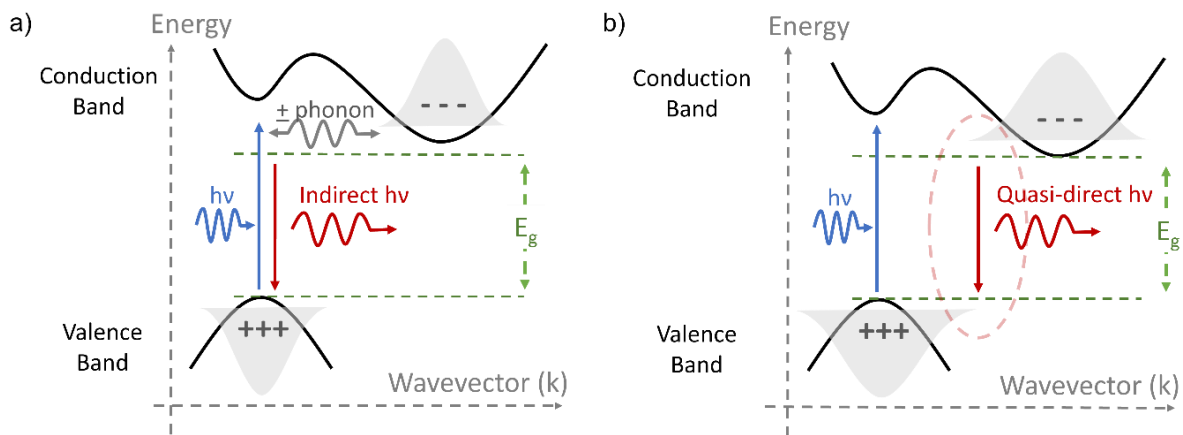


Figure 1.4. Simplified band structure diagram of (a) c-Si and (b) nanoscale Si. The broadened wavefunction in nanoscale Si induces a “quasi-direct” like band gap.

1.2.2 Preparation of Silicon Quantum Dots

Luminescence involving Si nanodomains in solid matrix at standard conditions was an exciting discovery, but the lack of defined structure limits the nanomaterials for practical applications. In contrast, free-standing silicon quantum dots (SiQDs) are more well-defined; they also exhibit higher luminescence.⁴⁰ The synthetic routes of these nanoparticles can be categorized broadly into the bottom-up or top-down approach as summarized in **Table 1.1**.⁵⁶ Top-down synthetic methods (i.e., laser ablation^{57, 58} and etching⁵⁹⁻⁶¹ of Si wafers) generally involve breaking bulk crystalline Si into nanoscale pieces. These methods often have poor size and shape control. Bottom-up syntheses in contrast prepare SiQDs by assembling Si atoms into larger nanoparticles. Solution- and gas- phase methods through thermal decomposition,⁶²⁻⁶⁵ nonthermal plasma⁶⁶⁻⁶⁸, and chemical reduction⁶⁹⁻⁷³ of silicon precursors have been developed to provide reasonable control on the sizes, and subsequently the photoluminescence (PL) of the SiQDs.

Table 1.1. A summary of the methods used to prepare SiQDs and their associate properties.⁵⁶

Category	Method	Diameter [nm]	PL range [nm]	PL efficiency [%]
Top-down	Laser ablation of Si wafer	2-100	400-750	10-70
	Etching bulk Si	2-35	300-500	12-25
Botto-up	Precursor thermal decomposition	1-200	530-1060	5-70
	Nonthermal plasma	2-10	690-920	0.5-70
	Chemical reduction	1.5-10	320-460	10-25

Silicon-rich oxides (SROs; SiO_x , $0 < x < 2$)⁷⁴⁻⁷⁶ and hydrogen silsesquioxane (HSQ; $(\text{HSiO}_{1.5})_n$)^{77, 78} are solid-state precursors that can be thermally treated to yield SiQDs (**Figure 1.5**). Depending on the heating temperature and time, SiNPs with a broad range of sizes ($d \sim 1 - 200$ nm) are obtained.^{76, 79, 80} Hydrofluoric (HF) etching subsequently removes the oxide matrix and liberate hydride-terminated SiQDs (H-SiQDs).⁸¹ Prolonged etching can reduce the particle sizes and subsequently blue-shifting the PL maxima of SiQDs.⁸² A recent study by Thiessen et al.

revealed that the H-SiQDs prepared from the thermally treated HSQ have a graded structure of c-Si core and a-Si shell,⁸³ which presents an avenue for novel structural, surface, and optical properties.⁸⁴⁻⁸⁶

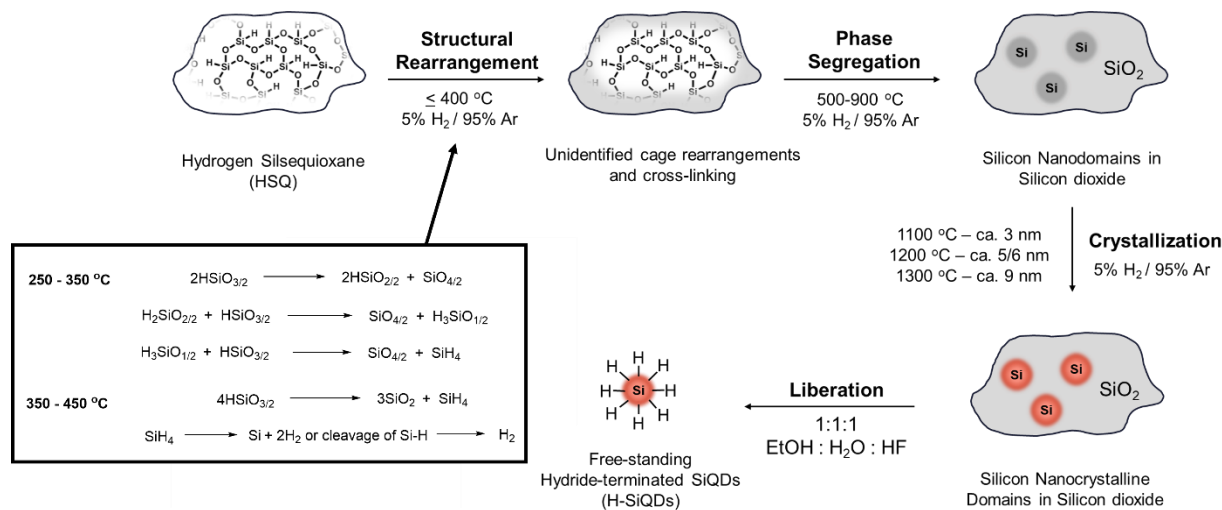


Figure 1.5. Preparing free-standing H-SiQDs from thermally processed solid-oxide precursors. Inset is an illustration depicting the graded structure of the QD.

1.2.3 Surface Functionalization of Silicon Quantum Dots

Surface functionalization of hydride-terminated SiQDs (H-SiQDs) is crucial for preventing the nanoparticles from oxidation, inducing colloidal stability, tuning and enhancing the luminescence response, and tailoring their surfaces for specific applications. The surface chemistry of SiQDs is typically originated from silicon hydrides or halides with appropriate ligands.⁸⁷⁻⁸⁹ Hydrosilylation (HS) is the most common approach to passivate the surfaces of H-SiQDs *via* the insertion of unsaturated bonds (e.g., alkene, alkyne) into the Si-H group.⁹⁰ To date, HS *via* thermal,⁹¹⁻⁹³ radical,⁹⁴⁻⁹⁶ photochemical,^{97,98} Pt-catalyzed,⁷⁰ Lewis-acid mediated,^{99,100} and etchant initiated^{101,102} processes have been developed to form stable Si-C bonds on SiQDs. With respect to applications for SiQDs, the commonly studied HS functionalization are limited to thermal, radical, and etchant (i.e., phosphorus pentachloride or PCl₅) initiated methods.

Generally, thermal and radical HS rely on the formation of radicals at the QD surface enabling the addition of alkenes. The inserted alkyl radicals then abstract the neighboring hydrides and propagate the reaction along the QD surface, as shown in **Figure 1.6**.^{91, 95, 96}

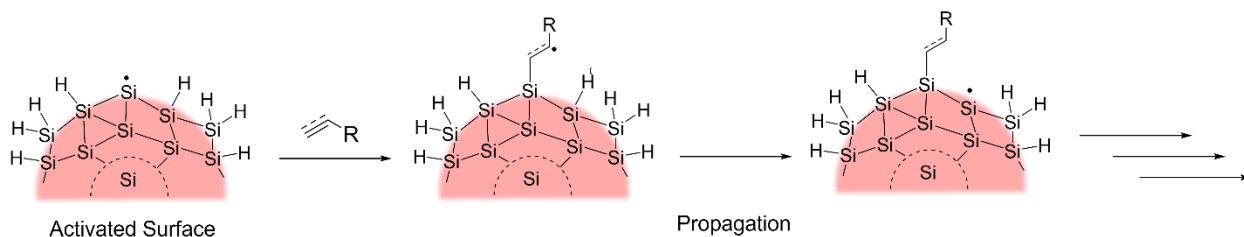


Figure 1.6. Schematic representation of radical abstraction and propagation along the silicon surface during hydrosilylation.

These functionalization methods enable surface coverage that can minimize surface oxidation and capable of simultaneous polymerization to form stable covalently-bonded SiQD-polymer hybrids.¹⁰³⁻¹⁰⁵ The requirement of elevated temperature, however, limits these HS to higher molecular weight alkenes. The high coverage of organic ligands (i.e. > 70% for dodecyl-SiQDs) electronically insulates the SiQDs leading to less efficient electronics like LEDs.^{106, 107} Room temperature PCl_5 -mediated HS uses $\text{Cl}\cdot$ radicals to activate the H-Si/Si-Si bonds and the reactions then proceed with unsaturated carbons like the radical HS.¹⁰¹ This functionalization method has been shown to yield relatively low ligand coverage (< 50% for dodecyl-SiQDs) that is beneficial for LED performance.^{101, 108}

An alternative room-temperature functionalization of SiQDs relies on organolithium reagents (OLRs). The OLRs activate the QD surface *via* direct insertion between the Si-Si bonds at room temperature (**Figure 1.7**).¹⁰⁹⁻¹¹¹ The Si-Li moiety can be readily quenched by HCl that produces Si-H species.¹⁰⁹ The resulting R-SiQDs have low surface coverage (i.e. ~ 40% for dodecyl-SiQDs) and thus enhanced the LED performances.^{106, 112} Owing to their respective

advantages and disadvantages, R-SiQDs resulting from thermal, radical, PCl₅, and OLR-mediated functionalization were explored for different purposes in Chapters 2-4.

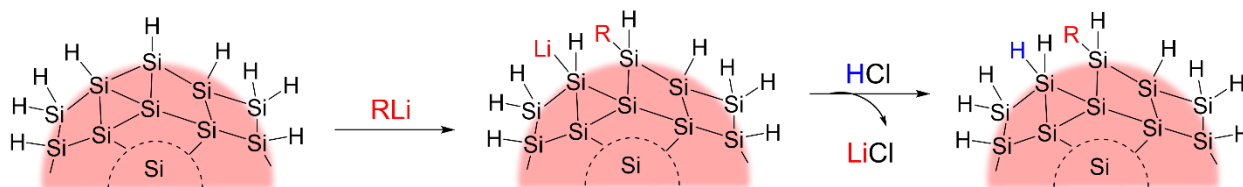


Figure 1.7. Scheme showing organolithium reagent-mediated functionalization on a silicon nanoparticle.

1.3 Luminescence of Silicon Quantum Dots

The room-temperature luminescence of SiQDs has garnered significant interests as sustainable alternatives for conventional QDs.⁷⁷ The optical properties of SiQDs are complex due to the interplay between particle structure and surfaces. The following section will summarize the current understanding and strategies employed to control the optical properties (i.e., luminescence wavelength, bandwidth, quantum efficiency, and photostability) of SiQDs. These efforts aim to unlock the full potential of this nanomaterial.

1.3.1 Luminescence Wavelength

As discussed in Section 1.1.3, the quantum confinement (QC) effect plays an important role in tuning the emission of QDs by changing the band gap energy. This relationship pertains to SiQDs as well, where blue-shifted PL was reported upon decreasing particle sizes (**Figure 1.8a**). The QC effect remained limited to account for surface impacts on the optical properties.⁴⁰

The PL emission of SiQDs is typically separated into two groups: size-dependent PL with microsecond long luminescence lifetime (S-band emission) and size-independent PL at higher energy that decays in nanoseconds (F-band emission), as summarized in **Figure 1.8b**.^{40, 87} The H- and alkyl-termination are commonly used to retain the core-induced S-band emission of SiQD,¹¹³⁻

¹¹⁵ where additional conjugated systems, such as phenylacetylene, can introduce in-gap states that narrows the bandgap and subsequently red-shift PL beyond the visible region.¹¹¹

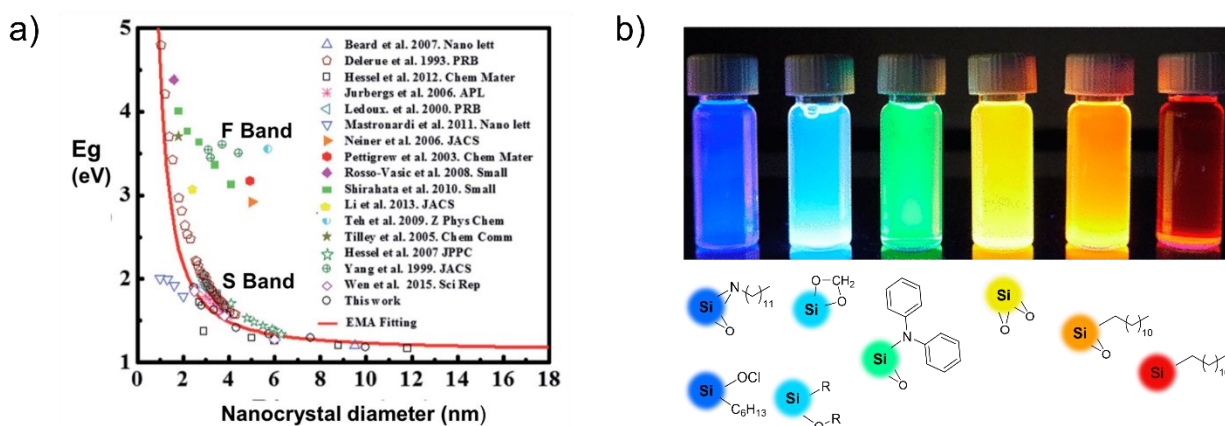


Figure 1.8. A summary of SiQDs PL correlating to (a) particle sizes (Reprinted with permission from *ref. 40*, Copyright 2020 The Royal Society of Chemistry) and (b) surface-species (Adapted with permission from *ref. 87*, Copyright 2014 American Chemical Society).

Surface oxides could have multiple effects on the SiQD PL including reducing the core size,¹¹⁶ localizing exciton Si–SiO₂ interface *via* phonon coupling to the Si-O-Si,¹¹⁷ and introducing various levels of trap-states.^{113, 118, 119} These factors are difficult to isolate and resulting oxidized QDs emitting at either S-band orange or F-band blue emission. Short-lived blue and green PL observed in nitrogen-containing SiQD are also considered as surface-mediated emissions, potentially through charge-transfer to the defect states introduced by the surface nitrogen moieties.¹¹³ Aside from surface effect, hole-trapping by amorphous Si and structural-induced bandgap changes have also been pinpointed for spectral changes in SiQDs, highlighting the complexity of SiQD photophysics.^{84, 120, 121}

1.3.2 Emission Bandwidth

The emission bandwidth, an important parameter in luminescence spectra, is quantified as the full-width-at-half-maximum (FWHM) of the peak (**Figure 1.9a**). Most often, a narrow FWHM (~ 20 nm) is desired for enhanced spectral purity, gamut coverage, and color saturation in displays.¹²²

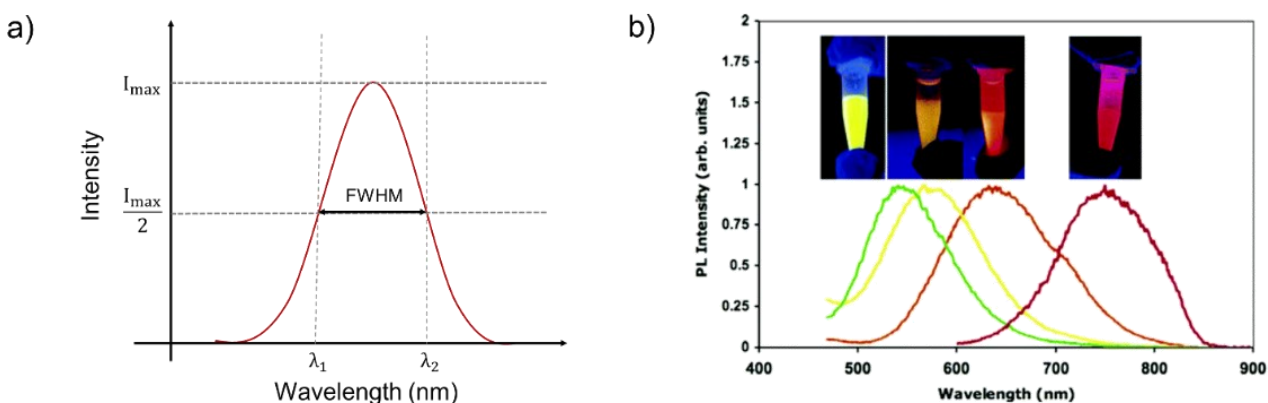


Figure 1.9. (a) An illustration of full-width-at-half-maximum (FWHM) of an emission peak. (b) Representative photoluminescence spectra of H-SiQDs prepared from thermally processed HSQ. (Reprint with permission from *ref.* 82, Copyright 2006 American Chemical Society)

In theory, the emission linewidth limit of a single nanoparticle is in the range of neV as restricted by the uncertainty principle.¹²³ In a SiQD assembly at ambient conditions, both homogeneous and inhomogeneous broadening of the emission peak are observed. A typical PL spectrum of SiQD thus is wide with FWHM exceeding 100 nm (equivalent to a few hundred of meV) as shown in **Figure 1.9b**.⁸⁴ This broad emission bandwidth holds both fundamental and practical significance for the development of optical applications.

Homogeneous broadening of SiQD PL has a uniform effect on each nanoparticle and is commonly observed at room temperature. The PL FWHM of a Si nanocrystal could decrease from ~ 40 nm (corresponding to ~ 100 meV) at room temperature to ~ 10 nm (corresponding to ~ 25 meV) at 80K; the peak narrowing sometimes accompanied with a peak split.¹²⁴ These phenomenon

stems from escalated lattice vibration, which leads to a greater number of phonon energy modes that alter the recombination energy of the exciton.¹²⁵ The impact of exciton-phonon interaction extends to inhomogeneous broadening that has different effect on individual particle. For example, single-particle analyses revealed that soft-organic-shell-capped SiQDs exhibited broader PL FWHM (~ 220 meV) in comparison to hard-oxide-shell-coated nanoparticles (FWHM ~ 25 meV).¹²³

In an ensemble spectrum, size distribution of SiQDs induces inhomogeneous broadening due to the size-dependent PL of each nanoparticle. Chromatography and density gradient ultracentrifugation have been employed to separate the particles by their sizes to afford size-monodisperse SiQDs and narrow the emission bandwidths.^{77, 126, 127} Despite these efforts, the ensemble PL FWHM remained at approximately 100 nm. Alternative or improved approaches toward narrowing SiQD luminescence bandwidths are needed to fully exploit the practical potential of Si emission.

1.3.3 Quantum Efficiency

Photoluminescence quantum yield or efficiency, (PLQY) is a key property of luminescent materials as it determines the efficiency of the emitter. It is governed by the competition between the specific radiative process and all non-radiative processes as described by the following equation:

$$PLQY (\%) = \frac{\textit{photons emitted}}{\textit{photons absorbed}} = \frac{k_r}{k_r + \sum k_{nr}} \quad (1.2)$$

where k_r is the radiative recombination rate and k_{nr} is the non-radiative rate.¹²⁸ Experimentally, the efficiency can be calculated by dividing the integrated intensity of the PL spectrum by the excitation intensity as shown:

$$PLQY (\%) = \frac{I_{PL,sample} - I_{PL,blank}}{I_{ex,blank} - I_{ex,sample}} \quad (1.3)$$

where I_{PL} is the integrated photoluminescence intensity and I_{ex} is the excitation intensity.

The competition between radiative and non-radiative recombination is observed from the size dependent PLQY of SiQDs. Referring to the QC effect on wavefunction in Si discussed in Section 1.2.1, stronger confinement of excitons with smaller SiQDs is expected to increase the probability of radiative recombination and consequently yield higher PLQY.¹²⁹ However, some experimental studies of size-separated SiQDs showed an opposite trend where larger SiQDs exhibited higher efficiencies.^{127, 130, 131} This phenomenon could be attributed to the more amorphous structure and presence of a higher proportion of surface defects in smaller nanoparticles.¹³² Size uniformity in SiQD films has also been demonstrated to enhance PL intensity by improving band alignment and optimizing the electronic overlap of neighboring nanocrystals.¹²⁷ The impact of structure is extended to amorphous SiQDs (a-SiQDs), which commonly exhibit reduced quantum efficiency, primarily ascribed to the presence of non-radiative recombination centers arising from structural disorders.¹³³⁻¹³⁵ Anthony and Kortshagen demonstrated that the absolute PLQY of a-SiQDs (< 2%) is significantly lower than that of crystalline particles (> 40%).¹³⁶

The passivation of defects through surface groups (e.g., H,^{137, 138} alkyl,^{139, 140} oxides,^{141, 139}) is a widely investigated strategy to enhance the PLQY of SiQDs. SiQDs tethered with anthracene¹⁴³ and pyrene¹⁴⁴ units furthermore exhibited 80 and 300% increase in PL intensities, respectively, through energy transfer from the antenna ligands to the nanoparticles. Etchant-induced (i.e., PCl_5 and XeF_2) functionalization also showed successes to improve the PLQY of alkyl-SiQDs from ~ 20% to up 60–70%.^{101, 102} The emission enhancement can be attributed to 1) removal of surface defects *via* surface reconstruction during the course of the reaction and 2) low degree of halogenation on the QD surface that potentially reduce non-radiative Auger

recombination. Precise control over the structural and surface properties undoubtedly is paramount for achieving highly emissive SiQDs.

1.3.4 Photostability

Photostability is a key concern for commercialization as it directly affects the working lifetime of the emitter. Just as the other photophysical properties, the stability of SiQDs luminescence is strongly dependent on their surface and structural chemistry. For example, Kortshagen and coworkers have shown that dodecyl-SiQDs synthesized *via* non-thermal plasma methods experienced $\sim 24 - 48\%$ loss from their original PLQY after a 4 hours of continuous UV irradiation ($\lambda_{\text{ex}} = 365 \text{ nm}$), under an inert atmosphere, without significant change in the emission peak energy (**Figure 1.10a**).^{145, 146} This phenomenon is attributed from the formation of dangling bonds (DBs) at the surface by breaking Si-H_x (B.E. $\sim 3.2 - 3.6 \text{ eV}$) and Si-Si (B.E. $\sim 2.0 - 2.7 \text{ eV}$) bonds. This light-induced degradation is known as the Staebler-Wronski effect (SWE) and has a prominent impact on amorphous Si (a-Si).^{147, 148}

Spatially resolved scanning tunneling microscopic (STM) measurements recently revealed the formation of reversible intragap states from the a-Si shell when appropriate voltage-current pulses are applied to a H-SiQD prepared from thermally-processed silicon-rich-oxide.⁸⁶ The local density of electronic states (LDOS) spectra showed that intragap peaks H_D^b and H_E^b appeared under a reversed bias scanning from -1.1 V to +1.6 V, corresponding to trapping of holes from the amorphous shell (**Figure 1.10b**). The states could persist unaltered until a reverse transition is induced. The LDOS peaks are attributed to reversible local structural deformation in the amorphous shell, which was implicated as a major source of PLQY decay in photoexcited SiQDs. Reports in free-standing SiQDs prepared by other methods and the influence of the structure on

the stability are limited. Such investigations are needed as they are crucial for the development of long-lasting SiQDs.

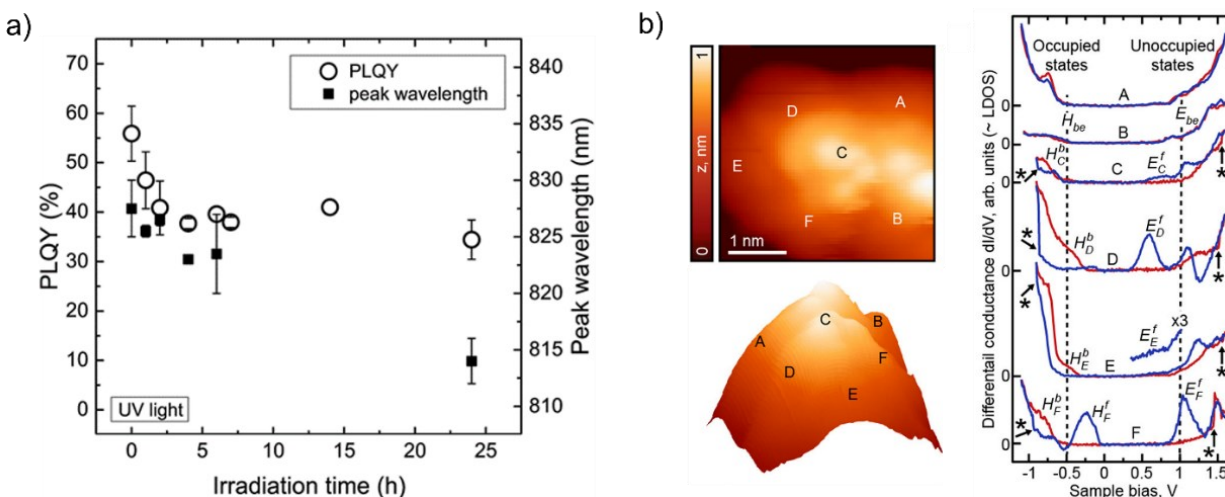


Figure 1.10. (a) Dodecyl-SiQDs in toluene showing PLQY (open circles) reduction under 365 nm UV light exposure under inert atmosphere. Minor decrease (< 20 nm) in peak wavelength (solid squares) was observed (Reprinted with permission from *ref. 146*. Copyright 2015 The Royal Society of Chemistry) **(b)** Scanning tunneling spectroscopic measurement of a H-SiQD with different applied voltages. Left is the topographic image of the QD showing the different measuring points. Right is the localized density of states spectra measured at points A to F under forward (from 1.6 to -1.1 V; blue line) and backward (from -1.1 to 1.6 V; red line) bias. (Reprinted with permission from *ref. 86*. Copyright 2018 American Chemical Society)

1.4 Applications of Luminescent Silicon Quantum Dots

Owing to their versatile chemical and luminescent properties, SiQDs have been exploited for various fields, spanning from medical to defense and energy applications. Silicon's non-toxicity, earth-abundance, and compatibility with current electronic technology make these emitters promising candidates for sustainable nanotechnology.

1.4.1. Biological Imaging

The biologically benign nature SiQDs make them attractive for biological imaging applications. To this end, a substantial body of literature has been focused on preparing water-soluble SiQDs for both *in vitro* and *in vivo* imaging.¹⁴⁹ The F-band emission ($\lambda_{em} = 400\text{--}550$ nm) of SiQDs can be absorbed by tissue, and makes them suitable mostly for *in vitro* studies.¹⁵⁰ The NIR S-band emissions ($\lambda_{em} = 700\text{--}900$ nm) are used *in vitro* and *in vivo* as they fit within the transmission window of tissue.^{151, 152} Moreover, the long-lived microsecond PL lifetime enables time-gated acquisition. This technique improves image contrast by avoiding background noise that arises from tissue autofluorescence and scattered excitation light.¹⁵² The short excitation wavelength ($\lambda_{ex} = 300\text{--}450$ nm) limits the detection depth of SiQDs for *in vivo* studies, however this limitation can be overcome by using two- and three-photon excitation using NIR sources.¹⁵³⁻¹⁵⁵ Further advancements regarding the PLQY and PL stability of the SiQD probes are also being sought.¹⁵⁶

1.4.2. Sensors

Luminescent sensors using Si nanomaterials were developed soon after the discovery of visible PL from porous Si.¹⁵⁷ These sensors have been reported to detect compounds through PL enhancements and shifts, with PL quenching being the major sensing mode.¹⁵⁸ To date, a vast array of SiQD-based sensors have been developed for detecting high energy compounds,¹⁵⁹ metal cations,¹⁶⁰ biologically relevant molecules like glucose¹⁶¹ and pesticides¹⁶². More recently, a SiQD

hybrid with green fluorescent protein demonstrated ratiometric detection of nitroaromatic nerve agents.^{163, 164} This sensor enabled improved visual detection as it gave clear visible change from yellow to green PL upon quenching the emission of SiQDs.

1.4.3. Luminescent Solar Concentrators

Bulk Si has a 1.12 eV band gap. This is well-matched to the solar spectrum, making it a key absorber material in solar cells.¹⁶⁵ On the other hand, SiQDs predominantly absorb UV light, making them more suitable for down-shifting high-energy photons into the NIR. This strategy can increase the efficiency of solar conversion, since traditional photovoltaic (PV) cells are not efficient in capturing UV. Luminescent solar concentrators (LSCs) using SiQDs can propagate SiQD PL to the edges of the devices and concentrate the emission to illuminate photovoltaic cells, as shown in **Figure 1.11**.¹⁶⁶ The light-guiding matrices mainly consist of polymers, such as poly(methyl methacrylate) (PMMA),^{167, 68} which enable transparency, convenient processibility, and integration into pre-existing structures like laminated glass¹⁰⁵ and antireflection coatings¹⁶⁹. This methodology shows promise as the power conversion efficiency of SiQD-based LSCs thus far has reached 4.25%,¹⁶⁸ compared to the record value of 9.1% of all LSCs.¹⁷⁰

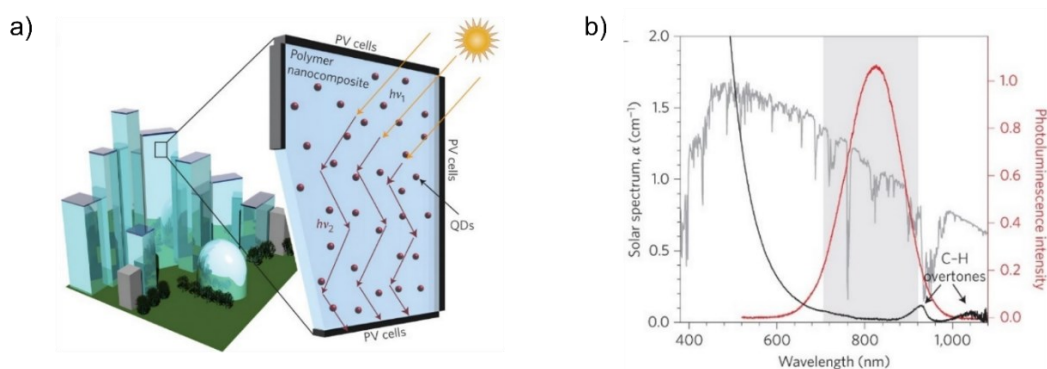


Figure 1.11. (a) Schematic representation of a luminescent solar concentrator of SiQDs. (b) Overlapped spectrum of solar energy (grey line), absorption (black line), and PL (red line) of 4.3 nm SiQDs. The transparency window is indicated by grey shading. (Adapted by permission from *ref. 166*. Copyright 2017 Springer Nature.)

1.4.4. Light-emitting Diodes

As previously shown in **Figure 1.3**, one of the largest markets for QDs is their applications in light-emitting devices. In the past, conventional systems relied on Cd-based QDs. However, the prohibition of Cd in electronics, as amended by the European Union Restriction of Hazardous Substances (RoHS) directive in 2017, has driven the surge for alternative materials.¹⁷¹ SiQDs are based on non-toxic Si and offer tunable electroluminescence (EL) ranging from orange to the NIR region.¹⁷²⁻¹⁷⁴

In 2000, the first LED using SiNPs was demonstrated in an inorganic device with a layer of SiNPs evaporated in between two layers of SiO₂.¹⁷⁵ However, this device had several drawbacks, which includes structural rigidity, poor carrier transport properties, and high operation voltages. Solution-processible SiQDs thereby are more attractive as they are more well-defined, versatile, tunable, and can be incorporated into hybrid LEDs. SiQD-hybrid LEDs (SiQD-LEDs) typically have a multilayered structure consisting of a QD thin film sandwiched between conductive layers comprising organic and/or inorganic materials. An example device is illustrated in **Figure 1.12a**, which consists layers of indium tin oxide ; ITO / poly(ethylenedioxythiophene):poly(styrenesulfonate) ; PEDOT:PSS / poly(N,N'-bis(4-butylphenyl)-N,N'-bis(phenyl)-benzidine) ; poly-TPD / SiQDs / zinc oxide ; ZnO / Ag.^{112, 176-178} The working principle is depicted by the energy diagram in **Figure 1.12b**. Upon application of an electrical current, electrons from the cathode (i.e., Ag) and holes from the anode (i.e., ITO) are injected into the device with the assistance of the injection layers (i.e., PEDOT:PSS). The charge carriers then travel through the charge-transporting layers (i.e., poly-TPD and ZnO) and recombine within the QDs, emitting photons. To further enhance the recombination efficiency, additional blocking layers (i.e., poly-TPD and ZnO) can be introduced to confine charge carriers within the SiQD layer. These

hybrid LEDs offer high tunability and flexibility, making them a promising option for future applications.^{179, 180}

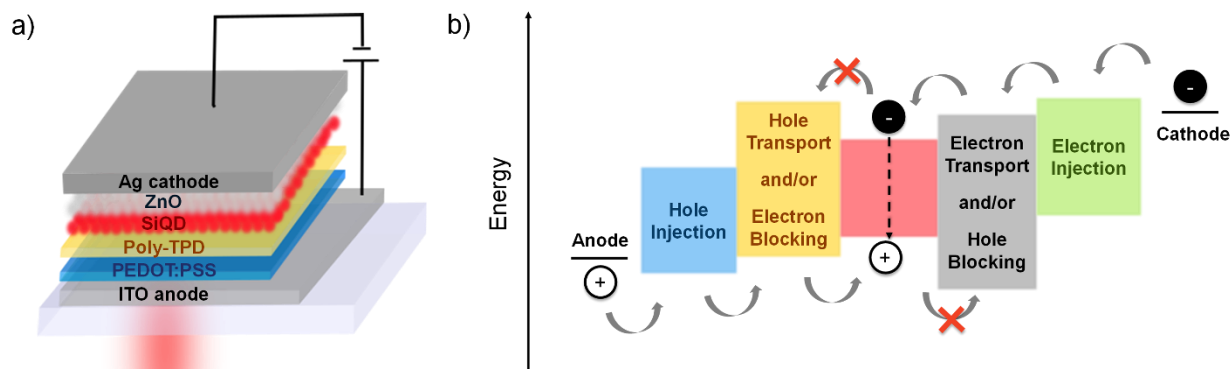


Figure 1.12. A schematic representation of (a) the multilayered structure and (b) an energy diagram showing the working principle of a SiQD-LED. (Reprint with permission from *ref. 180*. Copyright 2023 Wiley-VCH)

Currently, the highest external quantum efficiency (EQE) of SiQD-LEDs is 12.2% for red EL and 8.6% for NIR EL, with emission bandwidths exceeding 100 nm. The incorporation of monodispersed nanoparticles extended the device operation time to over 40 hours.^{172, 173, 181} Despite these advances, continuous efforts are needed to develop more efficient and stable devices. In particular, higher energy EL (i.e., yellow to blue) and narrowing the EL bandwidth of SiQDs are underexplored yet crucial aspects for the progress of SiQD-LEDs.

1.5 Interacting Silicon Nanomaterials with Optical Cavities

An optical cavity is a fundamental element in photonics that can control and enhance light-matter interactions. The synergistic combination of luminescent silicon nanomaterials and optical cavities opens up new possibilities in the field of photonics leading to a wide range of applications. The following section will discuss the basics of optical cavities and state of art of silicon nanomaterial-based photonic devices.

1.5.1. Basics of Optical Cavities

An optical cavity, also known as a resonator, consists of mirrors or optical elements that regulate light *via* the phenomenon of resonance.¹⁸² Three basic types of optical resonators include linear cavity, ring cavity, and photonic crystals.¹⁸³ The linear optical resonator is the fundamental and most widely used form of the cavity, whereby light bounces back and forth between two end mirrors. On the other hand, a ring resonator forms a closed-loop structure for circulating light, while photonic crystals utilize periodic arrangements of materials with different refractive indices to confine light within certain regions.

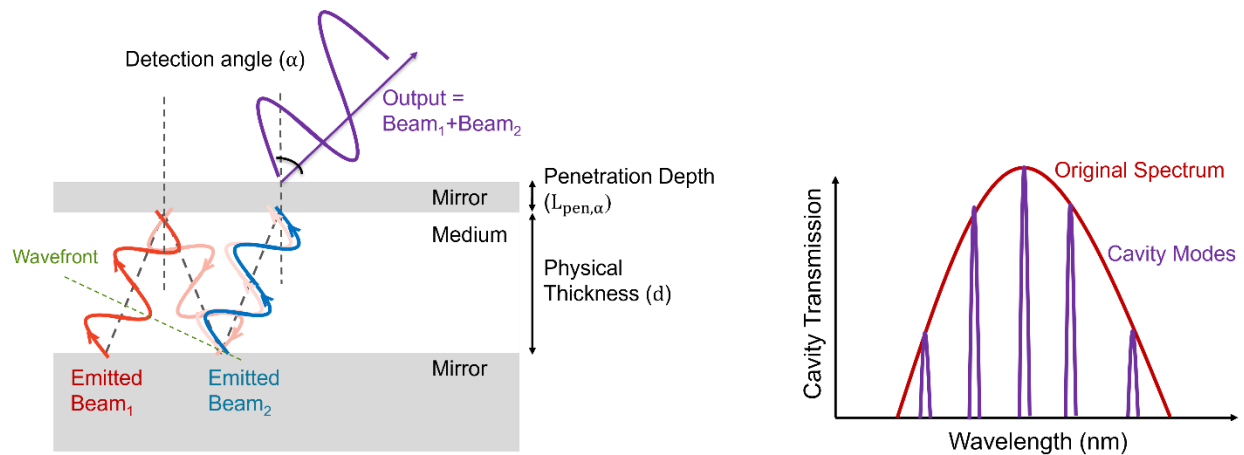


Figure 1.13. Illustration depicting the propagation of light within a Fabry-Pérot optical cavity (left) and the resulted spectrum (right).

A Fabry-Pérot (FP) cavity, a type of linear optical resonator, consists of a parallel arrangement of two flat mirrors and offers the generation of well-defined emissions (**Figure 1.13a**).¹⁸² As light enters the FP cavity, it undergoes multiple reflections between the mirrors and forms standing waves. The resulted constructive and destructive interferences reinforce certain frequencies of the radiation, known as the resonance modes, while suppressing others. The

resonant frequency (ν_m) depends on the round-trip distance that the photon travels within the cavity, which can be mathematically expressed as:

$$\nu_m = \frac{mc}{2l} \quad (1.3)$$

where m is an integer representing the mode number (1, 2, 3, ...), c is the speed of light, and l is the optical pathlength of the cavity.¹⁸⁴ The optical pathlength (l) is a function of the index of refraction (η), the physical thickness of the layers (d), the detection angle (α), and penetration depth of light at the mirror surfaces ($L_{pen,\alpha}$).^{185, 186} Utilizing the relationship between frequency and wavelength, the output resonant wavelength (λ_m) can be estimated using the following equation:

$$\lambda_m = \frac{2}{m} (\sum_i \eta_i d_i \cos\alpha + 2L_{pen,\alpha}) \quad (1.4)$$

The merits of spectral narrowing can be described by free spectral range (FSR), quality factor (Q-factor), and finesse. Details about Equation 1.4 and the merits are found in Appendix A. Through the enhancement and suppression of specific wavelengths, an optical cavity, even one as simple as FP cavity, provides a convenient approach to reducing the spectrum bandwidth of an emitter.

1.5.2. Silicon Nanomaterial-based Optical Cavities

Studies of Si nanomaterial-based photonic devices can be traced back to 1992 when Fujiwara et al. observed fringes in the PL spectra of thin porous Si (PSi) on bulk Si.¹⁸⁷ These structured PL fringes result from the interferences of light reflected at the mirrorlike PSi/bulk Si interface. A year later, Curtis et al. demonstrated the reversible shifting of these PL fringe spacings by changing the refractive index of the thin-film medium.¹⁸⁸ These early studies uncovered the potential of using Si nanomaterials in tunable cavity structures for applications such as interferometers and sensors.^{189, 190} Since then, SiNPs have been explored in different types of cavities, including distributed Bragg reflectors (DBR), distributed feedback cavities (DFB), whispering gallery modes

(WGM), photonic crystals, as well as Fabry-Perot cavities, all with the goal of maximizing the full potential of Si emission.

1.5.2.1 Distributed Bragg Reflector

Following the work of the research groups of Fujiwara and Curtis, Vincent et al. pioneered a multilayered structure composed of alternating layers of Si having different porosities and refractive indices.¹⁹¹ This photonic structure functions as a type of dielectric mirror known as distributed Bragg reflector (DBR).¹⁹² This creates a linear cavity that can be applied for sensing¹⁹³ and photovoltaic applications¹⁹⁴. Additionally, cavity light-emitting diodes (cLEDs) have been realized by encapsulating a layer of emissive PSi between two layers of DBR. This resulted in narrowed electroluminescence (EL) with FWHM as narrow as ~ 20 nm.^{195, 196} Spectral narrowing of free-standing SiQDs using DBR mirrors was realized, where a narrow PL peak (FWHM ~ 13 nm) emitting at 674 nm was observed transmitting through the top DBR mirror (**Figure 1.14**).¹⁹⁷ Devices based on a DBR cavity offer precisely narrowed and tuned spectra. However, the challenges respect to the rigid materials, low charge transport between the insulating layers, and charge transport discontinuities at interfaces limit their applications in harnessing the electroluminescence from SiQDs.

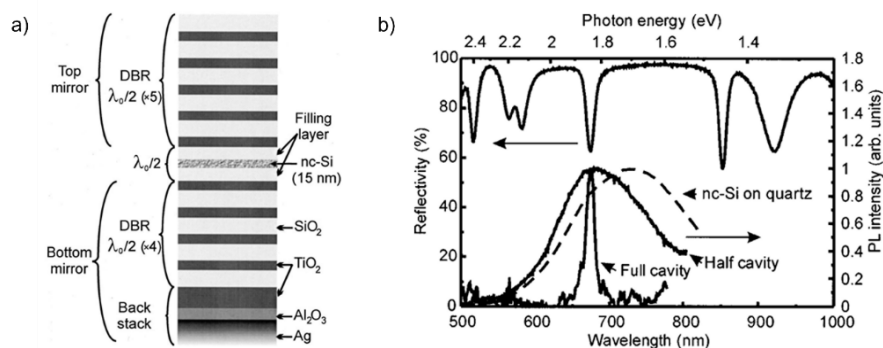


Figure 1.14. (a) Schematic representation and (b) the optical response of free-standing SiQDs inside a distributed Bragg reflector cavity. (Reprint with permission from *ref.* 197. Copyright 2004 AIP Publishing)

1.5.2.2 Distributed Feedback Cavity

A distributed feedback (DFB) cavity is a specific type of linear cavity comprising a periodic structure, which acts as a diffraction grating to resonate a specific wavelength at the edge. This photonic structure is fabricated by lithography and a key technology in generating lasers.¹⁹⁸ Dohnalová et al. investigated DFB cavities of silica gel mixed with PSi, but the output spectra were ill-defined due to the inhomogeneity of nanoparticle aggregates.¹⁹⁹ Instead of physical mixing, DFB cavities with SiNPs were constructed from a layer of patterned silicon oxide matrix with embedded Si nanoparticles. Lu and coworkers more recently employed thermally-processed hydrogen silsesquioxane (HSQ) embedded with SiNPs as the active grating. Using a laser as a pumped source, the authors successfully observed a lasing signal with a FWHM of 0.8 nm at the edge of the device, as shown in **Figure 1.15**.^{200, 201} However, the emission of the electrically driven system, was not well-defined showing several narrow EL fringes instead of a single emission peak.²⁰²

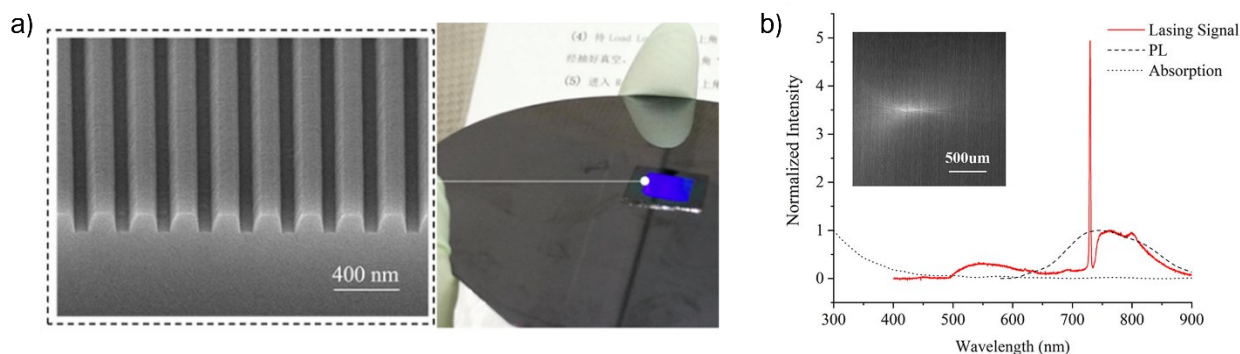


Figure 1.15. (a) Scanning electron microscopic images showing the structure of a distributed feedback grating of thermally processed HSQ. A digital photo of the device is attached on the right side. (b) Edge emission spectrum of the cavity pumped by a 400 nm pulsed laser with a pulse duration of 120 fs. (Reprint with permission from *ref. 201*. Copyright 2021 American Chemical Society)

1.5.2.3 Whispering Gallery Mode and Photonic Crystal

Whispering gallery modes (WGMs) are resonant modes that occur in ring cavities or curved optical structures, whereby light propagates around the circular cavity due to total internal reflection.¹⁸³ Earlier work was focused on silica microspheres coated with ion-implanted SiNPs.^{203, 204} Beltaos and Meldrum later improved the quality of the SiNP using particles derived from thermally-processed silicon-rich-oxides (SROs) as shown in **Figure 1.16**.²⁰⁵ Employing other silicon oxide precursors extended to create WGMs in microdisk array²⁰⁶ and hollow cylindrical microcavities²⁰⁷. Coupling SiNPs obtained from thermally-processed SiO_x with two-dimensional photonic crystal slabs has also shown some successes in reducing the emission bandwidth.^{208, 209} However, single-mode emissions (i.e., emitting at a single resonant mode) from these systems are yet to be seen.

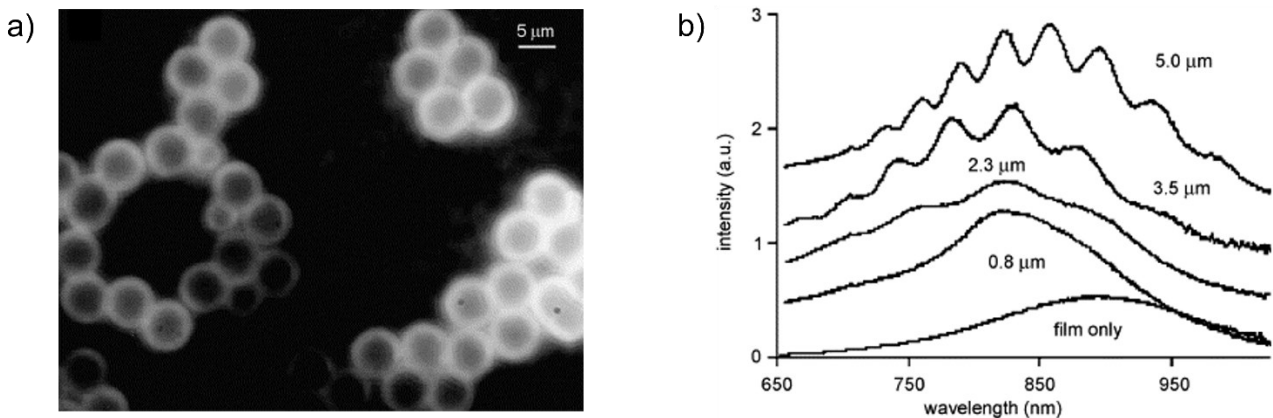


Figure 1.16. (a) Fluorescence image of 5 μm silica microspheres coated with 100 nm of thermally processed SRO. (b) Ensemble PL spectra showing whispering gallery modes from the microspheres at different sizes. (Reprint with permission from *ref. 205*. Copyright 2007 Elsevier)

1.5.2.4 Fabry- Pérot Cavity

Among all photonic structures, the simplicity and versatility of FP resonator make it the cornerstone of cavity technology. A FP cavity can be achieved within a waveguide structure without reflective mirrors, where light is confined in the medium and undergoes multiple reflections between the waveguide ends.^{210, 211} This structure has a drawback related to limited reflectivity and is restricted to edge emission. The use of metal mirrors is more straightforward that provides higher reflectivity and tunability. Hryciw et al. demonstrated spectral narrowing of SiNPs in SRO by sandwiching the emissive layer in between two reflective silver mirrors, as shown in **Figure 1.17a**.²¹² By gradually changing the thickness of the SRO, the graded FP cavity exhibited a gradient of PL across the blue to NIR region, with emission linewidths less than 40 nm (**Figure 1.17b**).

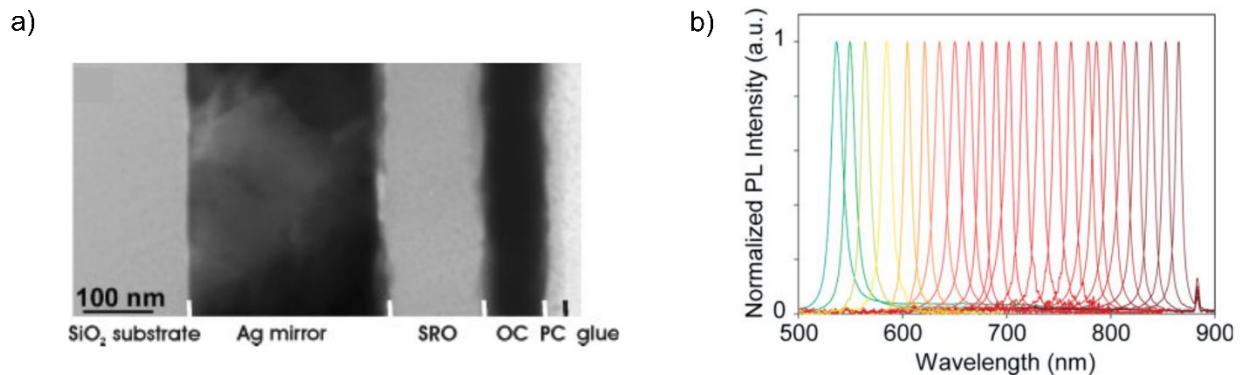


Figure 1.17. (a) Cross-sectional transmission electron microscopic image of a representative Fabry- Pérot cavity structure. This sample consists of the SiO₂ substrate, a thick silver mirror, an SRO active layer, an output coupler or a thinner silver mirror (OC), and a protective coating (PC). **(b)** Luminescence spectra representing the range achievable in the graded samples. (Reprint with permission from *ref. 212*. Copyright 2005 Wiley-VCH)

This strategy was later utilized in the fabrication of light-emitting devices. Specifically, a layer of SiNPs-in-SRO was sandwiched in between a partially reflective Au mirror and DBR.²¹³ However, the use of SiNPs embedded in the oxide matrix limited the cavity light-emitting-diode

to rigid structures and required a high turn-on voltage of 145 V. Moving forward, coupling solution-processible SiQDs with flexible matrices like polymers into optical cavities may overcome previous drawbacks. The enhancements in control and performance of SiQD-based optical systems would lead to new and diverse opportunities arise related to LEDs.

1.6 Thesis Outline

As discussed in this Chapter, SiQDs are promising nanomaterials for potential optical and energy applications. Despite the advances made in controlling the luminescent properties of SiQDs over the past few decades, the commercialization of SiQD-light emitting devices is hindered by the broad emission profile and limited stability of the material's optical response. This thesis aims to explore a practical method for narrowing the spectra of SiQD emissions by employing an optical cavity. Additionally, a fundamental part of research in this thesis relates to investigating the structural effects on the stability of the material's luminescent properties. These studies involve multidisciplinary efforts and are organized in the following chapters:

- Chapter 2 explores optically-driven Fabry-Pérot resonators comprised of SiQD-polymer hybrids and silver mirrors. Combinations of different polymers, preparation methods, sizes of nanoparticles, cavity thicknesses, and substrates resulted in a versatile structure that achieved narrowed and tunable SiQD PL.
- Chapter 3 extends the SiQD-based Fabry-Pérot cavity into the electrically-driven system. This thesis discusses the design, fabrication, and performance of hybrid cavity light-emitting diodes of SiQDs. The devices demonstrated narrowed and tunable EL, along with spectral/visual stability at high operation voltages.
- Chapter 4 investigates the effect of the amorphous shell on the photostability of optical response in SiQDs prepared from thermally-processed HSQ. Through compositional, structural, and optical analyses, the PL quantum yield of SiQDs with an amorphous shell is shown to decay more rapidly upon UV irradiation, potentially through the formation of dangling bonds.
- Chapter 5 summarizes the findings and outlook of this thesis.

1.7 References

1. M. Klein, *Archive for History of Exact Sciences*, 1961, **1**, 459-479.
2. Nobel Foundation, Nobel Prize Outreach AB 2023, <https://www.nobelprize.org/prizes/chemistry/2023/press-release/>, (accessed November 20th, 2023).
3. S. Bayda, M. Adeel, T. Tuccinardi, M. Cordani and F. Rizzolio, *Molecules*, 2019, **25**, 112.
4. N. N. Institue, About Nanotechnology, <https://www.nano.gov/about-nanotechnology>, (accessed June 23rd, 2023).
5. K. J. Klabunde and R. Richards, *Nanoscale Materials in Chemistry*. Wiley, 2nd edn., 2009.
6. F. P. Garcia de Arquer, D. V. Talapin, V. I. Klimov, Y. Arakawa, M. Bayer and E. H. Sargent, *Science*, 2021, **373**, eaaz8541.
7. M. L. Steigerwald and L. E. Brus, *Accounts of Chemical Research*, 1990, **23**, 183-188.
8. R. Hoffmann, *Angewandte Chemie International Edition in English*, 1987, **26**, 846-878.
9. B. D. Fahlman, *Materials Chemistry*, Springer International Publishing, 3 edn., 2018.
10. A. P. Alivisatos, *Science*, 1996, **271**, 933-937.
11. A. D. Yoffe, *Advances in Physics*, 2002, **51**, 799-890.
12. T. Trindade, *Nanoscale Materials*, Springer US, 2004.
13. A. I. Ekimov and A. A. Onushchenko, *Journal of Experimental and Theoretical Physics Letters*, 1981, **34**, 345-349
14. R. Rossetti, S. Nakahara and L. E. Brus, *The Journal of Chemical Physics*, 1983, **79**, 1086-1088.
15. A. L. Efros and A. V. Rodina, *Physical Review B*, 1993, **47**, 10005.
16. Y. Wang and N. Herron, *The Journal of Physical Chemistry*, 1991, **95**, 525-532.
17. A. R. Kortan, R. Hull, R. L. Opila, M. G. Bawendi, M. L. Steigerwald, P. J. Carroll and L. E. Brus, *Journal of the American Chemical Society*, 1990, **112**, 1327-1332.
18. D. Vasudevan, R. R. Gaddam, A. Trinchi and I. Cole, *Journal of Alloys and Compounds*, 2015, **636**, 395-404.
19. J. Lim, B. G. Jeong, M. Park, J. K. Kim, J. M. Pietryga, Y.-S. Park, V. I. Klimov, C. Lee, D. C. Lee and W. K. Bae, *Advanced Materials*, 2014, **26**, 8034-8040.
20. Y.-S. Park, W. K. Bae, L. A. Padilha, J. M. Pietryga and V. I. Klimov, *Nano Letters*, 2014, **14**, 396-402.
21. P. Maity, T. Debnath and H. N. Ghosh, *The Journal of Physical Chemistry C*, 2015, **119**, 26202-26211.
22. S. Kim, B. Fisher, H.-J. Eisler and M. Bawendi, *Journal of the American Chemical Society*, 2003, **125**, 11466-11467.

23. J. Bang, J. Park, J. H. Lee, N. Won, J. Nam, J. Lim, B. Y. Chang, H. J. Lee, B. Chon, J. Shin, J. B. Park, J. H. Choi, K. Cho, S. M. Park, T. Joo and S. Kim, *Chemistry of Materials*, 2010, **22**, 233-240.
24. M. S. Giroux, Z. Zahra, O. A. Salawu, R. M. Burgess, K. T. Ho and A. S. Adeleye, *Environmental Science: Nano*, 2022, **9**, 867-910.
25. W. W. Yu, L. Qu, W. Guo and X. Peng, *Chemistry of Materials*, 2003, **15**, 2854-2860.
26. S. E. Keuleyan, P. Guyot-Sionnest, C. Delerue and G. Allan, *ACS Nano*, 2014, **8**, 8676-8682.
27. D. Gammon, E. S. Snow, B. V. Shanabrook, D. S. Katzer and D. Park, *Science*, 1996, **273**, 87-90.
28. P. Ramasamy, N. Kim, Y.-S. Kang, O. Ramirez and J.-S. Lee, *Chemistry of Materials*, 2017, **29**, 6893-6899.
29. P. R. Brown, D. Kim, R. R. Lunt, N. Zhao, M. G. Bawendi, J. C. Grossman and V. Bulović, *ACS Nano*, 2014, **8**, 5863-5872.
30. L. Protesescu, S. Yakunin, M. I. Bodnarchuk, F. Krieg, R. Caputo, C. H. Hendon, R. X. Yang, A. Walsh and M. V. Kovalenko, *Nano Letters*, 2015, **15**, 3692-3696.
31. C.-H. Chen, S.-N. Cheng, L. Cheng, Z.-K. Wang and L.-S. Liao, *Advanced Energy Materials*, 2023, **13**, 2204144.
32. S. Ivanov, S. Zhuravsky, G. Yukina, V. Tomson, D. Korolev and M. Galagudza, *Materials*, 2012, **5**, 1873-1889.
33. J. Liu, F. Erogbogbo, K.-T. Yong, L. Ye, J. Liu, R. Hu, H. Chen, Y. Hu, Y. Yang, J. Yang, I. Roy, N. A. Karker, M. T. Swihart and P. N. Prasad, *ACS Nano*, 2013, **7**, 7303-7310.
34. M. Fleischer, *Journal of Chemical Education*, 1954, **31**, 446.
35. L. Venema, *Nature*, 2011, **479**, 309-309.
36. M. Jaroniec, *Nature Chemistry*, 2009, **1**, 166-166.
37. W. Bludau, A. Onton and W. Heinke, *Journal of Applied Physics*, 2003, **45**, 1846-1848.
38. L. Brus, *The Journal of Physical Chemistry*, 1994, **98**, 3575-3581.
39. D. J. L. Pavesi and Lorenzo, *Silicon Photonics*, Springer Berlin Heidelberg, 2004.
40. L. Canham, *Faraday Discuss*, 2020, **222**, 10-81.
41. R. A. Street, *Hydrogenated Amorphous Silicon*, Cambridge University Press, 1991.
42. V. L. Deringer, N. Bernstein, A. P. Bartók, M. J. Cliffe, R. N. Kerber, L. E. Marbella, C. P. Grey, S. R. Elliott and G. Csányi, *The Journal of Physical Chemistry Letters*, 2018, **9**, 2879-2885.
43. M. M. J. Treacy and K. B. Borisenko, *Science*, 2012, **335**, 950-953.
44. H. Dersch, J. Stuke and J. Beichler, *Applied Physics Letters*, 1981, **38**, 456-458.
45. P. Rava, F. Demichelis, G. Kaniadakis, P. Mpawenayo, A. Tagliaferro and E. Tresso, *Journal of Vacuum Science & Technology A*, 1987, **5**, 1795-1797.

46. W. Futako, T. Kamiya, C. M. Fortmann and I. Shimizu, *Journal of Non-Crystalline Solids*, 2000, **266-269**, 630-634.
47. K. Masuko, M. Shigematsu, T. Hashiguchi, D. Fujishima, M. Kai, N. Yoshimura, T. Yamaguchi, Y. Ichihashi, T. Mishima, N. Matsubara, T. Yamanishi, T. Takahama, M. Taguchi, E. Maruyama and S. Okamoto, *IEEE Journal of Photovoltaics*, 2014, **4**, 1433-1435.
48. R. A. Street, *Advances in Physics*, 2006, **30**, 593-676.
49. L. T. Canham, *Applied Physics Letters*, 1990, **57**, 1046-1048.
50. H. Takagi, H. Ogawa, Y. Yamazaki, A. Ishizaki and T. Nakagiri, *Applied Physics Letters*, 1990, **56**, 2379-2380.
51. L.-W. Wang and A. Zunger, *Physical Review Letters*, 1994, **73**, 1039-1042.
52. M. S. Hybertsen, *Physical Review Letters*, 1994, **72**, 1514-1517.
53. D. Kovalev, H. Heckler, M. Ben-Chorin, G. Polisski, M. Schwartzkopff and F. Koch, *Physical Review Letters*, 1998, **81**, 2803-2806.
54. B. G. Lee, J.-W. Luo, N. R. Neale, M. C. Beard, D. Hiller, M. Zacharias, P. Stradins and A. Zunger, *Nano Letters*, 2016, **16**, 1583-1589.
55. G. W. 't Hooft, Y. A. R. R. Kessener, G. L. J. A. Rikken and A. H. J. Venhuizen, *Applied Physics Letters*, 1992, **61**, 2344-2346.
56. S. Milliken, A. N. Thiessen, I. T. Cheong, K. M. O'Connor, Z. Li, R. W. Hooper, C. J. T. Robidillo and J. G. C. Veinot, *Nanoscale*, 2021, **13**, 16379-16404.
57. E. Werwa, A. A. Seraphin, L. A. Chiu, C. Zhou and K. D. Kolenbrander, *Applied Physics Letters*, 1994, **64**, 1821-1823.
58. V. Švrček, T. Sasaki, Y. Shimizu and N. Koshizaki, *Applied Physics Letters*, 2006, **89**, 213113.
59. J. Hwang, Y. Jeong, K. H. Lee, Y. Seo, J. Kim, J. W. Hong, E. Kamaloo, T. A. Camesano and J. Choi, *Industrial & Engineering Chemistry Research*, 2015, **54**, 5982-5989.
60. A. S. Heintz, M. J. Fink and B. S. Mitchell, *Advanced Materials*, 2007, **19**, 3984-3988.
61. B. Liao, W. Wang, X. Deng, B. He, W. Zeng, Z. Tang and Q. Liu, *RSC Advances*, 2016, **6**, 14465-14467.
62. S. Guruvanket, J. M. Hoey, K. J. Anderson, M. T. Frohlich, R. Krishnan, J. Sivaguru, M. P. Sibi and P. Boudjouk, *Journal of Materials Chemistry C*, 2016, **4**, 8206-8213.
63. L. E. Brus, P. F. Szajowski, W. L. Wilson, T. D. Harris, S. Schuppler and P. H. Citrin, *Journal of the American Chemical Society*, 1995, **117**, 2915-2922.
64. X. Li, Y. He, S. S. Talukdar and M. T. Swihart, *Langmuir*, 2003, **19**, 8490-8496.
65. J. D. Holmes, K. J. Ziegler, R. C. Doty, L. E. Pell, K. P. Johnston and B. A. Korgel, *Journal of the American Chemical Society*, 2001, **123**, 3743-3748.

66. L. Mangolini, E. Thimsen and U. Kortshagen, *Nano Letters*, 2005, **5**, 655-659.
67. A. Gupta, M. T. Swihart and H. Wiggers, *Advanced Functional Materials*, 2009, **19**, 696-703.
68. T. A. Pringle, K. I. Hunter, A. Brumberg, K. J. Anderson, J. A. Fagan, S. A. Thomas, R. J. Petersen, M. Sefannaser, Y. Han, S. L. Brown, D. S. Kilin, R. D. Schaller, U. R. Kortshagen, P. R. Boudjouk and E. K. Hobbie, *ACS Nano*, 2020, **14**, 3858-3867.
69. J. R. Heath, *Science*, 1992, **258**, 1131-1133.
70. R. D. Tilley, J. H. Warner, K. Yamamoto, I. Matsui and H. Fujimori, *Chemical Communications*, 2005, 1833-1835.
71. R. A. Bley and S. M. Kauzlarich, *Journal of the American Chemical Society*, 1996, **118**, 12461-12462.
72. J. Wang, S. Sun, F. Peng, L. Cao and L. Sun, *Chemical Communications*, 2011, **47**, 4941-4943.
73. C.-S. Yang, R. A. Bley, S. M. Kauzlarich, H. W. H. Lee and G. R. Delgado, *Journal of the American Chemical Society*, 1999, **121**, 5191-5195.
74. W. Sun, C. Qian, X. Cui, L. Wang, M. Wei, G. Casillas, A. S. Helmy and G. A. Ozin, *Nanoscale*, 2016, **8**, 3678-3684.
75. S. Terada, Y. Xin and K.-i. Saitow, *Chemistry of Materials*, 2020, **32**, 8382-8392.
76. N. Shirahata, J. Nakamura, J. I. Inoue, B. Ghosh, K. Nemoto, Y. Nemoto, M. Takeguchi, Y. Masuda, M. Tanaka and G. A. Ozin, *Nano Letter*, 2020, **20**, 1491-1498.
77. M. L. Mastronardi, E. J. Henderson, D. P. Puzzo and G. A. Ozin, *Adv Mater*, 2012, **24**, 5890-5898.
78. R. J. Clark, M. Aghajamali, C. M. Gonzalez, L. Hadidi, M. A. Islam, M. Javadi, M. H. Mobarok, T. K. Purkait, C. J. T. Robidillo, R. Sinelnikov, A. N. Thiessen, J. Washington, H. Yu and J. G. C. Veinot, *Chemistry of Materials*, 2016, **29**, 80-89.
79. C. M. Hessel, D. Reid, M. G. Panthani, M. R. Rasch, B. W. Goodfellow, J. Wei, H. Fujii, V. Akhavan and B. A. Korgel, *Chemistry of Materials*, 2011, **24**, 393-401.
80. E. J. Henderson, J. A. Kelly and J. G. C. Veinot, *Chemistry of Materials*, 2009, **21**, 5426-5434.
81. G. W. Trucks, K. Raghavachari, G. S. Higashi and Y. J. Chabal, *Physical Review Letters*, 1990, **65**, 504-507.
82. C. M. Hessel, E. J. Henderson and J. G. Veinot, *Chemistry of Materials*, 2006, **18**, 6139-6146.
83. A. N. Thiessen, M. Ha, R. W. Hooper, H. Yu, A. O. Oliynyk, J. G. C. Veinot and V. K. Michaelis, *Chemistry of Materials*, 2019, **31**, 678-688.
84. A. N. Thiessen, L. Zhang, A. O. Oliynyk, H. Yu, K. M. O'Connor, A. Meldrum and J. G. C. Veinot, *Chemistry of Materials*, 2020, **32**, 6838-6846.
85. S. Milliken, I. T. Cheong, K. Cui and J. G. C. Veinot, *ACS Applied Nano Materials*, 2022, **5**, 15785-15796.

86. D. A. Kislitsyn, J. M. Mills, S. K. Chiu, B. N. Taber, J. D. Barnes, C. F. Gervasi, A. M. Goforth and G. V. Nazin, *Journal of Physical Chemistry Letters*, 2018, **9**, 710-716.
87. M. Dasog, G. B. De los Reyes, L. V. Titova, F. A. Hegmann and J. G. C. Veinot, *ACS Nano*, 2014, **8**, 9636-9648.
88. M. Dasog, J. Kehrle, B. Rieger and J. G. Veinot, *Angewandte Chemie International Edition in English*, 2016, **55**, 2322-2339.
89. M. Dasog, K. Bader and J. G. C. Veinot, *Chemistry of Materials*, 2015, **27**, 1153-1156.
90. J. M. Buriak, *Chemical Reviews*, 2002, **102**, 1271-1308.
91. J. Holm and J. T. Roberts, *Langmuir*, 2009, **25**, 7050-7056.
92. Z. Yang, M. Iqbal, A. R. Dobbie and J. G. Veinot, *Journal of the American Chemical Society*, 2013, **135**, 17595-17601.
93. W. Sun, C. Qian, M. L. Mastronardi, M. Wei and G. A. Ozin, *Chemical Communications*, 2013, **49**, 11361-11363.
94. I. M. D. Höhle, J. Kehrle, T. Helbich, Z. Yang, J. G. C. Veinot and B. Rieger, *Chemistry - A European Journal*, 2014, **20**, 4212-4216.
95. Z. Yang, C. M. Gonzalez, T. K. Purkait, M. Iqbal, A. Meldrum and J. G. Veinot, *Langmuir*, 2015, **31**, 10540-10548.
96. J. Kehrle, S. Kaiser, T. K. Purkait, M. Winnacker, T. Helbich, S. Vagin, J. G. C. Veinot and B. Rieger, *Nanoscale*, 2017, **9**, 8489-8495.
97. J. A. Kelly and J. G. C. Veinot, *ACS Nano*, 2010, **4**, 4645-4656.
98. J. A. Kelly, A. M. Shukaliak, M. D. Fleischauer and J. G. Veinot, *Journal of the American Chemical Society*, 2011, **133**, 9564-9571.
99. T. K. Purkait, M. Iqbal, M. H. Wahl, K. Gottschling, C. M. Gonzalez, M. A. Islam and J. G. Veinot, *Journal of the American Chemical Society*, 2014, **136**, 17914-17917.
100. Y. Yu and B. A. Korgel, *Langmuir*, 2015, **31**, 6532-6537.
101. M. A. Islam, M. H. Mobarok, R. Sinelnikov, T. K. Purkait and J. G. C. Veinot, *Langmuir*, 2017, **33**, 8766-8773.
102. M. H. Mobarok, T. K. Purkait, M. A. Islam, M. Miskolzie and J. G. C. Veinot, *Angew Chem Int Ed Engl*, 2017, **56**, 6073-6077.
103. Z. Yang, M. Iqbal, A. R. Dobbie and J. G. C. Veinot, *Journal of the American Chemical Society*, 2013, **135**, 17595-17601.
104. Z. Yang, M. Dasog, A. R. Dobbie, R. Lockwood, Y. Zhi, A. Meldrum and J. G. C. Veinot, *Advanced Functional Materials*, 2014, **24**, 1345-1353.

105. A. Marinins, R. Zandi Shafagh, W. van der Wijngaart, T. Haraldsson, J. Linnros, J. G. C. Veinot, S. Popov and I. Sychugov, *ACS Applied Materials and Interfaces*, 2017, **9**, 30267-30272.
106. A. Angi, M. Loch, R. Sinelnikov, J. G. C. Veinot, M. Becherer, P. Lugli and B. Rieger, *Nanoscale*, 2018, **10**, 10337-10342.
107. Y. Xu, S. Terada, Y. Xin, H. Ueda and K.-I. Saitow, *ACS Applied Nano Materials*, 2022, **5**, 7787-7797.
108. T. Ono, Y. Xu, T. Sakata and K. I. Saitow, *ACS Applied Materials and Interfaces*, 2022, **14**, 1373-1388.
109. I. M. Hohlein, A. Angi, R. Sinelnikov, J. G. Veinot and B. Rieger, *Chemistry*, 2015, **21**, 2755-2758.
110. J. H. Song and M. J. Sailor, *Journal of the American Chemical Society*, 1998, **120**, 2376-2381.
111. A. Angi, R. Sinelnikov, A. Meldrum, J. G. Veinot, I. Balberg, D. Azulay, O. Millo and B. Rieger, *Nanoscale*, 2016, **8**, 7849-7853.
112. J. Mock, E. Groß, M. J. Klobner, B. Rieger and M. Becherer, *Advanced Photonics Research*, 2021, **2**, 2100083.
113. R. Sinelnikov, M. Dasog, J. Beamish, A. Meldrum and J. G. C. Veinot, *ACS Photonics*, 2017, **4**, 1920-1929.
114. F. A. Reboredo and G. Galli, *The Journal of Physical Chemistry B*, 2005, **109**, 1072-1078.
115. K. Kůsová, P. Hapala, J. Valenta, P. Jelínek, O. Cibulka, L. Ondič and I. Pelant, *Advanced Materials Interfaces*, 2014, **1**, 1300042.
116. Z. Kang, Y. Liu, C. H. A. Tsang, D. D. D. Ma, X. Fan, N.-B. Wong and S.-T. Lee, *Advanced Materials*, 2009, **21**, 661-664.
117. J. Martin, F. Cichos, F. Huisken and C. von Borczyskowski, *Nano Letters*, 2008, **8**, 656-660.
118. F. Koch, V. Petrova-Koch and T. Muschik, *Journal of Luminescence*, 1993, **57**, 271-281.
119. K. Dohnalová, A. N. Poddubny, A. A. Prokofiev, W. D. A. M. de Boer, C. P. Umesh, J. M. J. Paulusse, H. Zuilhof and T. Gregorkiewicz, *Light: Science & Applications*, 2013, **2**, e47-e47.
120. R. Mazzaro, F. Romano and P. Ceroni, *Physical Chemistry Chemical Physics*, 2017, **19**, 26507-26526.
121. C. C. Huang, Y. Tang, M. van der Laan, J. van de Groep, A. F. Koenderink and K. Dohnalova, *ACS Applied Nano Materials*, 2021, **4**, 288-296.
122. R. Zhu, Z. Luo, H. Chen, Y. Dong and S.-T. Wu, *Optics Express*, 2015, **23**, 23680-23693.
123. I. Sychugov, A. Fucikova, F. Pevero, Z. Yang, J. G. C. Veinot and J. Linnros, *ACS Photonics*, 2014, **1**, 998-1005.
124. I. Sychugov, R. Juhasz, A. Galeckas, J. Valenta and J. Linnros, *Optical Materials*, 2005, **27**, 973-976.

125. I. Sychugov, J. Valenta, K. Mitsuishi, M. Fujii and J. Linnros, *Physical Review B*, 2011, **84**.
126. W. L. Wilson, P. Szajowski and L. Brus, *Science*, 1993, **262**, 1242-1244.
127. J. B. Miller, A. R. Van Sickle, R. J. Anthony, D. M. Kroll, U. R. Kortshagen and E. K. Hobbie, *ACS Nano*, 2012, **6**, 7389-7396.
128. L. Canham, *Faraday Discussions*, 2020, **222**, 10-81.
129. C. Delerue, G. Allan and M. Lannoo, *Physical Review B*, 2001, **64**.
130. M. L. Mastronardi, F. Maier-Flaig, D. Faulkner, E. J. Henderson, C. Kubel, U. Lemmer and G. A. Ozin, *Nano Letters*, 2012, **12**, 337-342.
131. Y. Yu, G. Fan, A. Fermi, R. Mazzaro, V. Morandi, P. Ceroni, D.-M. Smilgies and B. A. Korgel, *The Journal of Physical Chemistry C*, 2017, **121**, 23240-23248.
132. W. Sun, C. Qian, L. Wang, M. Wei, M. L. Mastronardi, G. Casillas, J. Breu and G. A. Ozin, *Advanced Materials*, 2015, **27**, 746-749.
133. M. Molinari, H. Rinnert and M. Vergnat, *Europhysics Letters*, 2004, **66**, 674.
134. A. Irrera, F. Iacona, I. Crupi, C. D. Presti, G. Franzò, C. Bongiorno, D. Sanfilippo, G. Di Stefano, A. Piana and P. G. Fallica, *Nanotechnology*, 2006, **17**, 1428.
135. B. Ghosh, T. Hamaoka, Y. Nemoto, M. Takeguchi and N. Shirahata, *The Journal of Physical Chemistry C*, 2018, **122**, 6422-6430.
136. R. Anthony and U. Kortshagen, *Physical Review B*, 2009, **80**, 115407.
137. R. J. Anthony, D. J. Rowe, M. Stein, J. Yang and U. Kortshagen, *Advanced Functional Materials*, 2011, **21**, 4042-4046.
138. S. Godefroo, M. Hayne, M. Jivanescu, A. Stesmans, M. Zacharias, O. I. Lebedev, G. Van Tendeloo and V. V. Moshchalkov, *Nature Nanotechnology*, 2008, **3**, 174-178.
139. M. L. Mastronardi, E. J. Henderson, D. P. Puzzo, Y. Chang, Z. B. Wang, M. G. Helander, J. Jeong, N. P. Kherani, Z. Lu and G. A. Ozin, *Small*, 2012, **8**, 3647-3654.
140. B. Ghosh, M. Takeguchi, J. Nakamura, Y. Nemoto, T. Hamaoka, S. Chandra and N. Shirahata, *Scientific Reports*, 2016, **6**, 36951.
141. A. M. P. Botas, R. A. S. Ferreira, R. N. Pereira, R. J. Anthony, T. Moura, D. J. Rowe and U. Kortshagen, *The Journal of Physical Chemistry C*, 2014, **118**, 10375-10383.
142. K. Q. Loh, H. P. Andaraarachchi, V. E. Ferry and U. R. Kortshagen, *ACS Applied Nano Materials*, 2023, **6**, 6444-6453.
143. F. Erogbogbo, C. W. Chang, J. May, P. N. Prasad and M. T. Swihart, *Nanoscale*, 2012, **4**, 5163-5168.
144. M. Locritani, Y. Yu, G. Bergamini, M. Baroncini, J. K. Molloy, B. A. Korgel and P. Ceroni, *Journal of Physics Chemistry Letter*, 2014, **5**, 3325-3329.

145. J. Yang, R. Liptak, D. Rowe, J. Wu, J. Casey, D. Witker, S. A. Campbell and U. Kortshagen, *Applied Surface Science*, 2014, **323**, 54-58.
146. J. J. Wu and U. R. Kortshagen, *RSC Advances*, 2015, **5**, 103822-103828.
147. D. L. Staebler and C. R. Wronski, *Applied Physics Letters*, 1977, **31**, 292-294.
148. H. Plagwitz, B. Terheiden and R. Brendel, *Journal of Applied Physics*, 2008, **103**, 094506.
149. M. Montalti, A. Cantelli and G. Battistelli, *Chemical Society Reviews*, 2015, **44**, 4853-4921.
150. J. H. Warner, A. Hoshino, K. Yamamoto and R. D. Tilley, *Angewandte Chemie International Edition*, 2005, **44**, 4550-4554.
151. E. J. Henderson, A. J. Shuhendler, P. Prasad, V. Baumann, F. Maier-Flaig, D. O. Faulkner, U. Lemmer, X. Y. Wu and G. A. Ozin, *Small*, 2011, **7**, 2507-2516.
152. F. Romano, S. Angeloni, G. Morselli, R. Mazzaro, V. Morandi, J. R. Shell, X. Cao, B. W. Pogue and P. Ceroni, *Nanoscale*, 2020, **12**, 7921-7926.
153. G. S. He, Q. Zheng, K.-T. Yong, F. Erogbogbo, M. T. Swihart and P. N. Prasad, *Nano Letters*, 2008, **8**, 2688-2692.
154. L. Ravotto, Q. Chen, Y. Ma, S. A. Vinogradov, M. Locritani, G. Bergamini, F. Negri, Y. Yu, B. A. Korgel and P. Ceroni, *Chem*, 2017, **2**, 550-560.
155. C. Tu, X. Ma, P. Pantazis, S. M. Kauzlarich and A. Y. Louie, *Journal of the American Chemical Society*, 2010, **132**, 2016-2023.
156. H.-Y. Tsai, C. J. T. Robidillo, G. K. Matharu, K. O'Connor, I. T. Cheong, C. Ni, J. G. C. Veinot and W. R. Algar, *Nanoscale*, 2023, **15**, 12492-12505.
157. J. M. Lauerhaas and M. J. Sailor, *Science*, 1993, **261**, 1567-1568.
158. C. M. Gonzalez and J. G. Veinot, *Journal of Materials Chemistry C*, 2016, **4**, 4836-4846.
159. C. M. Gonzalez, M. Iqbal, M. Dasog, D. G. Piercey, R. Lockwood, T. M. Klapotke and J. G. Veinot, *Nanoscale*, 2014, **6**, 2608-2612.
160. B. Campos, M. Algarra, B. Alonso, C. Casado, J. Jimenez-Jimenez, E. Rodriguez-Castellon and J. E. da Silva, *Talanta*, 2015, **144**, 862-867.
161. Y. Yi, J. Deng, Y. Zhang, H. Li and S. Yao, *Chemical Communications*, 2013, **49**, 612-614.
162. Y. Yi, G. Zhu, C. Liu, Y. Huang, Y. Zhang, H. Li, J. Zhao and S. Yao, *Analytical Chemistry*, 2013, **85**, 11464-11470.
163. C. J. T. Robidillo, S. Wandelt, R. Dalangin, L. Zhang, H. Yu, A. Meldrum, R. E. Campbell and J. G. C. Veinot, *ACS Applied Materials Interfaces*, 2019, **11**, 33478-33488.
164. L. A. Milburn, C. J. T. Robidillo, R. Dalangin, Y. Shen and J. G. C. Veinot, *ACS Applied Nano Materials*, 2022, **5**, 11984-11990.
165. C. Battaglia, A. Cuevas and S. De Wolf, *Energy & Environmental Science*, 2016, **9**, 1552-1576.

166. F. Meinardi, S. Ehrenberg, L. Dharmo, F. Carulli, M. Mauri, F. Bruni, R. Simonutti, U. Kortshagen and S. Brovelli, *Nature Photonics*, 2017, **11**, 177-185.
167. S. K. E. Hill, R. Connell, C. Peterson, J. Hollinger, M. A. Hillmyer, U. Kortshagen and V. E. Ferry, *ACS Photonics*, 2018, **6**, 170-180.
168. R. Mazzaro, A. Gradone, S. Angeloni, G. Morselli, P. G. Cozzi, F. Romano, A. Vomiero and P. Ceroni, *ACS Photonics*, 2019, **6**, 2303-2311.
169. S. Ren, C. Shou, S. Jin, G. Chen, S. Han, Z. Chen, X. Chen, S. Yang, Y. Guo and C.-C. Tu, *ACS Photonics*, 2021, **8**, 2392-2399.
170. J. S. Van Der Burgt, D. R. Needell, T. Veeken, A. Polman, E. C. Garnett and H. A. Atwater, *ACS Applied Materials & Interfaces*, 2021, **13**, 40742-40753.
171. Restriction of Hazardous Substances in Electrical and Electronic Equipment (RoHS), https://environment.ec.europa.eu/topics/waste-and-recycling/rohs-directive_en#overview, 2023).
172. K. Y. Cheng, R. Anthony, U. R. Kortshagen and R. J. Holmes, *Nano Letter*, 2011, **11**, 1952-1956.
173. F. Maier-Flaig, J. Rinck, M. Stephan, T. Bocksrocker, M. Bruns, C. Kubel, A. K. Powell, G. A. Ozin and U. Lemmer, *Nano Letter*, 2013, **13**, 475-480.
174. H. Yamada, N. Saitoh, B. Ghosh, Y. Masuda, N. Yoshizawa and N. Shirahata, *The Journal of Physical Chemistry C*, 2020, **124**, 23333-23342.
175. P. Photopoulos and A. G. Nassiopoulou, *Applied Physics Letters*, 2000, **77**, 1816.
176. B. Ghosh, Y. Masuda, Y. Wakayama, Y. Imanaka, J.-i. Inoue, K. Hashi, K. Deguchi, H. Yamada, Y. Sakka, S. Ohki, T. Shimizu and N. Shirahata, *Advanced Functional Materials*, 2014, **24**, 7151-7160.
177. I. T. Cheong, J. Mock, M. Kallergi, E. Groß, A. Meldrum, B. Rieger, M. Becherer and J. G. C. Veinot, *Advanced Optical Materials*, 2022, **11**, 2201834.
178. J. Mock, M. Kallergi, E. Gros, M. Golibrzuch, B. Rieger and M. Becherer, *IEEE Photonics Journal*, 2022, **14**, 1-9.
179. L. Yao, T. Yu, L. Ba, H. Meng, X. Fang, Y. Wang, L. Li, X. Rong, S. Wang, X. Wang, G. Ran, X. Pi and G. Qin, *Journal of Materials Chemistry C*, 2016, **4**, 673-677.
180. B. Ghosh, H. Yamada, S. Chinnathambi, I. N. G. Ozbilgin and N. Shirahata, *Journal of Physical Chemistry Letter*, 2018, **9**, 5400-5407.
181. H. Yamada, J. Watanabe, K. Nemoto, H.-T. Sun and N. Shirahata, *Nanomaterials*, 2022, **12**, 4314.
182. N. Hodgson and H. Weber, in *Optical Resonators*, Springer London, 1997.
183. Z. Yuan, P. C. Wu and Y. C. Chen, *Laser & Photonics Reviews*, 2022, **16**, 2100202.
184. N. Ismail, C. C. Kores, D. Geskus and M. Pollnau, *Optics express*, 2016, **24**, 16366-16389.
185. H. Becker, S. E. Burns, N. Tessler and R. H. Friend, *Journal of Applied Physics*, 1997, **81**, 2825-2829.

186. F. Ma and X. Liu, *Applied Optics*, 2007, **46**, 6247-6250.
187. Y. Fujiwara, H. Nishitani, H. Nakata and T. Ohyama, *Japanese Journal of Applied Physics*, 1992, **31**, L1763.
188. C. L. Curtis, V. V. Doan, G. M. Credo and M. J. Sailor, *Journal of the Electrochemical Society*, 1993, **140**, 3492.
189. V. S.-Y. Lin, K. Motesharei, K.-P. S. Dancil, M. J. Sailor and M. R. Ghadiri, *Science*, 1997, **278**, 840-843.
190. M. J. Sailor and J. R. Link, *Chemical Communications* 2005, **11**, 1375-1383.
191. G. Vincent, *Applied Physics Letters*, 1994, **64**, 2367-2369.
192. L. Pavesi and V. Mulloni, *Journal of Luminescence*, 1998, **80**, 43-52.
193. V. Mulloni and L. Pavesi, *Applied Physics Letters*, 2000, **76**, 2523-2525.
194. F. Duerinckx, I. Kuzma-Filipek, K. Van Nieuwenhuysen, G. Beaucarne and J. Poortmans, *Progress in Photovoltaics: Research and Applications*, 2008, **16**, 399-407.
195. L. Pavesi, *Solid State Communications*, 1996, **97**, 1051-1053.
196. M. Araki, H. Koyama and N. Koshida, *Applied Physics Letters*, 1996, **69**, 2956-2958.
197. D. Amans, S. Callard, A. Gagnaire, J. Joseph, F. Huisken and G. Ledoux, *Journal of Applied Physics*, 2004, **95**, 5010-5013.
198. S. Jaiswal, J. Simpson, S. Withrow, C. White and P. Norris, *Applied Physics A*, 2003, **77**, 57-61.
199. K. Dohnalová, I. Pelant, P. Gilliot, O. Crégut and B. Hönerlage, *Applied Physics Letters*, 2006, **88**, 251105.
200. D.-C. Wang, C. Zhang, P. Zeng, W.-J. Zhou, L. Ma, H.-T. Wang, Z.-Q. Zhou, F. Hu, S.-Y. Zhang, M. Lu and X. Wu, *Science Bulletin*, 2018, **63**, 75-77.
201. P. Zeng, F. Wang, Y. Zhang, W. Zhou, Z. Guo, X. Wu, M. Lu and S. Zhang, *ACS Photonics*, 2021, **8**, 1353-1363.
202. Y.-C. Zhang, Z.-Y. Yu, F.-Y. Ma, X.-Y. Xue, K.-X. Liu, J. Sun, S.-Y. Wang and M. Lu, *Results in Physics*, 2022, **39**, 105734.
203. M. Ajgaonkar, Y. Zhang, H. Grebel and C. White, *Applied Physics Letters*, 1999, **75**, 1532-1534.
204. J. Valenta, J. Linnros, R. Juhasz, J.-L. Rehspringer, F. Huber, C. Hirlimann, S. Cheylan and R. G. Elliman, *Journal of Applied Physics*, 2003, **93**, 4471-4474.
205. A. M. Beltaos and A. Meldrum, *Journal of Luminescence*, 2007, **126**, 607-613.
206. R.-J. Zhang, S.-Y. Seo, A. P. Milenin, M. Zacharias and U. Gösele, *Applied Physics Letters*, 2006, **88**, 153120.
207. J. R. Rodríguez, J. G. C. Veinot, P. Bianucci and A. Meldrum, *Applied Physics Letters*, 2008, **92**, 131119.

208. C. D. Presti, A. Irrera, G. Franzò, I. Crupi, F. Priolo, F. Iacona, G. Di Stefano, A. Piana, D. Sanfilippo and P. G. Fallica, *Applied Physics Letters*, 2006, **88**, 033501.
209. L. Ondič, M. Varga, I. Pelant, J. Valenta, A. Kromka and R. G. Elliman, *Scientific Reports*, 2017, **7**, 5763.
210. J. N. Milgram, J. Wojcik, P. Mascher and A. P. Knights, *Optics Express*, 2007, **15**, 14679.
211. Z.-Y. Yu, Z.-H. Guo, Y.-C. Zhang, X. Zhang, Y. Wang, F.-Y. Ma, Y. Liu, X.-Y. Xue, Q.-Y. Jin, J. Li, J. Sun, S.-Y. Wang, D.-C. Wang and M. Lu, *Results in Physics*, 2022, **34**, 105336.
212. A. Hryciw, J. Laforge, C. Blois, M. Glover and A. Meldrum, *Advanced Materials*, 2005, **17**, 845-849.
213. C.-K. Tseng, M.-C. M. Lee, H.-W. Hung, J.-R. Huang, K.-Y. Lee, J.-M. Shieh and G.-R. Lin, *Journal of Applied Physics*, 2012, **111**, 074512.

Chapter 2

Silicon Quantum Dot-Polymer Fabry-Pérot Resonators with Narrowed and Tunable Emissions

A version of the chapter has been published:

Cheong, I. T.; Morrish, W.; Sheard, W.; Yu, H.; Tavares Luppi, B.; Milburn, L.; Meldrum, A.; Veinot, J. G. C. *ACS Applied Materials & Interfaces* 2021, 13 (23), 27149–27158.

2.1 Introduction

Quantum dots (QDs) are semiconductor particles of nanoscale dimensions that exhibit exquisitely tunable optoelectronic properties. Since Brus' first report more than thirty years ago,¹ the study of QDs has grown into a vast multidisciplinary research area that has captured, and benefited from, the imagination of countless researchers. Many reports outlining prototype applications (e.g., sensors, light-emitting diodes, and photovoltaics)²⁻⁷ have appeared and QDs are now widely deployed in consumer devices (e.g., televisions and mobile phones.) that exploit their photoluminescence (PL).⁸⁻¹⁰ Despite these impressive advances, the impact of QDs remains limited because of a reliance on regulated heavy metals.¹¹⁻¹³ As such, heavy metal-free QDs (e.g., silicon and carbon) have been the subjects of substantial research interest.¹³⁻¹⁶

Silicon stands out among available metal-free candidate materials because of its abundance,¹⁷ compatibility with existing complementary metal-oxide-semiconductor (CMOS) technologies,¹⁸⁻²⁰ established surface chemistry,²¹⁻²⁶ and biocompatibility.²⁷ Luminescent porous silicon and SiQDs were first reported in the 1990s.^{28,29} Since then, countless investigations aiming to understand, tune, and exploit their optical response have appeared.^{6,18,21,30-38} A detailed discussion of SiQD PL and its complexities is beyond the scope of the present contribution but a recent and detailed perspective has been published by Canham.³⁹ Reports claiming SiQD PL quantum yields ranging from 0.3 to 90% have appeared^{23,24,37,40-42} and SiQD PL maxima can be tuned throughout the visible and NIR spectral regions. Typical bandwidths (FWHM) for these emissions are in the range of ca. 40 to 200 nm.^{6,36,38,43-45} For display applications this metric must be narrowed to ≤ 50 nm if requisite color purity is to be achieved. Realizing this goal has obvious benefits for displays and appropriate design could also bring opportunities for new responsive materials that could interface with 'wearable' devices and sensors.

Single nanoparticle analyses of SiQDs has afforded PL FWHM values as narrow as 5 nm, suggesting this performance may be possible if well-defined ‘pure’ materials with narrow size distributions can be realized.^{46–48} Drawing on the established size dependence of SiQD PL, and that single particle analysis shows narrow bandwidth emission, it was reasonable to attempt to narrow the emission bandwidth by targeting size-monodisperse SiQDs using separation methods (e.g., chromatography, density gradient ultracentrifugation).^{30,47} Unfortunately, even these ‘monodispersed’ materials exhibited ensemble PL FWHM of 100 nm. Clearly, alternative approaches toward narrowing SiQD PL FWHM are needed if they are to realize their full practical potential.

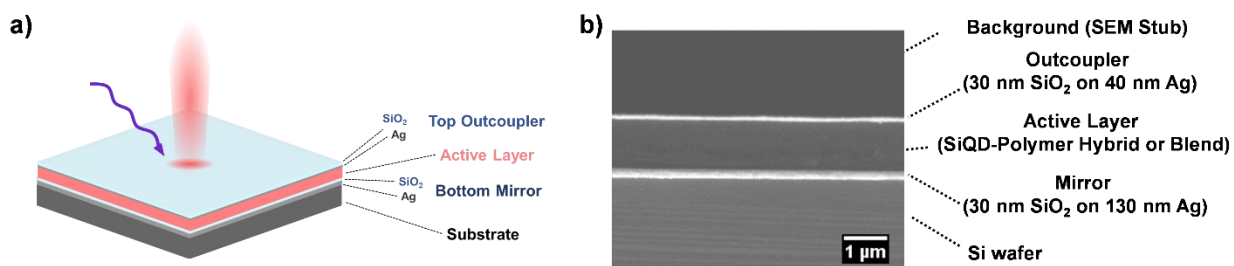


Figure 2.1. Illustration of (a) SiQD-polymer Fabry–Pérot microresonator and (b) a secondary electron SEM image of a representative device cross-section.

Optical structures such as Fabry–Pérot (FP) cavities provide an alternative approach for tuning PL maxima and narrowing spectral linewidths while simultaneously retaining SiQD benefits.⁴⁹ It is also reasonable that such devices could be made compatible with the multilayered structure of modern quantum dot display technologies.⁵⁰ FP cavities possess a layered structure (**Figure 2.1**) and behave like filters. The parallel arrangement of two reflective layers forms a standing wave of the emitted PL and the spectral width of the active layer is reduced to the bandwidth of its resonant mode. The resonant wavelengths (λ_m) are given by

$$\lambda_m = \frac{2}{m} (\sum_i \eta_i d_i \cdot \cos \alpha + 2L_{pen,\alpha}) \quad (2.1)$$

where m is an integer (the mode number), α is the detection angle, and $L_{pen,\alpha}$ is the penetration depth into the metal mirrors.^{51,52} The optical thickness of the active layer is given by the summation term and is here equal to $\eta_{SiO_2} d_{SiO_2} + \eta_p d_p$, where η is the index of refraction, d is the physical thickness, and the subscript p refers to the SiQD-polymer layer.⁵² Following Ref. 51 the penetration depth was estimated as $L_{pen,0} = \lambda(\pi - \beta)/(4\pi)$, where $\beta = \tan^{-1}[\text{Im}(r)/\text{Re}(r)]$ and r is the reflection coefficient which can be obtained from the complex index of refraction.

The utility of this general ‘filtering’ approach was demonstrated by Amans et al. who showed both narrowing and intensification of the PL arising from a layer of Si nanocrystals (SiNCs) obtained from laser decomposition of silane using a dielectric distributed Bragg reflector. While promising, this rigid and fragile complex multilayer structure is impractical for widespread application.⁵³ Hryciw et al. subsequently reported a more straightforward tunable microcavity consisting of a rigid silicon-rich oxide (SRO) active layer consisting of SiNCs within an SiO₂ matrix derived from thermal annealing of ‘SiO_x’. In the final version of the device the SRO layer was sandwiched between reflective silver thin films.⁵⁴ The comparative simplicity of this device raised the possibility of widespread application. However SROs are fragile and fabricated via vapor deposition procedures making the SiNC concentration is difficult to control; additionally the brightness/quantum yield of the associated PL is limited or low.

The recent realization of brightly emitting, high quantum yield colloidal SiQDs^{24,55} and their subsequent inclusion into polymers offer the possibility of combining: the solution processability, ambient and mechanical stability of the polymer,^{36,56} the tunable bright PL of colloidal SiQDs, and the narrow emission bandwidth afforded by FP optical cavities. Herein, we present the preparation of stable luminescent SiQD-polymer hybrids/blends and the convenient

fabrication of the first flexible SiQD-based optical structures. These structures that show narrow (i.e., FWHM = ca. 9 nm) photoluminescence linewidth PL spanning the red to blue spectral regions.

2.2 Experimental Details

2.2.1 Reagents and Materials

Hydrofluoric (Electronic grade, 48–50%) and sulfuric (reagent grade, 95–98%) acids were purchased from Fisher Scientific and Caledon Laboratory Chemicals, respectively. Fuming sulfuric acid (reagent grade, 20% free SO₃ bases), trichlorosilane (99%), toluene (HPLC grade), methanol (reagent grade), ethanol (reagent grade), isopropanol (reagent grade), styrene (99%), 1-dodecene, phosphorus pentachloride (95%), 2,2'-azobis(2-methylpropionitrile) (98%), methyl methacrylate (99%), polystyrene (M_w = ~192,000), and polymethylmethacrylate (M_w = ~97,000) were purchased from Sigma Aldrich. Styrene and methyl methacrylate were purified by passing over neutral alumina immediately prior to use. Dry toluene was obtained from a Pure-Solv purification system and collected immediately prior to use. All reagents and solvents were used as received unless otherwise specified.

2.2.2 Preparation of Hydrogen Silsesquioxane (HSQ)

HSQ was synthesized adapting a literature procedure.⁵⁷ Briefly, a mixture of concentrated (15 mL) and fuming (7 mL) sulfuric acid was diluted with dry toluene (45 mL) under an Ar atmosphere. A solution of dry toluene (110 mL) and trichlorosilane (16 mL) was prepared and then added dropwise to the sulfuric acid mixture over a few hours. The toluene layer was isolated and washed with aqueous sulfuric acid solution. After the organic layer was dried over MgSO₄ (neutralized with CaCO₃ overnight), the solvent was reduced using a rotary evaporator and then evaporated in vacuo to yield a white solid that was stored under vacuum until use.

2.2.3 Preparation of the H-SiQDs

A modified literature procedure was used to prepare H-SiQDs.⁵⁸ Briefly, an appropriate amount of HSQ (e.g., 2 g) was annealed in a standard tube furnace under flowing 5% H₂/95% Ar at 1100 °C. This procedure yielded oxide composite containing Si nanodomains. The resulting composite was ground using an agate mortar and pestle and shaken in a wrist action shaker with high purity glass beads for 24 h. The resulting powder was etched using a 1:1:1 solution of ethanol:deionized water:HF to liberate the H-SiQDs. The resulted emissions can be tuned from red to yellow by varying the etching time (ca. 1 h for red-emitting; ca. 1 h 15 min for orange-emitting; and 1 h 30 min for yellow-emitting SiQDs). The H-SiQDs were extracted by toluene and isolated by centrifugation (3000 rpm, 10 min) and immediately used in polymerization or functionalization procedures noted below.

2.2.4 Synthesis of SiQD-Polystyrene Hybrids (Si-PS).

Si-PS hybrids were formed by simultaneous thermal hydrosilylation and polymerization adapting an established literature procedure.⁵⁹ After etching ca. 0.5 g composite, the resulting H-SiQDs were dispersed in a 1:1 styrene:dry toluene mixture (10 mL in total) in a Schlenk flask equipped with a magnetic stir bar. The suspension was subjected to three freeze-pump-thaw cycles and backfilled with argon. The reaction then took place at 110 °C for ~16 h under an Ar atmosphere. The resulting transparent solution was purified following standard procedure using toluene/ethanol as solvent/antisolvent mixture and centrifugation (11,400 rpm, 20 min). After three cycles of purification, the isolated solid products were dried under vacuum for minimum 12 h and stored in vial for further usage.

2.2.5 Synthesis of SiQD-Poly(methyl methacrylate) Hybrid (Si-PMMA)

Si-PMMA hybrid was synthesized by AIBN-induced hydrosilylation and polymerization as outlined.³⁶ Briefly, a reaction mixture of orange-emitting H-SiQDs (liberated from ca. 0.4 g composite), methyl methacrylate (ca. 4 mL), AIBN (ca. 0.01 g) in dry toluene (ca. 3.6 mL) was prepared in a Schlenk flask equipped with a magnetic stir bar. The suspension was then heated at 60 °C for ~16 h under an Ar atmosphere to yield a clear, viscous solution. The product was diluted with toluene and drop-cast onto an aluminum foil. After drying overnight, orange polymer film was formed and peeled from the foil. The product was stored under ambient atmosphere and used without further purification.

2.2.6 Preparation of SiQD-Polymer Blends

Room temperature etchant initiated hydrosilylation was used to prepare styrene- and dodecyl-functionalized SiQDs.⁵⁵ H-SiQDs obtained from 1 h (red-emitting SiQD) or 1 h 15 min (orange-emitting SiQD) etching of ca. 0.5 g composite was dispersed in dry toluene (ca. 15 mL) in a Schlenk flask equipped with a magnetic stir bar, followed by addition of excess (ca. 5 mL) ligand of choice (i.e. styrene or 1-dodecene). After three freeze-pump-thaw cycles, PCl₅ (ca. 30 mg) was added to the reaction mixture under flowing argon and stirred for 2 h at room temperature to yield a translucent mixture. The reaction was then quenched with methanol (ca. 20 mL). After three dispersion/precipitation cycles using toluene/methanol as the solvent/antisolvent, the wet pellet of as-synthesized SiQDs was dispersed in dry toluene (ca. 2 mL) and filtered through a 0.45 μm PTFE syringe filter to obtain an amber solution. The SiQD solution (ca. 0.7 mL) was used to dissolve the commercial polymers (ca. 0.0565 g polystyrene or 0.063 g PMMA). The blend solution was dried under vacuum, which the resulted solid blends were redissolved in the appropriate amount of toluene to obtain the desired spin-coating concentrations.

2.2.7 Fabrication of Microresonator

The optical cavity devices were fabricated using physical deposition and spin-coating of desired material onto silicon substrates or polyimide film. Briefly, a thick silver mirror (130 nm) followed with a thin SiO₂ oxidation barrier (30 nm) was deposited onto the substrate (1 x 1 cm) by electron-beam evaporation. Prior to spin-coating, the substrates were rinsed with isopropanol/acetone three times and dried with nitrogen. The emissive polymer layers were subsequently spin-coated onto the specimens at various conditions as described in the main text. A thinner silver layer (40 nm) and SiO₂ oxidation barrier (30 nm) were deposited onto the polymer film as output coupler through electron-beam evaporation.

2.2.8 Fourier Transform Infrared Spectroscopy (FT-IR)

FT-IR samples were prepared on a silicon wafer by drop casting from toluene. The spectra were recorded on a Thermo Nicolet Continuum FT-IR microscope.

2.2.9 X-ray Photoelectron Spectroscopy (XPS)

XPS samples were prepared on a copper foil by drop casting from toluene. The measurement was performed with a Kratos Axis 165 Ultra X-ray photoelectron spectrometer. A monochromatic Al K α source operating at 210 W with an energy $h\nu = 1486.6$ eV was used. Survey spectra were collected with an analyzer pass energy of 160 eV and a step of 0.3 eV. For high-resolution spectra, the pass energy was 20 eV and the step was 0.1 eV with a dwell time of 200 ms. All spectra were calibrated to C 1s (284.4 eV) and fit to appropriate spin-orbit pairs using CasaXPS (VAMAS) software with a Shirley-type background to remove most of the extrinsic loss structure. The Si 2p region was fitted to Si 2p_{3/2} and Si 2p_{1/2} components, with doublet area ratio fixed at 2:1 and separated spin-orbit splitting fixed at 0.6 eV.

2.2.10 Gel-Permeation Chromatography (GPC)

GPC samples were prepared by dissolving the hybrids in THF (1mg/mL). The chromatography was performed with THF (flow rate = 0.5 mL/min) using a Viscotek T6000M column and a Viscotek VE 2001 autosampler. The detectors used were a right and low angle light scattering detectors (RALS and LALS, respectively) in a GPC 270 Max dual detector plus a refractive index detector (RI) Viscotek VE 3580. Absolute calibration was performed with a 99 kDa polystyrene standard and checked against a 235 kDa polystyrene standard (Malvern). The GPC data analysis was accomplished via the OmniSEC 4.6 software package.

2.2.11 Refractive Index Determination

A rSi-PS thin film was spin-coated onto a bare Si wafer using the same parameters for fabricating rSi-PS-3500T. The thin film was then measured by a variable angle spectroscopic ellipsometer. The index of refraction was obtained by fitting the data using Cauchy Model. A followed up General Oscillator model fitting was conducted to ensure Kramers-Kronig consistency between ϵ_1 and ϵ_2 in the analysis following the standard operating procedure: https://www.seas.upenn.edu/~nanosop/VAS_Ellipsometer_SOP.htm

2.2.12 Thin Film Thickness Determination

The thicknesses of the thin films were measured and determined by a Zygo optical profilometer.

2.2.13 Photoluminescence (PL) Characterization

Photoluminescence spectroscopy measurements were performed by exciting the samples using an argon ion laser (351 nm) or helium ion laser (488 nm). The photoluminescence was collected by an optic fiber connected to an Ocean Optics USB 2000+ Spectrometer with a spectral range from 300 nm to 1000 nm. A 425 nm long-pass filter (LPF) was used to eliminate scattered light from the excitation source. The spectral response was calibrated using a black-body radiator. Angle-

dependent measurements were conducted by attaching the specimens onto a custom setup which allowed the collection fiber to be rotated around the sample at a constant distance. The optical fiber was positioned normal to the sample unless otherwise specified. The PL spectrum of the laser was obtained by shining the laser directly into the optical fiber while being attenuated with a neutral density filter (NDF) and a 425 nm LPF.

2.2.14 Reflectivity Characterization

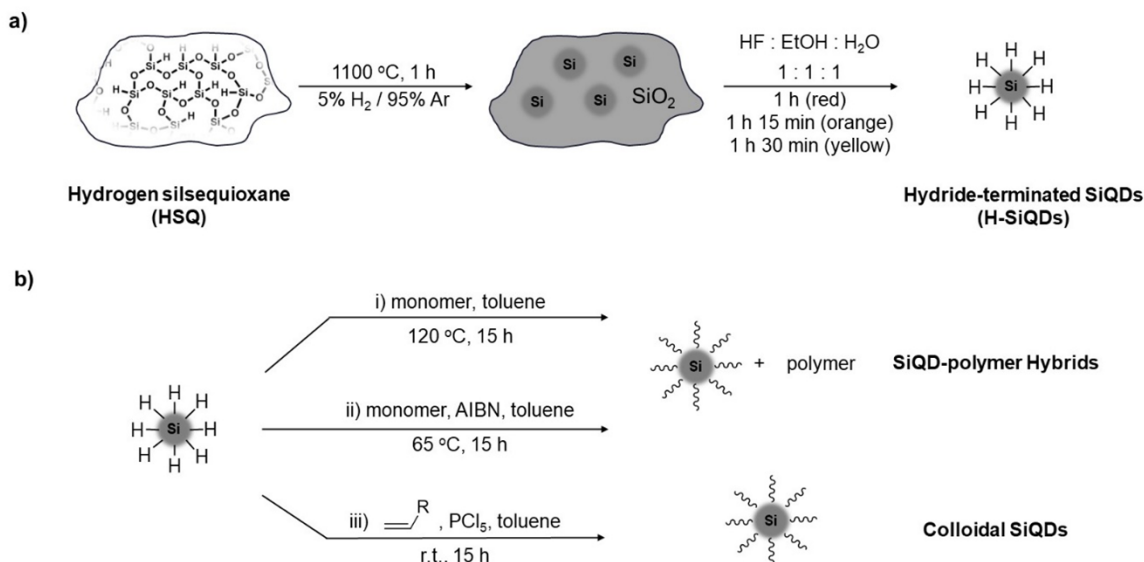
Reflectivity measurements were performed by illuminating the optical device with a black-body radiator. The reflections were collected by an optical fiber connected to an Ocean Optics USB 2000+ Spectrometer with a spectral range from 300 nm to 1000 nm. A 425 nm long-pass filter was used. The spectral response was calibrated using a blank specimen coated with the silver mirror (*i.e.*, 130 nm Ag layer with 30 nm SiO₂ oxidation barrier). The excitation source and detecting fiber were positioned normal to the sample.

2.3 Result and Discussion

2.3.1 Preparation of Si-Polymer Hybrids and their FP resonators

For the present study, the first step in fabricating FP resonators is identifying and preparing appropriate solution processable SiQD-polymer hybrids (or blends). Polystyrene (PS) and poly(methyl methacrylate) (PMMA) were chosen as polymer hosts. Due to their established optical properties (e.g., refractive index and optical clarity), solution characteristics, known compatibility with SiQDs,^{36,59-61} and industrial relevance. Luminescent SiQDs were prepared using well-established procedures developed in our laboratory.^{58,62} A composite consisting of oxide-embedded Si nanodomains was obtained from reductive thermal processing of hydrogen silsesquioxane (HSQ) and ethanolic hydrofluoric acid etching was used to liberate hydride-terminated SiQDs (H-SiQDs) from the oxide matrix (**Scheme 2.1a**).

Scheme 2.1. (a) Preparation of hydride-terminated SiQDs. (b) Synthesis of SiQD-polymer hybrids via i) thermal- or ii) radical-initiated copolymerization of H-SiQDs with the monomer of choice. Synthesis of colloidal SiQDs via iii) PCl_5 initiated hydrosilylation.



This procedure introduces a reactive surface suitable for further derivatization and/or interfacing with the polymer of choice, while also allowing some tailoring of the photoluminescence maximum.^{36,37,59} The H-SiQDs were combined with the monomer of choice (i.e., styrene or methyl methacrylate) and directly copolymerized or functionalized with alkenes (i.e., styrene or dodecene) via an established PCl_5 mediated reaction. The product was physically blended with commercial polymers.⁵⁵ Because our target was to narrow the SiQD PL FWHM using FP cavities, no additional effort was made to narrow the particle size distributions. In all cases investigated here, this procedure yielded uniform, transparent, glassy hybrids/blends that retained the SiQD PL and processability of the host polymer.^{36,59}

FT-IR spectra and X-ray photoelectron (XP) spectra of the associated materials are provided in **Figure 2.2** and **Figure 2.3**, which indicated successful functionalization and passivation of SiQDs. In agreement with previous reports,^{36,59} FT-IR spectra of SiQD-polystyrene

(Si-PS) and SiQD-poly(methyl methacrylate) (oSi-PMMA) hybrids prepared via thermal- or radical-initiated hydrosilylation (**Scheme 2.1b_i** and **b_{ii}**) resembled respective polymer hosts with the absence of Si-H_x stretches or bends. This suggested the formation of bulk materials in which the polymer matrix shielded the signal from the surface of SiQDs. High-resolution C 1s XP spectra (**Figure 2.3a and c**) of the polystyrene hybrids showed C=C (i.e., ~284 eV) and π - π^* (i.e., ~291 eV) signals; indicating the presence of aromatic groups that corresponding to the phenyl ring of the polymer. The two components – SiQDs grafted with PS (higher molecular weight) and free PS (lower molecular weight) – observed from the gel-permeation chromatograms further supported the formation of bulk polystyrene matrix. (**Figure 2.4**). Higher energy emission peaks from the oSi-PMMA C 1s XP spectra (**Figure 2.3e**) corresponded to the carbon species associated with electronegative ester functional group of poly(methyl methacrylate). All polymer hybrids (**Figure 2.3b, d, f**) exhibited emissions from elemental Si (i.e., ~99 eV) in the XP spectra and confirmed the presence of Si nanoparticles. In comparison, Si-H_x stretches at around 2100 cm⁻¹ were present in the FT-IR spectra of colloidal dodecyl- and styrene-terminated SiQDs (Dodecyl-oSi and Sty-rSi, respectively) that were functionalized *via* PCl₅-mediated hydrosilylation. The lower surface functionalization also led to more prominent Si (0) emissions in the corresponding Si 2p XP spectra (**Figure 2.3h and j**). Not surprisingly, dodecyl-oSi only exhibited aliphatic C-C emissions (i.e., 284.8 eV) in the C 1s XP spectrum (**Figure 2.3g**) and Sty-rSi exhibited both C-C (284.8 eV) and C=C (284.4 eV) emissions (**Figure 2.3i**).

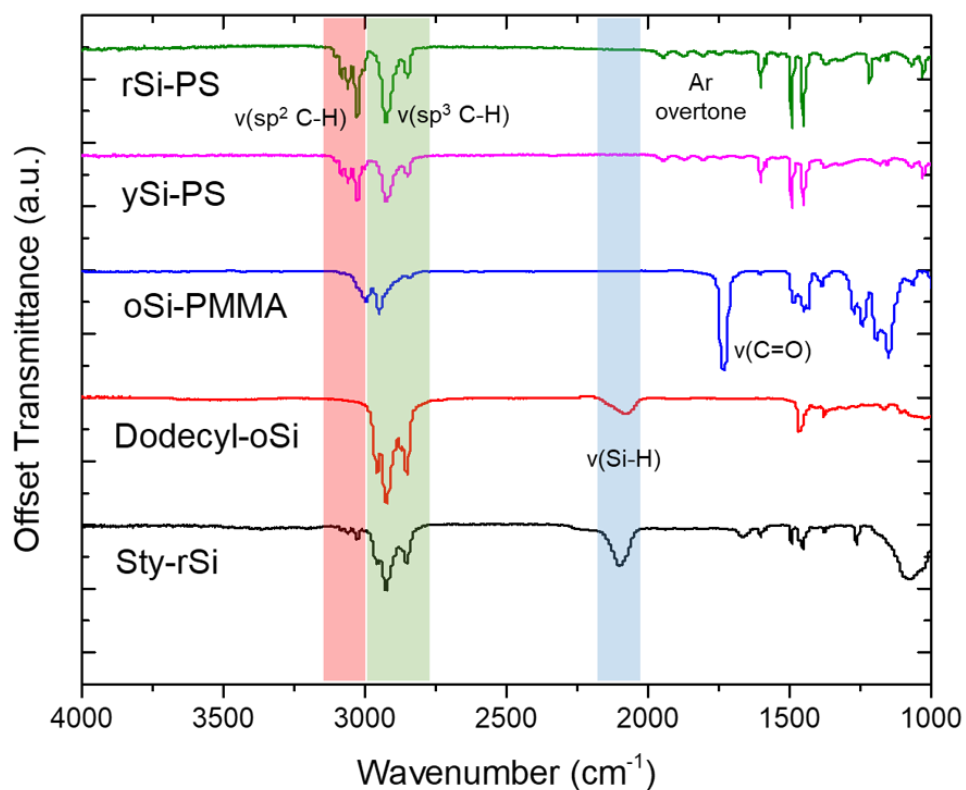


Figure 2.2. FT-IR spectra of red-emitting SiQD-polystyrene (rSi-PS, green), yellow-emitting SiQD-polystyrene (ySi-PS, pink), and orange-emitting SiQD-poly(methyl methacrylate) (oSi-PMMA, blue) hybrid; as well as dodecyl-functionalized (Dodecyl-oSi, red), and styrene-functionalized (Sty-rSi, black) colloidal SiQDs.

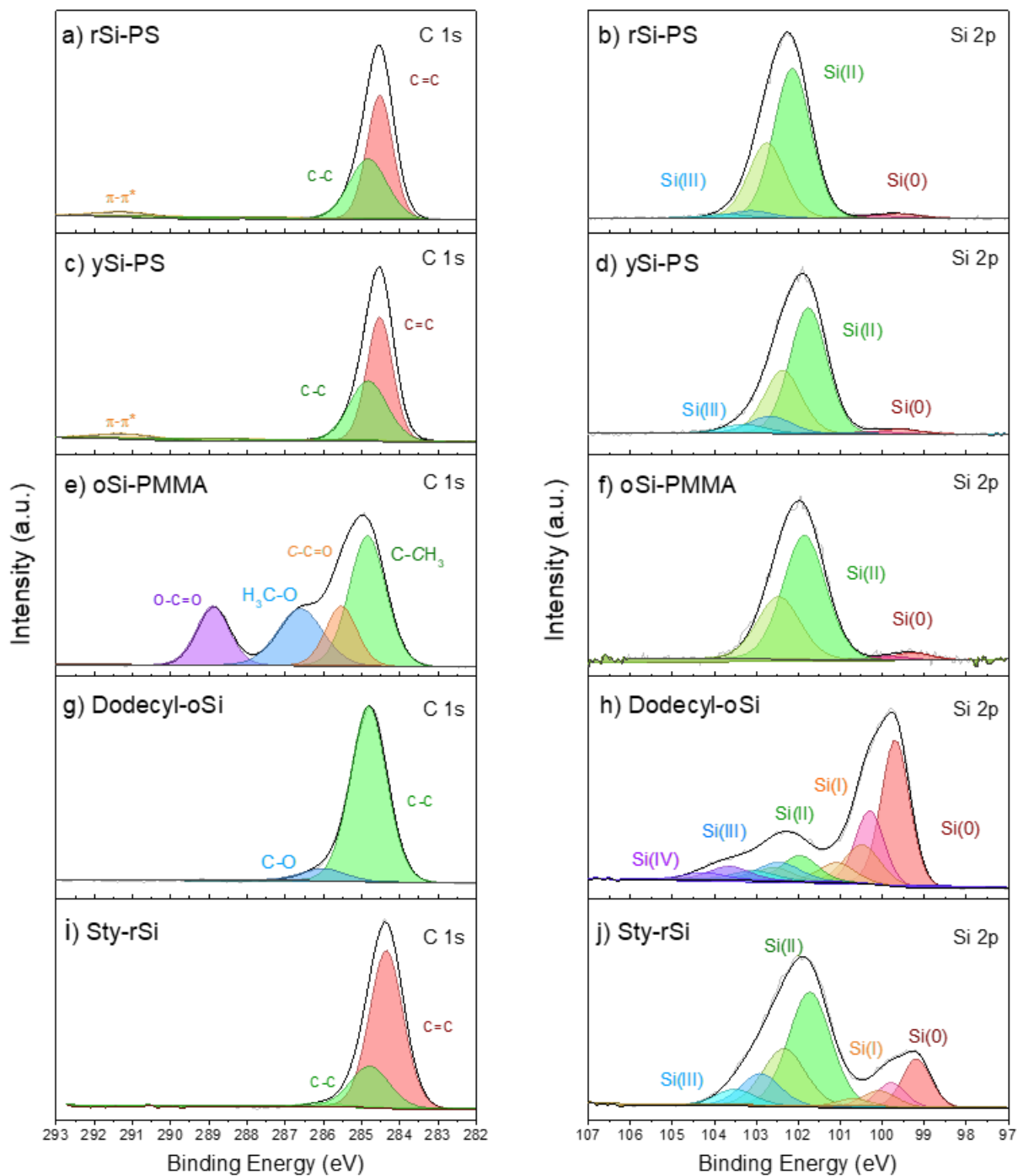


Figure 2.3. High-resolution C 1s XP spectra of (a) rSi-PS, (c) ySi-PS, (e) oSi-PMMA, (g) Dodecyl-oSi, and (i) Sty-rSi. High-resolution Si 2p XP spectra of (b) rSi-PS, (d) ySi-PS, (f) oSi-PMMA, (h) Dodecyl-oSi, and (j) Sty-rSi.

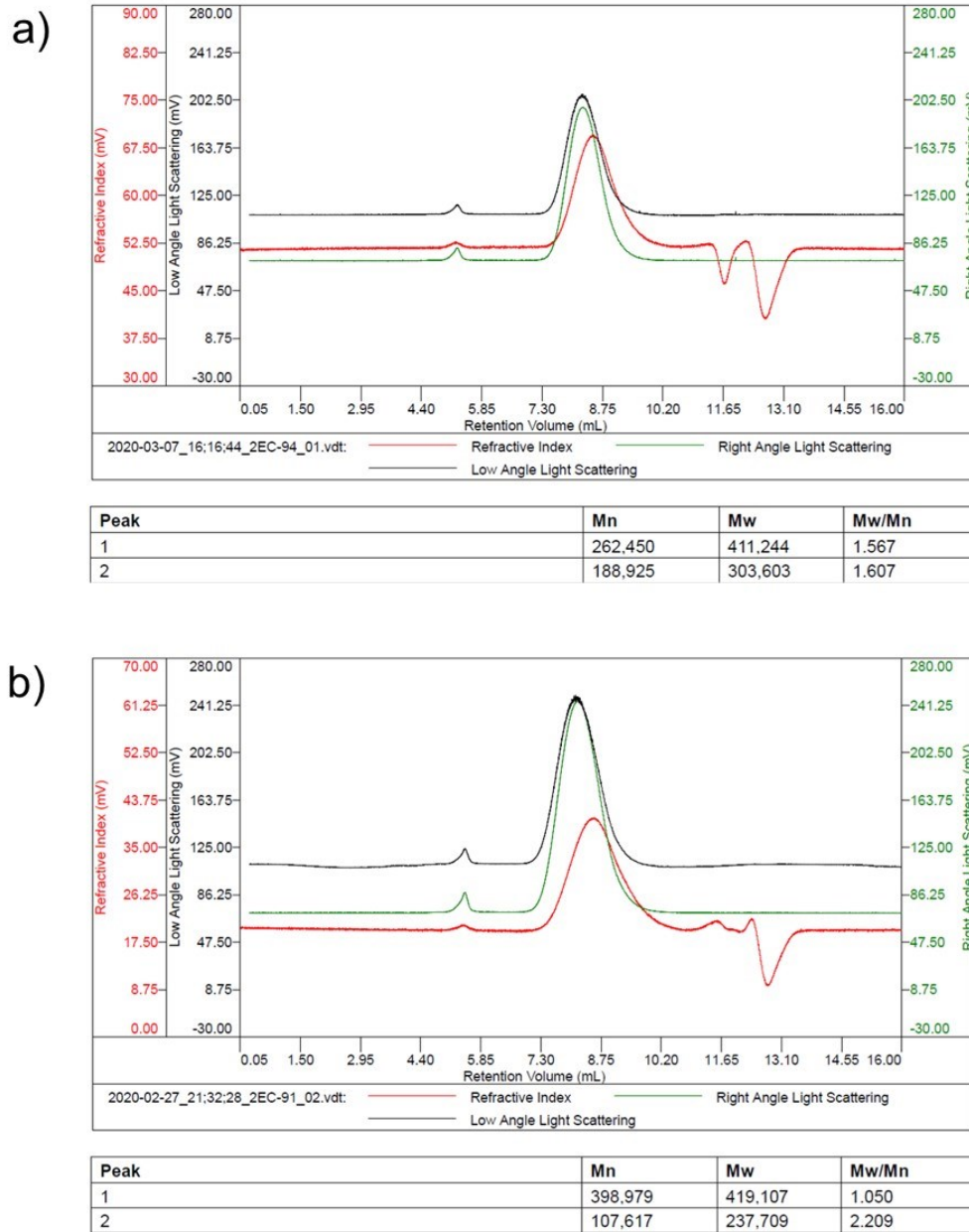


Figure 2.4. Gel permeation chromatogram of (a) rSi-PS and (b) ySi-PS hybrid.

To fabricate FP resonators, layers of silver (130 nm) and SiO₂ (30 nm) were thermally evaporated onto a silicon wafer. Subsequently, the SiQD-polymer solution of choice was spin-coated onto the SiO₂-protected silver mirror to yield thin layers of defined thickness. To complete the cavity another silver (40 nm) layer capped with 30 nm of SiO₂ (i.e., silver outcoupler) was deposited. Silver was selected as the mirror material because of its high reflectivity across the

visible spectrum and its transmittance in the UV that permits photoexcitation of the SiQDs (**Figure 2.5**). The as-prepared resonators possessed the layered structure shown in **Figure 2.1**.

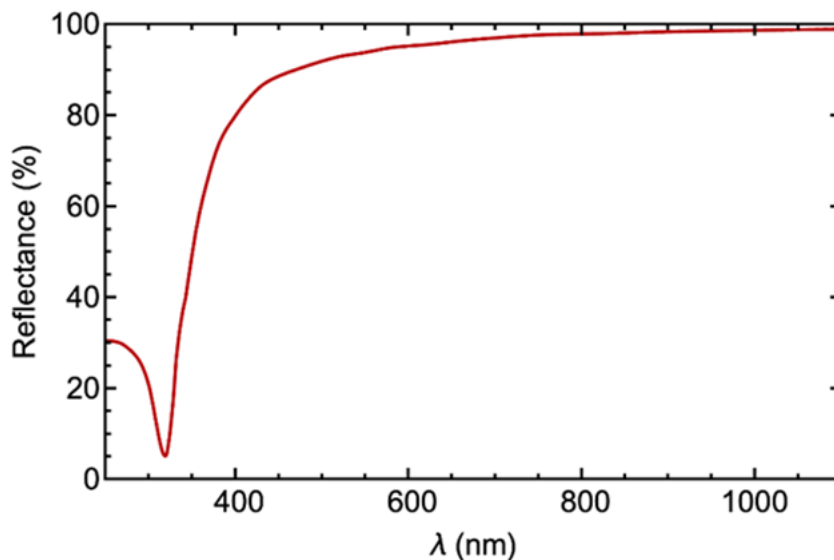


Figure 2.5. Simulated reflectivity spectrum of 40 nm thick silver output coupler.

A ‘red’-emitting covalently bonded SiQD-polystyrene hybrid (rSi-PS), prepared via direct reaction of H-SiQDs with styrene (i.e., thermally-induced hydrosilylation), was the first active layer material investigated.⁵⁹ Solution photoluminescence spectroscopy ($\lambda_{\text{ex}} = 352$ and 364 nm combined UV lines of an Ar ion laser; QDs suspended in toluene) of the rSi-PS yielded a peak emission of 693 nm and FWHM of ca. 124 nm (**Figure 2.6a**, solid line) and was characteristic of SiQDs. Spin-coating a toluene hybrid solution onto a silicon wafer (i.e., no cavity structure) afforded a polymer film that showed a similar response ($\lambda_{\text{em}} = 682$ nm; FWHM ca. 115 nm; **Figure 2.6a**, dashed line). Not surprisingly, the index of refraction of the hybrid was dominated by the polystyrene matrix (e.g., $n = 1.65$ at 350 nm compared to 1.62 for polystyrene, as measured by ellipsometry) (**Figure 2.7a**).⁶³ Introducing a bottom mirror (i.e., half-cavity) provided a weak

interference pattern (**Figure 2.6b**, bottom, dotted line) that arises because of the difference in index of refractive at the polymer/air interface. This observation gave an early indication to the potential of this approach.

Completing the cavity with a top silver mirror outcoupler resulted in a structure that, when excited at 351 nm (and 364 nm), provided a well-defined spectrum of narrow lines (**Figure 2.6b**, bottom, solid line). The intensities of the lines track the original PL envelope of the rSi-PS. By comparison with Equation 2.1, the resonant modes had orders between 8 and 15 with the $m = 10$ line being the most intense. The average FWHM of these resonant modes is ca. 9 nm and corresponds to a 14-fold narrowing of the linewidth for a compared to the parent rSi-PS hybrid in the solid state. The resonant modes were also evident in the cavity reflectance (**Figure 2.6b**, top). The angular dependency of the optical response of the cavity was evaluated whereby the isotropic SiQD PL was directed to the normal of the device surface and 20° from the normal (**Figure 2.7b**). A corresponding blue-shift (ca. 25 nm) arising from the angle-dependence of the cavity was in accordance with Equation 2.1.⁵³

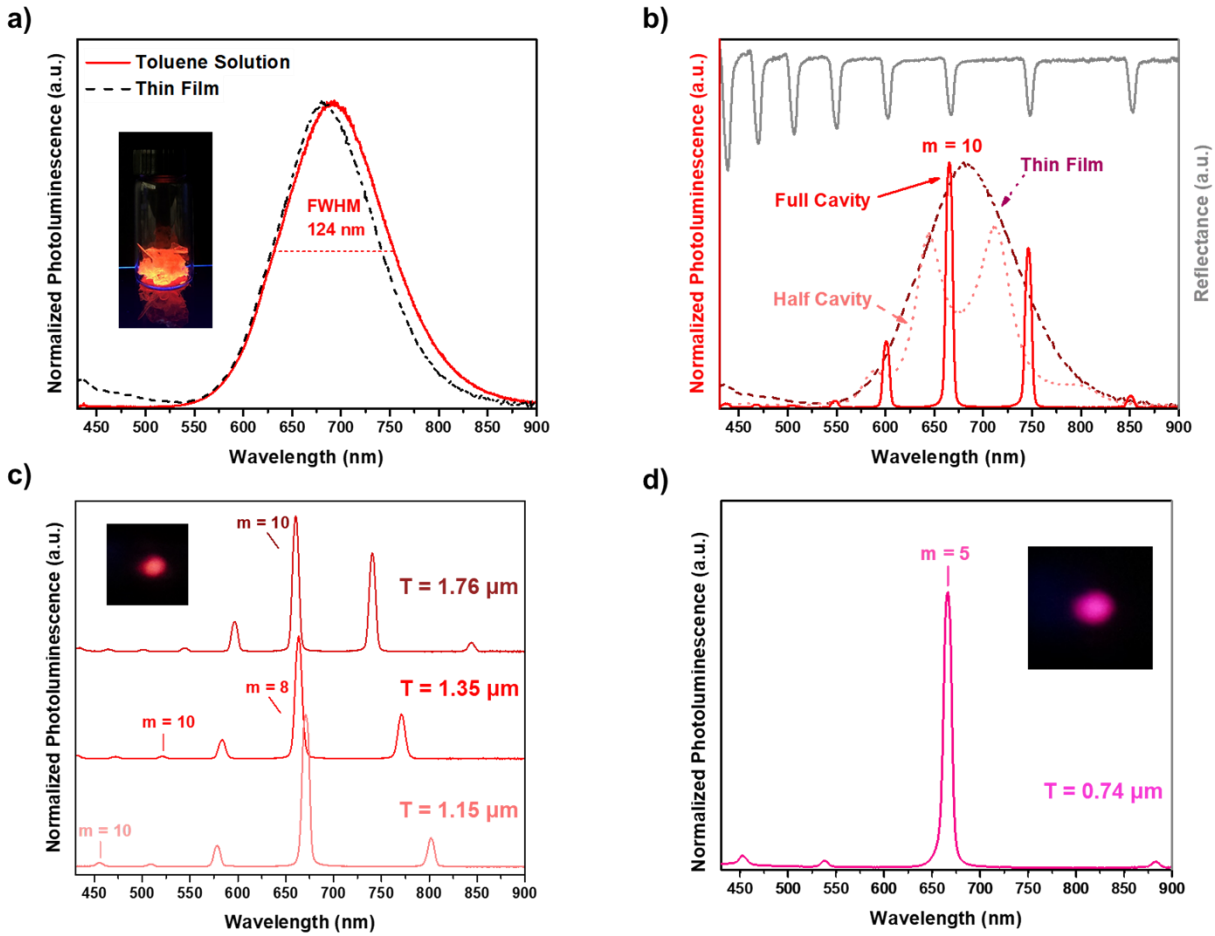


Figure 2.6. (a) Photoluminescence spectra ($\lambda_{\text{ex}} = 351 \text{ nm}$) of rSi-PS. Inset is a photo of the solid hybrid. (b) Luminescence spectra of rSi-PS when incorporated into a half- and a full-cavity (bottom) and reflectance spectrum confirming the resonance modes (top). (c) Tuning the PL spectra of rSi-PS FP microresonator by varying the measured active layer thicknesses through different spin-coating speeds. Inset is a photo of the resonator with a nominally $1.76 \mu\text{m}$ thick active layer. (d) PL spectrum of rSi-PS FP resonator with sub-micron active layer one major emission. The inset is a photo of the resonator.

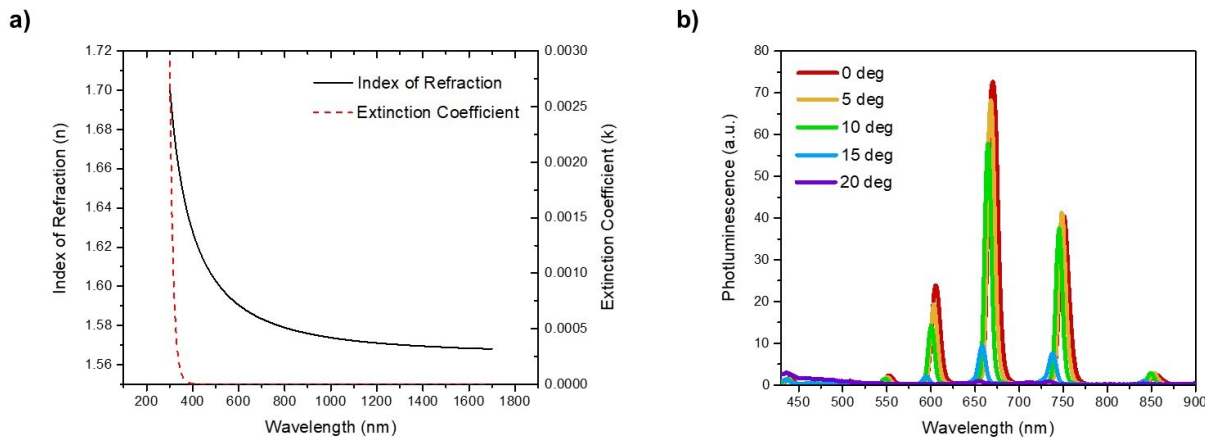


Figure 2.7. (a) Index of refraction and extinction coefficient of rSi-PS. **(b)** Angle-dependent PL spectra of rSi-PS Fabry-Perot resonator ($T = 1.76 \mu\text{m}$).

The solution processability of these polymer hybrids allows for convenient approaches (spin-coating, spray-coating, soft-lithography, etc.)^{64–66} to deposit and texture films and offers tuning of FP cavity response by defining its optical pathlength (OPL). In fact, thin (i.e., sub-1 micron) active layers may offer additional optimization of the emission spectral purity by providing fewer or even only one mode in the luminescence bandwidth. To determine the impact of active layer thickness, we first prepared active layers using different spin rates (**Table 2.1**). **Figure 2.6c** shows representative emission profiles for materials with active layer thicknesses, as measured by profilometry, of $T = 1.76$, 1.35 , and $1.15 \mu\text{m}$. These are reasonably close to the values calculated using Equation 2.1 to produce a match with the observed mode structure using full dispersion ($T' = 1.83$, 1.40 , and $1.20 \mu\text{m}$). The slight disagreement is unsurprising and is almost certainly due to observable variations in the film thickness caused by the spin-coating. For thinner active layers, the principal modes (e.g., most intense modes) were shifted toward shorter wavelengths and peak emission linewidths were consistently ca. 9 nm with Q-factors ca. 70. Note that the Q-factors are dependent upon emission wavelength (**Table 2.2**) and this is attributed to the

established wavelength dependent reflectance of the silver mirrors.⁶⁷ More importantly, thinner active layer thickness effectively increased the free spectral range (FSR) such that it was possible to have only one mode in the PL bandwidth. Although reducing the hybrid layer from 1.7 microns to 1.2 microns increased the average FSR by 27 nm, unfortunately the resulting visible emission remained distributed over numerous lines and could limit spectral ‘purity’. To improve this outcome, we prepared devices with even thinner active layers (i.e., $T = 0.74$ or $T' = 0.77$ μm) through rational variation of the spin-coating solution concentration and spin rate. The spectrum obtained from a representative device is shown in **Figure 2.6d** and displayed 78% of its integrated visible photoluminescence intensity concentrated at an emission peak centered at 666 nm (FWHM ca. 9 nm, $m = 5$).

Table 2.1. Spin-coating conditions for fabricating the SiQD-polymer active layers

Material	Sample [$T = \mu\text{m}$]	Solution Concentration [g material/ mL toluene]	Volume [μL]	Spin Speed [rpm]	Spin Time [sec]
rSi-PS	1.76	0.1	50	1500	30
	1.35	0.1	50	2500	30
	1.15	0.1	50	3500	30
	0.74	0.075	50	3500	80

Table 2.2. Q-factors of rSi-PS resonators

Sample [T = μm]	Resonance Mode	Center Wavelength [nm]	FWHM [nm]	Q-factor
1.76	15	436.00	9.91	43.99
	14	468.20	9.93	47.15
	13	504.85	9.92	50.90
	12	548.29	8.50	64.51
	11	600.34	7.83	76.69
	10	665.29	7.97	83.49
	9	746.09	7.70	96.89
	8	850.70	8.37	101.68
1.35	7	432.28	10.23	42.27
	8	472.25	11.28	41.85
	9	521.21	10.75	48.48
	10	583.68	8.59	67.95
	11	663.91	8.43	78.78
	12	770.99	8.86	87.03
1.15	6	455.65	9.69	47.04
	7	508.49	9.15	55.57
	8	578.70	8.17	70.81
	9	670.80	8.79	76.33
	10	802.14	8.35	96.03

Limited spectral tuning can be achieved through rational variation of the active layer thickness and, as expected, the PL response of the FP resonators clearly tracks the emission envelope of the SiQD-polymer hybrid in the active layer. In this regard, ‘yellow’-emitting covalently bonded SiQD-polystyrene hybrids, ySi-PS, were prepared via prolonged etching (i.e., 1.5 h) of the HSQ-derived composite followed by thermally-induced

hydrosilylation/polymerization (**Scheme 2.1bi**). The toluene solution PL spectrum of the ySi-PS shows a linewidth of ca. 110 nm and maximum intensity at 581 nm (**Figure 2.8a**). Under the same spin-coating conditions for fabricating the rSi-PS cavity with thickness of 1.15 μm , the FP microresonator of ySi-PS had an active layer thickness of ca. 1.32 μm and exhibited the response shown in **Figure 2.8b**. Like its red-emitting counterpart, this cavity afforded a similar Q-factor (~ 64) whereby the emission linewidth was narrowed from ca. 110 nm for a cavity-free thin film to ca. 9 nm when the cavity structure is presented. Comparing with the rSi-PS cavity with similar active thickness ($T = 1.35 \mu\text{m}$) where the strong $m = 8$ mode appears at 664 nm, the yellow QD-polymer sample favors the $m = 7$ mode appearing at 596 nm or modes at even shorter wavelengths. However, despite having a yellow-emitting active layer, the structure prepared in this way appeared bluish to the naked eye because of modes at 454 and 514 nm (**Figure 2.8b**). A similar feature was observed in a blank polystyrene FP resonator (**Figure 2.9**); and we attribute the blue emission bands to the excitation of defect-rich as-deposited SiO_2 (nominally SiO_x) protective layers in the structure. Qualitatively enhanced emissions are observed when cavities are present (**Figure 2.10**); SiO_2 blue emission is amplified more strongly compared to the relatively weak yellow-emitting SiQDs. The relative strength of the blue emission can be attributed to the higher transmittance of the thin silver mirror at shorter wavelengths. While the origin of overall enhancement is a subject of ongoing investigation, we believe that this issue of the device appearing blue can be addressed via increasing the intensity of the emission from the SiQDs by using a thicker active layer or higher SiQD concentration. In this regard, the structure successfully demonstrates potential for tuning the observable PL by changing the sizes of SiQDs therein.

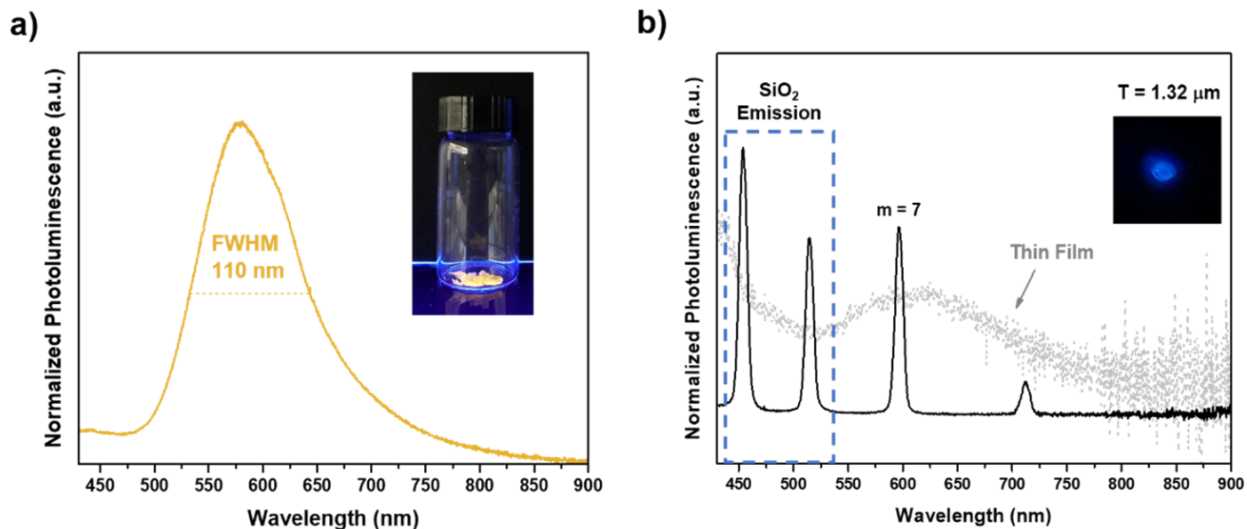


Figure 2.8. Photoluminescence spectra of (a) ySi-PS in toluene, (b) solid state thin film (dotted line), and cavity with an active layer thickness of 1.32 μm (solid line). Inset of (a) is a photograph of the solid hybrid upon UV illumination. A photograph of the ySi-PS FP resonator is shown at inset of (b).

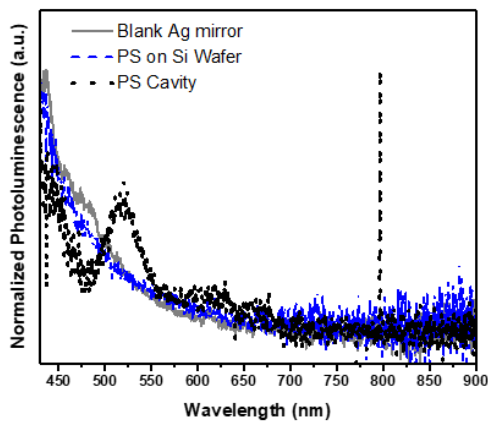


Figure 2.9. PL spectra measured from a blank Ag mirror (solid), PS on a Si wafer (dashed), and a PS cavity indicate presence of background PL signals from the FPR.

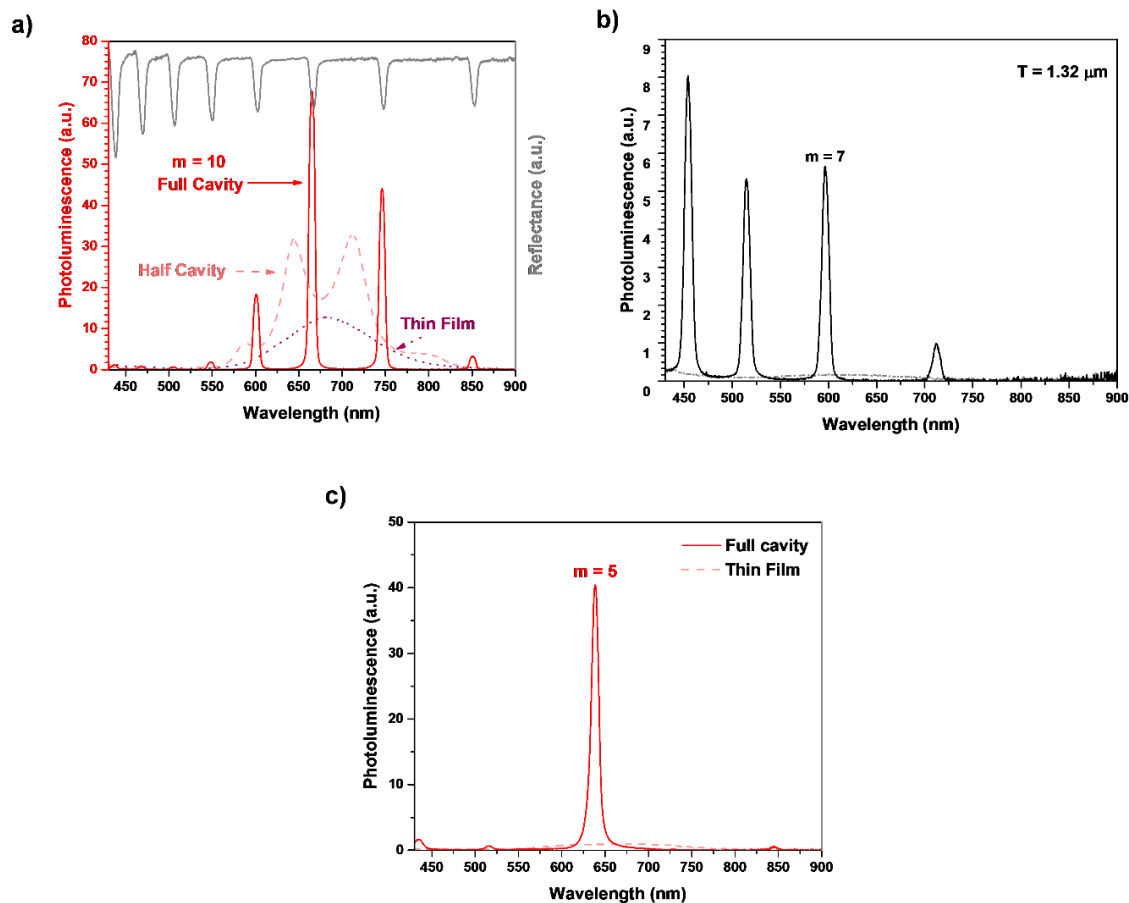


Figure 2.10. Non-normalized PL spectra of rSi-PS (a), ySi-PS (b), and rSi/PS (c) show qualitative enhancement emission intensities in cavity (solid) compared to solid thin film (dashed).

Having demonstrated that narrowing of the linewidth of red and yellow SiQD-based PL is possible, devices based upon poly(methyl methacrylate) (PMMA) were fabricated in order to characterize the effect of the polymer host. An ‘orange’-emitting oSi-PMMA hybrid was synthesized via simultaneous AIBN-initiated polymerization/hydrosilylation (**Scheme 2.1**). This procedure provided a solid, bonded hybrid that exhibits a broad (FWHM ca. 130 nm) emission centered at 637 nm in toluene (**Figure 2.11a**). Using the same parameters as for the rSi-PS devices (**Table 2.3**), the solution was then spin-coated onto the Ag mirror to fabricate the active layer of the FP cavities.. The oSi-PMMA cavities narrowed the emission linewidths to ca. 20 nm (**Figure**

2.11b). The slightly broader FWHM (Q-factor ~ 27) for the PMMA-based devices is attributed to rougher active layers (**Figure 2.12**); this may increase scattering losses or increase the loss into the guided modes. In addition to tuning the emission linewidth, changing the polymer host also allowed greater variation of the optical pathlength of the cavity as thinner films could be more easily fabricated by spin-coating. Unlike the micron-thick PS hybrid films, oSi-PMMA FP resonators with sub-micron active layers ($T = 0.50$ to $0.80 \mu\text{m}$) could be constructed; doing so limited the resonance modes to orders between $m = 4$ and 6 (**Figure 2.11b**). As was the case for the ySi-PS cavities, the oSi-PMMA devices appear blue despite being constructed using orange-emitting active layers. This feature of mixing the blue SiO_2 and orange SiQD PL caused cavities of different thicknesses to appear as different shades of blue. A thicker active layer (i.e., $T = 2.52 \mu\text{m}$) was also fabricated (**Table 2.3**) to increase the SiQD emission intensity, in this case the resulting device visually appeared light pink. Eliminating the SiO_2 -related emissions by using a different capping layer (e.g., TiO_2) can lead to a gamut of red to green cavities as shown by the predicted coordinates in the simulated Commission Internationale de l'éclairage (CIE) 1931 diagram (**Figure 2.13**).

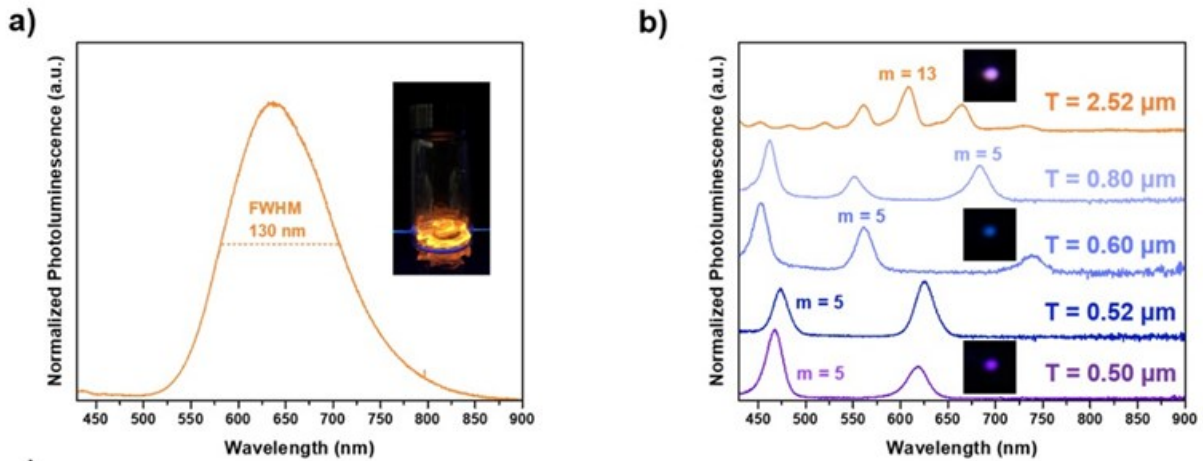


Figure 2.11. Photoluminescence spectra of (a) oSi-PMMA in toluene and (b) FP resonators of the material with various active layer thicknesses. Inset of (a) is a photo of the solid hybrid. Photographs of the $T = 2.52$, 0.60 , and 0.50 μm FP resonators are shown inside (b).

Table 2.3. Spin-coating conditions for fabricating the oSi-PMMA active layers

Sample [$T = \mu\text{m}$]	Solution Concentration [g material/ mL toluene]	Volume [μL]	Spin Speed [rpm]	Spin Time [sec]
2.52	0.2	50	1500	30
0.80	0.1	50	1500	30
0.60	0.1	50	2500	30
0.52	0.1	50	3500	30
0.50	0.075	50	4000	60

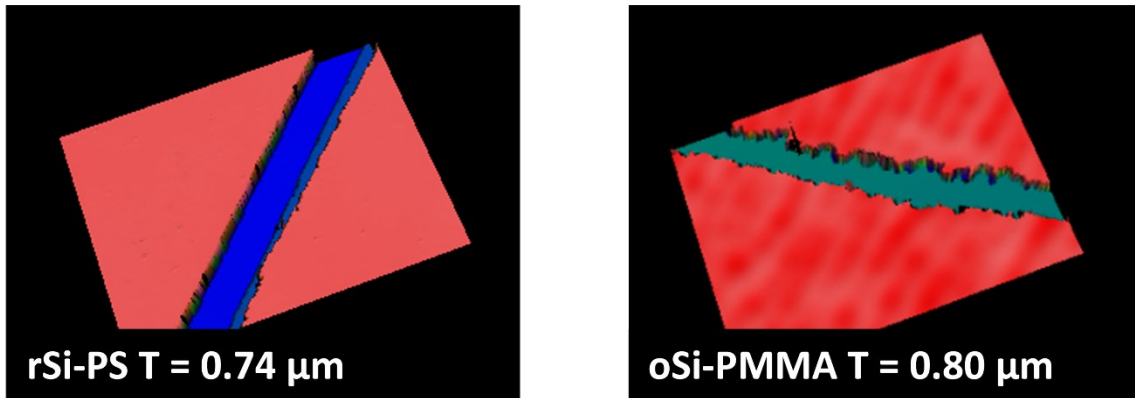


Figure 2.12. Three-dimensional models of representative rSi-PS (left) and oSi-PMMA (right) FPR obtained from optical profilometry.

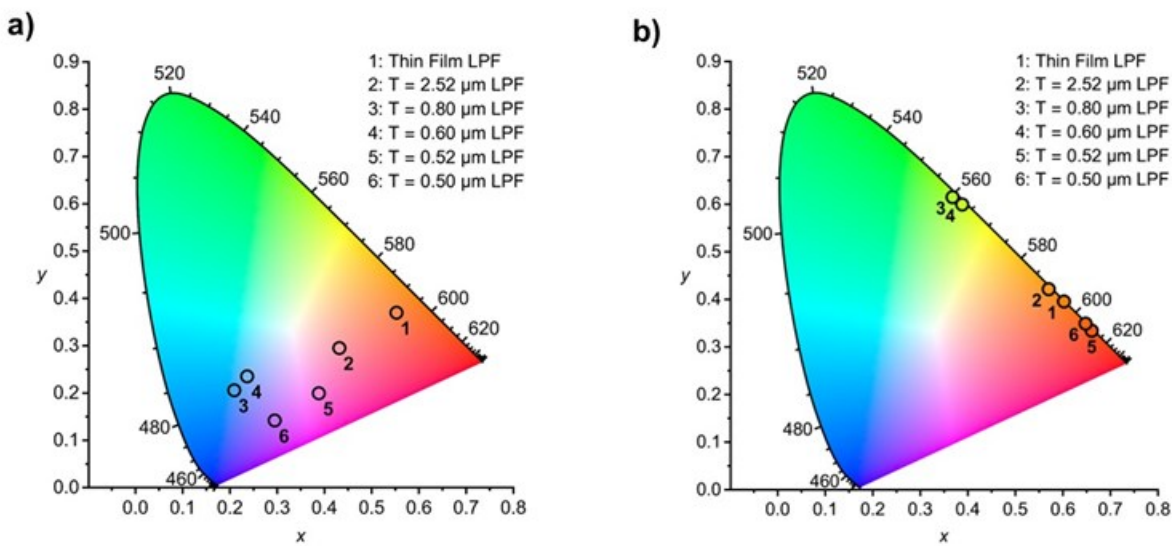


Figure 2.13. CIE 1931 plot of the fabricated oSi-PMMA FP cavity spectra (a) and a simulated diagram of the cavities after removing the SiO₂-related emissions (b).

While active layers made up of covalently bonded hybrids offer potential benefits related to material stability, establishing uniform and thin film formation is important in achieving color purity. There is an obvious appeal in blending highly luminescent, appropriately functionalized SiQDs with commercial polymers in defined polydispersity and molecular weight (M_w). Such materials would be expected to provide predictable film forming properties. Thermally-induced hydrosilylation reactions provide luminescent materials but they do not provide ready access to a range of PL maxima; other functionalization methods providing more efficient emitters that could yield brighter devices.^{24,55} In this regard, we prepared red-emitting styrene functionalized SiQDs using established PCl_5 based reactions (**Scheme 2.1biii**) and solution blended them with commercial polystyrene (avg. $M_w = \sim 192,000$ Da). A uniform ~ 630 nm thin film of the SiQD-polystyrene blend (rSi/PS) was prepared by spin-coating the parent toluene solution (0.075 g/mL toluene, 50 μ L, 3500 rpm, 80 sec). In the absence of a FP cavity structure, the film PL was centered at 665 nm and showed a broad linewidth of ca. 179 nm (**Figure 2.14a**, dash line). As with the full cavity of the bonded hybrids, the photoemission exhibited from the blend device was centered on a single mode ($m = 5$) at 639 nm, with a FWHM ca. 12 nm (**Figure 2.14a**, solid line). Resonators consisting of ‘orange’-emitting dodecyl functionalized SiQDs in commercial polymethylmethacrylate (avg. $M_w = \sim 97,000$ Da), oSi/PMMA, were also fabricated to explore the versatility of the blend FP resonator. The devices successfully reduced the emission of the SiQDs, in this case from ca. 102 nm (**Figure 2.14b**, dashed) to ca. 30 nm (**Figure 2.14b**, solid). Variable cavity response was also observed where, as for example, the $m = 9$ mode red-shifted by ca. 33 nm when the active layer thickness was increased from 1.35 to 1.52 μ m.

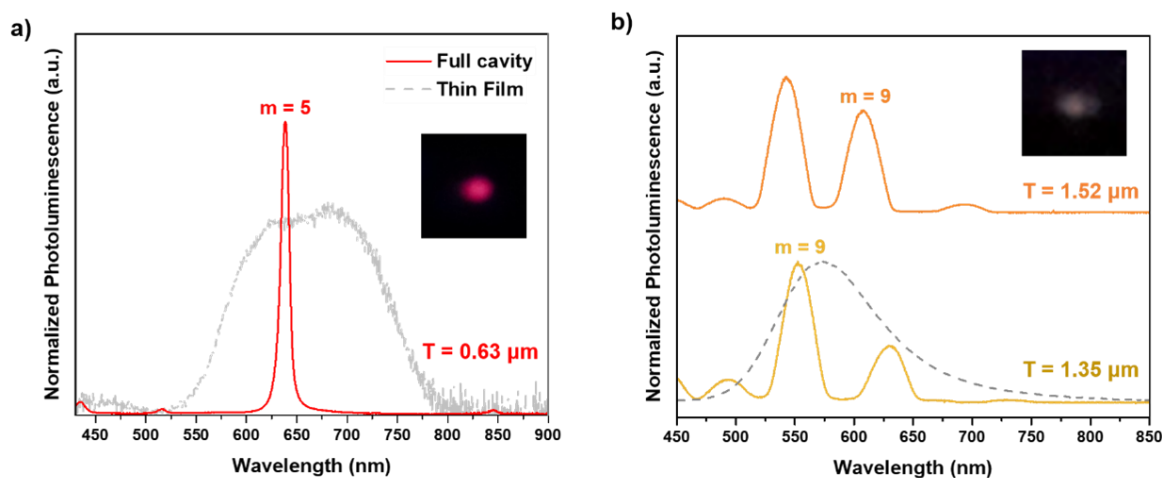


Figure 2.14. PL spectra of (a) ‘red’-emitting SiQDs blended with commercial PS, rSi/PS, thin film (dashed) and the corresponding FP resonator (solid line). (b) Tuning the cavity response of ‘orange’-emitting SiQDs mixed with PMMA by varying the active layer thickness (solid line) and the material’s original PL response (dashed line). Inset of (a) and (b) are the photographs of rSi/PS and oSi/PMMA ($T = 1.52 \mu\text{m}$) resonators.

As summarized in **Figure 2.15a-b** the PL of SiQD hybrids/polymer blends can be readily narrowed and tuned using Fabry–Pérot resonators. Next, we endeavored to incorporate flexible substrates and prepare a bendable FP resonator (**Figure 2.15c**, inset). The structure was fabricated using the same procedures used for constructing the rigid rSi-PS FP resonator with the exception that the Si wafer was replaced by a polymer substrate. The total thickness of the bendable structure was $125 \mu\text{m}$ and afforded a PL linewidth of ca. 11 nm with a single primary emission centered at 704 nm (**Figure 2.15c**, dashed line). The primary emission was minimally affected by bending the substrate to curvatures of ca. 0.74 and 1.57 rad cm^{-1} (**Figure 2.15c**, solid lines).

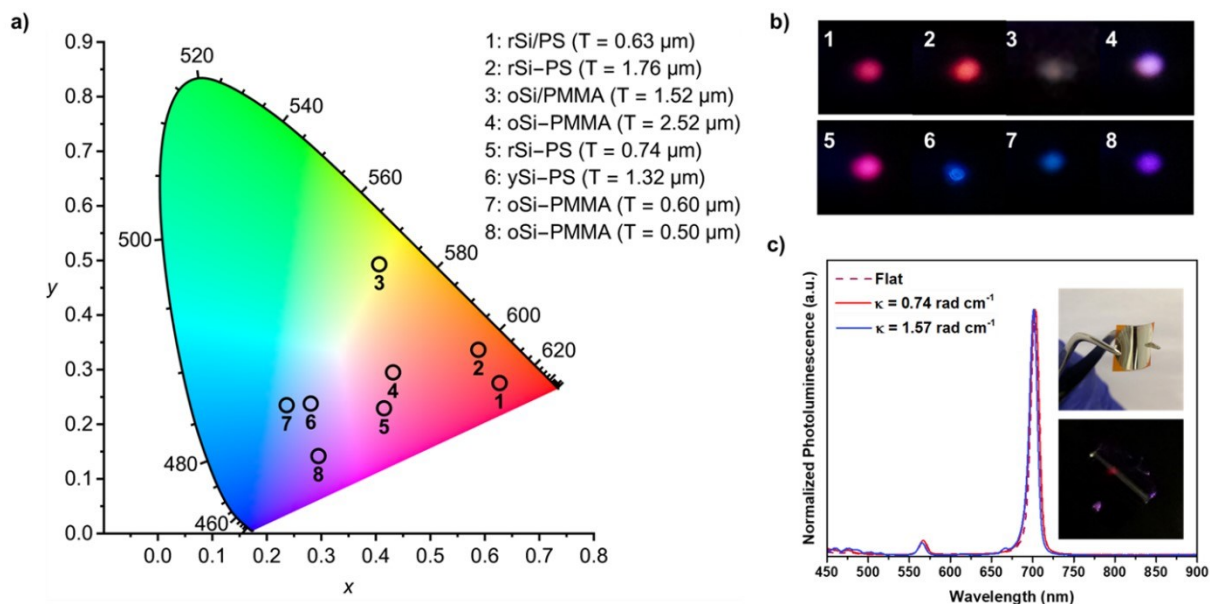


Figure 2.15. (a) CIE chromaticity diagram and (b) representative digital photos showed that the SiQD-polymer hybrid/blend Fabry-Pérot structure. (c) PL spectra of the narrowed emissions from the first bendable SiQD-based FP resonators when it was bent to two different curvatures. Insets are photographs of the bent device under ambient light (top) and being excited by an Ar ion laser in dark (bottom).

2.4 Conclusion

The broad SiQD photoluminescence linewidth was successfully narrowed from over 100 nm down to as narrow as ca. 9 nm using SiQD-polymer based Fabry-Pérot resonators. This was demonstrated on both rigid and flexible substrates. Tuning the emissions of the devices over a range of red and blue PL was achieved by changing the sizes of SiQDs and mixing with another emitter. The emission linewidth was also tunable to ca. 30 nm by changing the polymer host from polystyrene to poly(methyl methacrylate). Of note, the first bendable SiQD-based FPR with a narrowed emission (FWHM ca. 9 nm) was fabricated. This important discovery was based on using polymer hybrids/blends. The proposed Fabry-Pérot resonator using SiQD-polymer hybrid/blends as the active layer was shown to advantageously allow PL tunability via different

sizes of QDs, versatility over different polymer hosts and flexible (i.e, non-rigid) devices. This simple configuration thereby demonstrates potential to be incorporated into optoelectronics as a color filters. This is in accord with SiQDs pushing forward the next generation of non-toxic heavy-metal-free light-emitting technologies.

2.5 References

1. R. Rossetti, S. Nakahara and L. E. Brus, *Journal of Chemical Physics*, 1983, **79**, 1086–1088.
2. V. Colvin, M. C. Schlamp and A. P. Alivisatos, *Nature*, 1994, **370**, 354–357.
3. W. C. Chan, *Science*, 1998, **281**, 2016–2018.
4. I. L. Medintz, H. T. Uyeda, E. R. Goldman and H. Mattoussi, *Nature Materials*, 2005, **4**, 435–446.
5. G. Konstantatos, I. Howard, A. Fischer, S. Hoogland, J. Clifford, E. Klem, L. Levina and E. H. Sargent, *Nature*, 2006, **442**, 180–183.
6. K.-Y. Cheng, R. Anthony, U. R. Kortshagen and R. J. Holmes, *Nano Letter*, 2011, **11**, 1952–1956.
7. J. Song, J. Li, X. Li, L. Xu, Y. Dong and H. Zeng, *Advanced Materials*, 2015, **27**, 7162–7167.
8. M. K. Choi, J. Yang, T. Hyeon and D.-H. Kim, *Npj Flexible Electronics*, 2018, **2**, 10.
9. J. M. Pietryga, Y.-S. Park, J. Lim, A. F. Fidler, W. K. Bae, S. Brovelli and V. I. Klimov, *Chemical Reviews*, 2016, **116**, 10513–10622.
10. X. Dai, Y. Deng, X. Peng and Y. Jin, *Advanced Materials*, 2017, **29**, 1607022.
11. A. M. Derfus, W. C. W. Chan and S. N. Bhatia, *Nano Letter*, 2004, **4**, 11–18.
12. R. Hardman, *Environmental Health Perspect.*, 2006, **114**, 165–172.
13. W. Ke and M. G. Kanatzidis, *Nature Communications*, 2019, **10**, 965.
14. X. Li, M. Rui, J. Song, Z. Shen and H. Zeng, *Advanced Functional Materials*, 2015, **25**, 4929–4947.
15. M. V. Kovalenko, L. Manna, A. Cabot, Z. Hens, D. V. Talapin, C. R. Kagan, V. I. Klimov, A. L. Rogach, P. Reiss, D. J. Milliron, P. Guyot-Sionnest, G. Konstantatos, W. J. Parak, T. Hyeon, B. A. Korgel, C. B. Murray and W. Heiss, *ACS Nano*, 2015, **9**, 1012–1057.
16. S. Morozova, M. Alikina, A. Vinogradov and M. Pagliaro, *Frontiers in Chemistry*, 2020, **8**, 191.
17. J. Emsley, *Nature's Building Blocks: An A-Z Guide to the Elements*, Oxford University Press, New York, 2nd edn., 2011.
18. R. J. Walters, G. I. Bourianoff and H. A. Atwater, *Nature Materials*, 2005, **4**, 143–146.
19. M. J. Sailor and E. C. Wu, *Advanced Functional Materials*, 2009, **19**, 3195–3208.
20. C. Zhang, Y. Xu, J. Liu, J. Li, J. Xiang, H. Li, J. Li, Q. Dai, S. Lan and A. E. Miroshnichenko, *Nature Communication*, 2018, **9**, 2964.

21. M. Dasog, G. B. De los Reyes, L. V. Titova, F. A. Hegmann and J. G. C. Veinot, *ACS Nano*, 2014, **8**, 9636–9648.
22. R. J. Clark, M. K. M. Dang and J. G. C. Veinot, *Langmuir*, 2010, **26**, 15657–15664.
23. Z. Yang, C. M. Gonzalez, T. K. Purkait, M. Iqbal, A. Meldrum and J. G. C. Veinot, *Langmuir*, 2015, **31**, 10540–10548.
24. M. H. Mobarok, T. K. Purkait, M. A. Islam, M. Miskolzie and J. G. C. Veinot, *Angewandte Chemie International Edition.*, 2017, **56**, 6073–6077.
25. M. A. Islam, T. K. Purkait and J. G. C. Veinot, *Journal of the American Chemical Society*, 2014, **136**, 15130–15133.
26. M. Dasog, K. Bader and J. G. C. Veinot, *Chemistry of Materials*, 2015, **27**, 1153–1156.
27. S. Ivanov, S. Zhuravsky, G. Yukina, V. Tomson, D. Korolev and M. Galagudza, *Materials*, 2012, **5**, 1873–1889.
28. L. T. Canham, *Applied Physics Letters*, 1990, **57**, 1046–1048.
29. H. Takagi, H. Ogawa, Y. Yamazaki, A. Ishizaki and T. Nakagiri, *Applied Physics Letter*, 1990, **56**, 2379–2380.
30. W. L. Wilson, P. F. Szajowski and L. E. Brus, *Science*, 1993, **262**, 1242–1244.
31. I. Sychugov, R. Juhasz, J. Valenta and J. Linnros, *Physics Review Letter*, 2005, **94**, 087405.
32. M. Dasog, Z. Yang, S. Regli, T. M. Atkins, A. Faramus, M. P. Singh, E. Muthuswamy, S. M. Kauzlarich, R. D. Tilley and J. G. C. Veinot, *ACS Nano*, 2013, **7**, 2676–2685.
33. R. Sinelnikov, M. Dasog, J. Beamish, A. Meldrum and J. G. C. Veinot, *ACS Photonics*, 2017, **4**, 1920–1929.
34. N. Shirahata, J. Nakamura, J. Inoue, B. Ghosh, K. Nemoto, Y. Nemoto, M. Takeguchi, Y. Masuda, M. Tanaka and G. A. Ozin, *Nano Letter*, 2020, **20**, 1491–1498.
35. A. N. Thiessen, L. Zhang, A. O. Oliynyk, H. Yu, K. M. O'Connor, A. Meldrum and J. G. C. Veinot, *Chemistry of Materials*, 2020, **32**, 6838–6846.
36. A. Marinins, Z. Yang, H. Chen, J. Linnros, J. G. C. Veinot, S. Popov and I. Sychugov, *ACS Photonics*, 2016, **3**, 1575–1580.
37. C. M. Hessel, D. Reid, M. G. Panthani, M. R. Rasch, B. W. Goodfellow, J. Wei, H. Fujii, V. Akhavan and B. A. Korgel, *Chemistry of Materials*, 2012, **24**, 393–401.
38. A. Marinins, R. Zandi Shafagh, W. van der Wijngaart, T. Haraldsson, J. Linnros, J. G. C. Veinot, S. Popov and I. Sychugov, *ACS Applied Materials & Interfaces*, 2017, **9**, 30267–30272.
39. L. Canham, *Faraday Discussions*, 2020, **222**, 10–81.
40. D. Jurbergs, E. Rogojina, L. Mangolini and U. Kortshagen, *Applied Physics Letter*, 2006, **88**, 233116.

41. T. A. Pringle, K. I. Hunter, A. Brumberg, K. J. Anderson, J. A. Fagan, S. A. Thomas, R. J. Petersen, M. Sefannaser, Y. Han, S. L. Brown, D. S. Kilin, R. D. Schaller, U. R. Kortshagen, P. R. Boudjouk and E. K. Hobbie, *ACS Nano*, 2020, **14**, 3858–3867.
42. Q. Li, T.-Y. Luo, M. Zhou, H. Abroshan, J. Huang, H. J. Kim, N. L. Rosi, Z. Shao and R. Jin, *ACS Nano*, 2016, **10**, 8385–8393.
43. B. Ghosh, Y. Masuda, Y. Wakayama, Y. Imanaka, J. Inoue, K. Hashi, K. Deguchi, H. Yamada, Y. Sakka, S. Ohki, T. Shimizu and N. Shirahata, *Advanced Functional Materials*, 2014, **24**, 7151–7160.
44. C. M. Gonzalez and J. G. C. Veinot, *Journal of Materials Chemistry C*, 2016, **4**, 4836–4846.
45. M. Locritani, Y. Yu, G. Bergamini, M. Baroncini, J. K. Molloy, B. A. Korgel and P. Ceroni, *Journal of Physical Chemistry Letter*, 2014, **5**, 3325–3329.
46. M. D. Mason, G. M. Credo, K. D. Weston and S. K. Buratto, *Physical Review Letter*, 1998, **80**, 5405–5408.
47. M. L. Mastronardi, E. J. Henderson, D. P. Puzzo and G. A. Ozin, *Advanced Materials*, 2012, **24**, 5890–5898.
48. I. Sychugov, A. Fucikova, F. Pevere, Z. Yang, J. G. C. Veinot and J. Linnros, *ACS Photonics*, 2014, **1**, 998–1005.
49. N. Hodgson and H. Weber, in *Optical Resonators: Fundamentals, Advanced Concepts and Applications*, eds. N. Hodgson and H. Weber, Springer, London, 1997.
50. V. Wood and V. Bulović, *Nano Reviews*, 2010, **1**, 5202.
51. F. Ma and X. Liu, *Applied Optics*, 2007, **46**, 6247.
52. H. Becker, S. E. Burns, N. Tessler and R. H. Friend, *Journal of Applied Physics*, 1997, **81**, 2825–2829.
53. D. Amans, S. Callard, A. Gagnaire, J. Joseph, F. Huisken and G. Ledoux, *Journal of Applied Physics*, 2004, **95**, 5010–5013.
54. A. Hryciw, J. Laforge, C. Blois, M. Glover and A. Meldrum, *Advanced Materials*, 2005, **17**, 845–849.
55. M. A. Islam, M. H. Mobarok, R. Sinelnikov, T. K. Purkait and J. G. C. Veinot, *Langmuir*, 2017, **33**, 8766–8773.
56. M. Dasog, J. Kehrle, B. Rieger and J. G. C. Veinot, *Angewandte Chemie International Edition*, 2016, **55**, 2322–2339.
57. W. T. Collins, C. L. Frye, Patent US3615272, 1971,
58. C. M. Hessel, E. J. Henderson and J. G. C. Veinot, *Chemistry of Materials* **2006**, **18**, 6139–6146
59. Z. Yang, M. Dasog, A. R. Dobbie, R. Lockwood, Y. Zhi, A. Meldrum and J. G. C. Veinot, *Advanced Functional Materials*, 2014, **24**, 1345–1353.

60. S. K. E. Hill, R. Connell, C. Peterson, J. Hollinger, M. A. Hillmyer, U. Kortshagen and V. E. Ferry, *ACS Photonics*, 2019, **6**, 170–180.
61. M. X. Dung, J.-K. Choi and H.-D. Jeong, *ACS Applied Materials & Interfaces*, 2013, **5**, 2400–2409.
62. J. G. C. Veinot, *Chemical Communications.*, **2006**, 4160–4168.
63. J.-K. Choi, M. X. Dung and H.-D. Jeong, *Materials Chemical and Physics*, 2014, **148**, 463–472.
64. L.-M. Chen, Z. Hong, W. L. Kwan, C.-H. Lu, Y.-F. Lai, B. Lei, C.-P. Liu and Y. Yang, *ACS Nano*, 2010, **4**, 4744–4752.
65. M. Aghajamali, I. T. Cheong and J. G. C. Veinot, *Langmuir*, 2018, **34**, 9418–9423.
66. L. Hou, Q. Hou, Y. Mo, J. Peng and Y. Cao, *Applied Physics Letter*, 2005, **87**, 243504.

Chapter 3

Colloidal Silicon Quantum Dot-Based Cavity Light-Emitting Diodes with Narrowed and Tunable Electroluminescence

A version of the chapter has been published:

Cheong, I. T.; Mock, J.; Kallergi, M.; Groß, E.; Meldrum, A.; Rieger, B.; Becherer, M.; Veinot, J. G. C. *Advanced Optical Materials* 2022, 2201834.

3.1 Introduction

Colloidal quantum dots (QDs) are luminescent nanosized semiconductor particles that feature tunable optoelectronic properties. Following Brus' first report in 1980s,¹ study of colloidal QDs is now a multidisciplinary research area with interests and technological developments in areas such as photovoltaics,^{2,3} sensors,^{4,5} and photocatalysts.⁶⁻⁸ Utilizing electroluminescence (EL) from QDs in light-emitting diodes (LEDs) has attracted a great deal of interest with regards to energy-efficient portable electronics due to the solution processibility, high color-purity, and stability of the materials.⁹⁻¹¹ A significant limitation of commonly studied QD-LEDs is the reliance on non-earth abundant and/or toxic metals such as Cd, In, and Pb.¹²⁻¹⁵ Among the alternatives,¹⁶ Si is attractive because of its abundance, biocompatibility,¹⁷ compatibility with silicon-based electronics,¹⁸⁻²⁰ luminescent properties when formed as QDs, and established/tailorable surface chemistry.²¹⁻²⁶

First reported in the early 1990s and 2000s, the EL of silicon-based nanomaterials (e.g., porous silicon^{27,28} and Si nanocrystals in solid matrices²⁹⁻³¹) had low external quantum efficiencies (EQE) with values ranging from from 10^{-6} to 1 %. Of late, attention has shifted to colloidal silicon quantum dots (SiQDs) as potential active materials in hybrid organic light-emitting diodes (OLED) structures because of their promising EQE of up to 8.6 % for near infrared (NIR) EL and 6.2 % for red EL.¹⁸ Even with these improvements in EQE, the practical potential of SiQD-LEDs remains limited by broad EL bandwidths with full-width-at-half-maximum (FWHM) that can approach 100 nm.^{19, 22, 32-41} Note that display applications require emission bandwidths of ≤ 50 nm to ensure appropriate spectral purity.⁴² Improvements in EL bandwidth will undoubtedly contribute to the development of a variety of display technologies that exploit SiQDs.

Previous studies of SiQD photoluminescence (PL) show that narrow bandwidth luminescence can be achieved; under appropriate conditions, individual SiQDs can exhibit a PL FWHM as narrow as 5 nm.^{43, 44} From this observation alone, it could be surmised that narrow bandwidth emission, be it PL or EL, could be achieved by using well-defined materials of narrow size distributions. A variety of separation methods have been explored to narrow SiQD size distributions (e.g., size-selective precipitation⁴⁵ and density gradient ultracentrifugation⁴⁶) and by extension to reduce the PL FWHM. However, the SiQDs “purified” in these ways still exhibited ensemble PL and EL FWHM of ca. 100 nm.^{34, 38} From these results, it is evident that alternative approaches toward narrowing SiQD EL must be explored in order to realize practical systems for SiQD-based display technologies.

Fabry–Pérot (FP) cavities are planar structures comprising a luminescent layer that is sandwiched between two reflective layers.⁴⁷ Reports show they present a promising approach toward narrowing and tuning the spectral linewidths of QDs in lasers⁴⁸ and LEDs⁴⁹⁻⁵⁴. In these FP cavity structures, the light reflected between the two mirrors interferes; the resulting standing wave consequently reduces the emission spectrum to only the resonant modes of the cavity and narrows the observed emission FWHM. Optical cavities have been used to narrow SiQD emissions.⁵⁵⁻⁵⁷ For example, Amans et al., demonstrated that a distributed Bragg reflector comprising a multilayer dielectric structure that could be used to filter and narrow SiQD PL in order to achieve a FWHM of 13 nm in the 700 nm spectral region.⁵⁵ However, the fragility and complexity of this structure made it impractical for device applications. Recently, Zhang et al. presented an inorganic distributed feedback (DFB) LED of an oxide thin film containing SiQDs that exhibited an EL peak centered at ca. 638 nm with FWHM of ca. 33 nm.⁵⁸ This approach has limitations in that the emission spectrum is ill-defined and the fabrication (i.e., electron-beam lithography) of the DFB

grating is time consuming. Meldrum and co-workers demonstrated that sandwiching vapor deposited oxide-embedded Si nanocrystals (SiNCs) between two reflective metallic layers afforded a more straightforward approach toward PL narrowing. Although FWHM of ca. 10 nm for emissions spanning 480 to 1626 nm was seen; however, individual devices were not fabricated where the broad spectral range was achieved through a gradient thickness of silicon rich oxide.⁵⁶ Recently, we reported comparatively large area (i.e., 1 cm²) FP cavity structures prepared using solution processible SiQD-polymer hybrids and successfully narrowed the PL linewidth from more than 100 nm to ca. 9 nm.⁵⁹ Our approach also enabled a broad color gamut and the realization of the first flexible emissive SiQD-based FP cavity. These advances in optically excited devices provide the groundwork for the present study centered the fabrication of electrically driven self-emissive cavity-LEDs (cLED) based upon colloidal SiQD emitters.

3.2 Experimental Details

3.2.1 Reagents and Materials

Hydrofluoric or HF (Electronic grade, 48–50%) and sulfuric acids (reagent grade, 95–98%) were purchased from Fisher Scientific and Caledon Laboratory Chemicals, respectively. Fuming sulfuric acid (reagent grade, 20% free SO₃ bases), trichlorosilane (99%), toluene (high-performance liquid chromatography (HPLC) grade), methanol (reagent grade), ethanol (reagent grade), isopropanol or IPA (reagent grade), *n*-hexyllithium (2.3 M in hexane), and 1,2-dichlorobenzene were purchased from Sigma Aldrich. Dry solvents were obtained from a Pure-Solv purification system with N₂ as the operating gas. Poly(3,4-ethylenedioxythiophene) polystyrene sulfonate (Al 4038) solution, poly(N,N'-bis-4-butylphenyl-N,N'-bisphenyl), and ZnO nanoparticles (5.6% w/v in IPA) were purchased from Ossila, Solaris Chem, and Infinity PV. All reagents and solvents were used as received unless otherwise specified.

3.2.2 Preparation of Hydrogen Silsesquioxane (HSQ)

HSQ was synthesized adapting a literature procedure.⁶⁰ Briefly, a mixture of concentrated (15 mL) and fuming (7 mL) sulfuric acid was diluted with dry toluene (45 mL) under an Ar atmosphere. A solution of dry toluene (110 mL) and trichlorosilane (16 mL) was prepared and then added dropwise to the sulfuric acid mixture over a few hours. The toluene layer was isolated and washed with aqueous sulfuric acid solution. After the organic layer was dried over MgSO₄ (neutralized with CaCO₃ overnight), the solvent was reduced using a rotary evaporator and then evaporated in vacuo to yield a white solid that was stored under vacuum until use.

3.2.3 Preparation of Hydride-terminated Silicon Quantum Dots (H-SiQDs)

A modified literature procedure was used to prepare H-SiQDs.²² Briefly, an appropriate amount of HSQ (e.g., 2 g) was annealed in a standard tube furnace under flowing 5% H₂/95% N₂ at 1100 °C for 1 h. This procedure yielded oxide composite containing Si nanodomains. The resulting composite was ground using an agate mortar and pestle and shaken in ethanol within a wrist action shaker with high purity glass beads for 16 h. The resulting powder was obtained through vacuum filtration and dried overnight. The composite (300 mg) then was etched using a 1:1:1 solution of ethanol:deionized water:HF (3 mL : 3 mL : 3mL) to liberate the H-SiQDs. After 30 to 60 min, the solution turned pale orange. The SiQDs were then extracted from the aqueous layer using toluene and isolated by centrifugation (3000 rpm for 10 min or 9000 rpm for 4 min). Extracted particles were redispersed in 5 mL dry toluene and centrifuge again to remove residual etchant. The nanoparticle pellet was used immediately after the purification.

3.2.4 Preparation of the Hexyl-terminated SiQDs (Hexyl-SiQDs)

Functionalization of hydride-terminated SiQDs with organolithium reagent was adapted from previous literature procedure.²² Briefly, H-SiQDs obtained after liberation were immediately redispersed in dry toluene (2 mL) and transferred to an oven-dried Schlenk flask. The dispersion was degassed with three freeze-pump-thaw cycles and backfilled with argon. n-Hexyllithium solution (~ 0.4 mmol, ~ 0.2 mL) was immediately added to the reaction mixture. A dark brown solution was obtained after stirring at room temperature for 16 h. A 1 : 1 methanol : ethanol mixture (12 mL) acidified with HCl (~ 0.2 mL, ~12 drops) was prepared in Teflon tubes to act as a quenching solution to terminate the reaction. The functionalized particles were precipitated by dropwise addition of the reaction mixture into the quenching solution. The particles were then isolated *via* centrifugation (9000 rpm, 10 min). The solid pellet was resuspended in a minimum amount of toluene (~ 0.5 mL) and re-precipitated with the alcoholic mixture again. The purification cycle was repeated. The purified SiQDs were redispersed in benzene (2 mL), filtered through a 0.20 μm PTFE syringe filter, and freeze-dried. The hexyl-SiQD powder was ready to use or transferred into the glovebox for storage.

3.2.5 SiQD LED Fabrication

Normal SiQD LEDs were fabricated on prepatterned ITO (15 Ω/sq , 120 nm) glass substrates following Mock, *et al.*'s work.²² A poly-TPD solution (5 mg/mL in dry dichlorobenzene) and a diluted ZnO nanoparticles solution (1:3 weight ratio in dry isopropanol) were prepared a day ahead. All substrates were cleaned using sonication (10 min at 60 °C) using the following solutions in the order listed: detergent water, acetone, and isopropanol. Residual IPA on the substrates was removed with pressurized N₂ and with further drying on a hot plate at 140 °C for 2 min. To improve the wettability of the PEDOT:PSS aqueous solution, the PEDOT:PSS stock was diluted with

isopropanol (3:1 weight ratio) and filtered through a 0.45 μm regenerated cellulose filter immediately prior to deposition. The PEDOT:PSS layers (20 nm) were fabricated by static spin-coating ($\sim 70 \mu\text{L}$, $\sim 3000 \text{ rpm}$, 30 sec) and annealed for 10 min at 140 $^{\circ}\text{C}$ in ambient condition. Subsequently, the substrates were transferred into a nitrogen-filled glovebox for further processing. The poly-TPD layers (10 nm) were then fabricated by static spin-coating ($\sim 70 \mu\text{L}$, $\sim 4000 \text{ rpm}$, 30 sec). A freshly prepared SiQD solution (15 mg/mL in dry toluene) and the diluted ZnO nanoparticles solution were passed through 0.2 μm PTFE syringe filters. A 35 nm thick SiQD layer was obtained through dynamic spin-coating ($\sim 70 \mu\text{L}$, $\sim 4000 \text{ rpm}$, 30 sec). A ZnO layer (25 nm) was also fabricated through dynamic spin-coating ($\sim 100 \mu\text{L}$, $\sim 3000 \text{ rpm}$, 30 sec). Each layer was annealed at 140 $^{\circ}\text{C}$ for 10 min immediately after spin-coating. A $3 \times 3 \text{ mm}$ device area was defined via a shadow mask when depositing the Ag top electrodes (3 \AA s^{-1} , $<10^{-5} \text{ mbar}$). The Leybold Univex 350 PVD system used in this process was directly attached to the glovebox to avoid any material degradation. Finally, for further protection, a thin glass slide was glued on top of the SiQD LED, using an Araldite 2011 two-component epoxy resin.

3.2.5 SiQD Cavity-LED (SiQD-cLED) Fabrication

Cavity LEDs with structure of glass/Ag/SiO₂/ITO/PEDOT:PSS/Poly-TPD/SiQDs/ZnO/Ag were fabricated on blank glass substrates. All substrates were cleaned with acetone and isopropanol sonication baths, and subsequently blow dried with pressurized N₂ to remove solvent residues. The Ag output coupler (3 \AA s^{-1} , $<10^{-6} \text{ mbar}$) and the SiO₂ spacer (1.5 \AA s^{-1} , $<10^{-5} \text{ mbar}$) were then either thermally, or electron-beam evaporated onto the clean glass substrate. The ITO electrode (100 nm, 3.3 \AA s^{-1} , 4 μbar) was next sputtered onto the bottom layers via a patterned shadow mask. Lastly, the PEDOT:PSS, Poly-TPD, SiQDs, ZnO, and Ag top mirror electrode were fabricated using the same procedure as making the normal SiQD LED.

3.2.6 Fourier Transform Infrared Spectroscopy (FT-IR)

FT-IR spectrum was acquired with a liquid nitrogen-cooled Bruker Vertex 70 A on an attenuated total reflection module and a resolution of 4 cm^{-1} . The spectrum was processed by the software Opus.

3.2.7 Thermal Gravimetric Analysis (TGA)

TGA samples were prepared by freeze-drying SiQDs in benzene to obtain an orange powder. The measurement was carried out by a Netzsch TG 209 F 1 Libra inside a glovebox with the sample in an aluminum oxide pan. The heat rate was $10\text{ }^{\circ}\text{C min}^{-1}$ from 30 to $750\text{ }^{\circ}\text{C}$ under an argon flow of 20 mL min^{-1} . The data was processed with the software Netzsch Proteus 6. Surface area calculation was calculated by the equations in Appendix B.

3.2.8 X-ray Photoelectron Spectroscopy (XPS)

XPS samples were prepared by drop-casting benzene suspensions of the SiQDs on a copper foil. A Kratos Axis 165 Ultra X-ray photoelectron spectrometer was used to obtain survey and high-resolution spectra. A monochromatic Al $K\alpha$ source (140 W) with a set energy (1486.6 eV) was used to obtain the spectra. The electron takeoff angle for the spectra was 90° . The Si 2p spectra were calibrated to the aliphatic C 1s signal (284.8 eV) using CasaXP (VAMAS) software and using a Shirley-type background. To fit the Si 2p high-resolution spectrum to Si 2p_{3/2} and Si 2p_{1/2} components, the doublet area was fixed at a 2:1 ratio and separated by a spin-orbit splitting (0.61 eV). The spectra were fit using a symmetric Gaussian-Lorentzian line shape splitting into different energies.

3.2.9 Transmission Electron Microscopy (TEM)

TEM samples were prepared by drop-casting benzene suspension of the SiQDs onto a lacey carbon grid and solvent was evaporated in a vacuum chamber. The bright-field TEM images were acquired using a JEOL-2012 electron microscope equipped with LaB6 filament and operated at an accelerating voltage of 200 kV. Particle size distribution was calculated by counting at least 300 particles using ImageJ software. The corresponding average shifted histogram (ASH) was plotted using a web-application accessed at <http://maverick.chem.ualberta.ca/plot/ash>.⁶¹

3.2.10 Photoluminescence (PL) Characterization

Samples for the optical measurements were prepared by placing the SiQD benzene solution inside a quartz cuvette. The PL spectrum was recorded using an Avantes AvaSpec 2048 spectrometer coupled with a Prizmatix light source ($\lambda_{\text{ex}} = 365 \text{ nm}$) and processed with the software Avasoft 8. UV-Vis absorption spectrum was acquired by a Varian Cary 50 Scan spectrometer. The absolute quantum yield value was obtained using a Hamamatsu Absolute PL Quantum Yield C11347 spectrometer equipped with an integrated sphere. The measured values were calculated by the supplied software as outlined in Appendix C.

3.2.11 Reflectivity Characterization

The reflectance spectra of the Ag layers and cLEDs were measured by an AvaSpec 2048 spectrometer with a spectral range from 175 to 1300 nm. An AvaLight-DH-S-BAL ($\lambda = 215 - 2500 \text{ nm}$) was used as the excitation source, where the source and reflections was collected by a reflection probe positioned normal to the sample. The reflections of the Ag thin films were calibrated using a Thorlabs PF10-03-P01 mirror (Avg. reflectivity of ca. 97% at 700 nm); the cLED reflections were calibrated to a specimen coated with the 100 nm silver mirror.

3.2.12 Thin Film Characterizations

Profilometry measurements of LED layer thicknesses were measured over a thin cut on the reference films using a Bruker DektakXT stylus profilometer. The ITO work function was measured by Kelvin probe KP020 from KP Technology. Atomic force microscopic (AFM) images were recorded using Veeco Dimension Icon in tapping mode and analyzed with Gwyddion software. Refractive indices of the layers were collected a Woollam alpha-SE ellipsometer under angles of 65° , 70° , and 75° in the wavelength range from 380 nm to 900 nm. The data of ITO thin film was fitted with the Drude-Lorentz-model and the other active layers were fitted with the Cauchy-model.

3.2.13 Simulation of Reflection Spectra

The theoretical reflection spectra were simulated by TFCalc. The incident beam was set to be 700 nm wavelength illuminating with normal to the surface of the cavity. The substrate was set to be a 1.0 mm thick glass followed by cLED layers (e.g., Ag output coupler, SiO₂, ITO, PEDOT:PSS, etc.) added as front layers. The spectra were calculated using the experimental refractive indices of the materials meanwhile cavity thicknesses varied by SiO₂ thicknesses.

3.2.14 LED Characterizations

The electroluminescence spectra of the control SiQD-LED were collected by a calibrated AvaSpec-ULS2048 X 64 TEC spectrometer (Avantes) coupled with a Thorlabs IS200-4 integrating sphere. A two-channel Keithley 2602A source measure unit was used for characterizing the device's electronic properties. Coupled with the same AvaSpec spectrometer, the EL spectra of the cLED were collected with an optical fiber positioned at the normal. A two-channel Keithley 2636 source measure unit and a Thorlabs FDS10X10 photodiode were used for characterizing the

devices opto-electronically. The measurements were controlled and analyzed with Matlab, where detailed calculation of EQE was shown in Appendix D.

3.2.15 Cavity Analyses

The simulated transmittance spectra of the SiQD-cLEDs were calculated by software TFCalc35 with the experimental refractive indices of the active layers. More detailed calculations of the cavity FWHM, quality factor, and finesse can be found in the Appendix A.

3.3 Result and Discussion

The SiQDs used in the present cavity LED study were prepared using established procedures developed in our laboratories (**Scheme 3.1a**). These procedures afford well-defined particle sizes and tailored surface chemistry suitable for material device incorporation and performance. Organolithium reagent (OLR)-mediated surface passivation (**Scheme 3.1b**) was identified as the method of choice for introducing functionality to the surfaces of SiQDs.^{21, 26} OLR chemistry introduces a comparatively low number of surface bonded molecules (vs. thermally-induced hydrosilylation functionalization)⁶² through which carrier injection occurs more readily and facilitates dense packing of QDs; these factors are, in combination, expected to provide suitable film conductivity for SiQD cLEDs.²² For this reason, we chose to install a comparatively short surface group (i.e., hexyl; C₆ chain) in the presented SiQD LEDs.

The FT-IR spectrum of Hex-SiQDs (**Figure 3.1a**) shows the expected C-H_x stretching (ca. 2922 cm⁻¹) and bending (ca. 1465 cm⁻¹) arising from surface bonded hexyl moieties. We also note Si-H_x related features (ca. 2077 cm⁻¹), as well as some limited surface oxidation appearing as Si-O stretching (ca. 1044 cm⁻¹). Thermogravimetric analysis (TGA) showed 30% weight loss in the temperature range of 300 to 400 °C (**Figure 3.1b**); this corresponds to an approximate 52% surface

ligand coverage and is consistent with the expected limited degree of surface passivation afforded by OLR modification (**Table 3.1**).

Scheme 3.1. Schematic representation of the synthesis of Hex-SiQDs used in the present investigation. **(a)** Preparation of H-SiQDs from thermally processed hydrogen silsesquioxane. **(b)** Functionalization of H-SiQDs upon reaction with 1-hexyllithium to yield Hex-SiQDs.

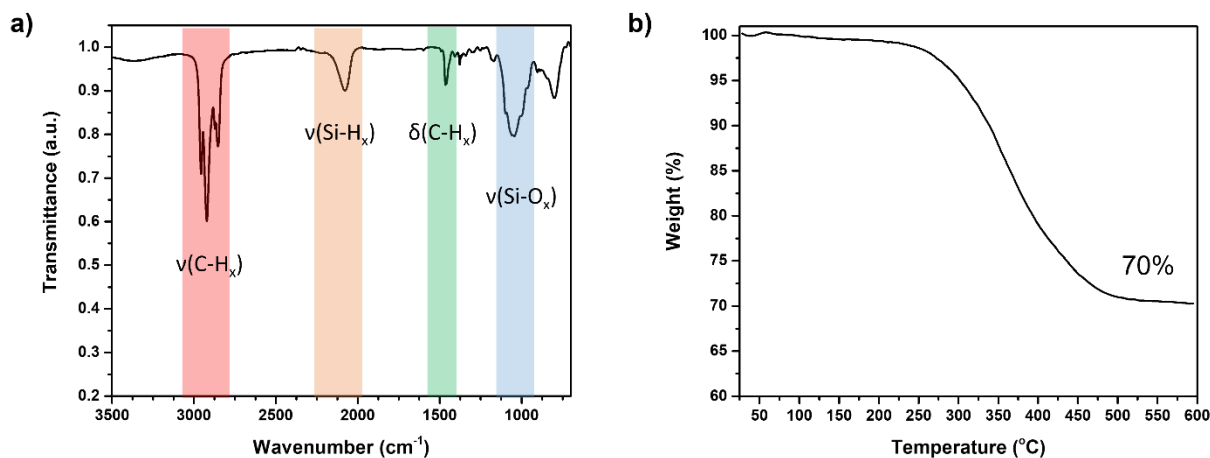
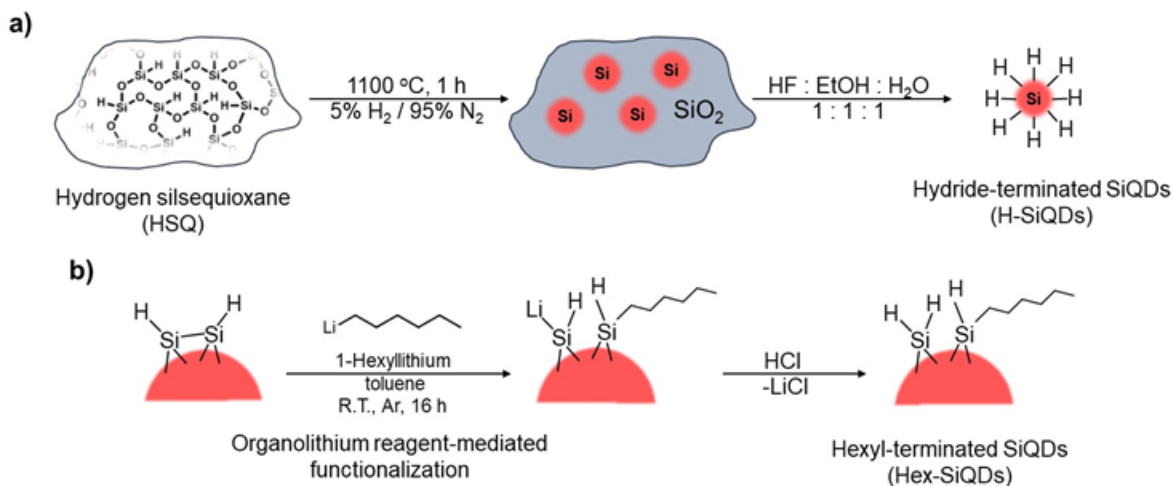


Figure 3.1. **(a)** FT-IR spectrum and **(b)** TGA of Hex-SiQDs.

Table 3.1. Comparing surface coverage of SiQD functionalized via different methods.

Functionalization Method	OLR (this work)	Radical initiated-hydrosilylation	Phosphorus pentachloride	Thermally-induced hydrosilylation*
Size of SiQDs (nm)	2.78, 3.1, ²¹ 3.5 ²²	3.1	3.4, ⁶³ 3.3 ⁶⁴	3.4
Ligand	Hexyl-	Hexyl-	Pentyl- / Dodecyl-	Dodecyl-
% Coverage	52, 51, ²¹ 48 ²²	71 (for 15 h reaction time) ²¹	82 (for 2 h reaction time) ⁶³ / 44 (for 2 h reaction time) ⁶³ , 37 (for 9 h reaction time) ⁶⁴	73.8 ⁶³

** It should be noted that thermally-induced hydrosilylation results surface oligomerization of ligands that passivate the surfaces and prevent carrier injection.⁶²

X-ray photoelectron (XP) spectra were acquired to probe the composition of, and element speciation within the Hex-SiQDs. The survey spectrum revealed the presence of only C (59.16 atomic %), Si (26.32 atomic %), O (14.52 atomic %), and traces of F arising from HF-etching (**Figure 3.2a**). The deconvoluted high-resolution Si 2p XP spectrum was calibrated to C 1s XP spectrum (**Figure 3.2b**) and showed a dominant Si (0) contribution at 99.3 eV indicating the elemental Si was preserved during functionalization (**Figure 3.2c**). Bright field TEM (BF-TEM) imaging (**Figure 3.3a**) provided a mean diameter of Hex-SiQDs of 2.78 ± 0.37 nm while PL spectroscopy of benzene dispersion provided an emission maximum of 726 nm with a FWHM of 144 nm (**Figure 3.3b**) and a quantum efficiency of 26%.

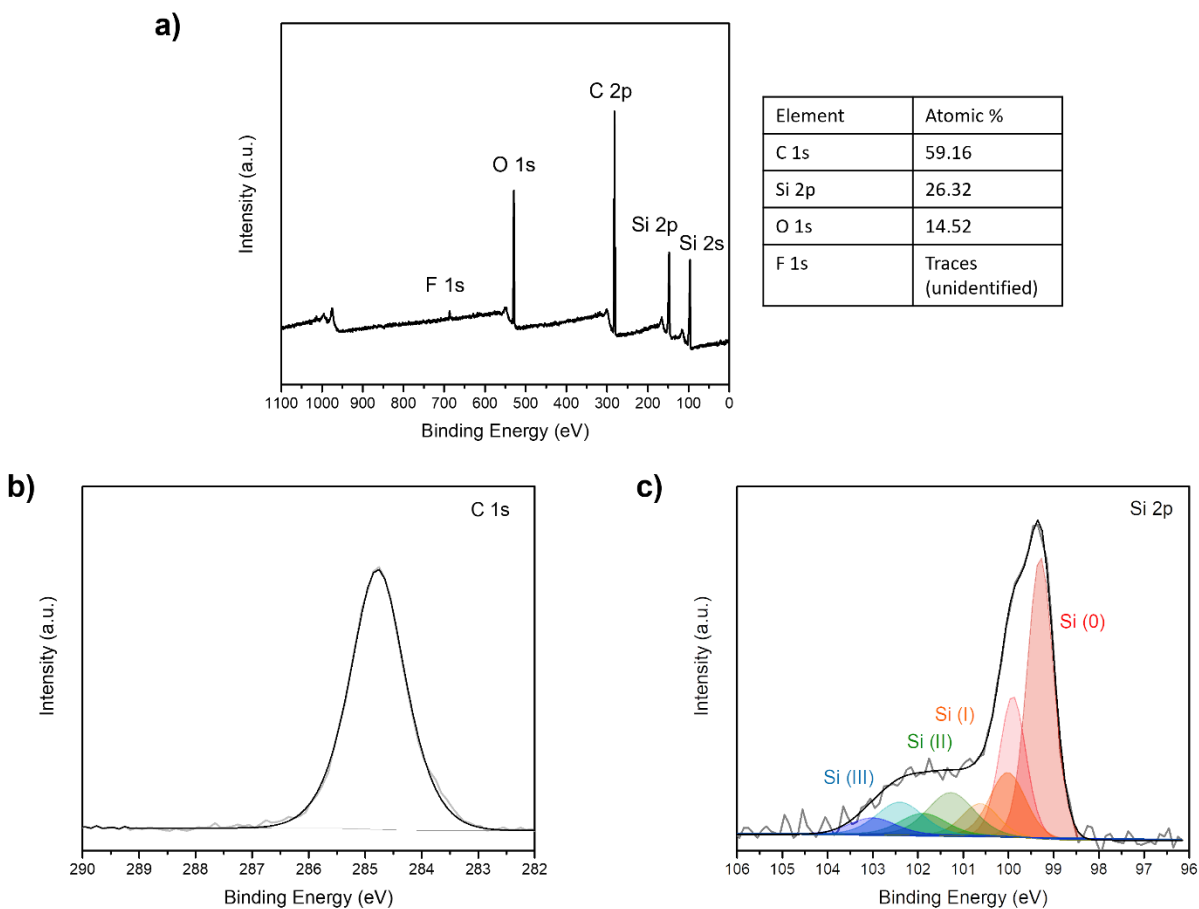


Figure 3.2. (a) Survey XP spectrum of Hex-SiQDs. High resolution XP spectra showing the (b) C 1s and (c) Si 2p features.

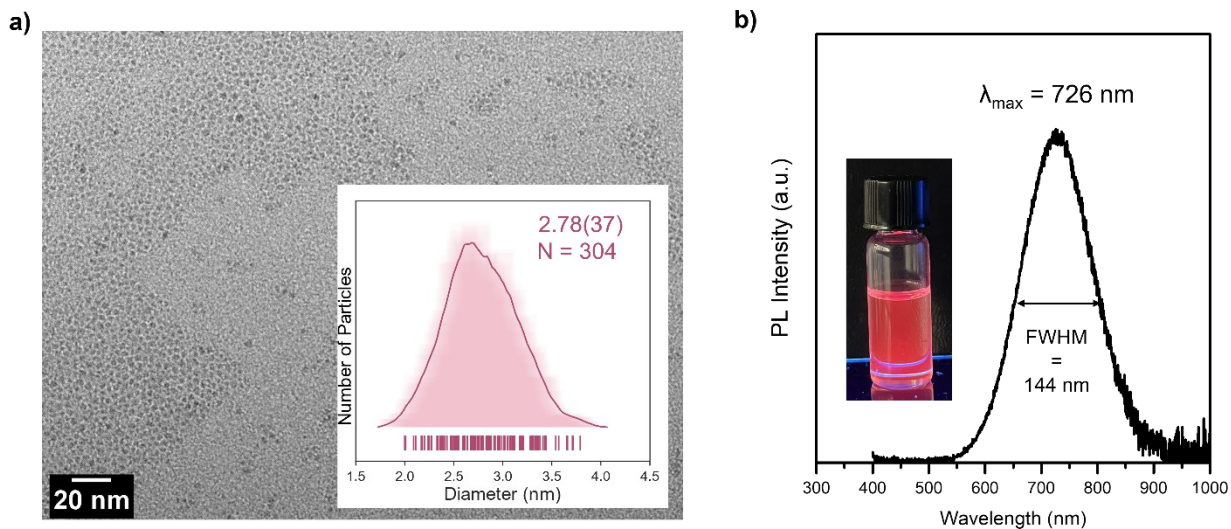


Figure 3.3. (a) BF-TEM image of Hex-SiQDs (Inset: Average shifted histogram presenting the size distribution of a representative sample of Hex-SiQDs.). (b) Photoluminescence spectrum ($\lambda_{\text{ex}} = 365 \text{ nm}$) of Hex-SiQDs in benzene (Inset: A photograph of the solution upon exposure to a standard transilluminator UV lamp.).

With suitable Hex-SiQDs in hand, cLEDs were designed and fabricated with the goal of narrowing the electroluminescence FWHM of a SiQD-LED. In general, the cLED structure incorporates a reflective mirror and SiO₂ layer into hybrid OLED stacks (**Figure 3.4a-b**). A thin, partially-reflective Ag layer (ca. 40 – 50 nm) and a transparent SiO₂ layer were first deposited on glass substrates via thermal and electron beam evaporation. The Ag layer (i.e., output coupler) exhibits a reflectance of 96.1 to 98.5% at 700 nm (comparable to a commercial silver mirror with a reflectivity of ca. 97%; **Figure 3.5**) throughout the visible region. This enables light to interfere within the cavity structure, leading to a narrowing of the spectral bandwidth while simultaneously allowing a fraction of the emission to escape. As part of the present investigation, the thickness of the SiO₂ layer was varied from 200 to 500 nm to define the optical pathlength of the cLED and tune the observed emission wavelengths. A indium tin oxide (ITO; work function = 4.92 eV; 100 nm; **Figure 3.6**) anode was then deposited and coated with a layer of poly(3,4-ethylene-

dioxythiophene) polystyrene sulfonate (PEDOT:PSS; 20 nm) to promote hole injection from the anode into the device. Poly(4-butylphenyldiphenylamine) (poly-TPD; 10 nm) was then deposited to ameliorate the injection barrier into the overlaying Hex-SiQDs. This was followed by the deposition of Hex-SiQDs (35 nm) and capped with a layer of zinc oxide (ZnO; 25 nm) that acts as a hole blocking and electron injection layer. Finally, an Ag cathode layer (100 nm) was deposited, which also serves as a mirror (99 % reflectance at 700 nm; **Figure 3.5**) to complete the FP cavity structure. **Figure 3.4c** shows an approximate energy level diagram for the present device.^{10, 21, 65,}

66

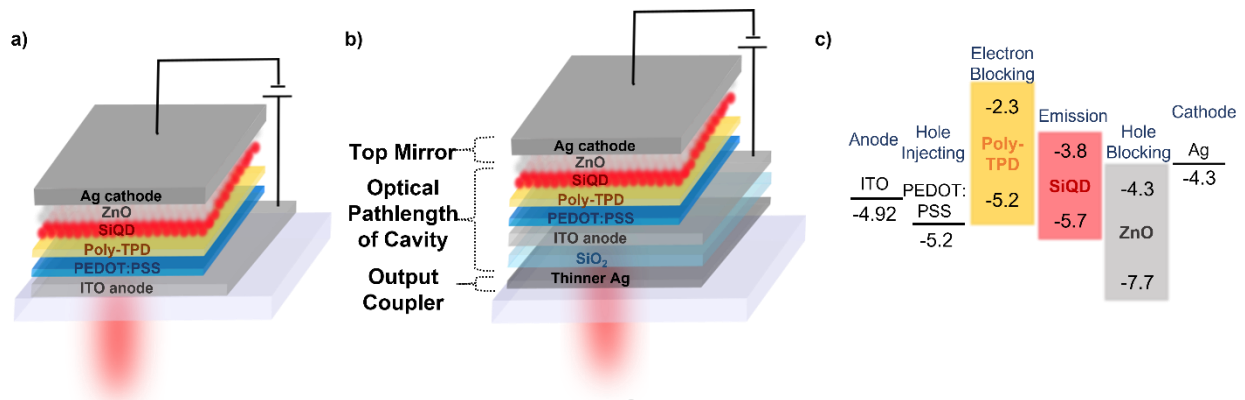


Figure 3.4. Schematic of the (a) cavity-free SiQD-LED, (b) SiQD-cLED device structure, and (c) associated energy level alignment. The thickness of the FP cavity can be tuned by defining the thickness of the SiO₂ layer.

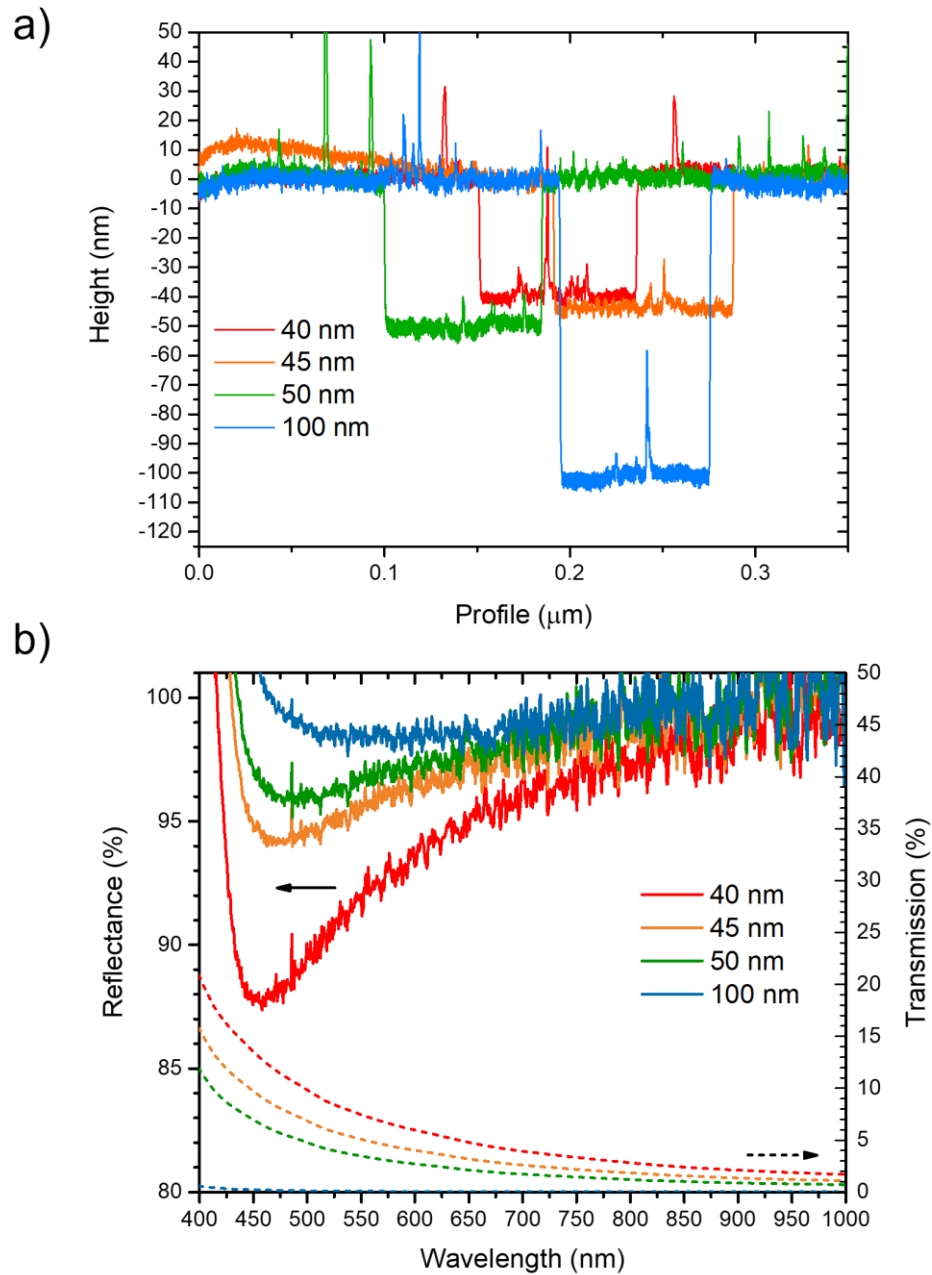


Figure 3.5. (a) Profilometry measurement of Ag thin films at 40, 45, 50, and 100 nm. (b) Reflectance spectra (solid line) and transmission spectra (dash line) of Ag thin films. The reflectance spectra were measured against a reference Thorlabs Ag mirror, and the transmission spectra were simulated using TFCalc software.

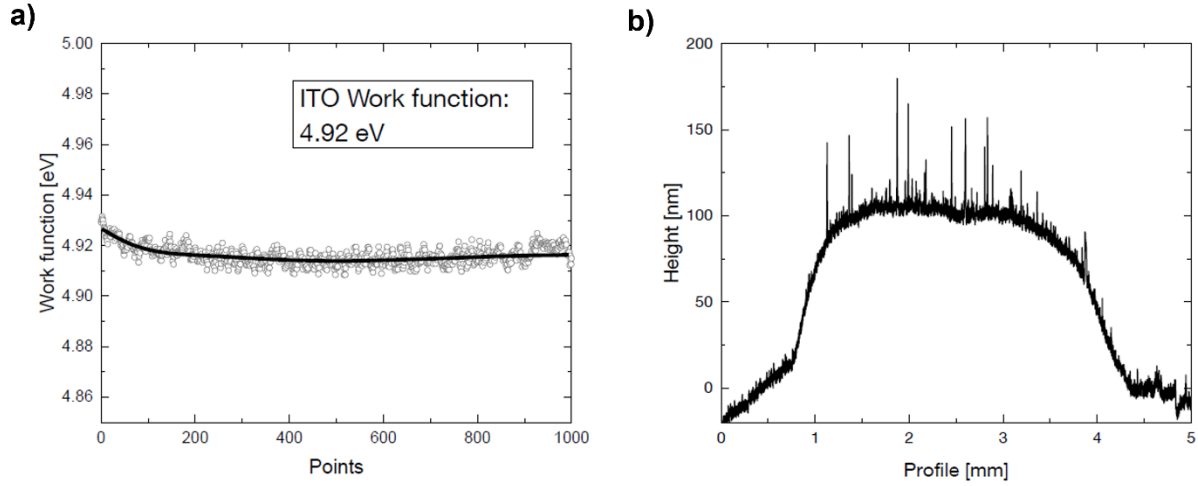


Figure 3.6. (a) Work function and **(b)** profilometry measurement of the as-deposited ITO layer.

The resonance condition of the presented cLED structure is established when a photon emitted from the electroluminescent Hex-SiQD layer is reflected between the semitransparent Ag output coupler and reflective Ag cathode. Resonant wavelengths (λ_m) of the cLED are given by Equation 3.1:

$$\lambda_m = \frac{2}{m} (\sum_i \eta_i d_i \cdot \cos\alpha + 2L_{pen,\alpha}) \quad (3.1)$$

where m is an integer defining the mode number, η_i and d_i are the refractive index and physical thickness of active layer i , α is the detection angle, and $L_{pen,\alpha}$ is the penetration depth in the metal mirrors. The total optical thickness is the summation

$$\begin{aligned} \sum_i \eta_i d_i = & \eta_{SiO_2} d_{SiO_2} + \eta_{ITO} d_{ITO} + \eta_{PEDOT:PSS} d_{PEDOT:PSS} + \eta_{poly-TPD} d_{poly-TPD} + \\ & \eta_{SiQD} d_{SiQD} + \eta_{ZnO} d_{ZnO} \end{aligned} \quad (3.2)$$

where all layers in between the two Ag mirrors are considered transmissive.

The refractive indices of each active layer were experimentally determined using ellipsometry and are provided in **Figure 3.7**. In addition to the active layers, each Ag mirror also induces a phase change upon the reflected photons. The penetration depth is estimated using Equation 3.3:

$$L_{pen,\alpha} = \frac{\lambda(\pi-\beta)}{4\pi} \quad (3.3)$$

where $\beta = \tan^{-1}[Im(r)/Re(r)]$ and r is the reflection coefficient obtained from the simulated complex index of refraction.⁶⁷ The cLED emission wavelength is tuned by varying the SiO₂ layer thickness while keeping all other layer thicknesses constant.

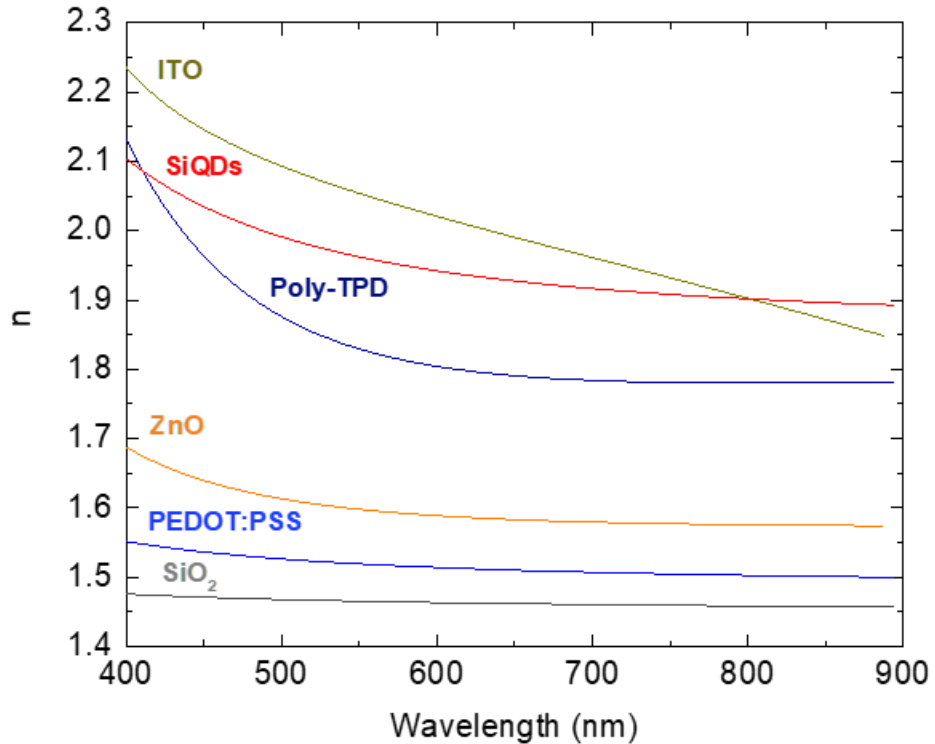


Figure 3.7. Refractive indices of the active layers in the SiQD-LED obtained by ellipsometry.

To provide a baseline for the evaluation of presented cLED structures, a cavity-free SiQD-LED comprising the same stack structure (without the semitransparent Ag output coupler and SiO₂ layer) was fabricated and evaluated. As shown in **Figure 3.8a**, this device exhibited visibly detectable emission at a turn-on voltage of + 2 V with an emission maximum at 828 nm and a FWHM = ca. 113 nm at + 2 V. **Figure 3.9** shows the absolute current density plotted against applied voltage (J-V plot) sweeping from - 4 to + 8 V for a standard SiQD-LED. No increase in passed current was observed under reverse bias conditions (i.e., applied voltage < 0 V) consistent with the device being “off”. For forward bias conditions, the J-V plot shows a clear current onset at + 2 V. The corresponding irradiance plot (**Figure 3.9b**) also shows an irradiance of 10 μW cm⁻² suggesting that, under this driving voltage, a sufficient optical output could be achieved to allow for detection. Prototype SiQD-LEDs investigated here showed external quantum efficiencies, EQE, approaching 1 % at a drive voltage of + 2 V (**Figure 3.9c**). We also noted that with increasing drive voltage from +2.0 to 5.0 V, the EL maximum blue-shifted from 828 to 735 nm and the spectral bandwidth broadened from 113 to 146 nm (**Figure 3.9a, Table 3.2**). These observations are commonly attributed to the inhomogeneous size distribution of the SiQDs, where the smaller QDs with larger band gaps can only be excited with increased driving voltages.^{20, 22, 34, 35, 39} Of note, the EL spectrum obtained for a drive voltage of + 4 V provided an emission maximum of ca. 743 nm with a FWHM of 146 nm that matched with the PL spectrum.

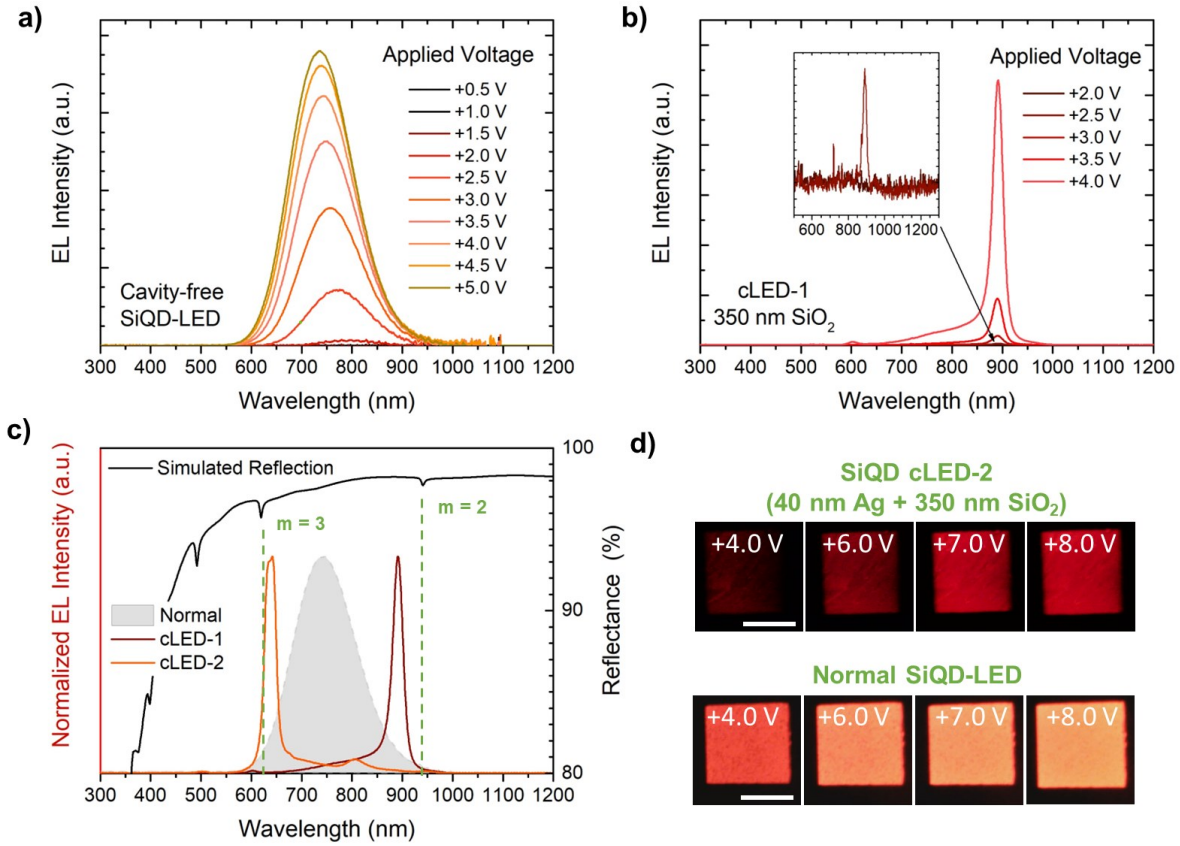


Figure 3.8. EL spectra of (a) cavity-free SiQD-LED and (b) cLED with 350 nm SiO₂ spacer (cLED-1) at different applied voltages. (c) Simulated reflectance spectrum (top) and EL spectra (bottom) of two different cLEDs with 350 nm SiO₂ spacer under +4 V. (d) Digital photographs comparing cavity-free LED and cLED-2 at different applied voltages. Inset scale bars are 2 mm.

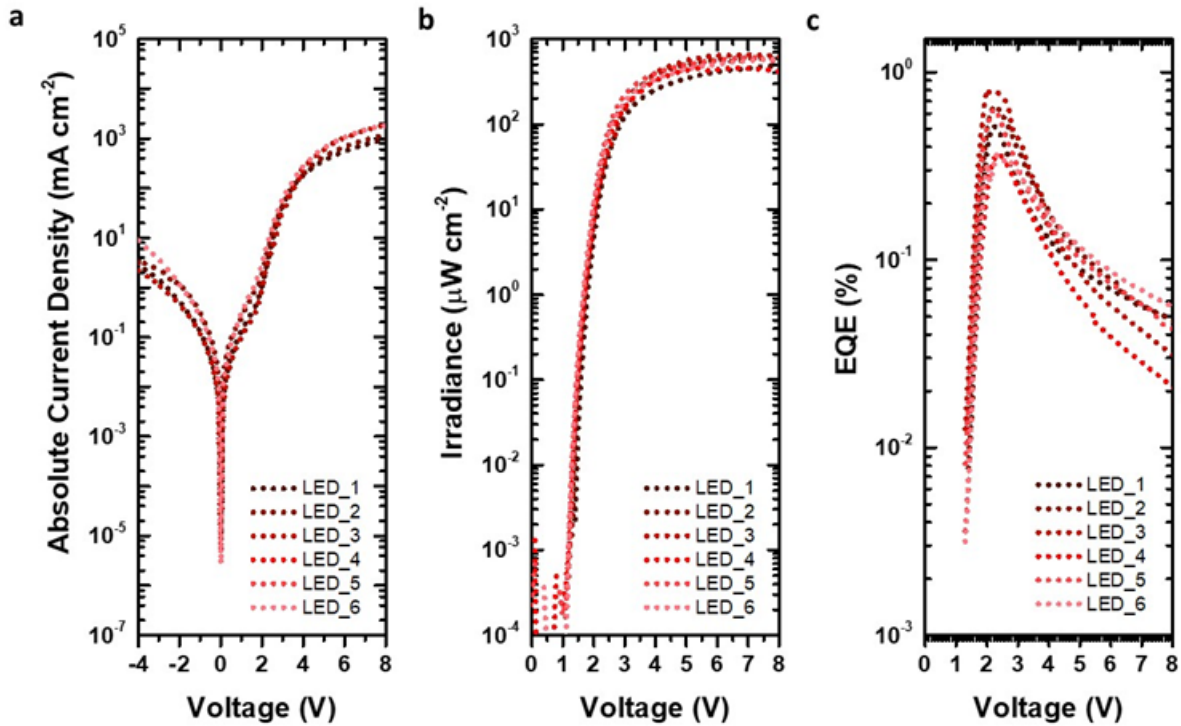


Figure 3.9. (a) Absolute current density, (b) irradiance, and (c) EQE of control SiQD-LED at different voltages.

Table 3.2. Analysis of the SiQD-LED EL spectra at different voltage.

LED	Applied Voltage [V]	Center Wavelength [nm]	FWHM [nm]
Control	2.0	828	113
	2.5	776	137
	3.0	755	143
	3.5	750	144
	4.0	743	146
	4.5	740	146
	5.0	735	146

The cLED reflectance spectra were simulated to determine the appropriate SiO₂ thicknesses to provide cavities with resonant modes in the EL range of SiQDs from 650 to 900 nm (**Figure 3.10**). For the present application, SiO₂ layers with thicknesses in the range of $d = 200$ to 350 nm were desirable. For example, the model cavity structures with 350 nm thick SiO₂ layers

provide an $m = 2$ resonance in the NIR region at 940 nm. The low resonance order is appropriate for films in the range of a few hundred nm thick. It ensures a relatively large free spectral range (FSR), preventing multiple orders from occurring within the luminescence bandwidth. Decreasing the layer thickness to 200 nm blue-shifted this mode to approximately 700 nm. We limited our models to a maximum thickness of 500 nm because beyond this value the $m = 2$ emission would be out of the range of the SiQD EL spectrum.

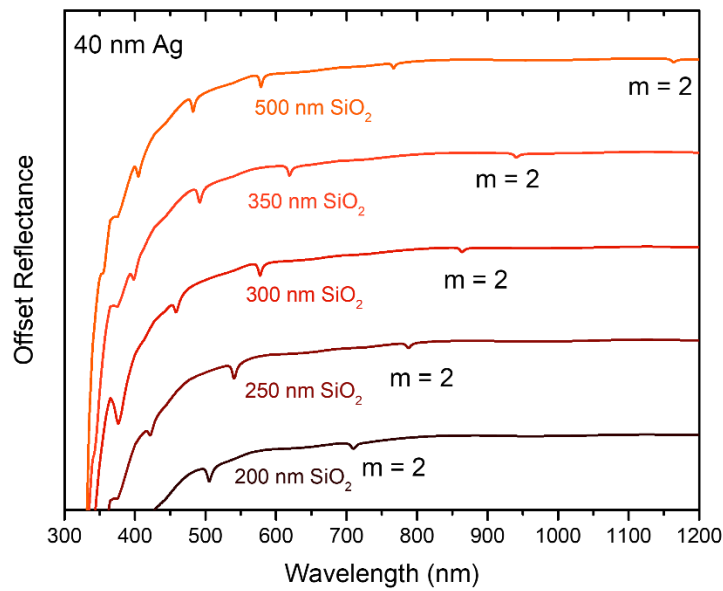


Figure 3.10. Simulated reflectance spectra of SiQD-cLED with 40 nm Ag output coupler and different SiO₂ thicknesses.

Drawing on our cavity simulation results, we fabricated SiQD-cLEDs with 40 nm Ag output coupler and 350 nm thick SiO₂ layer (cLED-1). At an applied voltage of + 2.5 V, the optical cavity confined the SiQD EL into a dominant peak centered at 891 nm with a linewidth of ca. 24 nm (**Figure 3.8b**). This is substantially narrower than the EL bandwidth obtained from a cavity-free SiQD-LED (i.e., FWHM = 113 nm; **Figure 3.8a**). The peak EL wavelength obtained for cLED-1 appeared at 891 nm, and was consistent with the $m = 2$ peak for a net optical thickness

~5% less than the expected value. This is quite reasonable given the uncertainties associated with the deposition of multiple layers. The $m = 3$ mode occurred at *ca.* 602 nm which is at the short-wavelength edge of the non-cavity EL spectrum (**Figure 3.11**). Additional resonances corresponding to the $m = 3$ to $m = 6$ features were observed by reflectance spectroscopy (**Figure 3.12, Table 3.3**).

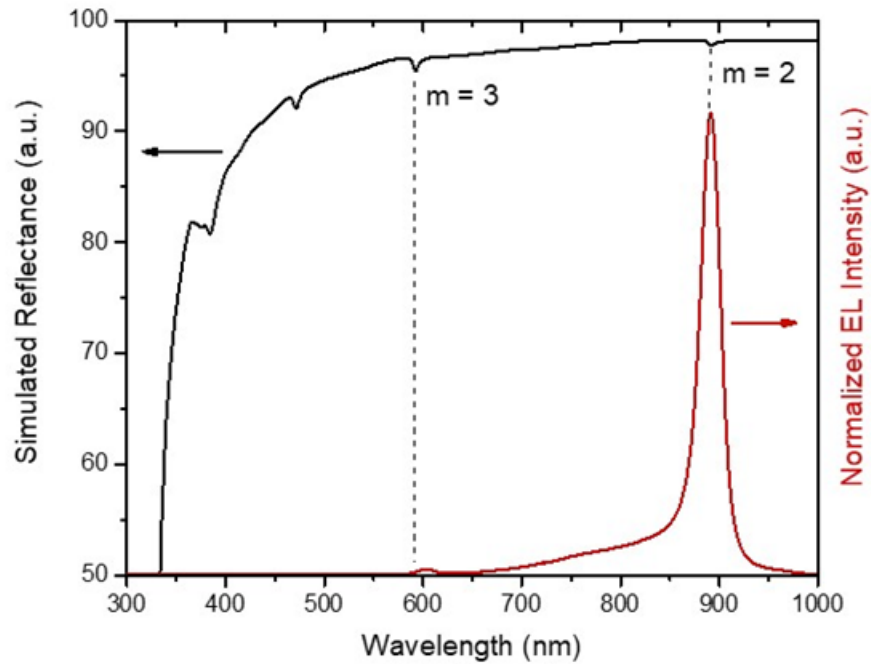


Figure 3.11. Correlation between cLED-1 EL spectrum (right) and simulated reflectance spectrum (left) with 40 nm Ag output coupler and 319 nm SiO₂.

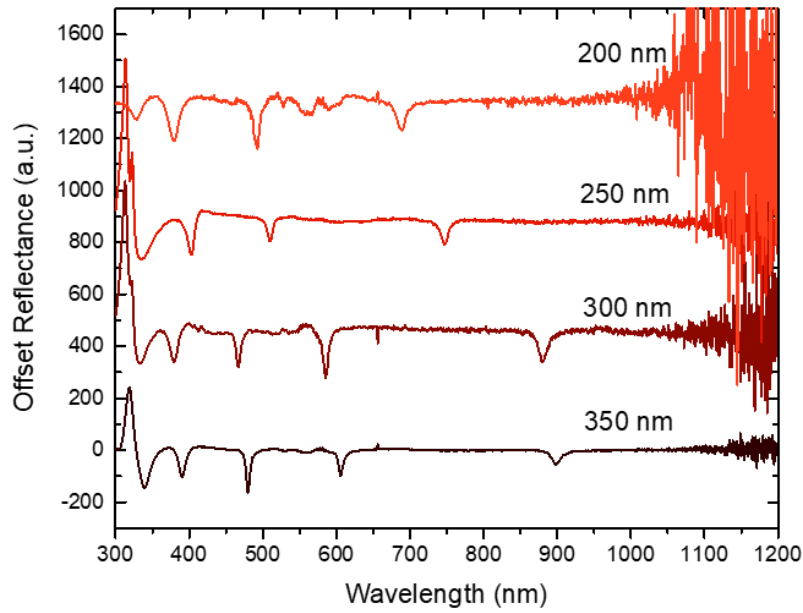


Figure 3.12. Reflectance spectra of SiQD-cLED with 40 nm Ag output coupler and different SiO₂ thicknesses.

Table 3.3. Reflectance spectra analysis of SiQD-cLEDs with 40 nm Ag output coupler

SiO ₂ Thickness [nm]	Center Wavelength [nm]	FWHM [nm]	FSR ($\lambda_{m+1} - \lambda_m$) [nm]	Resonance mode
200	329	13	51	5
	380	13	113	4
	493	8	196	3
	689	13		2
250	335	25	68	5
	403	10	106	4
	509	8	238	3
	747	12		2
300	332	17	47	6
	379	12	87	5
	466	8	119	4
	585	9	293	3
	879	16		2
350	340	16	51	6
	391	9	89	5
	480	6	126	4
	606	8	292	3
	898	14	314	2
	1213	7		1

Looking to the device performance of cLED-1, the cavity-based device exhibits a higher apparent turn-on voltage than the equivalent cavity-free device (i.e., + 2.5 V vs + 2.0 V). This can be attributed to the comparatively low transmittance of the Ag output coupler (ca. 2 % at 891 nm, **Figure 3.5**). Despite the necessity of a higher drive voltage, the cLED-1 emitted at a constant wavelength as opposed to the equivalent cavity-free device spectrally shifted with increasing voltage. The principal EL maximum remained at *ca.* 891 nm for applied voltages in the range of + 2.5 to + 4 V with an average linewidth of ca. 25 nm and an average Q-factor of 36 (**Figure 3.8b**; **Table 3.4**). We also note a minor EL emission peak corresponding to the $m = 3$ mode centered at 601 nm (FWHM = 24 nm, Q-Factor = 25) that emerged at higher voltages. The difference between the intensity of the two modes (i.e., 891 vs 601 nm) originates from the EL of SiQDs, as the cavity output traces the shape of the no-cavity spectrum. Under higher applied voltages, a shoulder emission was observed between the two modes. This leakage may be due to pinholes and inhomogeneity across the deposited layers as shown in the surface profile of the ITO layer (**Figure 3.6**).

Table 3.4. Electroluminescence analysis of SiQD-cLEDs with 40 nm Ag output coupler.

SiO ₂ Thickness [nm]	Applied Voltage [V]	Center Wavelength [nm]	FWHM [nm]	Q-factor
200	4.0	668	44	15
250	4.0	728	63	12
300	5.5	583	47	12
		776	105	7
350	2.5	891	24	37
	3.0	890	25	35
	3.5	890	25	35
	4.0	891	25	36

The opportunity to couple SiQD EL to the modes of a device-embedded optical cavity to provide EL spectral tuning and bandwidth narrowing is further exemplified by cLED-2- a device fabricated under the same conditions as cLED-1. **Figure 3.8c** shows the EL spectrum of cLED-2 which is dominated by an emission at 641 nm ($m = 3$) with a minor peak at 947 nm ($m = 2$). The side band at approximately 800 nm is reasonably attributed to film inhomogeneity across the device similar to what was noted for cLED-1. The observed resonant modes for cLED-2 are slightly red-shifted from the simulated spectrum suggesting the total cavity optical thickness is within ca. 4% of the targeted value (**Figure 3.13**). As a result, the $m = 2$ peak is shifted beyond the SiQD EL envelope (i.e., $\lambda_{em} > 900$ nm) and the $m = 3$ peak is moved closer to the center of the SiQD EL spectrum. The $m = 3$ mode (i.e., $\lambda_{em} = 641$ nm) dominates the device response and the cLED-2 shows visible emission. It is clear from visual inspection (**Figure 3.8d top**) that the cLED-2 EL remained red (i.e., the wavelength did not change) with increasing voltage from + 4 to + 8 V. This is again in contrast to the spectral response of the cavity-free SiQD-LED for which EL shifted from red to orange (**Figure 3.8d, bottom**).

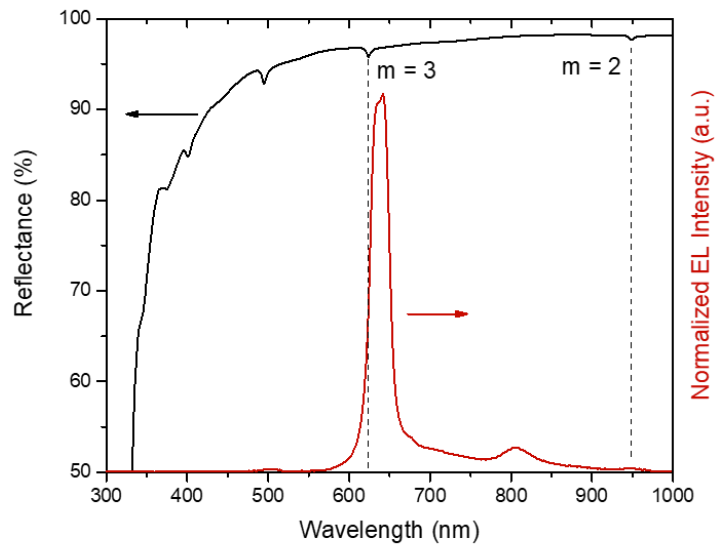


Figure 3.13. Correlation between cLED-2 EL spectrum (right) and simulated reflectance spectrum (left) with 40 nm Ag output coupler and 355 nm SiO₂.

The difference in the EL spectrum between cLED-1 and cLED-2, arising from minor variations in the cavity thickness, points to the opportunity for device spectral tuning through rational definition of the cavity optical pathlength. **Figure 3.14a** illustrates how controlling the SiO₂ thickness in the range of 350 to 200 nm allows tuning of the emission maximum from NIR to red/orange. These cLEDs emitted at 776, 728, and 668 nm for nominal SiO₂ layer thicknesses of 300, 250, and 200 nm, respectively. As expected, the reflectance spectra of these cLED cavities also showed an increasing FSR with decreasing thicknesses (**Figure 3.12**). The EL bandwidths of thinner devices (i.e., SiO₂ thicknesses of 350 to 200 nm) are in the range of 43 to 105 nm, exhibiting Q-factors of only 7 to 15 (**Table 3.4**). This can be attributed to inconsistencies in the surface morphologies of the layers across different samples.^{68, 69} When the SiO₂ layer thickness was increased to 500 nm, observed principal EL was centered at 691 nm with a FWHM of 31 nm and a Q-factor of ca. 23 (**Figure 3.14b**). This device was found to have more uniform microscopic

morphology, as revealed by the three-dimensional atomic force microscopic (AFM) profile in **Figure 3.15a**. The two-dimensional AFM profiles in **Figure 3.15b** show that the root mean square (RMS) surface roughness of the full stack cLED is 2.45 nm where the roughness of each layer is between 0.36 to 2.20 nm.

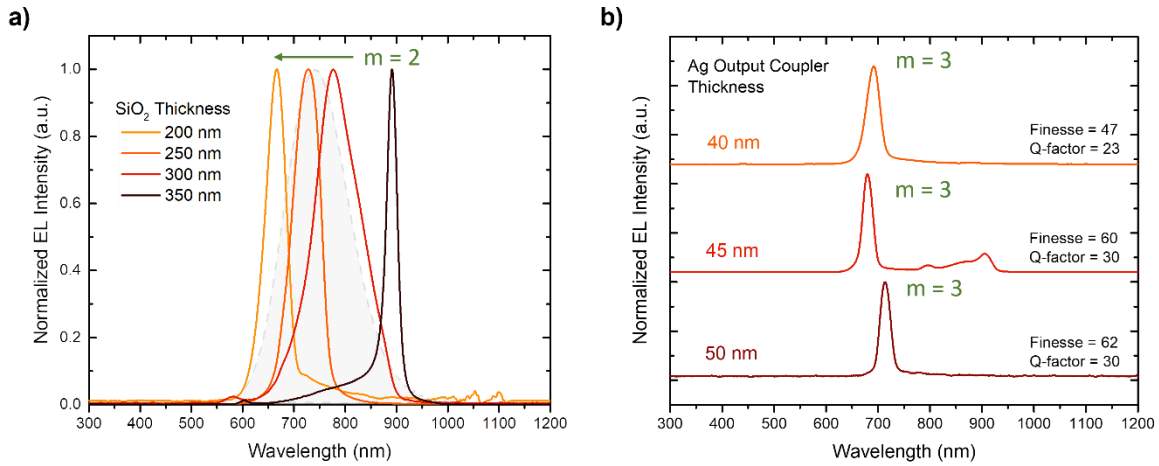


Figure 3.14. (a) EL spectra of SiQD-cLEDs with different SiO₂ thicknesses showing tunable emission ranging from red/orange to NIR. The grey spectrum corresponds to the EL of the control LED. (b) EL spectra of cLEDs with different Ag output coupler thickness; all devices were deposited with 500 nm SiO₂

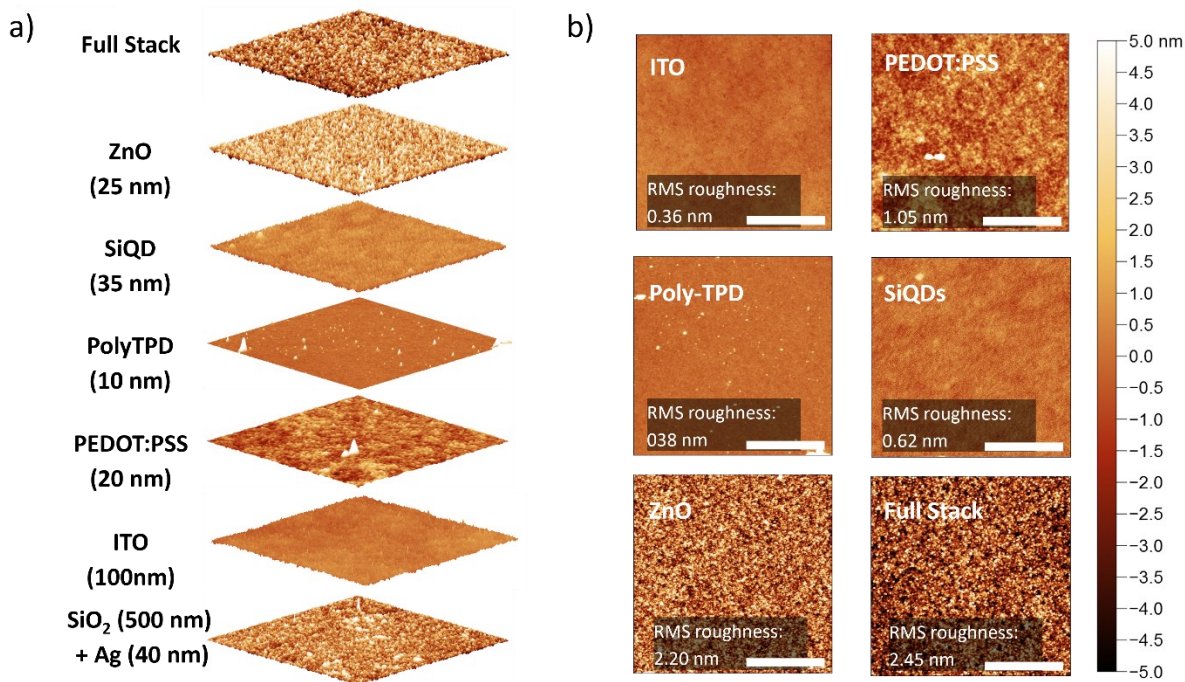


Figure 3.15. Smooth surface profile of SiQD-cLED with 40 nm Ag and 500 nm SiO₂ spacer revealed by (a) three-dimensional and (b) two-dimensional AFM images. Inset scale bars are 2 μm .

In general, more reflective mirrors are expected to narrow the emission spectrum. Therefore, SiQD-cLEDs with 40, 45, and 50 nm thick Ag output couplers were fabricated and tested. As discussed previously (**Figure 3.5**), a 40-nm-thick Ag output coupler has a reflectance of 96.1 % at 700 nm, this increases to 97.8 and 98.5% when the thickness is increased to 45 and 50 nm, respectively. With the same SiO₂ spacer thickness of 500 nm, the cLEDs exhibited principal $m = 3$ EL emission centered at ca. 695 ± 18 nm (**Figure 3.14b**). The minor spectral leakages observed (i.e., shoulder emission) could be due to film inhomogeneity as evidenced by the reflectance spectra (**Figure 3.16a**, **Table 3.5**). Notably, the emission bandwidths of the devices with 45 and 50 nm thick Ag output couplers (i.e., 45-cLED and 50-cLED) were ca. 24 % narrower (FWHM = ca. 23 and 24 nm) as compared to the cLED with 40 nm Ag (40-cLED, FWHM = ca. 31 nm). Simulations showed a similar relative change in the cavity Q-factor (**Figure 3.16b**, **Table**

3.6 - Table 3.7). It is important to note that deviations in the amount of peak narrowing provided by a cavity may be influenced by film inhomogeneity as shown in the profilometry characterization of Ag output coupler and ITO layer (**Figure 3.5-3.6**). For the present systems, lower experimental Q-factors may arise in part because surface roughness apparent in the presented AFM images (**Figure 3.15**).

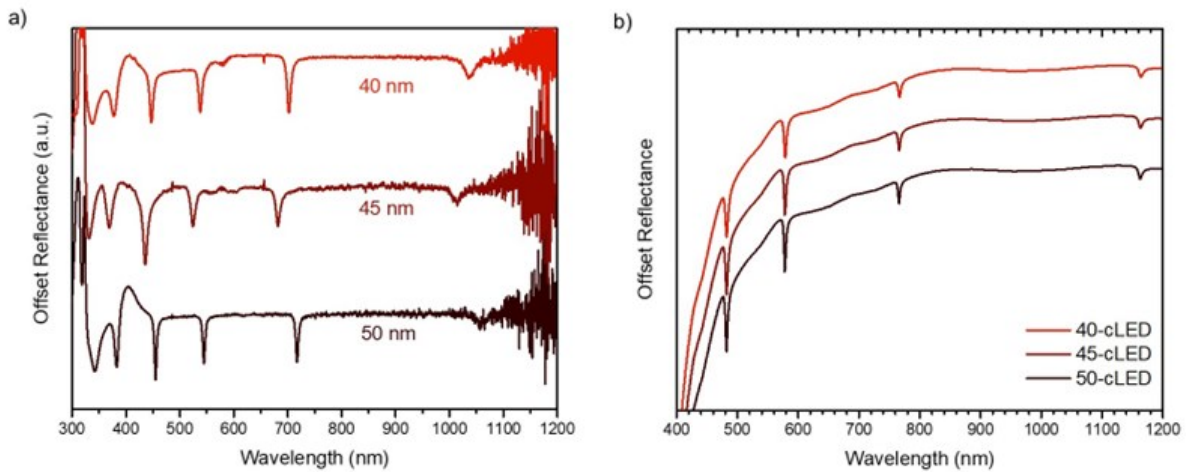


Figure 3.16. Experimental (a) and simulated (b) reflectance spectra of SiQD-cLED with 500 nm SiO₂ spacers and different Ag.

Table 3.5. Reflectance spectra analysis of SiQD-cLEDs with 500 nm SiO₂.

Ag Thickness [nm]	Center Wavelength [nm]	FSR ($\lambda_{m+1} - \lambda_m$) [nm]	FSR [THz]	Resonance mode
40	338	41	7391	7
	378	69	4347	6
	447	90	3317	5
	538	164	1824	4
	702	333	900	3
	1035			2
45	331	38	7963	7
	369	67	4455	6
	436	88	3422	5
	524	158	1900	4
	682	333	900	3
	1015			2
50	318	65	4634	7
	383	72	4172	6
	455	90	3341	5
	545	173	1737	4
	717	348	862	3
	1065			2

Table 3.6. Electroluminescence analysis of SiQD-cLEDs with 500 nm SiO₂ spacer at + 4.0 V.

Ag Thickness [nm]	Center Wavelength [nm]	FWHM [nm]	Q-factor	Finesse
40	691	31	23	47
45	679	23	30	60
50	713	24	30	62

Table 3.7. Simulated reflectance spectra analysis of SiQD-cLED cavities with 500 nm SiO₂.

Ag Thickness [nm]	Center Wavelength [nm]	FWHM [nm]	Q-factor	Finesse
40	762	5	157	280
45	762	4	196	378
50	762	4	206	397

For another 50-cLED, prepared using the method described previously, the emission bandwidth remained ca. 30 nm when the detection angle was changed from normal incidence to 15° off normal (**Figure 3.17**). The complementary angle-dependent measurement also revealed a narrow cone of cLED emission of +15° from the surface normal with a slight blue-shift (ca. 10 nm); this is congruent with the optical characteristic of a FP cavity.⁴⁷ This directional emission could potentially reduce spectral overlap associated with nearby pixels in display device configurations.⁷⁰ In comparison, the broad and weak background emission showed no angular dependence.

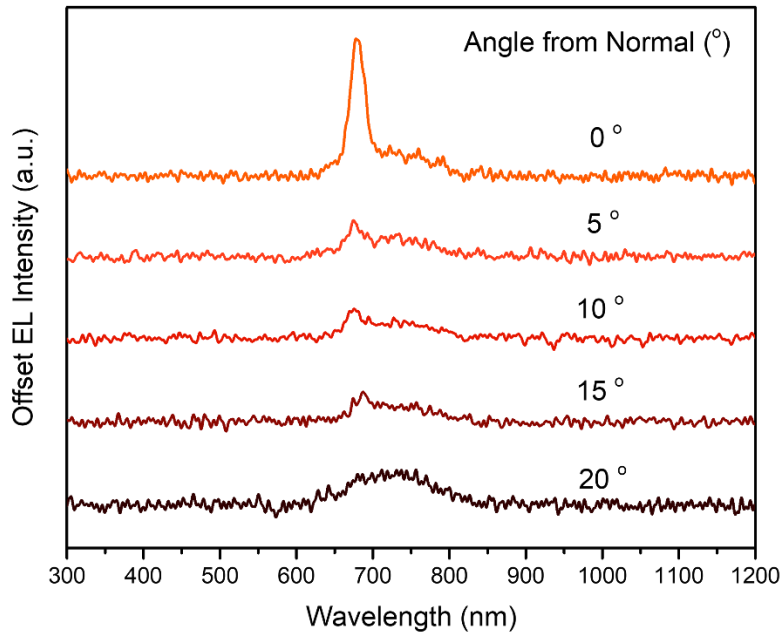


Figure 3.17. Angle-dependent EL spectra of SiQD-cLED with 500 nm SiO₂ spacers and 50 nm Ag.

Similar to the SiQD-cLED with a 40 nm thick Ag mirror discussed in **Figure 3.8c**, the 50-cLED exhibited stable emission under different applied voltages (i.e., + 3.5 to + 5 V) with a center wavelength around ca. 714 nm and a Q-factor of ca. 30 (**Figure 3.18, Table 3.5**). Despite the impressive advances compared to the non-cavity device, the 50-cLED exhibited higher current densities up to + 4 V and a higher turn-on voltage of + 3.5 V as shown in the J-V and irradiance plot (**Figure 3.19a**). Additionally, the maximum irradiance of the 50-cLEDs was only around $60 \mu\text{W cm}^{-2}$ with an EQE of ca. 0.004% (**Figure 3.19b-c**). The reduced efficiency of the cLED could be attributed to low transmittance at visible wavelengths, as well as inhomogeneities of the layered structure.

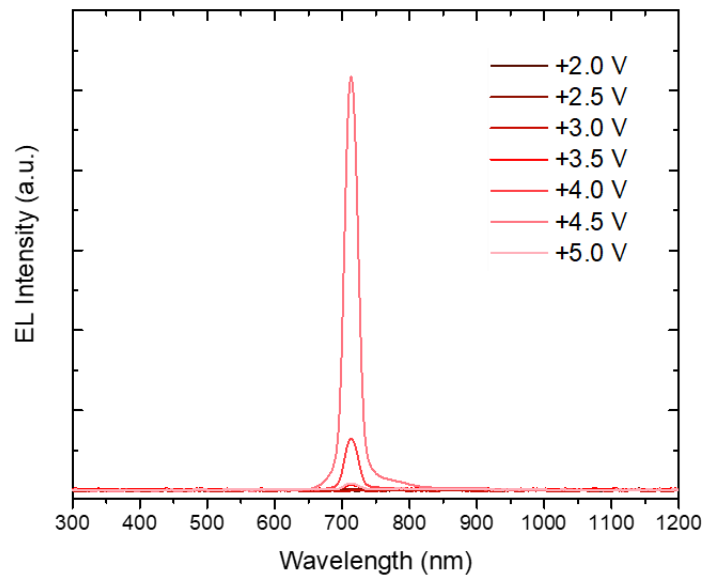


Figure 3.18. EL spectra of SiQD-cLED with 500 nm SiO₂ spacers and 50 nm Ag at different applied voltages.

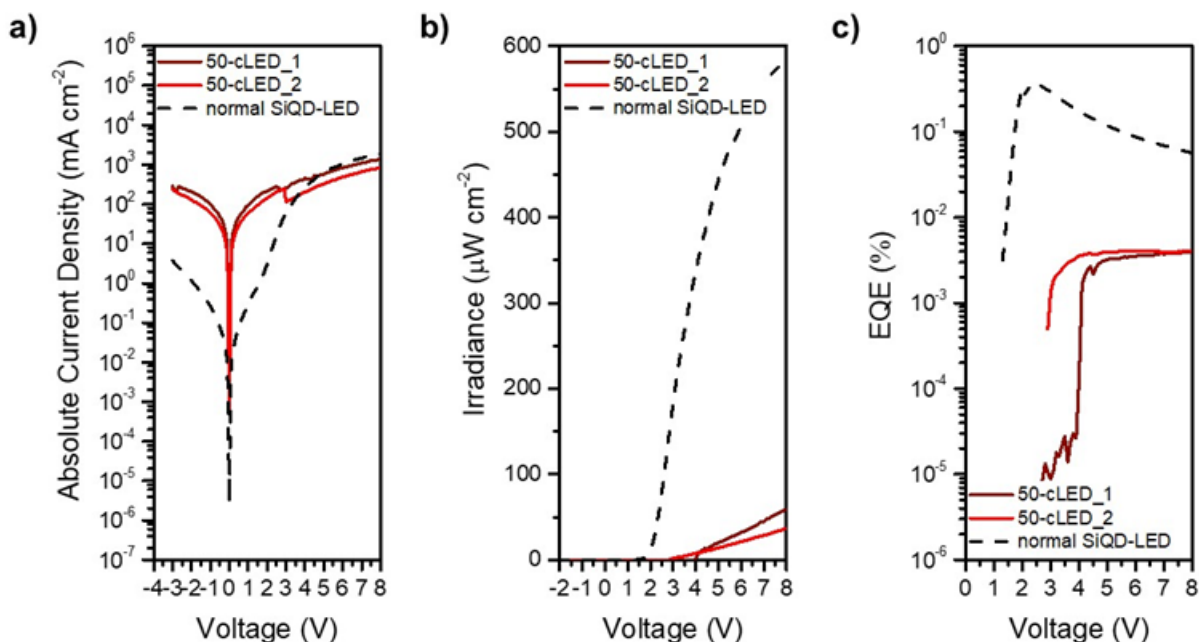


Figure 3.19. (a) Absolute current density, (b) irradiance, and (c) EQE of SiQD-cLED with 500 SiO₂ nm and 50 nm Ag at different voltages.

The incorporation of SiQDs obtained *via* alternative functionalization methods^{23, 71, 72} that exhibit brighter emission and/or implementing an output coupler with higher transmittance (e.g., WO₃/W)^{73, 74} may provide improved output intensity and EQE of the cLEDs. Optimizing QD surface coverage to lower than 50% as suggested by Xu et al. may also prove useful.⁶⁴ Optimizing the fabrication procedure and the device structure^{20, 39, 51, 75} to improve the stability, spectral response, and reproducibility of the cLEDs are the focus of ongoing investigations. Despite the stated limitations, this work demonstrated the first example of a SiQD microcavity-based hybrid LED that exhibited defined emission and spectral tunability.

3.4 Conclusion

The broad SiQD electroluminescence linewidth was successfully reduced from over 100 nm to as narrow as ca. 23 nm by incorporating hybrid SiQD-LEDs in a Fabry–Pérot cavity. These cavity-LEDs also demonstrated excellent spectral and visual stability over a range of applied voltages. Using the same SiQDs, tuning the LED emission from visible (red-orange) to NIR was achieved by intentionally and rationally varying the thickness of the SiO₂ spacer inside the structure. The emission linewidth was also tunable *via* variations in the Ag thickness. The SiQD cavity-LEDs reported in this Chapter offer a narrower emission spectrum, improved wavelength stability, and facile spectral tunability. This straightforward configuration demonstrates the potential for the development of spectrally pure SiQD LEDs and represents a step toward future heavy-metal free SiQD-based light-emitting technologies.

3.5 References

1. R. Rossetti, S. Nakahara and L. E. Brus, *The Journal of Chemical Physics*, 1983, **79**, 1086-1088.
2. W. Ke and M. G. Kanatzidis, *Nature Communications*, 2019, **10**, 965.
3. Q. Xu, I. T. Cheong, L. Meng, J. G. C. Veinot and X. Wang, *ACS Nano*, 2021, **15**, 18429-18436.
4. I. L. Medintz, H. T. Uyeda, E. R. Goldman and H. Mattoussi, *Nature Materials*, 2005, **4**, 435-446.
5. Q.-B. Zhu, B. Li, D.-D. Yang, C. Liu, S. Feng, M.-L. Chen, Y. Sun, Y.-N. Tian, X. Su, X.-M. Wang, S. Qiu, Q.-W. Li, X.-M. Li, H.-B. Zeng, H.-M. Cheng and D.-M. Sun, *Nature Communications*, 2021, **12**, 1798.
7. D. T. Yonemoto, C. M. Papa, C. Mongin and F. N. Castellano, *Journal of the American Chemical Society*, 2020, **142**, 10883-10893.
8. N. Li, X. Chen, J. Wang, X. Liang, L. Ma, X. Jing, D.-L. Chen and Z. Li, *ACS Nano*, 2022, **16**, 3332-3340.

9. Z. Liu, C. H. Lin, B. R. Hyun, C. W. Sher, Z. Lv, B. Luo, F. Jiang, T. Wu, C. H. Ho, H. C. Kuo and J. H. He, *Light: Science & Applications*, 2020, **9**, 83.
10. Y. Shirasaki, G. J. Supran, M. G. Bawendi and V. Bulović, *Nature Photonics*, 2012, **7**, 13-23.
11. X. Dai, Y. Deng, X. Peng and Y. Jin, *Advanced Materials*, 2017, **29**.
12. M. K. Choi, J. Yang, T. Hyeon and D.-H. Kim, *npj Flexible Electronics*, 2018, **2**, 10.
13. Y. Yin, Z. Hu, M. U. Ali, M. Duan, L. Gao, M. Liu, W. Peng, J. Geng, S. Pan, Y. Wu, J. Hou, J. Fan, D. Li, X. Zhang and H. Meng, *Advanced Materials Technologies*, 2020, **5**, 2000251.
14. Y.-H. Won, O. Cho, T. Kim, D.-Y. Chung, T. Kim, H. Chung, H. Jang, J. Lee, D. Kim and E. Jang, *Nature*, 2019, **575**, 634-638.
15. F. P. Garcia de Arquer, D. V. Talapin, V. I. Klimov, Y. Arakawa, M. Bayer and E. H. Sargent, *Science*, 2021, **373**.
16. A. Das and P. T. Snee, *Chemphyschem*, 2016, **17**, 598-617.
17. S. Ivanov, S. Zhuravsky, G. Yukina, V. Tomson, D. Korolev and M. Galagudza, *Materials*, 2012, **5**, 1873-1889.
18. K. Y. Cheng, R. Anthony, U. R. Kortshagen and R. J. Holmes, *Nano Letters*, 2011, **11**, 1952-1956.
19. S. Zhao, X. Liu, X. Pi and D. Yang, *Journal of Semiconductors*, 2018, **39**.
20. B. Ghosh, H. Yamada, S. Chinnathambi, I. N. G. Ozbilgin and N. Shirahata, *Journal of Physical Chemistry Letter*, 2018, **9**, 5400-5407.
21. A. Angi, M. Loch, R. Sinelnikov, J. G. C. Veinot, M. Becherer, P. Lugli and B. Rieger, *Nanoscale*, 2018, **10**, 10337-10342.
22. J. Mock, E. Groß, M. J. Kloberg, B. Rieger and M. Becherer, *Advanced Photonics Research*, 2021, **2**, 2100083.
23. T. Ono, Y. Xu, T. Sakata and K. I. Saitow, *ACS Applied Materials & Interfaces*, 2022, **14**, 1373-1388.
24. J. G. Veinot, *Chemical Communications*, 2006, 4160-4168.
25. S. Milliken, A. N. Thiessen, I. T. Cheong, K. M. O'Connor, Z. Li, R. W. Hooper, C. J. T. Robidillo and J. G. C. Veinot, *Nanoscale*, 2021, **13**, 16379-16404.

26. I. M. Hohlein, A. Angi, R. Sinelnikov, J. G. Veinot and B. Rieger, *Chemistry*, 2015, **21**, 2755-2758.
27. A. Halimaoui, C. Oules, G. Bomchil, A. Bsiesy, F. Gaspard, R. Herino, M. Ligeon and F. Muller, *Applied Physics Letters*, 1991, **59**, 304-306.
28. N. Koshida and H. Koyama, *Applied Physics Letters*, 1992, **60**, 347-349.
29. R. K. Ligman, L. Mangolini, U. R. Kortshagen and S. A. Campbell, *Applied Physics Letters*, 2007, **90**, 061116.
30. P. Photopoulos and A. G. Nassiopoulou, *Applied Physics Letters*, 2000, **77**, 1816.
31. R. J. Walters, G. I. Bourianoff and H. A. Atwater, *Nature Materials*, 2005, **4**, 143-146.
32. D. P. Puzzo, E. J. Henderson, M. G. Helander, Z. Wang, G. A. Ozin and Z. Lu, *Nano Letter*, 2011, **11**, 1585-1590.
33. M. L. Mastronardi, E. J. Henderson, D. P. Puzzo, Y. Chang, Z. B. Wang, M. G. Helander, J. Jeong, N. P. Kherani, Z. Lu and G. A. Ozin, *Small*, 2012, **8**, 3647-3654.
34. F. Maier-Flaig, J. Rinck, M. Stephan, T. Bocksrocker, M. Bruns, C. Kubel, A. K. Powell, G. A. Ozin and U. Lemmer, *Nano Letter*, 2013, **13**, 475-480.
35. X. Liu, S. Zhao, W. Gu, Y. Zhang, X. Qiao, Z. Ni, X. Pi and D. Yang, *ACS Applied Materials & Interfaces*, 2018, **10**, 5959-5966.
36. J. Watanabe, H. Yamada, H.-T. Sun, T. Moronaga, Y. Ishii and N. Shirahata, *ACS Applied Nano Materials*, 2021, **4**, 11651-11660.
37. V. Kveder, M. Badylevich, E. Steinman, A. Izotov, M. Seibt and W. Schröter, *Applied Physics Letters*, 2004, **84**, 2106-2108.
38. F. Maier-Flaig, C. Kubel, J. Rinck, T. Bocksrocker, T. Scherer, R. Prang, A. K. Powell, G. A. Ozin and U. Lemmer, *Nano Letter*, 2013, **13**, 3539-3545.
39. L. Yao, T. Yu, L. Ba, H. Meng, X. Fang, Y. Wang, L. Li, X. Rong, S. Wang, X. Wang, G. Ran, X. Pi and G. Qin, *Journal of Materials Chemistry C*, 2016, **4**, 673-677.
40. S. Terada, H. Ueda, T. Ono and K.-i. Saitow, *ACS Sustainable Chemistry & Engineering*, 2022, **10**, 1765-1776.
41. Y. C. Zhang, Z. Y. Yu, X. Y. Xue, F. L. Wang, S. Li, X. Y. Dai, L. Wu, S. Y. Zhang, S. Y. Wang and M. Lu, *Optic Express*, 2021, **29**, 34126-34134.
42. D. V. Talapin and J. Steckel, *MRS Bulletin*, 2013, **38**, 685-691.
43. I. Sychugov, R. Juhasz, J. Valenta and J. Linnros, *Physics Review Letters*, 2005, **94**, 087405.

44. I. Sychugov, A. Fucikova, F. Pevere, Z. Yang, J. G. C. Veinot and J. Linnros, *ACS Photonics*, 2014, **1**, 998-1005.
45. M. L. Mastronardi, F. Maier-Flaig, D. Faulkner, E. J. Henderson, C. Kubel, U. Lemmer and G. A. Ozin, *Nano Letters*, 2012, **12**, 337-342.
46. M. L. Mastronardi, F. Hennrich, E. J. Henderson, F. Maier-Flaig, C. Blum, J. Reichenbach, U. Lemmer, C. Kubel, D. Wang, M. M. Kappes and G. A. Ozin, *Journal of the American Chemical Society*, 2011, **133**, 11928-11931.
47. N. Hodgson and H. Weber, in *Optical Resonators*, Springer London, 1997.
48. H. Zhu, W. Zhang, and S. F. Yu, *Nanoscale* **2013**, 5 (5), 1797-1802
49. X. Yang, E. Mutlugun, C. Dang, K. Dev, Y. Gao, S. T. Tan, X. W. Sun, and H. V. Demi, *ACS Nano* **2014**, 8 (8), 8224-8231.
50. D. Li, B. Kristal, Y. Wang, J. Feng, Z. Lu, G. Yu, Z. Chen, Y. Li, X. Li, and X. Xu, *ACS Applied Materials & Interfaces* **2019**, 11 (37), 34067-34075.
51. Y. Miao, L. Cheng, W. Zou, L. Gu, J. Zhang, Q. Guo, Q. Peng, M. Xu, Y. He, S. Zhang, Y. Cao, R. Li, N. Wang, W. Huang, and J. Wang, *Light: Science & Applications* **2020**, 9 (1), 89.
52. M. Lu, J. Guo, S. Sun, P. Lu, J. Wu, Y. Wang, S. V. Kershaw, W. W. Yu, A. L. Rogach, and Y. Zhang, *Nano Letters* **2020**, 20 (4), 2829-2836.
53. L. Wang, J. Lin, Y. Lv, B. Zou, J. Zhao, and X. Liu, *ACS Applied Nano Materials* **2020**, 3 (6), 5301-5310.
54. G. Liu, X. Zhou, and S. Chen, *ACS Appl Mater Interfaces* **2016**, 8 (26), 16768-16775.
55. D. Amans, S. Callard, A. Gagnaire, J. Joseph, F. Huisken and G. Ledoux, *Journal of Applied Physics*, 2004, **95**, 5010-5013
56. A. Hryciw, J. Laforge, C. Blois, M. Glover and A. Meldrum, *Advanced Materials*, 2005, **17**, 845-849.
57. P. Zeng, F. Wang, Y. Zhang, W. Zhou, Z. Guo, X. Wu, M. Lu and S. Zhang, *ACS Photonics*, 2021, **8**, 1353-1363.
58. Y.-C. Zhang, Z.-Y. Yu, F.-Y. Ma, X.-Y. Xue, K.-X. Liu, J. Sun, S.-Y. Wang and M. Lu, *Results in Physics*, 2022, **39**, 105734.

59. I. T. Cheong, W. Morrish, W. Sheard, H. Yu, B. Tavares Luppi, L. Milburn, A. Meldrum and J. G. C. Veinot, *ACS Applied Materials & Interfaces*, 2021, **13**, 27149-27158.
60. C. M. Hessel, E. J. Henderson, and J. G. C. Veinot, *Chemistry of Materials* **2006**, *18* (26), 6139-6146.
61. S. L. Anderson, E. J. Lubber, B. C. Olsen, and J. M. Buriak, *Chemistry of Materials* **2016**, *28* (17), 5973-5975.
62. Z. Yang, M. Iqbal, A. R. Dobbie, and J. G. C. Veinot, *Journal of the American Chemical Society* **2013**, *135* (46), 17595-17601.
63. M. A. Islam, M. H. Mobarok, R. Sinelnikov, T. K. Purkait, and J. G. C. Veinot, *Langmuir* **2017**, *33* (35), 8766-8773.
64. Y. Xu, S. Terada, Y. Xin, H. Ueda, and K. Saitow, *ACS Applied Nano Materials* **2022**.
65. K.-Y. Cheng, R. Anthony, U. R. Kortshagen and R. J. Holmes, *Nano Letters*, 2010, **10**, 1154-1157.
66. J. Mock, M. Kallergi, E. Gro, M. Golibrzuch, B. Rieger and M. Becherer, *IEEE Photonics Journal*, 2022, **14**, 1-9.
67. F. Ma and X. Liu, *Applied Optics*, 2007, **46**, 6247-6250.
68. D. Hunger, T. Steinmetz, Y. Colombe, C. Deutsch, T. W. Hänsch and J. Reichel, *New Journal of Physics*, 2010, **12**. 065038
69. T. Klaassen, M. P. van Exter and J. P. Woerdman, *Applied Optics*, 2007, **46**, 5210-5215.
70. L. Chen, Z. Qin, and S. Chen, *Small Methods* **2022**, *6* (1), e2101090.
71. E. A. Weiss, *ACS Energy Letters*, 2017, **2**, 1005-1013.
72. M. H. Mobarok, T. K. Purkait, M. A. Islam, M. Miskolzie, and J. G. C. Veinot, *Angewandte Chemie International Edition* **2017**, *56* (22), 6073-6077.
73. J. Chen, Z. Wang, Z. Chen, S. Cong and Z. Zhao, *Nano Letter*, 2020, **20**, 1915-1922
74. Z. Wang, X. Wang, S. Cong, J. Chen, H. Sun, Z. Chen, G. Song, F. Geng, Q. Chen and Z. Zhao, *Nature Communications*, 2020, **11**, 302.
75. Q. Zhang, Q. Jin, A. Mertens, C. Rainer, R. Huber, J. Fessler, G. Hernandez-Sosa, and U. Lemmer, *Advanced Materials*, **2022**, *34* (33), e2201348.

Chapter 4

Photostability of Silicon Quantum Dots with and without a Thick Amorphous Shell

I Teng Cheong, LiYifan Yang Szepesvari, Chuyi Ni, Cole Butler, Kevin M. O'Connor, Riley Hooper, Alkiviathes Meldrum, Jonathan G.C. Veinot

4.1 Introduction

Quantum dots are nanosized semiconductor particles that have tunable optical and electronic properties. Silicon quantum dots (SiQDs) are a subclass of these materials that exhibit luminescence throughout the visible to infrared spectral regions with tailorable surface functionalities.¹⁻⁴ The biocompatibility⁵⁻⁷ and abundance of silicon make SiQDs attractive as promising alternatives for toxic heavy metals-containing nanoparticles.⁸⁻¹⁰ Notably, various SiQD-based prototypes for applications such as light-emitting diodes,¹¹⁻¹⁵ solar concentrators,¹⁶⁻¹⁹ photodetectors,^{20, 21} biological labels,²²⁻²⁵ and photocatalysts²⁶⁻²⁸ have emerged. However, if SiQDs are to realize their full practical utility in these areas, and other far-reaching applications, it is essential that photoluminescence (PL) maxima tunability, narrow emission bandwidth, and high quantum yield (QY) are all achieved while maintaining long-term stability.

The photoluminescence maximum of SiQDs is size dependent and is influenced by the confinement of charged carriers in the geometric dimensions of the particles (i.e., quantum confinement).^{1, 29-34} Synthesis methods such as thermal pyrolysis of silicon oxides,³⁵⁻⁴⁰ nonthermal plasma synthesis from appropriate precursors,⁴¹⁻⁴⁵ and pulsed laser ablation of silicon precursors⁴⁶⁻⁴⁸ have been developed and all provide some measure of control over the SiQD sizes, and by extension, tailorability of the PL maxima. The complement to this size-based tuning is the unique opportunity to manipulate SiQD emission maximum through the exploitation of surface-state-mediated relaxation involving surface heteroatoms (e.g., N, O, and Cl).^{4, 49-51} Single-dot spectroscopy of individual SiQDs also suggests that emission linewidth is affected by the particle surface chemistry and the corresponding interface with their host matrix.^{52, 53} It is an understatement to say the recombination of charge carriers in SiQDs is complex, since it is intimately dependent on the nanoparticle size, shape, structure, and interface.

So called ‘dangling bonds’ (DBs), unsaturated Si atoms that can act as nonradiative recombination centers for the carriers,⁵⁴ are known to adversely impact SiQD PLQY. The introduction of covalently bonded surface species (alkyl, polymers, oxides, etc.)^{42, 55-63} has been met with differing degrees of success in passivating defect states, preventing oxidation, and minimizing DB formation. Among the various approaches, alkyl-functionalized SiQDs are convenient systems for evaluating photostability because the functionalization increases solution processibility while imposing negligible effects on the optical band gap of the nanoparticles.⁶⁴⁻⁶⁶ The Kortshagan group studied 1-dodecyl functionalized SiQDs synthesized via plasma decomposition of silane and noted an approximate 60% decrease in PLQY after 4 h of UV irradiation. This was attributed to the formation of DBs via UV-induced homolytic cleavage of Si-H or Si-Si bonds.^{57, 58} It is well-established that amorphous silicon (a-Si) is susceptible to light-induced degradation known as the Staebler-Wronski effect (SWE) which manifests as a decrease in a-Si photoconductivity after prolonged UV light exposure.^{67, 68} Anthony et al. also observed that increasing structural disorder (i.e., SiQDs with greater amorphous character) in plasma-generated SiQDs leads to decreased PLQY as compared to more crystalline SiQDs.⁶⁹

Recently, our group reported the presence of an ordered crystalline core for SiQDs with $d > 6$ nm, obtained from thermal processing of hydrogen silsesquioxane (HSQ) before terminating in an amorphous ‘shell’. We subsequently demonstrated that the amorphous Si (a-Si) layer can be reduced by ‘over-etching’ samples with ethanolic hydrofluoric acid (HF).^{70, 71} With the a-Si ($E_g = \sim 1.7$ eV) shell present, the particles resembled Type-I core-shell QDs due to the comparatively smaller band gap ($E_g = \sim 1.1$ eV) of the nanocrystalline Si core (nc-Si).^{62, 72-74} This wider band gap of the a-Si is expected to provide a barrier to charge carriers (i.e., holes and electrons) migrating to the particle surface resulting in less non-radiative recombination and an increased PLQY.

However, the question remains if the amorphous shell will protect the SiQD core and provide access to higher PLQYs. In addition, will the impact of the SWE on the amorphous shell result in decreased photostability and, by extension, lower PLQYs? Herein, we explore the impact of the amorphous shell on the photostability of 1-dodecyl-terminated SiQDs obtained from the reductive thermal processing of HSQ.

4.2 Experimental Details

4.2.1 Reagents and Materials

Sulfuric acid (reagent grade, 95 – 98%) was purchased from Caledon Laboratory Chemicals. Hydrofluoric acid (HF; electronics grade, 48–50%) was purchased from Fisher Scientific. Fuming sulfuric acid (reagent grade, 20% free SO₃ bases), trichlorosilane (99%), toluene (HPLC grade), methanol (reagent grade), ethanol (reagent grade), 2,2'-azobis(2-methyl propionitrile) (98%), 1-dodecene (95.0%), and benzene (anhydrous, 99.8%) were purchased from Sigma Aldrich. A PureSolv purification system equipped with N₂ as the operating gas was used for preparing dried solvents. All reagents and solvents were used as received unless otherwise specified.

4.2.2 Preparation of Hydrogen Silsesquioxane (HSQ)

HSQ was synthesized using a modified literature procedure.⁷⁵ Briefly, a mixture of concentrated (15 mL) and fuming (7 mL) sulfuric acid was prepared in a three-neck round bottom flask purged with argon and equipped with an addition funnel and Teflon coated stir bar. Dry toluene (45 mL) was then added to the acids via the addition funnel. A mixture of dry toluene (110 mL) and trichlorosilane (16 mL) was prepared and subsequently added dropwise into the acid-toluene mixture to obtain two-layers. The toluene layer was isolated and washed with an aqueous sulfuric acid (33% v/v) solution. The organic layer was then dried over solid MgSO₄ and CaCO₃ for 12

hours, after which the solvent volume was removed using rotary evaporation and finally dried in vacuo to yield a white solid.

4.2.3 Preparation of SiQDs/SiO₂ Composite

SiQDs were prepared by way of thermally-induced disproportionation of HSQ using a well-established procedure developed in our laboratory.⁷⁶ HSQ (5 g) was placed in a standard tube furnace with a flowing 5% H₂/Ar atmosphere at 1200 or 1300°C to yield oxide composites containing ca. 5 or 9 nm inclusions of elemental silicon, respectively. The composite was then mechanically ground using an agate mortar and pestle and shaken with glass beads in ethanol (~300 mL) to provide a fine powder that was used in subsequent etching procedures.

4.2.4 Preparation of Hydride-terminated SiQDs

Hydride-terminated SiQDs (H-SiQDs) were liberated from appropriate oxide composites via ethanolic HF-etching of the ground composite.⁷¹ Composite (~500 mg) obtained from processing HSQ at 1200°C was etched using a solution (16.5 mL) of ethanol: distilled water: 49% HF (1:1:1) in a PET beaker that was equipped with a Teflon coated stir bar for a predetermined time. The liberated freestanding SiQDs were then extracted into a minimum amount of toluene (~30 mL) and collected with centrifugation before redispersing twice in toluene (~10 mL) dried over molecular sieves. These two subsequent centrifugations washes remove any residual HF. For convenience in the present discussion, we refer to “normal” H-SiQDs as those obtained from etching “1200°C composites” for 1 h. “Over-etched” H-SiQDs were prepared similarly by etching composite (~700 mg) prepared by thermally processing HSQ at 1300°C with a solution (24 mL) of ethanol:distilled water:HF (1:1:1) for ca. 3.5 - 4 h until the suspension colour resembles that of the 1hr etch of ‘1200°C composites’. The H-SiQDs were used immediately in functionalization reactions (*vide infra*).

4.2.5 Preparation of Dodecyl-terminated SiQDs

Radical-initiated hydrosilylation was used to functionalize the H-SiQD surfaces and render them solution processible.⁶⁴ Briefly, ‘normal’ H-SiQDs (~0.5 g) were dispersed in dry toluene (10 mL), 1-dodecene (6 mL), and AIBN (300 mg) in an Ar-purged Schlenk flask equipped with a Teflon coated stir bar. The reaction mixture was subsequently degassed *via* three sequential freeze-pump-thaw cycles and placed in an oil bath at 70°C for 17-19 h under flowing Ar. After cooling to room temperature, surface functionalized SiQDs isolated from the reaction mixture via centrifugation with toluene and methanol. ‘Over-etched’ H-SiQDs (~0.7 g) were functionalized using the same procedure in dry toluene (14 mL) and 1-dodecene (8.4 mL) with an AIBN (420 mg) initiator. After purification, the wet pellets of SiQDs were dispersed in a minimum amount of benzene (ca. 1 mL), filtered using a 0.45 μm PTFE syringe filter into a pre-weighted vial, and freeze-dried. Solid dodecyl-SiQDs were massed in the vial, transferred into the glovebox, redispersed with dry toluene (~2 mg ml⁻¹), and stored in subdued light until needed.

4.2.6 Photodegradation of Dodecyl-terminated SiQDs Suspensions

Photodegradation experiments were performed using a custom the Schlenk flask equipped with a quartz insert to facilitate exposure to the emission from a UV light LED source (365 nm, Nichia, model NCSU033A operated at 4.5 V). In an Ar-filled glovebox, the toluene suspension of functionalized SiQDs (i.e., normal or over-etched) was transferred to the Schlenk flask that was already equipped with a pre-dried Teflon stir bar and the quartz insert was affixed. The sealed flask containing the SiQD suspension was then removed from the glovebox and affixed to a standard Schlenk manifold with Ar working gas. The flask was wrapped with aluminum foil and irradiation commenced under flowing Ar while the apparatus was maintained at 10 °C. Aliquots were taken

at predefined time intervals using a glass syringe and stored in the glovebox until needed for analyses.

4.2.7 Optical Characterization

Optical characterization of all SiQD suspensions was performed in a quartz cuvette (1 cm x 1 cm). Photoluminescence (PL) spectra were acquired by exciting samples using the combined 351 and 364 nm lines of an argon ion laser and collecting the emission using an optic fiber connected to an Ocean Optics USB 2000+ Spectrometer. A 425 nm long-pass filter (LPF) was used to eliminate scattered light from the excitation source. The spectral response was calibrated using a blackbody radiator. Time-resolved PL (PL lifetime) measurements were acquired using the same laser (20 mW) interfaced to an acoustic-optic modulator (50 ns response time) operated at a frequency of 100 Hz with a 50% duty cycle. The PL was captured by an optic fiber, sent through a 500 nm long-pass filter, and counted by a Hamamatsu H7422P-50 photomultiplier tube (PMT) interfaced with a Becker-Hickl PMS-400A gated photon counter. The data was collected without wavelength selection and used 1 μ s time steps. The mean PL decay lifetimes were found by fitting the data using a log-normal lifetime distribution function.^{51, 77} UV-vis absorption spectra were measured using the Ocean Optics USB 2000+ spectrometer with a MINI-D2T Deuterium Tungsten light source ($\lambda_{\text{ex}} = 200 - 1000$ nm).

Absolute PL quantum yield (PLQY) measurements were performed using an integrating sphere with a 365 nm light-emitting diode excitation source. Solutions were diluted to have an absorbance between 0.08 to 0.13 at 400 nm. The PL and excitation intensities were measured through an optical fiber and analyzed with an Ocean Optics 2000+ spectrometer using a NIST-calibrated light source for absolute irradiance measurements. The measurements were done in triplicate.

4.2.8 Fourier Transform Infrared Spectroscopy (FT-IR)

SiQDs were drop-cast onto a silicon wafer from dry toluene suspensions and the toluene was evaporated under ambient conditions. FT-IR spectra were acquired using a Thermo Nicolet 8700 FTIR Spectrometer equipped with a microscope.

4.2.9 X-ray Photoelectron Spectroscopy (XPS)

Samples were prepared by drop-casting toluene suspensions of SiQDs onto copper foil. XP spectra were measured using Kratos Axis 165 Ultra X-ray photoelectron spectrometer with a monochromatic Al K α source operating at 210 W with an energy $h\nu = 1486.6$ eV. Survey spectra were acquired using an analyzer pass energy of 160 eV and a step size of 0.3 eV. For high-resolution spectra, a pass energy of 20 eV and a step size of 0.1 eV were used. All spectra were calibrated to C 1s (284.4 eV) using CasaXPS (VAMAS) software with a Shirley-type background to remove most of the extrinsic loss structure. The Si 2p region was fit to appropriate spin-orbit splitting with Si 2p_{3/2} and Si 2p_{1/2} components – the doublet area ratio fixed at 2:1 and separated spin-orbit splitting fixed at 0.62 eV.

4.2.10 Thermal Gravimetric analysis (TGA)

Dried SiQDs were transferred to an appropriate platinum pan that was placed in a Mettler Toledo TGA/DSC 1 star system. The sample weight loss was monitored in a N₂ atmosphere over the temperature range of 25 to 700 °C at a temperature ramp rate of 10 °C/min. Estimation of ligand surface coverage was determined using an established literature procedure.¹⁵

4.2.11 X-ray Diffraction (XRD)

XRD samples were prepared by drop-casting toluene suspensions of SiQDs onto a zero-background Si wafer and measured in a thin film orientation using a Rigaku Ultima IV multipurpose X-ray diffraction system equipped with a Cu K α source. For thin-film diffraction, a parallel beam was used with a glancing angle of 0.5°. The XRD peaks were analyzed with the Debye-Scherrer equation: $d_{xrd} = \frac{K\lambda}{\beta \cos\theta}$, where d_{xrd} is the mean size of the crystalline domain, K is the shape factor ($K = 0.94$ for spherical crystals with cubic lattice),⁷⁸ λ is the X-ray wavelength ($\lambda_{\text{CuK}\alpha} = 0.15406$ nm), β is the full-width-at-half-maximum (FWHM) of the reflections (rad), and θ is the Bragg angle (rad).

4.2.12 Raman Spectroscopy

Samples were prepared by drop-casting toluene suspensions of SiQDs onto a copper foil. Spectra were acquired using a Renishaw Raman microscope InVia upon excitation with a 532 nm laser.

4.2.13 Electron Paramagnetic Resonance (EPR)

EPR samples were prepared in EPR tubes containing a capillary tube with SiQDs toluene suspension (0.2 mL) inside a nitrogen-filled glovebox. The EPR tubes were capped and sealed with Parafilm to minimize exposure to ambient atmosphere throughout the EPR measurement. Spectra were acquired on a Bruker EMX Nano spectrometer at room temperature with X-band microwave (applied frequency of 9.636859 GHz) and a microwave attenuation of 25 dB. The field was centered at 3434 G with a sweep width of 500 G and sweep time of 75 s. A receiver gain of 30 dB and modulated amplitude of 5 G were set. Each spectrum was measured with 2 scans.

4.2.14 Transmission Electron Microscopy (TEM)

TEM samples were prepared by depositing a drop of a dilute toluene suspension of the sample in question onto a holey or ultra-thin carbon-coated copper grid (obtained from Electron Microscopy Inc.). The grid bearing the sample was subsequently transferred to a vacuum chamber at a base pressure of 0.2 bar for at least 24 h prior to data collection. Bright field TEM images were acquired using a JEOL JEM-ARM200CF S/TEM electron microscope with an accelerating voltage of 200 kV. High-resolution (HR) TEM images were processed using Gatan Digital Micrograph software (Version 3.4.1).

4.3 Result and Discussion

‘Normal’ (N) SiQDs bearing thick a-Si shell and ‘over-etched’ (O) SiQDs with thin-to-no amorphous layer were subjected to the emission from a 365 nm UV lamp for up to 72 h. The integrity of the SiQDs was evaluated using optical, structural, and compositional analyses before and after exposure. To investigate the impact of an a-Si shell on the photostability of SiQD optical properties, it was necessary to prepare nanoparticles with the same physical dimensions but different crystallinity (i.e., crystalline core/a-Si shell vs. crystalline). To realize these SiQD classes, we thermally processed HSQ at 1200 and 1300 °C in a slightly reducing atmosphere to yield different oxide composites containing elemental silicon inclusions with dimensions of ca. 5 and ca. 9 nm, respectively (**Figure 4.1**). SiQDs were then liberated from the protective silicon oxide matrix via alcoholic HF etching. Materials prepared in this way comprise a crystalline core and amorphous shell; the majority of the a-Si shell can then be removed with prolonged HF etching.⁷¹ For ease of understanding, our present discussion refers to the SiQDs bearing a thicker amorphous shell obtained from the 1200 °C-processed composite and subjected to aqueous ethanolic HF etching for 1 h as ‘normal’. ‘Over-etched’ SiQDs were prepared by prolonged etching (i.e., 3.5-4

h) of the composite processed at 1300 °C. The extended etching simultaneously removes the thick amorphous shell and reduces particle dimensions to align closely with those of the N-SiQDs obtained at 1200 °C. Both classes of SiQDs were then surface modified with 1-dodecene via AIBN-initiated radically-induced hydrosilylation to yield solution-stable dodecyl-SiQDs. Four batches of N-SiQDs and five batches of over-etched O-SiQDs were prepared.

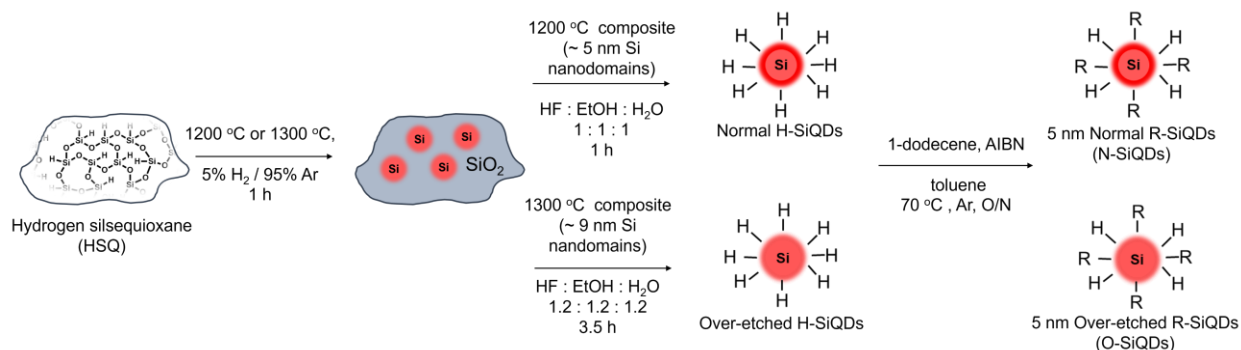


Figure 4.1. Preparation of ‘normal’ and ‘over-etched’ dodecyl-functionalized SiQDs. Freestanding H-SiQDs were liberated from HF-etching of thermally-processed HSQ, followed by radical-initiated hydrosilylation with 1-dodecene.

Representative bright-field TEM images (**Figure 4.2a and b**) indicate that dodecyl functionalized N-SiQDs and O-SiQDs possessed statistically indistinguishable physical dimensions of 5.1 ± 1.2 nm (**Figure 4.2c**) and 5.3 ± 1.1 nm (**Figure 4.2d**), respectively. As expected, corresponding dark-field TEM images (**Figure 4.2e-h**) also revealed equivalent sizes. In contrast to our TEM analysis, Debye-Scherrer analyses of the XRD patterns (**Figure 4.3a**) indicates N-SiQDs possess an XRD crystallite size of ca. 3.5 nm while O-SiQDs exhibit an average XRD crystallite size of ca. 4.9 nm. This observation is expected and consistent with previous studies.⁷¹ Raman spectroscopy was used to probe the order/disorder structures present in the nanoparticles. **Figure 4.3b** shows the Raman spectra of both SiQD classes comprising a sharp peak at ca. 512 cm^{-1} that is attributed to nanocrystalline Si (nc-Si).^{79, 80} In contrast to the single,

asymmetric Lorentzian peak observed for O-SiQDs, a broad shoulder at approximately 470 cm^{-1} arises from a-Si is also present in the spectrum of the N-SiQDs.⁸¹ The combined TEM, XRD, and Raman analyses, as well as our previous report,⁷⁰ all point to over-etching being effective in the removal of the amorphous shell from O-SiQDs. The FT-IR and XP (**Figure 4.3**) spectra were measured and suggest the two sets of nanoparticles were of equivalent composition and thus only differ in crystallinity. In addition, a weight loss of ca. 45% noted in TGA (**Figure 4.3**) for both sets of SiQDs further suggesting a similar degree of surface functionalization (i.e., ca. 55%).

The PL of the as-produced SiQDs is summarized in **Table 4.1** and compared using boxplots (See **Figure 4.4**). Both N- and O-SiQDs exhibited featureless UV-vis absorption spectra (**Figure 4.5-Figure 4.6**). The QDs all emitted near-infrared PL centered in the range of 810 to 940 nm with broad emission bandwidths (full-width-at-half-maximum (FWHM) in the range of ca. 129 to 234 nm). Characteristic S-band Si PL lifetimes of 160 to 400 μs were also observed for both classes of QDs.⁸² The O-SiQDs exhibited similar mean PL maxima and longer mean PL lifetime than the N-SiQDs, but no statistical differences in these properties were found between the two classes of samples (**Figure 4.4a-b**).

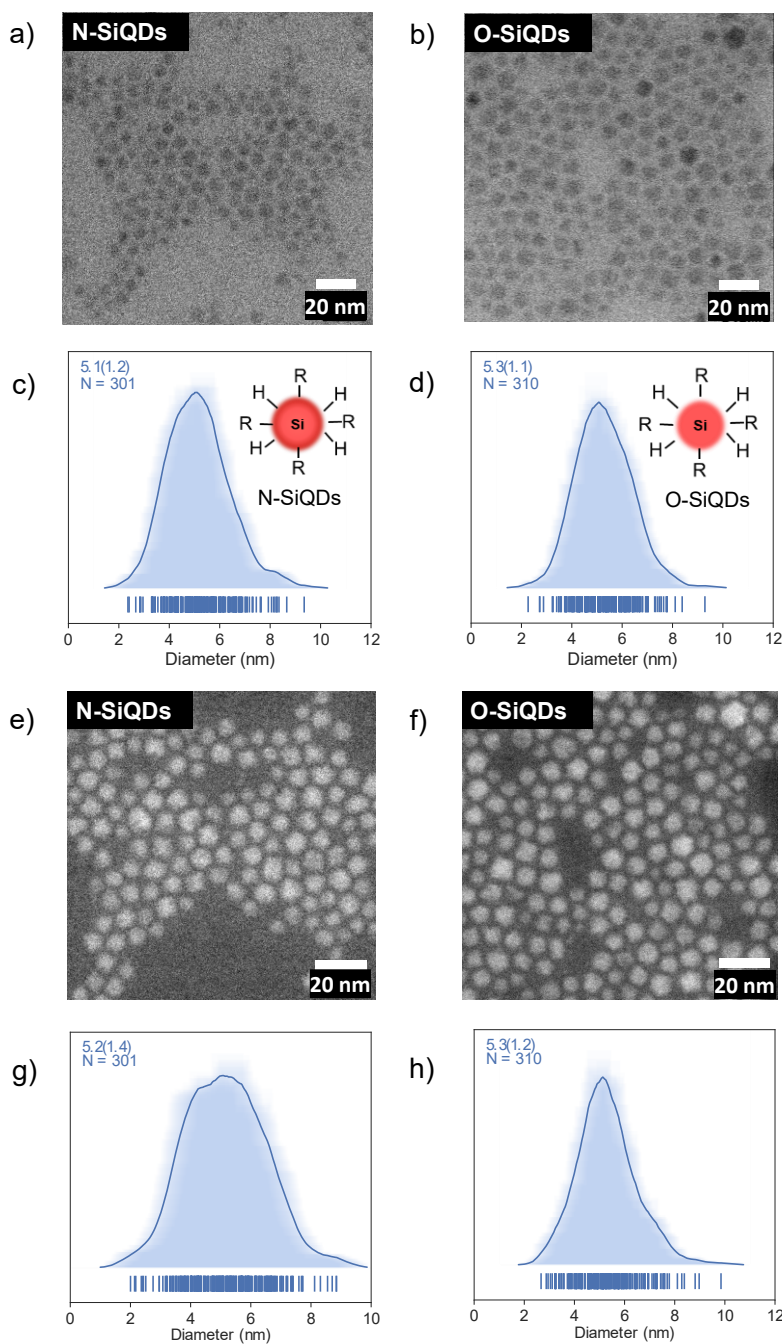


Figure 4.2. Transmission electron microscopic (TEM) images of the dodecyl-SiQDs used in this study. Bright-field TEM images show equivalent physical dimensions of **(a)** N-SiQDs (5.1 ± 1.2 nm) and **(b)** O-SiQDs (5.3 ± 1.1 nm). The respective size distributions, **(c)** and **(d)**, are presented as average-shifted histograms. Dark-field TEM images show equivalent physical dimensions of **(e)** N-SiQDs (5.2 ± 1.4 nm) and **(f)** O-SiQDs (5.3 ± 1.2 nm). The respective size distributions, **(g)** and **(h)**, are presented as average-shifted histograms.

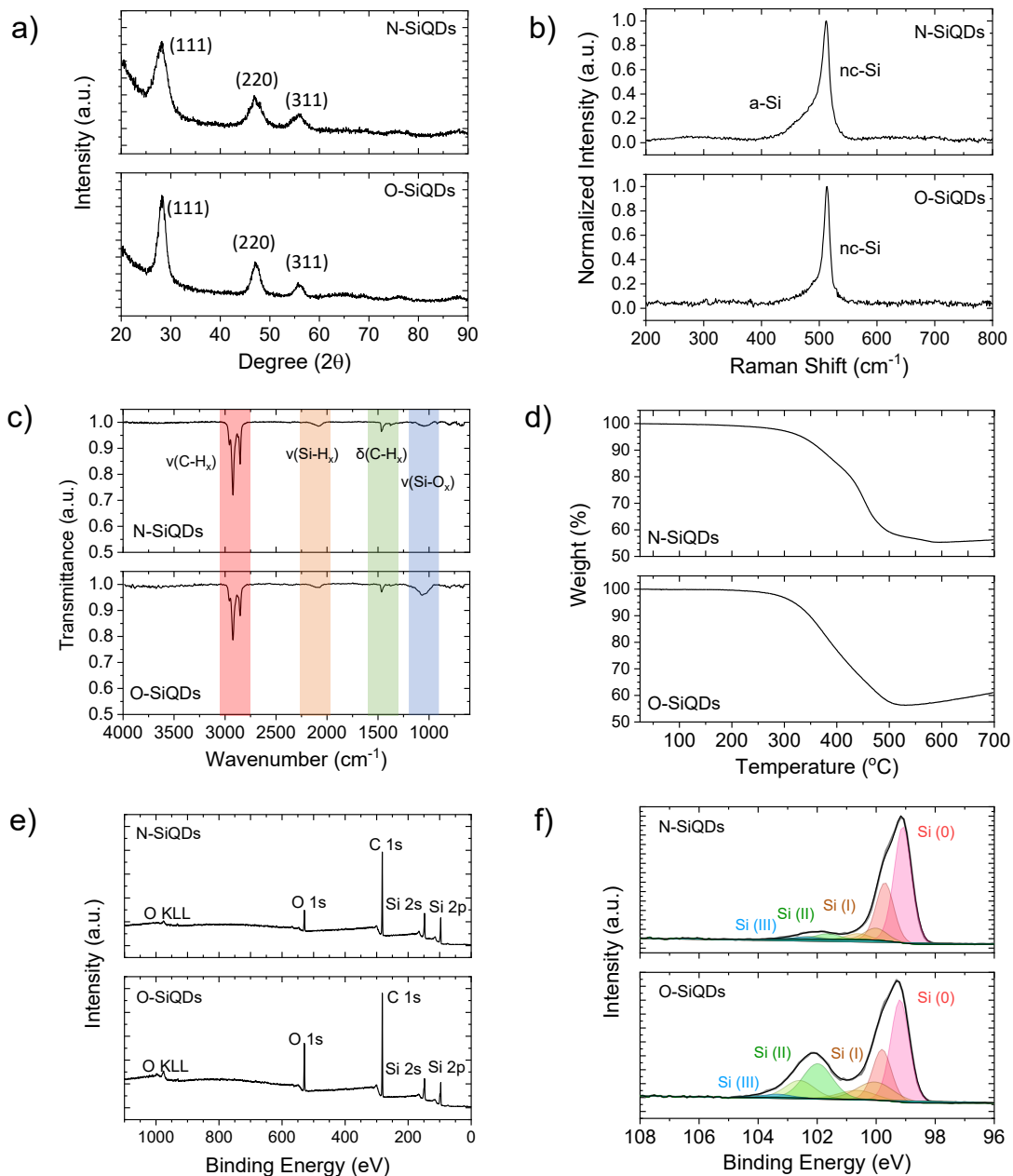


Figure 4.3. Structural and compositional analyses of the as-produced dodecyl-SiQDs. **(a)** XRD patterns and **(b)** Raman spectra show evidence of greater long-range order in O-SiQDs. **(c)** FT-IR spectra and **(d)** TGA of the SiQDs. **(e)** Survey and **(f)** high-resolution Si 2p XPS spectra of the as-produced nanoparticles.

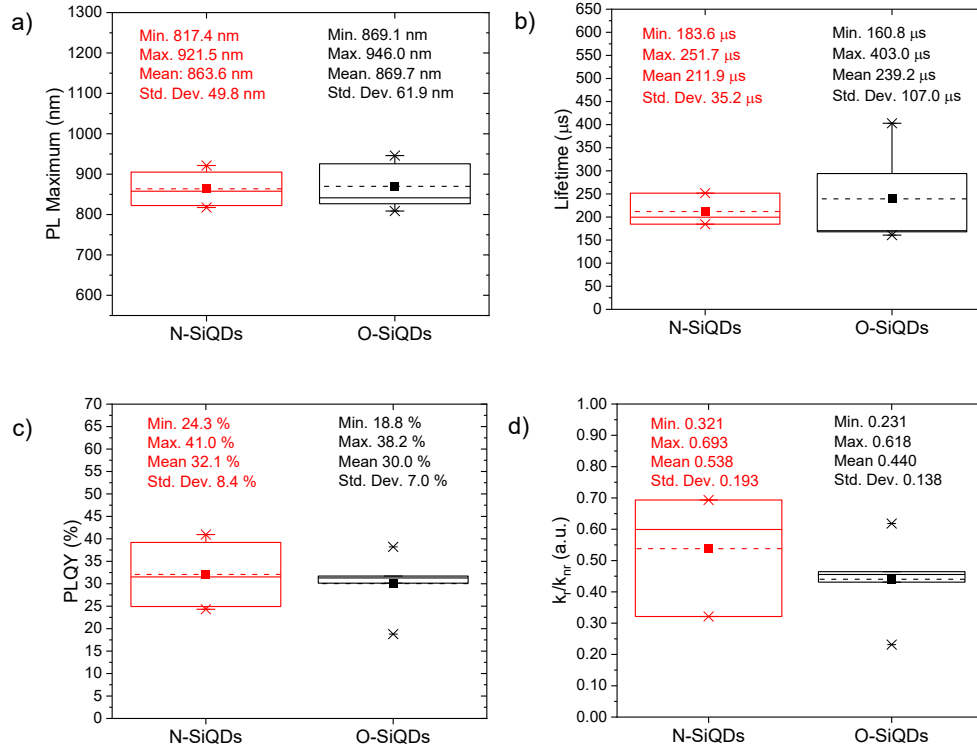


Figure 4.4. Boxplots comparing the (a) PL max, (b) mean PL lifetime, (c) PLQY, and (d) k_r/k_{nr} of the as-produced N-SiQDs and O-SiQDs. Mean and median of the distributions are represented by dash and solid lines in the boxes, respectively.

Table 4.1. Summary of Optical Properties for the As-produced SiQDs

Sample	PL Max [nm]	FWHM [nm]	PLQY [%]	τ [μ s]	τ_r [μ s]	k_r [μ s ⁻¹]	τ_{nr} [μ s]	k_{nr} [μ s ⁻¹]	k_r/k_{nr}
N-1	888	163	41.0	251.6	614.5	1.63E-03	426.2	2.35E-03	0.693
N-2	817	183	37.5	199.5	532.5	1.88E-03	319.1	3.13E-03	0.599
N-3	921	137	25.6	N/A	N/A	N/A	N/A	N/A	N/A
N-4	827	220	24.3	184.6	759.2	1.32E-03	243.9	4.10E-03	0.321
Average	864	176	32.1	211.9	635.4	1.61E-03	329.7	3.19E-03	0.538
O-1	926	177	30.1	294.1	976.4	1.02E-03	420.9	2.38E-03	0.431
O-2	809	175	38.2	160.8	420.8	2.38E-03	260.2	3.84E-03	0.618
O-3	827	168	31.7	167.8	529.2	1.89E-03	245.8	4.07E-03	0.464
O-4	841	234	31.3	170.4	544.4	1.84E-03	248.0	4.03E-03	0.455
O-5	946	129	18.8	403.0	2144.4	4.66E-04	496.3	2.01E-03	0.231
Average	870	177	30.0	239.2	923.05	1.52E-03	334.2	3.27E-03	0.440

N = normally-etched SiQDs

O = over-etched SiQDs

The PLQY of the as-produced SiQDs was measured to establish whether the inclusion of an a-Si shell influences the radiative recombination of excitons. Recall that PLQY quantifies the efficiency of QDs in producing emitted photons from absorbed photons and depends upon the specific radiative and all non-radiative processes as summarized in Equations 4.1 and 4.2:

$$PLQY(\eta) = \frac{\text{photons emitted}}{\text{photons absorbed}} = \frac{k_r}{k_r + \sum k_{nr}} \quad (4.1)$$

where k_r is radiative recombination rate (μs^{-1}) and k_{nr} is non-radiative recombination rate (μs^{-1}). Expressed in terms of the lifetimes,

$$PLQY(\eta) = \frac{\tau_{pl}}{\tau_r} = \frac{1/\tau_r}{(1/\tau_r + 1/\tau_{nr})} \quad (4.2)$$

where τ_{pl} is photoluminescence lifetime (μs), τ_r is radiative recombination lifetime, and τ_{nr} is non-radiative recombination lifetime.⁸³ The PLQY of the batches of as-produced N-SiQDs was in the range of 24 to 41%, whereas the PLQY of O-SiQD batches ranged between 19 to 38% (**Figure 4.4c**). The respective radiative recombination rate ratio (k_r/k_{nr}) ranged between 0.25 to 0.69 (**Figure 4.4d**). Of note, a narrower distribution of PLQY and k_r/k_{nr} was observed from O-SiQDs. In addition, the mean PLQY and k_r/k_{nr} of N-SiQDs are higher than that of O-SiQDs, although the differences are not statistically significant.

The bulk band gap of a-Si is larger than that of bulk crystalline silicon (e.g., ca. 1.7 eV⁷³ vs. ca. 1.1 eV⁷⁴). Hence, an a-Si shell is expected to provide a passivation layer that would confine photo-excited charge carriers to the crystalline core and limit surface state-related non-radiative recombination pathways directly analogous to what is observed from traditional Type-I QDs. However, we note that N-SiQDs have similar PLQY as the O-SiQDs. One must consider that a 1 to 3 nm thick a-Si layer may have a varying number of trap states in the band gap which could lead

to electron-hole delocalization at the a-Si:c-Si interface.⁸⁴ We hypothesize that the positive effects of the large band gap a-Si shell are counteracted by the negative effects of defects introduced by the amorphous structure. The balanced effect therefore showed minimal improvement in the radiative recombination in N-SiQDs. We note that the thin and disordered structure of the amorphous shell showed minimal improvement in the radiative recombination in N-SiQDs despite the large band gap of a-Si. The removal of this a-Si shell, which affects with the loss of corresponding trap states, could lead to the narrower distribution of radiation recombination rates observed for O-SiQDs (*vide supra*). A detailed investigation of the relationship between the thickness and/or quality of the amorphous layer on the optical properties of the nanoparticles would be of interest to uncover the potential of core-shell structure. However, precise control in tuning the amorphous shell is yet to be explored and is beyond the scope of this study.

To study the photostability of N-SiQDs and O-SiQDs, the materials were suspended in dry toluene and irradiated by 365 nm UV-LEDs at 4.5 V under an Ar atmosphere for 72 h. Aliquots were extracted at predefined time intervals and evaluated by PL, UV-vis absorption, emission lifetime, and PLQY as summarized in **Figure 4.7**. A small shift in PL maximum (< 10 nm; **Figure 4.4a**) was occasionally observed that we attribute to trace oxidation occurring during material handling and data acquisition. Of important note, these shifts were negligible compared to previously reported, and prominent, oxidation-induced blue-shift.^{51, 85}

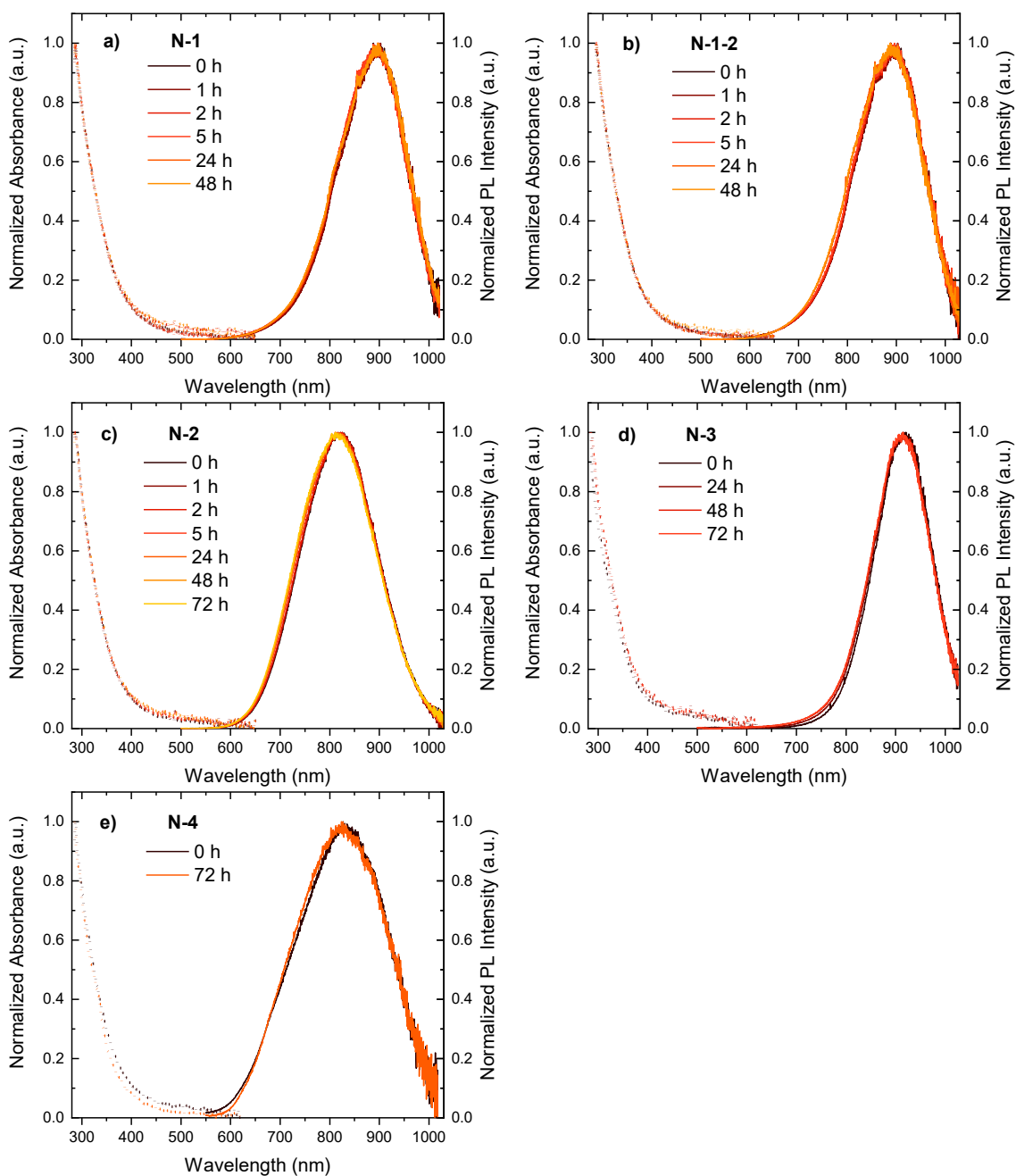


Figure 4.5. UV-vis absorption (dotted) and PL (solid) spectra of N-SiQDs. The numbering corresponds to **Table 4.2**.

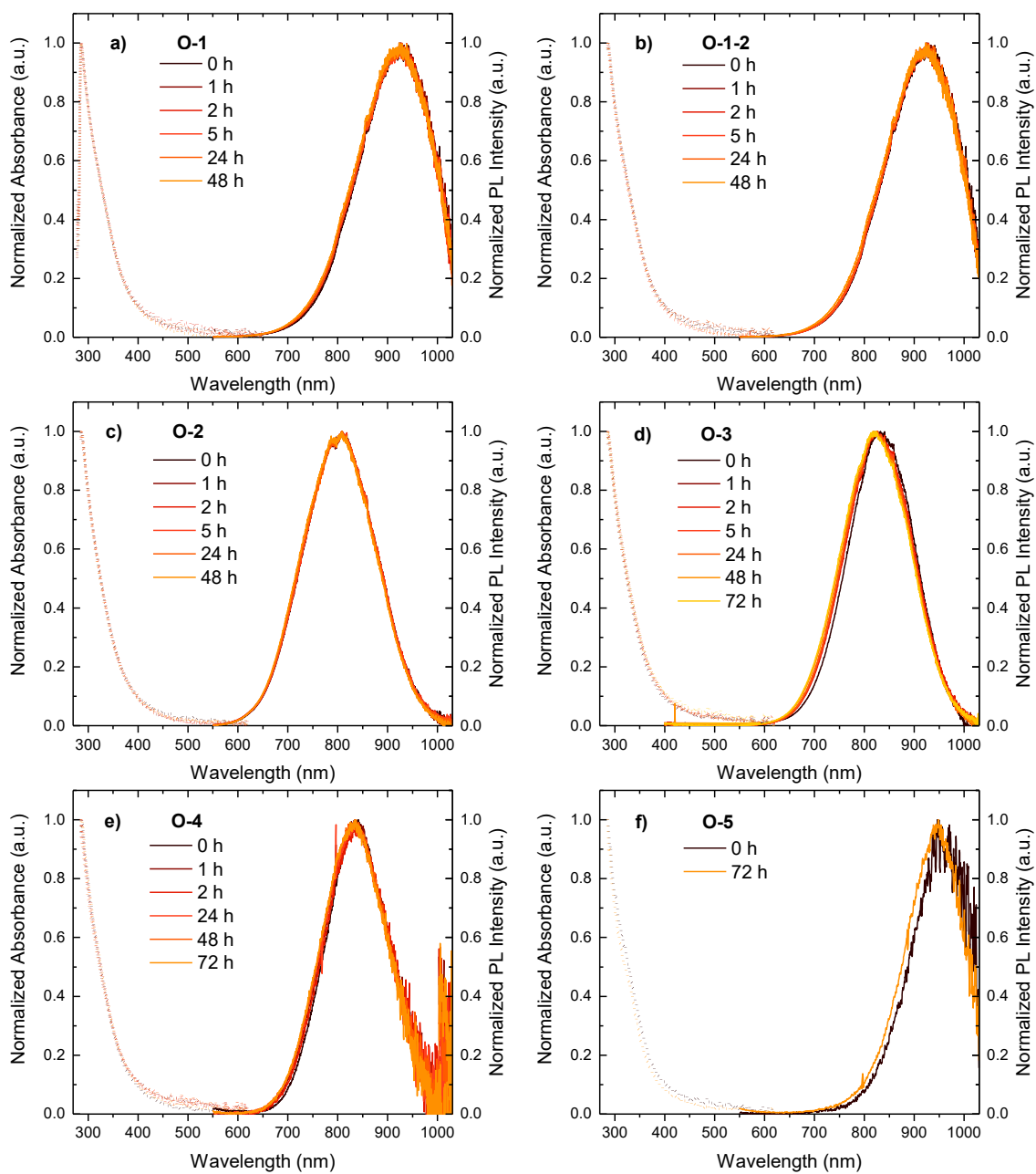


Figure 4.6. UV-vis absorption (dotted) and PL (solid) spectra of O-SiQDs. The numbering corresponds to **Table 4.3**.

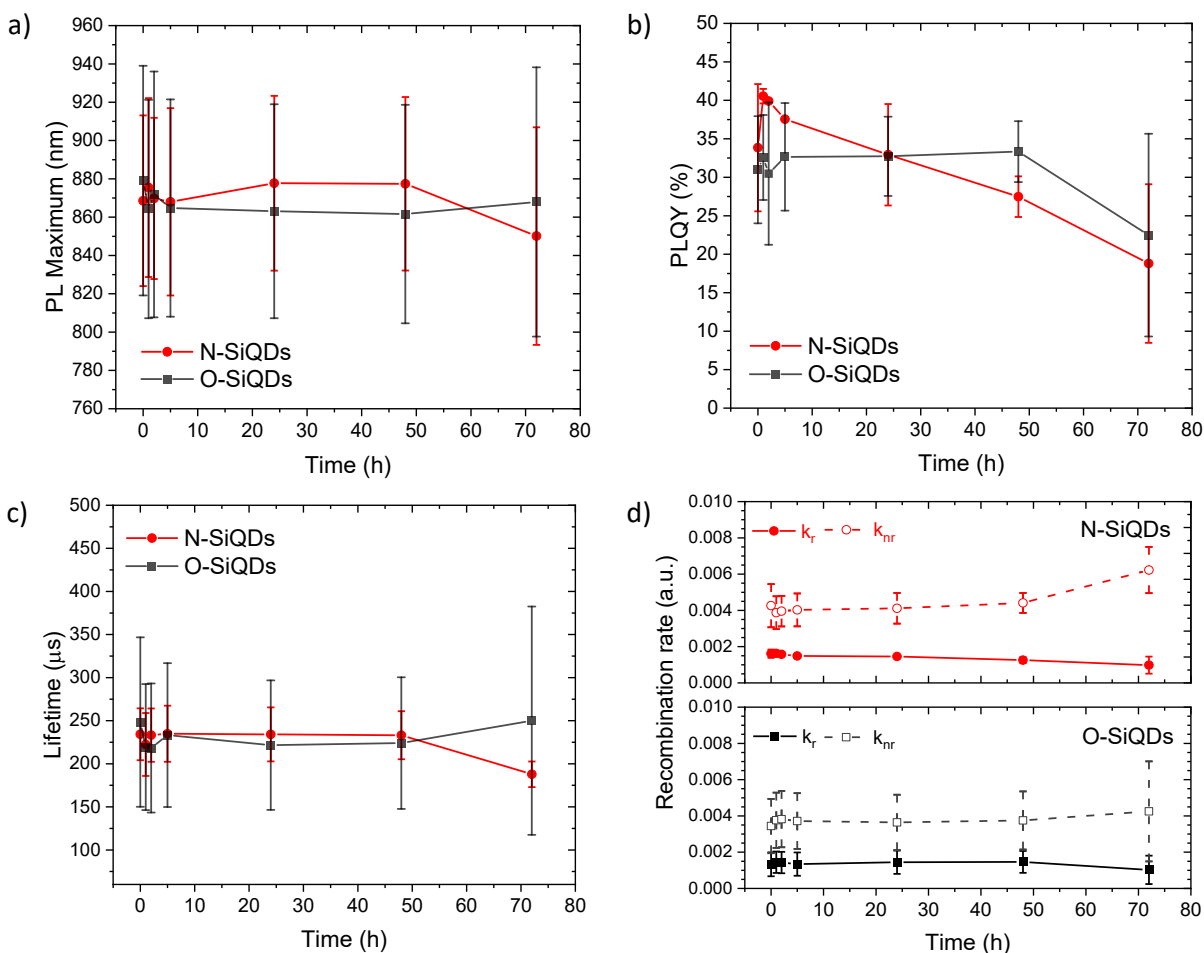


Figure 4.7. A summary of the optical properties of N-SiQDs (red circles) and O-SiQDs (black squares). **(a)** PL maxima, **(b)** PLQY, **(c)** PL lifetime, and **(d)** recombination rate ratio as a function of time over a period of 72 h of UV irradiation. Error bars represent the 95% limit of measurement. Representative PL and UV-vis absorption spectra of each sample are plotted in Figure 4.5-Figure 4.6.

Table 4.2. Summary of Optical Properties for N-SiQDs Throughout Photo-degradation

Sample	Degradation Time [h]	PL Maximum [nm]	FWHM [nm]	PLQY [%]	τ [μ s]	k_r [μ s ⁻¹]	k_{nr} [μ s ⁻¹]	k_r/k_{nr}	Relative Abs @ 365 nm
N-1	0	888	163	41.0	251.6	0.0016	0.0023	0.69	0.22
	1	902	164	41.1	251.1	0.0016	0.0023	0.70	0.22
	2	899	166	39.9	250.6	0.0016	0.0024	0.64	0.23
	5	897	165	37.6	254.7	0.0015	0.0025	0.60	0.22
	24	897	167	36.2	251.1	0.0014	0.0025	0.57	0.23
	48	897	169	28.8	248.4	0.0012	0.0029	0.40	0.24
N-1-2*	0	888	163	41.0	251.6	0.0016	0.0023	0.69	0.22
	1	902	163	41.1	256.2	0.0016	0.0023	0.65	0.21
	2	888	163	39.9	251.6	0.0016	0.0024	0.78	0.23
	5	896	165	37.6	252.7	0.0015	0.0025	0.68	0.22
	24	888	169	36.2	253.2	0.0014	0.0025	0.55	0.22
	48	888	170	27.8	250.1	0.0012	0.0029	0.38	0.23
N-3	0	817	183	37.5	199.5	0.0019	0.0031	0.60	0.22
	1	822	187	31.9	198.0	0.0016	0.0034	0.47	0.22
	2	822	184	43.7	197.6	0.0016	0.0035	0.47	0.23
	5	812	185	30.1	197.4	0.0015	0.0036	0.43	0.22
	24	812	188	29.4	198.0	0.0015	0.0036	0.42	0.22
	48	812	188	29.0	200.9	0.0014	0.0035	0.41	0.23
	72	812	189	26.1	198.3	0.0013	0.0037	0.35	0.23
N-4	0	921	137	25.6	N/A	N/A	N/A	N/A	0.20
	24	915	138	23.0	N/A	N/A	N/A	N/A	0.22
	48	914	141	23.5	N/A	N/A	N/A	N/A	0.22
	72	915	140	21.0	N/A	N/A	N/A	N/A	0.24
N-5	0	827	220	24.3	184.6	0.0013	0.0041	0.32	0.22
	72	824	224	11.5	177.3	0.0006	0.0050	0.13	0.17
Average	0	869	173	33.9	221.9	0.0016	0.0030	0.58	0.22
	1	875	171	38.0	235.1	0.0016	0.0027	0.61	0.22
	2	870	171	41.2	233.3	0.0016	0.0028	0.63	0.23
	5	868	172	35.1	234.9	0.0015	0.0028	0.57	0.22
	24	878	165	31.2	234.1	0.0015	0.0029	0.51	0.22
	48	877	167	27.3	233.2	0.0013	0.0031	0.40	0.23
	72	850	185	19.5	187.8	0.0010	0.0044	0.24	0.21

*N-1-2 is a separate degradation trial using the same SiQDs as N-1.

Table 4.3. Summary of Optical Properties for O-SiQDs Throughout Photo-degradation

Sample	Degradation Time [h]	PL Maximum [nm]	FWHM [nm]	PLQY [%]	τ [μ s]	k_r [μ s ⁻¹]	k_{nr} [μ s ⁻¹]	k_r/k_{nr}	Relative Abs @ 365 nm
O-1	0	926	177	30.1	294.1	0.0010	0.0024	0.43	0.22
	1	926	182	27.7	299.8	0.0009	0.0024	0.43	0.22
	2	926	177	26.1	297.7	0.0009	0.0024	0.41	0.23
	5	928	179	26.1	304.0	0.0009	0.0023	0.38	0.22
	24	923	181	26.9	304.0	0.0009	0.0024	0.35	0.22
	48	923	184	27.9	303.7	0.0010	0.0022	0.35	0.22
O-1-2*	0	926	177	30.1	294.1	0.0010	0.0024	0.43	0.22
	1	926	178	28.0	298.6	0.0010	0.0023	0.37	0.23
	2	928	178	26.8	302.8	0.0010	0.0024	0.39	0.22
	5	923	178	27.9	307.1	0.0009	0.0024	0.39	0.21
	24	923	180	27.9	303.1	0.0009	0.0024	0.37	0.22
	48	923	180	30.7	308.6	0.0009	0.0024	0.45	0.22
O-3	0	809	175	38.2	160.8	0.0023	0.0039	0.60	0.21
	1	809	176	39.8	159.0	0.0023	0.0040	0.59	0.20
	2	809	178	41.8	159.7	0.0023	0.0039	0.60	0.20
	5	809	175	41.3	157.8	0.0023	0.0041	0.56	0.21
	24	809	175	38.3	158.4	0.0023	0.0040	0.58	0.21
	48	809	178	36.1	154.2	0.0022	0.0043	0.52	0.20
O-4	0	827	168	31.7	167.8	0.0013	0.0060	0.32	0.19
	1	824	162	30.3	164.2	0.0013	0.0061	0.30	0.22
	2	824	162	30.2	163.5	0.0013	0.0061	0.30	0.20
	5	827	162	30.8	164.2	0.0013	0.0061	0.31	0.22
	24	824	164	30.5	163.5	0.0013	0.0061	0.30	0.22
	48	819	165	29.8	161.3	0.0013	0.0062	0.30	0.21
	72	819	164	27.5	161.3	0.0011	0.0062	0.27	0.23
O-5	0	841	234	31.3	170.4	0.0018	0.0040	0.46	0.20
	1	837	169	30.3	175.2	0.0017	0.0040	0.44	0.22
	2	837	209	27.8	167.6	0.0017	0.0043	0.39	0.20
	24	837	209	33.7	178.9	0.0019	0.0037	0.51	0.22
	48	834	195	37.6	192.1	0.0020	0.0033	0.60	0.22
	72	837	236	32.4	186.4	0.0017	0.0036	0.48	0.21
O-6	0	946	129	18.8	403.0	0.0005	0.0020	0.23	0.22
	72	948	135	7.5	402.2	0.0002	0.0023	0.08	0.18
Average	0	870	177	30.0	239.2	0.0014	0.0037	0.41	0.21
	1	864	173	31.2	219.4	0.0014	0.0038	0.42	0.22
	2	865	181	30.6	218.2	0.0014	0.0038	0.42	0.21
	5	872	173	31.5	233.2	0.0013	0.0037	0.41	0.21
	24	863	182	31.5	221.6	0.0014	0.0037	0.42	0.22
	48	862	180	32.4	224.0	0.0015	0.0037	0.45	0.21
	72	868	179	22.5	250.0	0.0010	0.0040	0.28	0.21

*O-1-2 is a separate degradation trial using the same SiQDs as O-1.

The decrease of the PLQY (**Table 4.2-Table 4.3**) observed for the SiQD suspensions results primarily from the influence of surface defects and/or DBs created as a result of UV irradiation. On average, both classes of SiQDs maintained ca. 90% of their initial PLQYs during the first 24 h of irradiation (**Figure 4.7b**). After this time, the average PLQY of N-SiQDs continued to decrease to ca. 80% of its original value after 48 h irradiation and finally to ca. 70% after 72 h. In contrast, the O-SiQDs maintained ca. 90% of their initial PLQY for the first 48 h before eventually decreasing to ca. 70% after 72 h. A similar photostability study by Wu et al. using SiQDs synthesized using non-thermal plasma methods showed a plateau in PLQY loss after reaching ca. 20% in SiQDs.⁵⁸ However, it is unclear if these particles possess an a-Si shell. Regardless, both studies suggest dodecyl-SiQDs reach a steady state of ca. 20-30% decrease from their “as prepared” original PLQY following prolonged UV irradiation. Although the quantum efficiency decreased as a result of irradiation, the PL lifetimes remained fairly consistent (**Figure 4.7c**). Using Equation 4.1-4.2, the radiative and non-radiative decay rates can be determined independently (**Figure 4.7d**). The trends of recombination rates are fitted with a linear regression (**Figure 4.8 ; Table 4.4**). In general, for N-SiQDs with amorphous shells, the non-radiative rate increased with a decrease in radiative rate upon irradiation; whereas for the O-SiQDs the radiative and non-radiative rates remained constant. These observations further point to the reduced optical stability of N-SiQDs.

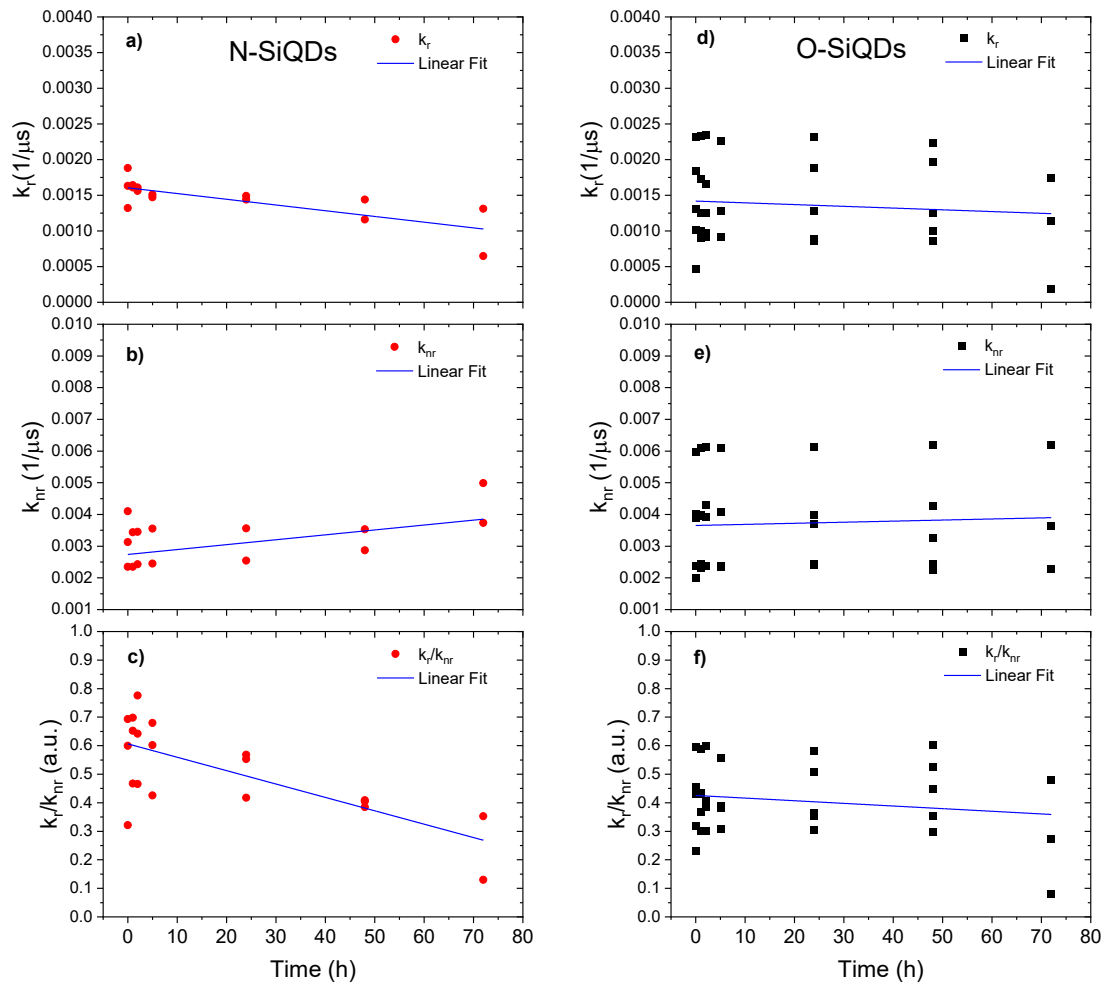


Figure 4.8. Linear fit of k_r , k_{nr} , and k_r/k_{nr} of SiQDs (a-c for N-SiQDs and c-d for O-SiQDs).

Table 4.4. Summary of Linear Fit for SiQDs Recombination Rate

Sample			Value	Standard Error	t-value	P-value
N-SiQDs	k_r	Intercept	0.0016	4.32375E-5	37.11502	0
		Slope	-8.02471E-6	1.43376E-6	-5.59697	2.13358E-5
	k_{nr}	Intercept	0.00274	1.72603E-4	15.86944	2.03459E-12
		Slope	1.54649E-5	5.72354E-6	2.70198	0.01413
	k_r/k_{nr}	Intercept	0.60632	0.03175	19.09527	7.37188E-14
		Slope	-0.00469	0.00105	-4.45414	2.72092E-4
O-SiQDs	k_r	Intercept	0.00142	1.308E-4	10.84687	4.44089E-12
		Slope	-2.4474E-6	4.33258E-6	-0.56488	0.57622
	k_{nr}	Intercept	0.00365	3.25774E-4	11.21471	1.93623E-12
		Slope	3.41376E-6	1.07909E-5	0.31636	0.75385
	k_r/k_{nr}	Intercept	0.4256	0.02634	16.16049	2.22045E-16
		Slope	-9.2474E-4	8.72351E-4	-1.06005	0.29731

The t-value is a measure of how many standard errors the estimated value is away from zero (i.e., slope = zero). A higher absolute t-value suggests that the estimate is more likely to be reliable. The P-value indicates the likelihood of the null hypothesis (i.e., there is no relationship between the independent variable and the dependent variable). A low p-value (typically < 0.05) suggests that one can reject the null hypothesis.

We hypothesize that these observations can be understood in the context of the Staebler-Wronski effect, in which irradiation of a-Si could generate dangling bonds that reduce radiative recombination. A recent STM study reported by Kisilitsyn et al. provides a more direct visualization of generating dangling bonds, along with deep charge traps, in a-Si by applying electrons to the amorphous shell of SiQDs through the STM tip.⁸¹ In addition to the defects formed at the surface of a-Si, the formation of dangling bonds at the amorphous-Si:crystalline-Si interface (a-Si:c-Si) could also lead to a decrease in radiative recombination efficiency. Plagwitz et al. similarly attributed an increase in the surface recombination rate to defects at the a-Si:c-Si interface.⁶⁸ A potential mechanism for decreased k_r involves charge carrier tunneling from the QD core to the interface, where the charge carriers non-radiatively recombine. In contrast, O-SiQDs exhibit minimal changes in recombination rate under similar conditions; this underscores the unique role of the a-Si shell in modulating radiative recombination dynamics during prolonged illumination.⁸⁶ Nevertheless, it is important to note that the slope is two to three orders of magnitude (10^{-5} to 10^{-6}) smaller than the k values (10^{-3}) and the sample size of N-SiQDs is smaller than O-SiQDs. Studies that are beyond the scope of the present paper are ongoing to explore the origin of the decrease. A prospective transient absorption and scanning tunneling spectroscopic^{81, 87, 88} study provided insights into the photophysics and electronics of the different SiQDs under illumination.

The creation of dangling bonds through Si-H and Si-Si cleavage will certainly lead to a decrease in PL and conductivity and result in surface species desorption from the nanoparticles in the form of $\cdot\text{SiH}_3(\text{g})$ and $\cdot\text{H}(\text{g})$.^{89, 90} To account for this, samples of SiQDs with and without 72 h of irradiation were characterized by XPS and FT-IR to probe any changes in their structure and compositions. As expected, XP spectra of the SiQDs were the same (**Figure 4.9**) showing similar Si species regardless of the degradation, suggesting minimal oxidation. Likewise, both classes of

SiQDs show comparable features in their FT-IR spectra, aside from a minor increase in the Si-O_x stretches at $\sim 1100\text{ cm}^{-1}$ caused by exposure to oxygen during the measurement (**Figure 4.10a-b**).

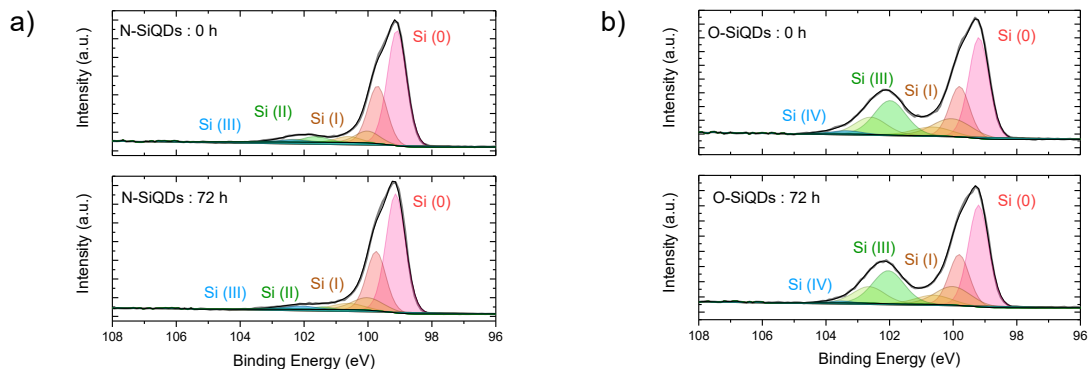


Figure 4.9. High-resolution Si 2p XP spectra of (a) N-SiQDs and (b) O-SiQDs with (top) and without (bottom) 72 h of UV irradiation.

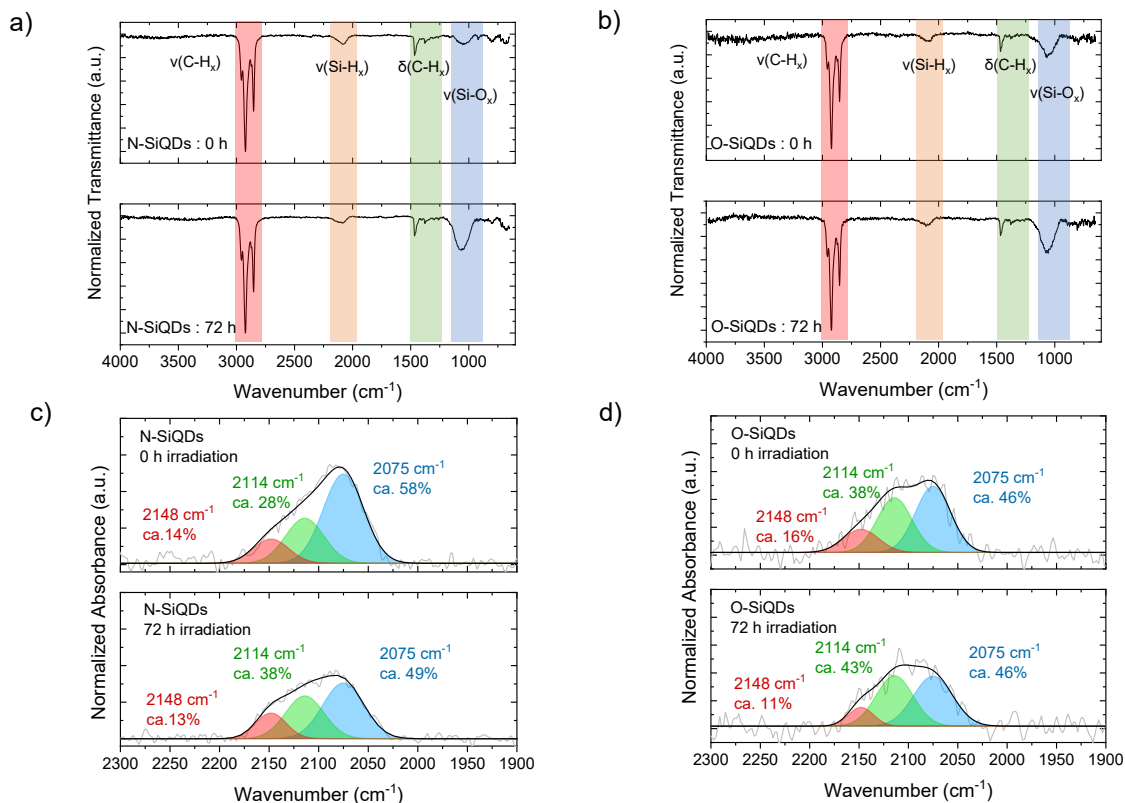


Figure 4.10. FT-IR spectra of (a) N-SiQDs and (b) O-SiQDs with (top) and without (bottom) 72 h of UV irradiation showing similar surface species. The Si-H_x stretches are deconvoluted in spectra (c) and (d) for N-SiQDs and O-SiQDs, respectively.

The Si-H_x stretching features in FT-IR spectra (**Figure 4.10**) can be readily deconvoluted into ≡SiH ($\nu = 2075 \text{ cm}^{-1}$), =SiH₂ ($\nu = 2114 \text{ cm}^{-1}$), and -SiH₃ ($\nu = 2148 \text{ cm}^{-1}$) to probe potential surface changes induced by exposure to 365 nm UV ($E_{\text{hv}} = 3.4 \text{ eV}$) irradiation.^{85,91} The as prepared samples that were not exposed to UV irradiation show that the ≡SiH peak being the dominant surface species followed by =SiH₂, and -SiH₃ with a relative peak area ratio of ≡SiH:=SiH₂:-SiH₃ is 58 : 28 : 14 and 46 : 38 : 16 for N- and O-SiQDs, respectively. The different ratios of the SiH_x species may be attributed to changes in the QD surface morphology upon removal of a-Si shell. The impact of extended HF etching on the surface species is, however, beyond the scope of the study and remains the subject of ongoing investigations. Upon UV exposure, ca. 20% and 6% decrease in Si-H_x stretches are observed for N-SiQDs and O-SiQDs, respectively. This observation is expected as the irradiation can cleave bonds within the SiQDs as summarized in **Figure 4.11**. The deconvoluted FT-IR spectra after irradiation reveal a decrease in the relative intensity of features associated with -SiH₃ and ≡SiH and an increase in those associated with =SiH₂. The reduction in the -SiH₃ signal (11% for N-SiQDs and 33% for O-SiQDs) is frequently attributed to ·SiH₃(g) desorption from homolytic cleavage of Si-SiH₃ (B.E. ~ 2.0 - 2.7 eV).^{90,92,93} The H-Si bond of =SiH₂ (B.E. ~ 3.2 eV) on the strained SiQD surface is also susceptible to bond cleavage yielding ·H_(g) and ·SiH_(s).^{90,92,93} Comparatively, the ≡SiH silane bond should be most stable with a B.E. of ~3.6 eV.⁸⁹ The decrease in the concentration of monohydrides (i.e., ≡SiH) and increase dihydrides (i.e., =SiH₂) can be understood in the context of the complex surface structure of the nanoparticles. A bulk silicon surface comprises specific crystal planes (e.g., Si(100) containing =SiH₂ ; Si(111) containing ≡SiH), however the small SiQDs used in this study do not have well-defined facets.⁹⁶⁻⁹⁸ The silicon hydrides on the nanoparticles cannot be said to reside on ordered planes, rather, they are located on a small crystal terrace with numerous steps and edges. Upon

release of volatile $\cdot\text{SiH}_3(\text{g})$ and $\cdot\text{H}(\text{g})$, it is reasonable that the liberated species could further react with neighboring silicon hydrides, resulting in silanes ($\text{SiH}_x(\text{g})$) and hydrogen gas ($\text{H}_2(\text{g})$).^{90, 99, 100} The complex SiQD structure together with the reactive radicals could enable $=\text{SiH}_2$ formation at the expense of normally less reactive $\equiv\text{SiH}$. The consistent loss of $-\text{SiH}_3$ components suggests surface species desorption resulted from SiQDs photodegradation.

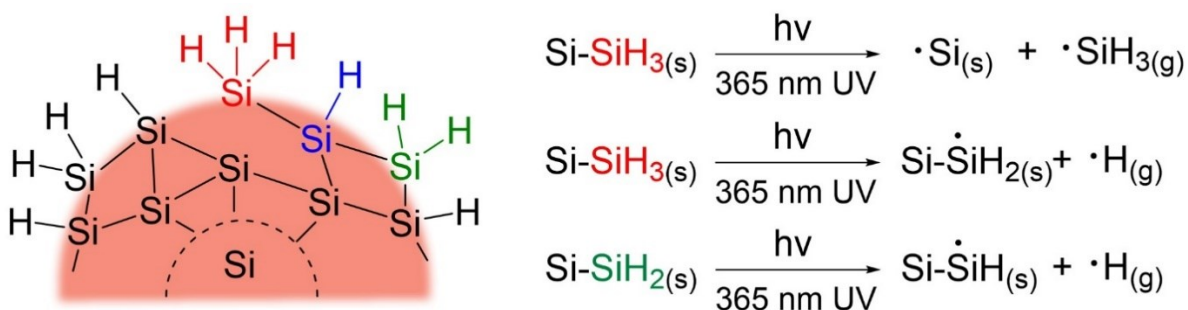


Figure 4.11. Summary of possible bond breakages in SiQDs upon 365 nm UV irradiation

The size and shape of the SiQDs after UV irradiation were also evaluated by TEM. The corresponding microscopy images (**Figure 4.12** and **Figure 4.13**) revealed the preservation of the spheroidal shapes in both sets of nanoparticles. The size distributions of the corresponding images indicated a 2% shrinkage in N-SiQDs and a 4% decrease in O-SiQDs consistent with surface atom desorption. However, it is important to note that these changes are within the error of the method and should not be over emphasized. The Raman spectra (**Figure 4.14a**) of the irradiated particles remain similarly unchanged from the as-produced nanoparticles. An investigation using in-situ TEM¹⁰¹ and solid-state NMR¹⁰² could potentially provide additional insight into these small, but possibly important, structural changes that occur on the evolving SiQD surface, however such studies are outside the current capability of our instrumentation.

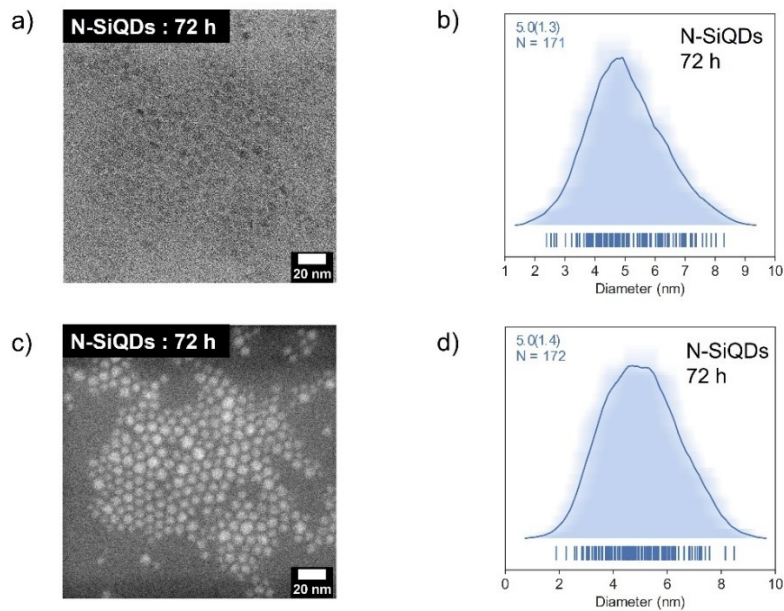


Figure 4.12. Bright-field (a) and dark-field (c) TEM images showing preservation of spheroidal shape and sizes of N-SiQDs after 72 h irradiation. The respective size distributions, (b) and (d), were plotted as average-shifted histograms.

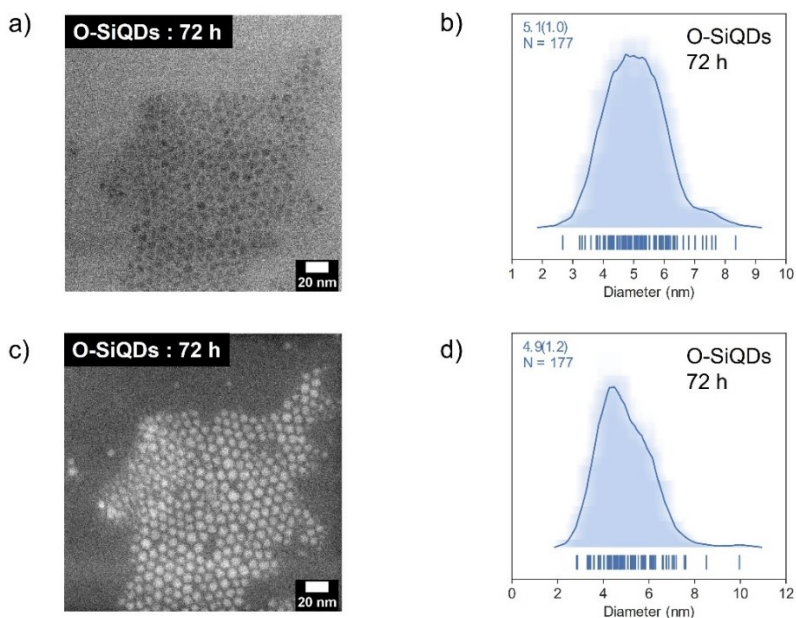


Figure 4.13. Bright-field (a) and dark-field (c) TEM images showing preservation of spheroidal shape and sizes of O-SiQDs after 72 h irradiation. The respective size distributions, (b) and (d), were plotted as average-shifted histograms.

With the knowledge that the instability of radiative recombination in SiQDs is a result of the generation of defects at the nanoparticle surfaces, EPR spectroscopy was used to assess the relative densities of unpaired electron spins in the both N-SiQDs and O-SiQDs. Toluene solutions of as-prepared and 72-hour-irradiated SiQDs (2 mg/mL) were evaluated (**Figure 4.14b**). For both systems, the EPR signal appeared in the range of g-factor 2.00 to 2.01. This can be ascribed to dangling bonds on silicon in a disordered environment (g_D at ~ 2.005) and asymmetric P_b centers at the interface of the Si nanocrystal and its oxide shell (g_{\perp} at ~ 2.008 and g_{\parallel} at ~ 2.002).^{80, 103} The EPR signal from N-SiQDs was qualitatively more than twice as intense as that from O-SiQDs before and after irradiation; this observation is consistent with our observations of decreased PLQY and k_r/k_{nr} values. Given the two sets of nanoparticles had a similar degree of alkyl passivation, the more intense EPR signals of N-SiQDs can reasonably be ascribed to a greater number defects at the a-Si surface and a more disordered Si:SiO_x and a-Si:nc-Si interface. This observation aligns with a density functional theory (DFT) study by Bushlanova et al., which indicated that amorphous Si_nH_{2m} nanoclusters with sizes of ~ 1 nm, in contrast to their crystalline counterpart, contained dangling bonds at the cluster surface.¹⁰⁴ Future work could utilize in-situ characterization, pump-probe spectroscopy, and STM measurements to further understand the photophysics and degradation mechanisms between the different nanoparticles.

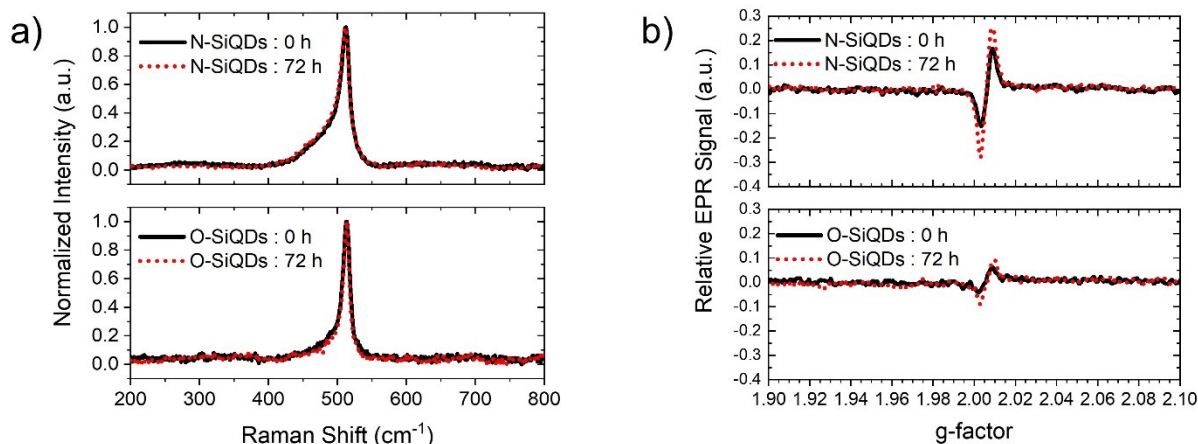


Figure 4.14. Structural analyses comparing N-SiQDs (top) and O-SiQDs (bottom) before and after 72 h of irradiation. **(a)** Raman spectra showing negligible changes in structural orderliness for both classes of nanoparticles. More intense EPR signal **(b)** of N-SiQDs is observed in comparison to O-SiQDs after exposure to UV. Black solid lines and red dotted lines indicate data obtained from nanoparticles before and after irradiation, respectively.

4.4 Conclusions

In this study, ca. 5 nm dodecyl-functionalized silicon quantum dots, with (N-SiQDs) and without (O-SiQDs) ‘thick’ amorphous shells, were prepared. The presence of an amorphous layer did not significantly affect the optical properties (i.e., photoluminescence maxima, lifetime, and photoluminescence yield) of the as-produced nanoparticles. However, the loss of quantum yield for N-SiQDs was more pronounced upon prolonged UV irradiation as compared to O-SiQDs. Structural analyses presented here indicate the adverse effects of the amorphous shell can be reasonably attributed to the generation of defects in the disordered SiQD structure. Our study provides valuable initial insight into the photostability of SiQDs; a better understanding of their core-shell structure may provide information needed to generate even more stable luminescent systems.

4.5 References

1. G. Ledoux, J. Gong, F. Huisken, O. Guillois and C. Reynaud, *Applied Physics Letters*, 2002, **80**, 4834-4836.
2. R. J. Clark, M. K. Dang and J. G. Veinot, *Langmuir*, 2010, **26**, 15657-15664.
3. C. M. Hessel, D. Reid, M. G. Panthani, M. R. Rasch, B. W. Goodfellow, J. Wei, H. Fujii, V. Akhavan and B. A. Korgel, *Chemistry of Materials*, 2012, **24**, 393-401.
4. M. Dasog, G. B. De los Reyes, L. V. Titova, F. A. Hegmann and J. G. C. Veinot, *ACS Nano*, 2014, **8**, 9636-9648.
5. S. Ivanov, S. Zhuravsky, G. Yukina, V. Tomson, D. Korolev and M. Galagudza, *Materials*, 2012, **5**, 1873-1889.
6. A. Das and P. T. Snee, *Chemphyschem*, 2016, **17**, 598-617.
7. A. Shiohara, S. Hanada, S. Prabakar, K. Fujioka, T. H. Lim, K. Yamamoto, P. T. Northcote and R. D. Tilley, *Journal of the American Chemical Society*, 2010, **132**, 248-253.
8. National Toxicology Program. Toxicology and carcinogenesis studies of indium phosphide (CAS No. 22398-90-7) in F344/N rats and B6C3F1 mice (inhalation studies). *Natl Toxicol Program Tech Rep Ser*. 2001, 7-340. PMID: 12087422.
9. R. Hardman, *Environmental Health Perspect*, 2006, **114**, 165-172.
10. J. Sobhanan, J. V. Rival, A. Anas, E. Sidharth Shibu, Y. Takano and V. Biju, *Advanced Drug Delivery Reviews*, 2023, **197**, 114830.
11. K. Y. Cheng, R. Anthony, U. R. Kortshagen and R. J. Holmes, *Nano Letter*, 2011, **11**, 1952-1956.
12. B. Ghosh, Y. Masuda, Y. Wakayama, Y. Imanaka, J.-i. Inoue, K. Hashi, K. Deguchi, H. Yamada, Y. Sakka, S. Ohki, T. Shimizu and N. Shirahata, *Advanced Functional Materials*, 2014, **24**, 7151-7160.
13. J. Watanabe, H. Yamada, H.-T. Sun, T. Moronaga, Y. Ishii and N. Shirahata, *ACS Applied Nano Materials*, 2021, **4**, 11651-11660.
14. Y. C. Zhang, Z. Y. Yu, X. Y. Xue, F. L. Wang, S. Li, X. Y. Dai, L. Wu, S. Y. Zhang, S. Y. Wang and M. Lu, *Optic Express*, 2021, **29**, 34126-34134.
15. I. T. Cheong, J. Mock, M. Kallergi, E. Groß, A. Meldrum, B. Rieger, M. Becherer and J. G. C. Veinot, *Advanced Optical Materials*, 2022, **11**, 2201834.
16. F. Meinardi, S. Ehrenberg, L. Dharmo, F. Carulli, M. Mauri, F. Bruni, R. Simonutti, U. Kortshagen and S. Brovelli, *Nature Photonics*, 2017, **11**, 177-185.
17. R. Mazzaro, A. Gradone, S. Angeloni, G. Morselli, P. G. Cozzi, F. Romano, A. Vomiero and P. Ceroni, *ACS Photonics*, 2019, **6**, 2303-2311.

18. S. Han, G. Chen, C. Shou, H. Peng, S. Jin and C.-C. Tu, *ACS Applied Materials & Interfaces*, 2020, **12**, 43771-43777.
19. J. Huang, J. Zhou, E. Jungstedt, A. Samanta, J. Linnros, L. A. Berglund and I. Sychugov, *ACS Photonics*, 2022, **9**, 2499-2509.
20. T. Lin, X. Liu, B. Zhou, Z. Zhan, A. N. Cartwright and M. T. Swihart, *Advanced Functional Materials*, 2014, **24**, 6016-6022.
21. M. Dutta, L. Thirugnanam, P. V. Trinh and N. Fukata, *ACS Nano*, 2015, **9**, 6891-6899.
22. E. J. Henderson, A. J. Shuhendler, P. Prasad, V. Baumann, F. Maier-Flaig, D. O. Faulkner, U. Lemmer, X. Y. Wu and G. A. Ozin, *Small*, 2011, **7**, 2507-2516.
23. C. J. T. Robidillo, M. A. Islam, M. Aghajamali, A. Faramus, R. Sinelnikov, X. Zhang, J. Boekhoven and J. G. C. Veinot, *Langmuir*, 2018, **34**, 6556-6569.
24. Z. F. Li and E. Ruckenstein, *Nano Letters*, 2004, **4**, 1463-1467.
25. D. Yang, Z. Cui, Z. Wen, Z. Piao, H. He, X. Wei, L. Wang, S. Mei, W. Zhang and R. Guo, *ACS Materials Letters*, 2023, **5**, 985-1008.
26. Z. Kang, C. H. A. Tsang, N.-B. Wong, Z. Zhang and S.-T. Lee, *Journal of the American Chemical Society*, 2007, **129**, 12090-12091.
27. T. Kojima, H. Sugimoto and M. Fujii, *The Journal of Physical Chemistry C*, 2018, **122**, 1874-1880.
28. M. Iqbal, T. K. Purkait, G. G. Goss, J. R. Bolton, M. Gamal El-Din and J. G. Veinot, *ACS Nano*, 2016, **10**, 5405-5412.
29. W. L. Wilson, P. Szajowski and L. Brus, *Science*, 1993, **262**, 1242-1244.
30. T. van Buuren, L. N. Dinh, L. L. Chase, W. J. Siekhaus and L. J. Terminello, *Physical Review Letters*, 1998, **80**, 3803-3806.
31. J. D. Holmes, K. J. Ziegler, R. C. Doty, L. E. Pell, K. P. Johnston and B. A. Korgel, *Journal of the American Chemical Society*, 2001, **123**, 3743-3748.
32. D. C. Hannah, J. Yang, P. Podsiadlo, M. K. Y. Chan, A. Demortière, D. J. Gosztola, V. B. Prakapenka, G. C. Schatz, U. Kortshagen and R. D. Schaller, *Nano Letters*, 2012, **12**, 4200-4205.
33. N. Shirahata, J. Nakamura, J. I. Inoue, B. Ghosh, K. Nemoto, Y. Nemoto, M. Takeguchi, Y. Masuda, M. Tanaka and G. A. Ozin, *Nano Letters*, 2020, **20**, 1491-1498.
34. D. S. English, L. E. Pell, Z. Yu, P. F. Barbara and B. A. Korgel, *Nano Letters*, 2002, **2**, 681-685.
35. M. Zacharias, J. Heitmann, R. Scholz, U. Kahler, M. Schmidt and J. Bläsing, *Applied Physics Letters*, 2002, **80**, 661-663.
36. J. G. Veinot, *Chemical Communications*, 2006, 4160-4168.
37. S. Godefroo, M. Hayne, M. Jivanescu, A. Stesmans, M. Zacharias, O. I. Lebedev, G. Van Tendeloo and V. V. Moshchalkov, *Nature Nanotechnology*, 2008, **3**, 174-178.

38. W. Sun, C. Qian, X. Cui, L. Wang, M. Wei, G. Casillas, A. S. Helmy and G. A. Ozin, *Nanoscale*, 2016, **8** 6, 3678-3684.
39. Y. Yu, G. Fan, A. Fermi, R. Mazzaro, V. Morandi, P. Ceroni, D.-M. Smilgies and B. A. Korgel, *The Journal of Physical Chemistry C*, 2017, **121**, 23240-23248.
40. J. Zhou, J. Huang, H. Chen, A. Samanta, J. Linnros, Z. Yang and I. Sychugov, *The Journal of Physical Chemistry Letters*, 2021, **12**, 8909-8916.
41. L. Mangolini, E. Thimsen and U. Kortshagen, *Nano Letters*, 2005, **5**, 655-659.
42. A. Gupta, M. T. Swihart and H. Wiggers, *Advanced Functional Materials*, 2009, **19**, 696-703.
43. Z. Li and U. R. Kortshagen, *Chemistry of Materials*, 2019, **31**, 8451-8458.
44. Y. Ding, R. Yamada, R. Gresback, S. Zhou, X. Pi and T. Nozaki, *Journal of Physics D: Applied Physics*, 2014, **47**, 485202.
45. T. A. Pringle, K. I. Hunter, A. Brumberg, K. J. Anderson, J. A. Fagan, S. A. Thomas, R. J. Petersen, M. Sefannaser, Y. Han, S. L. Brown, D. S. Kilin, R. D. Schaller, U. R. Kortshagen, P. R. Boudjouk and E. K. Hobbie, *ACS Nano*, 2020, **14**, 3858-3867.
46. T. Orii, M. Hirasawa and T. Seto, *Applied Physics Letters*, 2003, **83**, 3395-3397.
47. T. Nakamura, Z. Yuan, K. Watanabe and S. Adachi, *Applied Physics Letters*, 2016, **108**.
48. A. V. Kabashin, A. Singh, M. T. Swihart, I. N. Zavestovskaya and P. N. Prasad, *ACS Nano*, 2019, **13**, 9841-9867.
49. M. Dasog, Z. Yang, S. Regli, T. M. Atkins, A. Faramus, M. P. Singh, E. Muthuswamy, S. M. Kauzlarich, R. D. Tilley and J. G. Veinot, *ACS Nano*, 2013, **7**, 2676-2685.
50. M. Dasog, K. Bader and J. G. C. Veinot, *Chemistry of Materials*, 2015, **27**, 1153-1156.
51. R. Sinelnikov, M. Dasog, J. Beamish, A. Meldrum and J. G. C. Veinot, *ACS Photonics*, 2017, **4**, 1920-1929.
52. I. Sychugov, A. Fucikova, F. Pevero, Z. Yang, J. G. C. Veinot and J. Linnros, *ACS Photonics*, 2014, **1**, 998-1005.
53. A. Fucikova, I. Sychugov and J. Linnros, *Faraday Discussions*, 2020, **222**, 135-148.
54. E. Cartier, J. H. Stathis and D. A. Buchanan, *Applied Physics Letters*, 1993, **63**, 1510-1512.
55. M. Rosso-Vasic, E. Spruijt, B. van Lagen, L. De Cola and H. Zuilhof, *Small*, 2008, **4**, 1835-1841.
56. K. Sato, N. Fukata, K. Hirakuri, M. Murakami, T. Shimizu and Y. Yamauchi, *Chemistry: An Asian Journal*, 2010, **5**, 50-55.
57. J. Yang, R. Liptak, D. Rowe, J. Wu, J. Casey, D. Witker, S. A. Campbell and U. Kortshagen, *Applied Surface Science*, 2014, **323**, 54-58.
58. J. J. Wu and U. R. Kortshagen, *RSC Advances*, 2015, **5**, 103822-103828.

59. A. Marinins, R. Zandi Shafagh, W. van der Wijngaart, T. Haraldsson, J. Linnros, J. G. C. Veinot, S. Popov and I. Sychugov, *ACS Applied Materials & Interfaces*, 2017, **9**, 30267-30272.
60. D. Kajiya and K. I. Saitow, *RSC Advances*, 2018, **8**, 41299-41307.
61. K. Fujimoto, T. Hayakawa, Y. Xu, N. Jingu and K.-i. Saitow, *ACS Sustainable Chemistry & Engineering*, 2022, **10**, 14451-14463.
62. K. Q. Loh, H. P. Andaraarachchi, V. E. Ferry and U. R. Kortshagen, *ACS Applied Nano Materials*, 2023, **6**, 6444-6453.
63. X. Li, Y. He and M. T. Swihart, *Langmuir*, 2004, **20**, 4720-4727.
64. Z. Yang, C. M. Gonzalez, T. K. Purkait, M. Iqbal, A. Meldrum and J. G. Veinot, *Langmuir*, 2015, **31**, 10540-10548.
65. F. A. Reboredo and G. Galli, *The Journal of Physical Chemistry B*, 2005, **109**, 1072-1078.
66. O. Wolf, M. Dasog, Z. Yang, I. Balberg, J. G. C. Veinot and O. Millo, *Nano Letters*, 2013, **13**, 2516-2521.
67. D. L. Staebler and C. R. Wronski, *Applied Physics Letters*, 1977, **31**, 292-294.
68. H. Plagwitz, B. Terheiden and R. Brendel, *Journal of Applied Physics*, 2008, **103**, 094506.
69. R. Anthony and U. Kortshagen, *Physical Review B*, 2009, **80**.
70. A. N. Thiessen, M. Ha, R. W. Hooper, H. Yu, A. O. Oliynyk, J. G. C. Veinot and V. K. Michaelis, *Chemistry of Materials*, 2019, **31**, 678-688.
71. A. N. Thiessen, L. Zhang, A. O. Oliynyk, H. Yu, K. M. O'Connor, A. Meldrum and J. G. C. Veinot, *Chemistry of Materials*, 2020, **32**, 6838-6846.
72. R. A. Street, *Advances in Physics*, 2006, **30**, 593-676.
73. G. D. Cody, T. Tiedje, B. Abeles, B. Brooks and Y. Goldstein, *Physical Review Letters*, 1981, **47**, 1480-1483.
74. W. Bludau, A. Onton and W. Heinke, *Journal of Applied Physics*, 2003, **45**, 1846-1848.
75. I. T. Cheong, W. Morrish, W. Sheard, H. Yu, B. Tavares Luppi, L. Milburn, A. Meldrum and J. G. C. Veinot, *ACS Applied Materials & Interfaces*, 2021, **13**, 27149-27158.
76. C. M. Hessel, E. J. Henderson and J. G. Veinot, *Chemistry of Materials*, 2006, **18**, 6139-6146.
77. A. F. van Driel, I. S. Nikolaev, P. Vergeer, P. Lodahl, D. Vanmaekelbergh and W. L. Vos, *Physical Review B*, 2007, **75**, 035329.
78. J. I. Langford and A. J. C. Wilson, *Journal of Applied Crystallography*, 1978, **11**, 102-113.
79. P. Yogi, M. Tanwar, S. K. Saxena, S. Mishra, D. K. Pathak, A. Chaudhary, P. R. Sagdeo and R. Kumar, *Analytical Chemistry*, 2018, **90**, 8123-8129.
80. B. P. Falcão, J. P. Leitão, M. R. Soares, L. Ricardo, H. Águas, R. Martins and R. N. Pereira, *Physical Review Applied*, 2019, **11**, 024054.

81. D. A. Kisilitsyn, J. M. Mills, S. K. Chiu, B. N. Taber, J. D. Barnes, C. F. Gervasi, A. M. Goforth and G. V. Nazin, *Journal of Physical Chemistry Letters*, 2018, **9**, 710-716.
82. L. Canham, *Faraday Discussions*, 2020, **222**, 10-81.
83. M. L. Mastronardi, F. Maier-Flaig, D. Faulkner, E. J. Henderson, C. Kubel, U. Lemmer and G. A. Ozin, *Nano Letters*, 2012, **12**, 337-342.
84. M. Nolan, M. Legesse and G. Fagas, *Physical Chemistry Chemical Physics*, 2012, **14**, 15173-15179.
85. X. D. Pi, L. Mangolini, S. A. Campbell and U. Kortshagen, *Physical Review B*, 2007, **75**, 085423.
86. X. Liu, Y. Zhang, T. Yu, X. Qiao, R. Gresback, X. Pi and D. Yang, *Particle & Particle Systems Characterization*, 2016, **33**, 44-52.
87. T. L. Cocker, V. Jelic, M. Gupta, S. J. Molesky, J. A. J. Burgess, G. D. L. Reyes, L. V. Titova, Y. Y. Tsui, M. R. Freeman and F. A. Hegmann, *Nature Photonics*, 2013, **7**, 620-625.
88. T. M. Atkins, A. Thibert, D. S. Larsen, S. Dey, N. D. Browning and S. M. Kauzlarich, *Journal of the American Chemical Society*, 2011, **133**, 20664-20667.
89. P. Gupta, V. L. Colvin and S. M. George, *Phys Rev B Condens Matter*, 1988, **37**, 8234-8243.
90. P. Martín, J. F. Fernández and C. R. Sánchez, *physica status solidi (a)*, 2000, **182**, 255-260.
91. B. N. Jariwala, N. J. Kramer, M. C. Petcu, D. C. Bobela, M. C. M. v. d. Sanden, P. Stradins, C. V. Ciobanu and S. Agarwal, *The Journal of Physical Chemistry C*, 2011, **115**, 20375-20379.
92. R. Walsh, *Accounts of Chemical Research*, 1981, **14**, 246-252.
93. R. T. Sanderson, *Journal of the American Chemical Society*, 1983, **105**, 2259-2261.
94. T. M. Hafshejani, J. Wohlgemuth and P. Thissen, *The Journal of Physical Chemistry C*, 2021, **125**, 19811-19820.
95. Y. Shu, U. R. Kortshagen, B. G. Levine and R. J. Anthony, *The Journal of Physical Chemistry C*, 2015, **119**, 26683-26691.
96. Y. Q. Wang, R. Smirani and G. G. Ross, *Nano Letters*, 2004, **4**, 2041-2045.
97. G. Hadjisavvas, I. N. Remediakis and P. C. Kelires, *Physical Review B*, 2006, **74**, 165419.
98. H. F. Wilson and A. S. Barnard, *The Journal of Physical Chemistry C*, 2014, **118**, 2580-2586.
99. S. M. Gates, R. R. Kunz and C. M. Greenlief, *Surface Science*, 1989, **207**, 364-384.
100. M. Suemitsu, H. Nakazawa and N. Miyamoto, *Surface science*, 1996, **357**, 555-559.
101. A. M. Žak, *Nano Letters*, 2022, **22**, 9219-9226.
102. M. P. Hanrahan, E. L. Fought, T. L. Windus, L. M. Wheeler, N. C. Anderson, N. R. Neale and A. J. Rossini, *Chemistry of Materials*, 2017, **29**, 10339-10351.
103. R. N. Pereira, D. J. Rowe, R. J. Anthony and U. Kortshagen, *Physical Review B*, 2012, **86**, 085449.
104. N. Bushlanova, V. Baturin, S. Lepeshkin and Y. Uspenskii, *Nanoscale*, 2021, **13**, 19181-19189.

Chapter 5

Conclusions and Future Directions

5.1 Conclusions

Luminescent silicon quantum dots (SiQDs) are nanoparticles that are biologically compatible and based on earth-abundant Si.¹ These materials exhibit visible and near-infrared (NIR) luminescence, thus making them suitable for light-emitting devices.^{2,3} However, control of the SiQDs optical properties, especially regarding their broad luminescence bandwidths and photostability, remains an ongoing endeavor and is needed to push forward the applications of the materials. This thesis is the culmination of multidisciplinary efforts aimed at addressing these challenges in order to facilitate the realization of practical SiQD light-emitting devices.

In Chapter 2, Fabry-Pérot (FP) cavities of SiQD-polymer hybrids were developed and explored for their potential to narrow the photoluminescence (PL) linewidths of the materials. A thin film of these hybrids was sandwiched between two silver mirrors yielding micron-thick optical resonators. This straightforward configuration successfully reduced the full-width-at-half-maximum (FWHM) of the SiQDs thin film PL from over 100 nm to as narrow as ca. 9 nm. By varying the sizes of the nanoparticles, the polymer host, and thicknesses of the active layer, the cavities were able to exhibit tunable emissions centered on the blue and orange-to-red spectral region. Importantly, the first bendable SiQD-based FP resonator with a narrowed emission (FWHM ca. 9 nm) was achieved by using appropriately flexible mediums.

Chapter 3 expanded the investigation of SiQD-FP cavities into the electrically driven system. Here, colloidal SiQDs-based cavity light-emitting diodes (SiQD-cLEDs) were designed, fabricated, and tested. By using silver mirrors as reflectors and SiO₂ as the spacer, the FP cavity could be conveniently incorporated into existing SiQD-LEDs configurations. Normal SiQD-LEDs exhibited EL with emission bandwidths exceeding 100 nm. The c-LEDs fabricated and studied showed significant reduction in the FWHM to as narrow as ca. 23 nm, which is comparable to

commercial QD-LEDs. The output wavelength is defined by the optical pathlength of the cavity, thus varying the thicknesses of SiO₂ in the cLED could tune the EL maximum from orange to NIR using the same SiQDs. The selectivity arising from the cavity structure furthermore enabled the SiQD-cLED to emit stable wavelengths under different applied voltages. Successes were achieved in narrowing the SiQD emissions using the optical cavity, nevertheless optimization and stability of the devices should be pursued to push forward the practicality of the structure.

While external photonic structure provides a convenient platform to tune the emission of SiQDs, structural and surface tailoring of the materials are fundamental, and ongoing, areas of study. Chapter 4 investigates how the outer amorphous silicon (a-Si) layer could impact SiQDs' PL under prolonged UV irradiation. In the study, dodecyl-functionalized SiQDs of similar physical dimensions ($d \sim 5$ nm), with (normal SiQDs; N-SiQDs) and without (over-etched SiQDs; O-SiQDs) a “thick” amorphous shell, were prepared from thermally processed hydrogen silsesquioxane (HSQ). A combination of complementary techniques was employed to compare the structure, composition, and optical properties of these two classes of nanoparticles. Notably, the presence of a-Si did not significantly impact the PL maxima, lifetime, and photoluminescence quantum yield (PLQY) of the as-produced materials. However, after 48 h of continuous UV irradiation under an inert atmosphere, the PLQY of the N-SiQDs decreased significantly more than O-SiQDs. Structural characterizations suggested that the lesser photostability of N-SiQDs could be attributed, at least partially, to the generation of DBs in a-Si. Additional investigations are needed to fully understand the impact of the amorphous shell.

5.2 Future Directions

From engineering optical resonators to investigating the impact of the amorphous shell on the optical properties of SiQDs, this thesis carries an overarching theme of exploring diverse, but complementary, approaches to study, and ultimately, harness the full potential of SiQDs for light-emitting applications. This multidisciplinary endeavor underscores that the future of SiQD hinges on collaborative efforts across various fields (**Figure 5.1**). The prospect of SiQD-based optical cavities relies on the optimization and tailoring of solution processible SiQD in photonic structures. Meanwhile, ongoing investigations into the internal structure and surfaces of the SiQDs are fundamental in understanding impact of the structure on the properties or the materials.

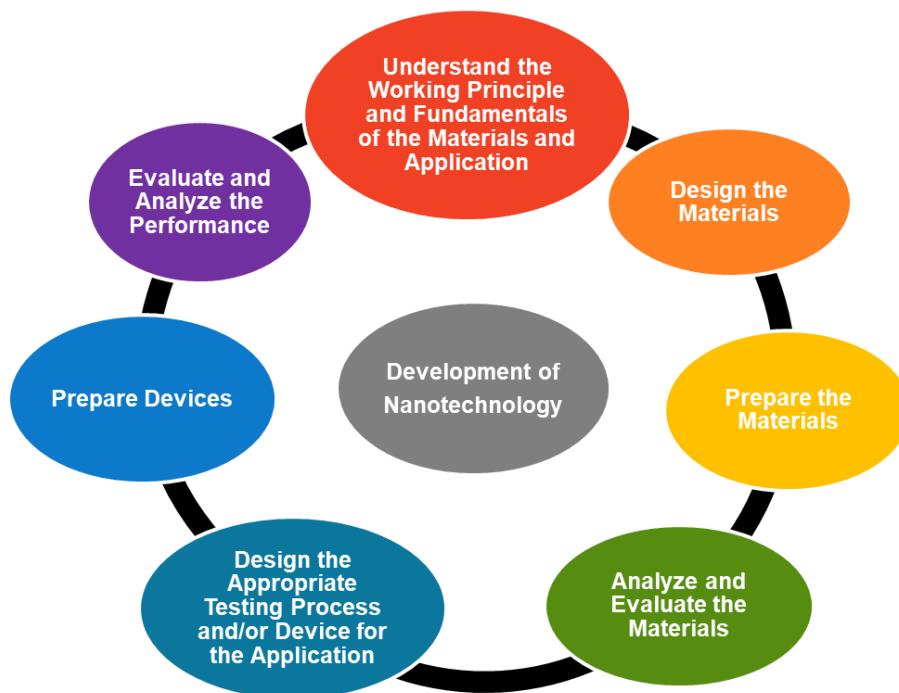


Figure 5.1. Workflow in developing nanotechnology.

5.2.1 SiQD-based Optical Cavities

The FP microresonators in Chapter 2 and 3 represent important advancements in narrowing the luminescence bandwidths of SiQDs. Ongoing characterizations (e.g., output efficiency, radiative lifetime, and stability) and optimization (i.e., fabrication process and layer structure) of the cavities are expected to improve performance metrics. Investigating edge-emission from the FP cavity could also contribute to the development of SiQD-based lasers and luminescent solar concentrators (LSCs).^{4, 5} Furthermore, the versatility of the free-standing SiQDs and their polymer hybrids expands the potential for photonic structures beyond the current FP cavity system.

5.2.1.1 Expanding the Scope of SiQD-based Photonic Structures

FP cavities were demonstrated in Chapter 2, but the use of SiQD-polymer hybrids can be extended for applications in whispering gallery modes (WGMs) and distributed feedback (DFB) cavities. In contrast to conventional systems using silicon nanoparticles (SiNPs) in solid-state silicon oxide matrices, solution-processible polymer hosts offer notable advantages. As shown in Chapter 2, these hybrids exhibited structural flexibility, adaptability to diverse matrices and QDs, assurance of uniform nanoparticle distribution in the active layer, and versatility regarding various processing methods. As an example, the existing SiQD-polystyrene hybrid can be used to prepare microspheres for WGMs or patterned for diffraction grating.^{6, 7}

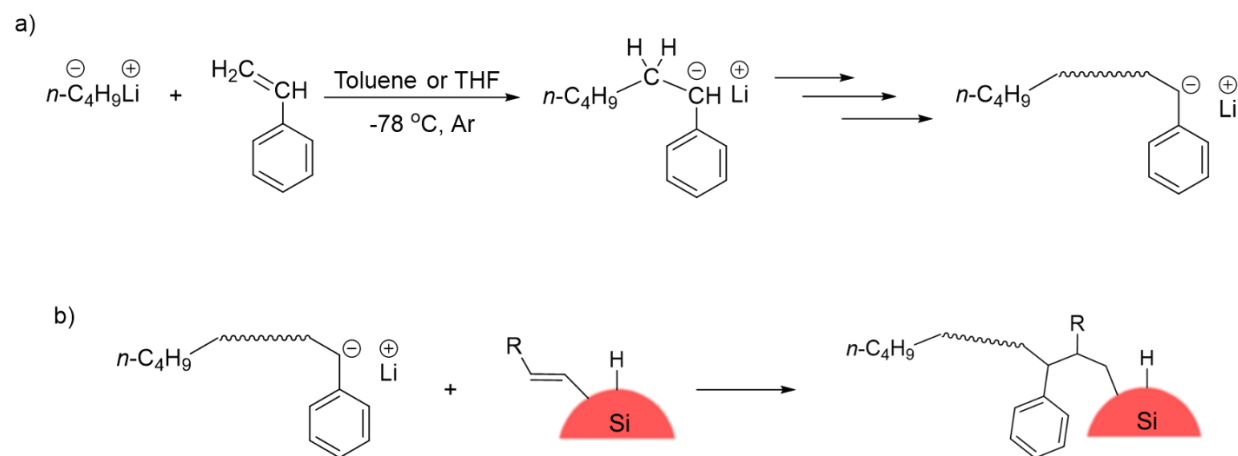
5.2.1.2 Tailoring the SiQDs for Future Cavity Development

The vast surface chemistry of the SiQDs provides an important avenue for tailoring towards cavity applications. Anchoring antennas onto the SiQDs can enhance the efficiency of the devices.⁸ Additionally, expanding the spectral range of cavities can be achieved by passivating QDs with oxynitrides, conjugated ligands, and suboxides.^{9, 10} Given that the merits of polymer-based resonators rely on the quality of the hybrids, growing well-defined polymers onto SiQDs becomes

of paramount importance.¹¹ Living anionic polymerization is particularly attractive as it offers predictable molecular weights, narrow molecular weight distributions, and architectural polymers.

¹² **Scheme 5.1** outlines a potential synthetic route in anchoring ‘living’ polystyrene onto the SiQDs. First, an organolithium reagent will initiate and propagate the polymerization of styrene.¹³ Addition of vinyl-SiQDs will quench and terminate the resulting living polystyrene anions. Integrating this polymerization method with surface-tailored SiQDs holds the potential for achieving well-defined SiQD-polymer hybrids for far-reaching applications.

Scheme 5.1. Schematic representation of growing well-defined polystyrene onto SiQDs. (a) A living polymer anion is first prepared from *n*-butyllithium and styrene, of which will then be (b) quenched and terminated by vinyl-SiQDs.



5.2.2 Expanding Insights into the Graded Structure

The study outlined in Chapter 4 delved into the optical properties of SiQDs, both with (N-SiQDs) and without (O-SiQDs) a thick a-Si shell. The experiment relied on HF-etching to tune the a-Si layer and the two classes of materials were comprehensively characterized using a combination of techniques. It is important to note that the current study cannot fully account for inherent oxidation within the partially functionalized SiQDs and discrepancies in shell thickness or a-Si coverage. These factors contribute to variations in the emission performances. To probe the correlation more

comprehensively between the SiQDs structure and its properties, additional strategies must be developed.

5.2.2.1 Characterization and Photophysics of the Graded Structure

Future experiments comparing H-SiQDs, in order to better elucidate the relationship between the optical changes and the initial internal structure, will circumvent the partial oxidation introduced during surface functionalization. Monitoring the materials *in-situ* upon irradiation under different conditions (i.e., Ar, dry O₂, wet Ar, and wet O₂) would be informative. In addition to the characterization techniques used in Chapter 4, solid-state nuclear magnetic resonance spectroscopy can further probe the surface and graded structure of the SiQDs.^{14, 15} Complementary scanning tunneling spectroscopy (STS) is useful in directly visualizing the local structural changes of the QDs upon applied voltages and would also allow a comparison for the electronic structure of the O- and N-SiQDs.¹⁶ The structural impact on the charge carrier dynamics can be investigated using optical pump-probe spectroscopy.¹⁷⁻¹⁹ A low-temperature single-dot spectroscopic study comparing N- and O-SiQDs would enable determination of the impact of amorphous shell on the luminescent bandwidth.²⁰

5.2.2.2 Tuning the Amorphous Shell in SiQDs

The photostability project raised an important question concerning the impact of amorphous shell characteristics (i.e., thickness, hydrogen content, and surface-core interface) on the optical properties of the SiQDs. To progress in this direction, it is crucial to develop reliable protocols for controlling the a-Si layer. The growth of the nanoparticles within the oxide matrix is inherently assigned to Si atoms diffusing throughout the host material. The resulting graded structure can be attributed to the lattice mismatch between the SiO₂ matrix and the crystalline SiQD core.^{21, 22} Given this, adjusting the cross-linked density in the silicon oxide precursors^{23, 24} as well as the thermal treatment conditions (i.e., the reaction gas, dwell time, multi-step annealing, and ramping

process)²⁵⁻²⁸ may shed light on the formation of the graded structure. This fundamental study could be expanded upon for future research related to the development of the core-shell structure.

5.2.3 Expanding Insights into HF Etching

All of the SiQDs studied in this thesis rely on etching thermally processed HSQ using diluted HF. This procedure simultaneously releases SiQDs from the oxide matrix, removes surface silicon atoms, and introduces reactive silicon-hydride surface species. However, the impact of the etching conditions on the surfaces and structure of the nanoparticles has not been explicitly studied.

Examination of the FT-IR spectra (**Figure 5.2a-b**) taken of aliquots of H-SiQDs at different etching times reveals changes in the surface species. H-SiQDs obtained after 35 – 60 min of etching exhibit distinctive $\equiv\text{SiH}$, $=\text{SiH}_2$, and $-\text{SiH}_3$ stretches regardless of the processing temperature of the HSQ precursor (i.e., 1100 °C and 1200 °C). As the etching time extends, the intensities of $\equiv\text{SiH}$ and $-\text{SiH}_3$ peaks decrease and the three distinctive peaks merge toward the $=\text{SiH}_2$ peak. This observation aligns with the relatively constant signal observed at 900 cm^{-1} , which can be attributed to $=\text{SiH}_2$ scissoring mode.²⁹ While H-SiQDs prepared by gas and solution phase syntheses exhibit two signals in the SiH_x bending IR region,^{30,31} the single peak here points to potential morphological differences to SiQDs prepared from the solid-state precursor.

Further work evaluating the data and employing other characterization methods will help to understand the morphological and structural changes. The origin of these different surface hydride species and their subsequent impact on the SiQD reactivity is fundamental to understanding both stability and functionalization. This can further be extended to other Si nanostructures using, for example, anisotropic etching for the study of shape-dependent optical properties.³²⁻³⁴

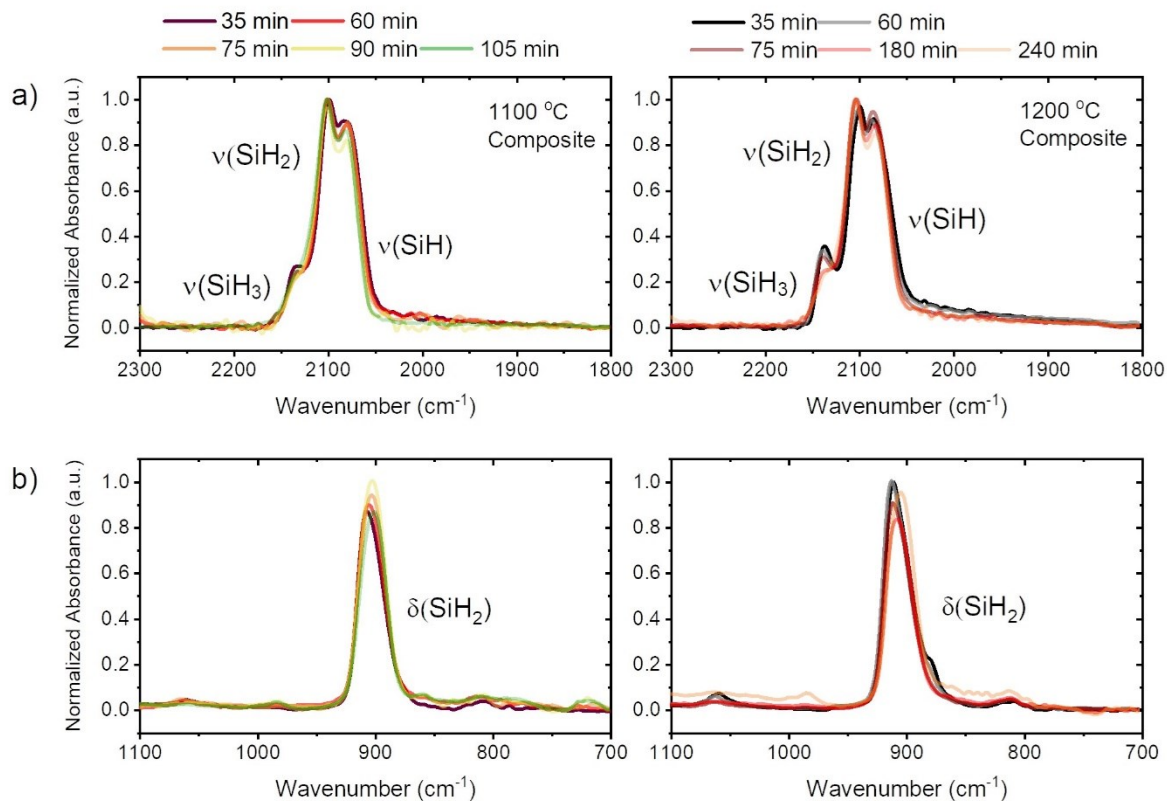


Figure 5.2. FT-IR spectra of H-SiQDs obtained from different HF etching time. The evolution of Si-H_x stretches is presented in (a) and Si-H_x bends are highlighted in (b). Left are H-SiQDs obtained from HSQ processed at 1100 °C for 1 h under 5% H₂. Right are H-SiQDs obtained from HSQ processed at 1200 °C for 1 h under 5% H₂.

5.3 References

1. S. Pramanik, S. K. E. Hill, B. Zhi, N. V. Hudson-Smith, J. J. Wu, J. N. White, E. A. McIntire, V. S. S. K. Kondeti, A. L. Lee, P. J. Bruggeman, U. R. Kortshagen and C. L. Haynes, *Environmental Science: Nano*, 2018, **5**, 1890-1901.
2. F. Maier-Flaig, J. Rinck, M. Stephan, T. Bockrocker, M. Bruns, C. Kubel, A. K. Powell, G. A. Ozin and U. Lemmer, *Nano Letters*, 2013, **13**, 475-480.
3. F. Meinardi, S. Ehrenberg, L. Dharmo, F. Carulli, M. Mauri, F. Bruni, R. Simonutti, U. Kortshagen and S. Brovelli, *Nature Photonics*, 2017, **11**, 177-185.
4. Z.-Y. Yu, Z.-H. Guo, Y.-C. Zhang, X. Zhang, Y. Wang, F.-Y. Ma, Y. Liu, X.-Y. Xue, Q.-Y. Jin, J. Li, J. Sun, S.-Y. Wang, D.-C. Wang and M. Lu, *Results in Physics*, 2022, **34**, 105336.

5. H.-J. Song, B. G. Jeong, J. Lim, D. C. Lee, W. K. Bae and V. I. Klimov, *Nano Letters*, 2018, **18**, 395-404.
6. K. Gardner, M. Aghajamali, S. Vagin, J. Pille, W. Morrish, J. G. C. Veinot, B. Rieger and A. Meldrum, *Advanced Functional Materials*, 2018, **28**, 1802759.
7. C. Park, J. Na, M. Han and E. Kim, *ACS Nano*, 2017, **11**, 6977-6984.
8. F. Romano, Y. Yu, B. A. Korgel, G. Bergamini and P. Ceroni, in *Photoactive Semiconductor Nanocrystal Quantum Dots: Fundamentals and Applications*, ed. A. Credi, Springer International Publishing, 2017.
9. M. Dasog, G. B. De los Reyes, L. V. Titova, F. A. Hegmann and J. G. C. Veinot, *ACS Nano*, 2014, **8**, 9636-9648.
10. A. Angi, R. Sinelnikov, A. Meldrum, J. G. Veinot, I. Balberg, D. Azulay, O. Millo and B. Rieger, *Nanoscale*, 2016, **8**, 7849-7853.
11. M. Dasog, J. Kehrle, B. Rieger and J. G. Veinot, *Angewandte Chemie International Edition*, 2016, **55**, 2322-2339.
12. T. Ishizone and R. Goseki, in *Encyclopedia of Polymeric Nanomaterials*, eds. S. Kobayashi and K. Müllen, Springer Berlin Heidelberg, Berlin, Heidelberg, 2015.
13. K. Ratkanthwar, J. Zhao, H. Zhang, N. Hadjichristidis and J. Mays, in *Anionic Polymerization: Principles, Practice, Strength, Consequences and Applications*, eds. N. Hadjichristidis and A. Hirao, Springer Japan, Tokyo, 2015.
14. M. P. Hanrahan, E. L. Fought, T. L. Windus, L. M. Wheeler, N. C. Anderson, N. R. Neale and A. J. Rossini, *Chemistry of Materials*, 2017, **29**, 10339-10351.
15. A. N. Thiessen, M. Ha, R. W. Hooper, H. Yu, A. O. Oliynyk, J. G. C. Veinot and V. K. Michaelis, *Chemistry of Materials*, 2019, **31**, 678-688.
16. D. A. Kislitsyn, J. M. Mills, S. K. Chiu, B. N. Taber, J. D. Barnes, C. F. Gervasi, A. M. Goforth and G. V. Nazin, *Journal of Physical Chemistry Letters*, 2018, **9**, 710-716.
17. V. I. Klimov, C. J. Schwarz, D. W. McBranch and C. W. White, *Applied Physics Letters*, 1998, **73**, 2603-2605.
18. J. Z. Zhang, *The Journal of Physical Chemistry B*, 2000, **104**, 7239-7253.
19. M. R. Bergren, P. K. B. Palomaki, N. R. Neale, T. E. Furtak and M. C. Beard, *ACS Nano*, 2016, **10**, 2316-2323.
20. I. Sychugov, A. Fucikova, F. Pevero, Z. Yang, J. G. C. Veinot and J. Linnros, *ACS Photonics*, 2014, **1**, 998-1005.
21. B. G. Lee, D. Hiller, J.-W. Luo, O. E. Semonin, M. C. Beard, M. Zacharias and P. Stradins, *Advanced Functional Materials*, 2012, **22**, 3223-3232.

22. Y. Su, C. Wang, Z. Hong and W. Sun, *Frontiers in Chemistry*, 2021, **9**, 721454.
23. E. J. Henderson, J. A. Kelly and J. G. C. Veinot, *Chemistry of Materials*, 2009, **21**, 5426-5434.
24. S. Terada, Y. Xin and K.-i. Saitow, *Chemistry of Materials*, 2020, **32**, 8382-8392.
25. C. M. Hessel, E. J. Henderson and J. G. C. Veinot, *The Journal of Physical Chemistry C*, 2007, **111**, 6956-6961.
26. B. Garrido Fernandez, M. López, C. García, A. Pérez-Rodríguez, J. R. Morante, C. Bonafos, M. Carrada and A. Claverie, *Journal of Applied Physics*, 2002, **91**, 798-807.
27. T. Lopez and L. Mangolini, *Nanoscale*, 2014, **6**, 1286-1294.
28. S. Niesar, R. N. Pereira, A. R. Stegner, N. Erhard, M. Hoeb, A. Baumer, H. Wiggers, M. S. Brandt and M. Stutzmann, *Advanced Functional Materials*, 2012, **22**, 1190-1198.
29. M. K. Weldon, K. T. Queeney, A. B. Gurevich, B. B. Stefanov, Y. J. Chabal and K. Raghavachari, *The Journal of Chemical Physics*, 2000, **113**, 2440-2446.
30. D. Neiner and S. M. Kauzlarich, *Chemistry of Materials*, 2010, **22**, 487-493.
31. J. Holm and J. T. Roberts, *Journal of the American Chemical Society*, 2007, **129**, 2496-2503.
32. T. Hawa and M. R. Zachariah, *The Journal of Physical Chemistry C*, 2008, **112**, 14796-14800.
33. A. S. Barnard and H. F. Wilson, *The Journal of Physical Chemistry C*, 2015, **119**, 7969-7977.
34. H. F. Wilson, L. McKenzie-Sell and A. S. Barnard, *Journal of Materials Chemistry C*, 2014, **2**, 9451-9456.

Bibliography

Chapter 1

1. M. Klein, *Archive for History of Exact Sciences*, 1961, **1**, 459-479.
2. Nobel Foundation, Nobel Prize Outreach AB 2023, <https://www.nobelprize.org/prizes/chemistry/2023/press-release/>, (accessed November 20th, 2023).
3. S. Bayda, M. Adeel, T. Tuccinardi, M. Cordani and F. Rizzolio, *Molecules*, 2019, **25**, 112.
4. N. N. Institute, About Nanotechnology, <https://www.nano.gov/about-nanotechnology>, (accessed June 23rd, 2023).
5. K. J. Klabunde and R. Richards, *Nanoscale Materials in Chemistry*. Wiley, 2nd edn., 2009.
6. F. P. Garcia de Arquer, D. V. Talapin, V. I. Klimov, Y. Arakawa, M. Bayer and E. H. Sargent, *Science*, 2021, **373**, eaaz8541.
7. M. L. Steigerwald and L. E. Brus, *Accounts of Chemical Research*, 1990, **23**, 183-188.
8. R. Hoffmann, *Angewandte Chemie International Edition in English*, 1987, **26**, 846-878.
9. B. D. Fahlman, *Materials Chemistry*, Springer International Publishing, 3 edn., 2018.
10. A. P. Alivisatos, *Science*, 1996, **271**, 933-937.
11. A. D. Yoffe, *Advances in Physics*, 2002, **51**, 799-890.
12. T. Trindade, *Nanoscale Materials*, Springer US, 2004.
13. A. I. Ekimov and A. A. Onushchenko, *Journal of Experimental and Theoretical Physics Letters*, 1981, **34**, 345-349
14. R. Rossetti, S. Nakahara and L. E. Brus, *The Journal of Chemical Physics*, 1983, **79**, 1086-1088.
15. A. L. Efros and A. V. Rodina, *Physical Review B*, 1993, **47**, 10005.
16. Y. Wang and N. Herron, *The Journal of Physical Chemistry*, 1991, **95**, 525-532.
17. A. R. Kortan, R. Hull, R. L. Opila, M. G. Bawendi, M. L. Steigerwald, P. J. Carroll and L. E. Brus, *Journal of the American Chemical Society*, 1990, **112**, 1327-1332.
18. D. Vasudevan, R. R. Gaddam, A. Trinchin and I. Cole, *Journal of Alloys and Compounds*, 2015, **636**, 395-404.
19. J. Lim, B. G. Jeong, M. Park, J. K. Kim, J. M. Pietryga, Y.-S. Park, V. I. Klimov, C. Lee, D. C. Lee and W. K. Bae, *Advanced Materials*, 2014, **26**, 8034-8040.
20. Y.-S. Park, W. K. Bae, L. A. Padilha, J. M. Pietryga and V. I. Klimov, *Nano Letters*, 2014, **14**, 396-402.
21. P. Maity, T. Debnath and H. N. Ghosh, *The Journal of Physical Chemistry C*, 2015, **119**, 26202-26211.
22. S. Kim, B. Fisher, H.-J. Eisler and M. Bawendi, *Journal of the American Chemical Society*, 2003, **125**, 11466-11467.
23. J. Bang, J. Park, J. H. Lee, N. Won, J. Nam, J. Lim, B. Y. Chang, H. J. Lee, B. Chon, J. Shin, J. B. Park, J. H. Choi, K. Cho, S. M. Park, T. Joo and S. Kim, *Chemistry of Materials*, 2010, **22**, 233-240.
24. M. S. Giroux, Z. Zahra, O. A. Salawu, R. M. Burgess, K. T. Ho and A. S. Adeleye, *Environmental Science: Nano*, 2022, **9**, 867-910.
25. W. W. Yu, L. Qu, W. Guo and X. Peng, *Chemistry of Materials*, 2003, **15**, 2854-2860.
26. S. E. Keuleyan, P. Guyot-Sionnest, C. Delerue and G. Allan, *ACS Nano*, 2014, **8**, 8676-8682.

27. D. Gammon, E. S. Snow, B. V. Shanabrook, D. S. Katzer and D. Park, *Science*, 1996, **273**, 87-90.
28. P. Ramasamy, N. Kim, Y.-S. Kang, O. Ramirez and J.-S. Lee, *Chemistry of Materials*, 2017, **29**, 6893-6899.
29. P. R. Brown, D. Kim, R. R. Lunt, N. Zhao, M. G. Bawendi, J. C. Grossman and V. Bulović, *ACS Nano*, 2014, **8**, 5863-5872.
30. L. Protesescu, S. Yakunin, M. I. Bodnarchuk, F. Krieg, R. Caputo, C. H. Hendon, R. X. Yang, A. Walsh and M. V. Kovalenko, *Nano Letters*, 2015, **15**, 3692-3696.
31. C.-H. Chen, S.-N. Cheng, L. Cheng, Z.-K. Wang and L.-S. Liao, *Advanced Energy Materials*, 2023, **13**, 2204144.
32. S. Ivanov, S. Zhuravsky, G. Yukina, V. Tomson, D. Korolev and M. Galagudza, *Materials*, 2012, **5**, 1873-1889.
33. J. Liu, F. Erogbogbo, K.-T. Yong, L. Ye, J. Liu, R. Hu, H. Chen, Y. Hu, Y. Yang, J. Yang, I. Roy, N. A. Karker, M. T. Swihart and P. N. Prasad, *ACS Nano*, 2013, **7**, 7303-7310.
34. M. Fleischer, *Journal of Chemical Education*, 1954, **31**, 446.
35. L. Venema, *Nature*, 2011, **479**, 309-309.
36. M. Jaroniec, *Nature Chemistry*, 2009, **1**, 166-166.
37. W. Bludau, A. Onton and W. Heinke, *Journal of Applied Physics*, 2003, **45**, 1846-1848.
38. L. Brus, *The Journal of Physical Chemistry*, 1994, **98**, 3575-3581.
39. D. J. L. Pavesi and Lorenzo, *Silicon Photonics*, Springer Berlin Heidelberg, 2004.
40. L. Canham, *Faraday Discuss*, 2020, **222**, 10-81.
41. R. A. Street, *Hydrogenated Amorphous Silicon*, Cambridge University Press, 1991.
42. V. L. Deringer, N. Bernstein, A. P. Bartók, M. J. Cliffe, R. N. Kerber, L. E. Marbella, C. P. Grey, S. R. Elliott and G. Csányi, *The Journal of Physical Chemistry Letters*, 2018, **9**, 2879-2885.
43. M. M. J. Treacy and K. B. Borisenko, *Science*, 2012, **335**, 950-953.
44. H. Dersch, J. Stuke and J. Beichler, *Applied Physics Letters*, 1981, **38**, 456-458.
45. P. Rava, F. Demichelis, G. Kaniadakis, P. Mpawenayo, A. Tagliaferro and E. Tresso, *Journal of Vacuum Science & Technology A*, 1987, **5**, 1795-1797.
46. W. Futako, T. Kamiya, C. M. Fortmann and I. Shimizu, *Journal of Non-Crystalline Solids*, 2000, **266-269**, 630-634.
47. K. Masuko, M. Shigematsu, T. Hashiguchi, D. Fujishima, M. Kai, N. Yoshimura, T. Yamaguchi, Y. Ichihashi, T. Mishima, N. Matsubara, T. Yamanishi, T. Takahama, M. Taguchi, E. Maruyama and S. Okamoto, *IEEE Journal of Photovoltaics*, 2014, **4**, 1433-1435.
48. R. A. Street, *Advances in Physics*, 2006, **30**, 593-676.
49. L. T. Canham, *Applied Physics Letters*, 1990, **57**, 1046-1048.
50. H. Takagi, H. Ogawa, Y. Yamazaki, A. Ishizaki and T. Nakagiri, *Applied Physics Letters*, 1990, **56**, 2379-2380.
51. L.-W. Wang and A. Zunger, *Physical Review Letters*, 1994, **73**, 1039-1042.
52. M. S. Hybertsen, *Physical Review Letters*, 1994, **72**, 1514-1517.
53. D. Kovalev, H. Heckler, M. Ben-Chorin, G. Polisski, M. Schwartzkopff and F. Koch, *Physical Review Letters*, 1998, **81**, 2803-2806.
54. B. G. Lee, J.-W. Luo, N. R. Neale, M. C. Beard, D. Hiller, M. Zacharias, P. Stradins and A. Zunger, *Nano Letters*, 2016, **16**, 1583-1589.

55. G. W. 't Hooft, Y. A. R. R. Kessener, G. L. J. A. Rikken and A. H. J. Venhuizen, *Applied Physics Letters*, 1992, **61**, 2344-2346.
56. S. Milliken, A. N. Thiessen, I. T. Cheong, K. M. O'Connor, Z. Li, R. W. Hooper, C. J. T. Robidillo and J. G. C. Veinot, *Nanoscale*, 2021, **13**, 16379-16404.
57. E. Werwa, A. A. Seraphin, L. A. Chiu, C. Zhou and K. D. Kolenbrander, *Applied Physics Letters*, 1994, **64**, 1821-1823.
58. V. Švrček, T. Sasaki, Y. Shimizu and N. Koshizaki, *Applied Physics Letters*, 2006, **89**, 213113.
59. J. Hwang, Y. Jeong, K. H. Lee, Y. Seo, J. Kim, J. W. Hong, E. Kamaloo, T. A. Camesano and J. Choi, *Industrial & Engineering Chemistry Research*, 2015, **54**, 5982-5989.
60. A. S. Heintz, M. J. Fink and B. S. Mitchell, *Advanced Materials*, 2007, **19**, 3984-3988.
61. B. Liao, W. Wang, X. Deng, B. He, W. Zeng, Z. Tang and Q. Liu, *RSC Advances*, 2016, **6**, 14465-14467.
62. S. Guruvenket, J. M. Hoey, K. J. Anderson, M. T. Frohlich, R. Krishnan, J. Sivaguru, M. P. Sibi and P. Boudjouk, *Journal of Materials Chemistry C*, 2016, **4**, 8206-8213.
63. L. E. Brus, P. F. Szajowski, W. L. Wilson, T. D. Harris, S. Schuppler and P. H. Citrin, *Journal of the American Chemical Society*, 1995, **117**, 2915-2922.
64. X. Li, Y. He, S. S. Talukdar and M. T. Swihart, *Langmuir*, 2003, **19**, 8490-8496.
65. J. D. Holmes, K. J. Ziegler, R. C. Doty, L. E. Pell, K. P. Johnston and B. A. Korgel, *Journal of the American Chemical Society*, 2001, **123**, 3743-3748.
66. L. Mangolini, E. Thimsen and U. Kortshagen, *Nano Letters*, 2005, **5**, 655-659.
67. A. Gupta, M. T. Swihart and H. Wiggers, *Advanced Functional Materials*, 2009, **19**, 696-703.
68. T. A. Pringle, K. I. Hunter, A. Brumberg, K. J. Anderson, J. A. Fagan, S. A. Thomas, R. J. Petersen, M. Sefannaser, Y. Han, S. L. Brown, D. S. Kilin, R. D. Schaller, U. R. Kortshagen, P. R. Boudjouk and E. K. Hobbie, *ACS Nano*, 2020, **14**, 3858-3867.
69. J. R. Heath, *Science*, 1992, **258**, 1131-1133.
70. R. D. Tilley, J. H. Warner, K. Yamamoto, I. Matsui and H. Fujimori, *Chemical Communications*, 2005, 1833-1835.
71. R. A. Bley and S. M. Kauzlarich, *Journal of the American Chemical Society*, 1996, **118**, 12461-12462.
72. J. Wang, S. Sun, F. Peng, L. Cao and L. Sun, *Chemical Communications*, 2011, **47**, 4941-4943.
73. C.-S. Yang, R. A. Bley, S. M. Kauzlarich, H. W. H. Lee and G. R. Delgado, *Journal of the American Chemical Society*, 1999, **121**, 5191-5195.
74. W. Sun, C. Qian, X. Cui, L. Wang, M. Wei, G. Casillas, A. S. Helmy and G. A. Ozin, *Nanoscale*, 2016, **8**, 3678-3684.
75. S. Terada, Y. Xin and K.-i. Saitow, *Chemistry of Materials*, 2020, **32**, 8382-8392.
76. N. Shirahata, J. Nakamura, J. I. Inoue, B. Ghosh, K. Nemoto, Y. Nemoto, M. Takeguchi, Y. Masuda, M. Tanaka and G. A. Ozin, *Nano Letter*, 2020, **20**, 1491-1498.
77. M. L. Mastronardi, E. J. Henderson, D. P. Puzzo and G. A. Ozin, *Adv Mater*, 2012, **24**, 5890-5898.
78. R. J. Clark, M. Aghajamali, C. M. Gonzalez, L. Hadidi, M. A. Islam, M. Javadi, M. H. Mobarok, T. K. Purkait, C. J. T. Robidillo, R. Sinelnikov, A. N. Thiessen, J. Washington, H. Yu and J. G. C. Veinot, *Chemistry of Materials*, 2016, **29**, 80-89.

79. C. M. Hessel, D. Reid, M. G. Panthani, M. R. Rasch, B. W. Goodfellow, J. Wei, H. Fujii, V. Akhavan and B. A. Korgel, *Chemistry of Materials*, 2011, **24**, 393-401.
80. E. J. Henderson, J. A. Kelly and J. G. C. Veinot, *Chemistry of Materials*, 2009, **21**, 5426-5434.
81. G. W. Trucks, K. Raghavachari, G. S. Higashi and Y. J. Chabal, *Physical Review Letters*, 1990, **65**, 504-507.
82. C. M. Hessel, E. J. Henderson and J. G. Veinot, *Chemistry of Materials*, 2006, **18**, 6139-6146.
83. A. N. Thiessen, M. Ha, R. W. Hooper, H. Yu, A. O. Oliynyk, J. G. C. Veinot and V. K. Michaelis, *Chemistry of Materials*, 2019, **31**, 678-688.
84. A. N. Thiessen, L. Zhang, A. O. Oliynyk, H. Yu, K. M. O'Connor, A. Meldrum and J. G. C. Veinot, *Chemistry of Materials*, 2020, **32**, 6838-6846.
85. S. Milliken, I. T. Cheong, K. Cui and J. G. C. Veinot, *ACS Applied Nano Materials*, 2022, **5**, 15785-15796.
86. D. A. Kislitsyn, J. M. Mills, S. K. Chiu, B. N. Taber, J. D. Barnes, C. F. Gervasi, A. M. Goforth and G. V. Nazin, *Journal of Physical Chemistry Letters*, 2018, **9**, 710-716.
87. M. Dasog, G. B. De los Reyes, L. V. Titova, F. A. Hegmann and J. G. C. Veinot, *ACS Nano*, 2014, **8**, 9636-9648.
88. M. Dasog, J. Kehrle, B. Rieger and J. G. Veinot, *Angewandte Chemie International Edition in English*, 2016, **55**, 2322-2339.
89. M. Dasog, K. Bader and J. G. C. Veinot, *Chemistry of Materials*, 2015, **27**, 1153-1156.
90. J. M. Buriak, *Chemical Reviews*, 2002, **102**, 1271-1308.
91. J. Holm and J. T. Roberts, *Langmuir*, 2009, **25**, 7050-7056.
92. Z. Yang, M. Iqbal, A. R. Dobbie and J. G. Veinot, *Journal of the American Chemical Society*, 2013, **135**, 17595-17601.
93. W. Sun, C. Qian, M. L. Mastronardi, M. Wei and G. A. Ozin, *Chemical Communications*, 2013, **49**, 11361-11363.
94. I. M. D. Höhle, J. Kehrle, T. Helbich, Z. Yang, J. G. C. Veinot and B. Rieger, *Chemistry - A European Journal*, 2014, **20**, 4212-4216.
95. Z. Yang, C. M. Gonzalez, T. K. Purkait, M. Iqbal, A. Meldrum and J. G. Veinot, *Langmuir*, 2015, **31**, 10540-10548.
96. J. Kehrle, S. Kaiser, T. K. Purkait, M. Winnacker, T. Helbich, S. Vagin, J. G. C. Veinot and B. Rieger, *Nanoscale*, 2017, **9**, 8489-8495.
97. J. A. Kelly and J. G. C. Veinot, *ACS Nano*, 2010, **4**, 4645-4656.
98. J. A. Kelly, A. M. Shukaliak, M. D. Fleischauer and J. G. Veinot, *Journal of the American Chemical Society*, 2011, **133**, 9564-9571.
99. T. K. Purkait, M. Iqbal, M. H. Wahl, K. Gottschling, C. M. Gonzalez, M. A. Islam and J. G. Veinot, *Journal of the American Chemical Society*, 2014, **136**, 17914-17917.
100. Y. Yu and B. A. Korgel, *Langmuir*, 2015, **31**, 6532-6537.
101. M. A. Islam, M. H. Mobarok, R. Sinelnikov, T. K. Purkait and J. G. C. Veinot, *Langmuir*, 2017, **33**, 8766-8773.
102. M. H. Mobarok, T. K. Purkait, M. A. Islam, M. Miskolzie and J. G. C. Veinot, *Angew Chem Int Ed Engl*, 2017, **56**, 6073-6077.
103. Z. Yang, M. Iqbal, A. R. Dobbie and J. G. C. Veinot, *Journal of the American Chemical Society*, 2013, **135**, 17595-17601.

104. Z. Yang, M. Dasog, A. R. Dobbie, R. Lockwood, Y. Zhi, A. Meldrum and J. G. C. Veinot, *Advanced Functional Materials*, 2014, **24**, 1345-1353.
105. A. Marinins, R. Zandi Shafagh, W. van der Wijngaart, T. Haraldsson, J. Linnros, J. G. C. Veinot, S. Popov and I. Sychugov, *ACS Applied Materials and Interfaces*, 2017, **9**, 30267-30272.
106. A. Angi, M. Loch, R. Sinelnikov, J. G. C. Veinot, M. Becherer, P. Lugli and B. Rieger, *Nanoscale*, 2018, **10**, 10337-10342.
107. Y. Xu, S. Terada, Y. Xin, H. Ueda and K.-I. Saitow, *ACS Applied Nano Materials*, 2022, **5**, 7787-7797.
108. T. Ono, Y. Xu, T. Sakata and K. I. Saitow, *ACS Applied Materials and Interfaces*, 2022, **14**, 1373-1388.
109. I. M. Hohlein, A. Angi, R. Sinelnikov, J. G. Veinot and B. Rieger, *Chemistry*, 2015, **21**, 2755-2758.
110. J. H. Song and M. J. Sailor, *Journal of the American Chemical Society*, 1998, **120**, 2376-2381.
111. A. Angi, R. Sinelnikov, A. Meldrum, J. G. Veinot, I. Balberg, D. Azulay, O. Millo and B. Rieger, *Nanoscale*, 2016, **8**, 7849-7853.
112. J. Mock, E. Groß, M. J. Kloberg, B. Rieger and M. Becherer, *Advanced Photonics Research*, 2021, **2**, 2100083.
113. R. Sinelnikov, M. Dasog, J. Beamish, A. Meldrum and J. G. C. Veinot, *ACS Photonics*, 2017, **4**, 1920-1929.
114. F. A. Reboredo and G. Galli, *The Journal of Physical Chemistry B*, 2005, **109**, 1072-1078.
115. K. Kůsová, P. Hapala, J. Valenta, P. Jelínek, O. Cibulka, L. Ondič and I. Pelant, *Advanced Materials Interfaces*, 2014, **1**, 1300042.
116. Z. Kang, Y. Liu, C. H. A. Tsang, D. D. D. Ma, X. Fan, N.-B. Wong and S.-T. Lee, *Advanced Materials*, 2009, **21**, 661-664.
117. J. Martin, F. Cichos, F. Huisken and C. von Borczyskowski, *Nano Letters*, 2008, **8**, 656-660.
118. F. Koch, V. Petrova-Koch and T. Muschik, *Journal of Luminescence*, 1993, **57**, 271-281.
119. K. Dohnalová, A. N. Poddubny, A. A. Prokofiev, W. D. A. M. de Boer, C. P. Umesh, J. M. J. Paulusse, H. Zuilhof and T. Gregorkiewicz, *Light: Science & Applications*, 2013, **2**, e47-e47.
120. R. Mazzaro, F. Romano and P. Ceroni, *Physical Chemistry Chemical Physics*, 2017, **19**, 26507-26526.
121. C. C. Huang, Y. Tang, M. van der Laan, J. van de Groep, A. F. Koenderink and K. Dohnalova, *ACS Applied Nano Materials*, 2021, **4**, 288-296.
122. R. Zhu, Z. Luo, H. Chen, Y. Dong and S.-T. Wu, *Optics Express*, 2015, **23**, 23680-23693.
123. I. Sychugov, A. Fucikova, F. Pevero, Z. Yang, J. G. C. Veinot and J. Linnros, *ACS Photonics*, 2014, **1**, 998-1005.
124. I. Sychugov, R. Juhasz, A. Galeckas, J. Valenta and J. Linnros, *Optical Materials*, 2005, **27**, 973-976.
125. I. Sychugov, J. Valenta, K. Mitsuishi, M. Fujii and J. Linnros, *Physical Review B*, 2011, **84**.
126. W. L. Wilson, P. Szajowski and L. Brus, *Science*, 1993, **262**, 1242-1244.
127. J. B. Miller, A. R. Van Sickle, R. J. Anthony, D. M. Kroll, U. R. Kortshagen and E. K. Hobbie, *ACS Nano*, 2012, **6**, 7389-7396.
128. L. Canham, *Faraday Discussions*, 2020, **222**, 10-81.

129. C. Delerue, G. Allan and M. Lannoo, *Physical Review B*, 2001, **64**.
130. M. L. Mastronardi, F. Maier-Flaig, D. Faulkner, E. J. Henderson, C. Kubel, U. Lemmer and G. A. Ozin, *Nano Letters*, 2012, **12**, 337-342.
131. Y. Yu, G. Fan, A. Fermi, R. Mazzaro, V. Morandi, P. Ceroni, D.-M. Smilgies and B. A. Korgel, *The Journal of Physical Chemistry C*, 2017, **121**, 23240-23248.
132. W. Sun, C. Qian, L. Wang, M. Wei, M. L. Mastronardi, G. Casillas, J. Breu and G. A. Ozin, *Advanced Materials*, 2015, **27**, 746-749.
133. M. Molinari, H. Rinnert and M. Vergnat, *Europhysics Letters*, 2004, **66**, 674.
134. A. Irrera, F. Iacona, I. Crupi, C. D. Presti, G. Franzò, C. Bongiorno, D. Sanfilippo, G. Di Stefano, A. Piana and P. G. Fallica, *Nanotechnology*, 2006, **17**, 1428.
135. B. Ghosh, T. Hamaoka, Y. Nemoto, M. Takeguchi and N. Shirahata, *The Journal of Physical Chemistry C*, 2018, **122**, 6422-6430.
136. R. Anthony and U. Kortshagen, *Physical Review B*, 2009, **80**, 115407.
137. R. J. Anthony, D. J. Rowe, M. Stein, J. Yang and U. Kortshagen, *Advanced Functional Materials*, 2011, **21**, 4042-4046.
138. S. Godefroo, M. Hayne, M. Jivanescu, A. Stesmans, M. Zacharias, O. I. Lebedev, G. Van Tendeloo and V. V. Moshchalkov, *Nature Nanotechnology*, 2008, **3**, 174-178.
139. M. L. Mastronardi, E. J. Henderson, D. P. Puzzo, Y. Chang, Z. B. Wang, M. G. Helander, J. Jeong, N. P. Kherani, Z. Lu and G. A. Ozin, *Small*, 2012, **8**, 3647-3654.
140. B. Ghosh, M. Takeguchi, J. Nakamura, Y. Nemoto, T. Hamaoka, S. Chandra and N. Shirahata, *Scientific Reports*, 2016, **6**, 36951.
141. A. M. P. Botas, R. A. S. Ferreira, R. N. Pereira, R. J. Anthony, T. Moura, D. J. Rowe and U. Kortshagen, *The Journal of Physical Chemistry C*, 2014, **118**, 10375-10383.
142. K. Q. Loh, H. P. Andaraarachchi, V. E. Ferry and U. R. Kortshagen, *ACS Applied Nano Materials*, 2023, **6**, 6444-6453.
143. F. Erogbogbo, C. W. Chang, J. May, P. N. Prasad and M. T. Swihart, *Nanoscale*, 2012, **4**, 5163-5168.
144. M. Locritani, Y. Yu, G. Bergamini, M. Baroncini, J. K. Molloy, B. A. Korgel and P. Ceroni, *Journal of Physics Chemistry Letter*, 2014, **5**, 3325-3329.
145. J. Yang, R. Liptak, D. Rowe, J. Wu, J. Casey, D. Witker, S. A. Campbell and U. Kortshagen, *Applied Surface Science*, 2014, **323**, 54-58.
146. J. J. Wu and U. R. Kortshagen, *RSC Advances*, 2015, **5**, 103822-103828.
147. D. L. Staebler and C. R. Wronski, *Applied Physics Letters*, 1977, **31**, 292-294.
148. H. Plagwitz, B. Terheiden and R. Brendel, *Journal of Applied Physics*, 2008, **103**, 094506.
149. M. Montalti, A. Cantelli and G. Battistelli, *Chemical Society Reviews*, 2015, **44**, 4853-4921.
150. J. H. Warner, A. Hoshino, K. Yamamoto and R. D. Tilley, *Angewandte Chemie International Edition*, 2005, **44**, 4550-4554.
151. E. J. Henderson, A. J. Shuhendler, P. Prasad, V. Baumann, F. Maier-Flaig, D. O. Faulkner, U. Lemmer, X. Y. Wu and G. A. Ozin, *Small*, 2011, **7**, 2507-2516.
152. F. Romano, S. Angeloni, G. Morselli, R. Mazzaro, V. Morandi, J. R. Shell, X. Cao, B. W. Pogue and P. Ceroni, *Nanoscale*, 2020, **12**, 7921-7926.
153. G. S. He, Q. Zheng, K.-T. Yong, F. Erogbogbo, M. T. Swihart and P. N. Prasad, *Nano Letters*, 2008, **8**, 2688-2692.
154. L. Ravotto, Q. Chen, Y. Ma, S. A. Vinogradov, M. Locritani, G. Bergamini, F. Negri, Y. Yu, B. A. Korgel and P. Ceroni, *Chem*, 2017, **2**, 550-560.

155. C. Tu, X. Ma, P. Pantazis, S. M. Kauzlarich and A. Y. Louie, *Journal of the American Chemical Society*, 2010, **132**, 2016-2023.
156. H.-Y. Tsai, C. J. T. Robidillo, G. K. Matharu, K. O'Connor, I. T. Cheong, C. Ni, J. G. C. Veinot and W. R. Algar, *Nanoscale*, 2023, **15**, 12492-12505.
157. J. M. Lauerhaas and M. J. Sailor, *Science*, 1993, **261**, 1567-1568.
158. C. M. Gonzalez and J. G. Veinot, *Journal of Materials Chemistry C*, 2016, **4**, 4836-4846.
159. C. M. Gonzalez, M. Iqbal, M. Dasog, D. G. Piercey, R. Lockwood, T. M. Klapotke and J. G. Veinot, *Nanoscale*, 2014, **6**, 2608-2612.
160. B. Campos, M. Algarra, B. Alonso, C. Casado, J. Jimenez-Jimenez, E. Rodriguez-Castellon and J. E. da Silva, *Talanta*, 2015, **144**, 862-867.
161. Y. Yi, J. Deng, Y. Zhang, H. Li and S. Yao, *Chemical Communications*, 2013, **49**, 612-614.
162. Y. Yi, G. Zhu, C. Liu, Y. Huang, Y. Zhang, H. Li, J. Zhao and S. Yao, *Analytical Chemistry*, 2013, **85**, 11464-11470.
163. C. J. T. Robidillo, S. Wandelt, R. Dalangin, L. Zhang, H. Yu, A. Meldrum, R. E. Campbell and J. G. C. Veinot, *ACS Applied Materials Interfaces*, 2019, **11**, 33478-33488.
164. L. A. Milburn, C. J. T. Robidillo, R. Dalangin, Y. Shen and J. G. C. Veinot, *ACS Applied Nano Materials*, 2022, **5**, 11984-11990.
165. C. Battaglia, A. Cuevas and S. De Wolf, *Energy & Environmental Science*, 2016, **9**, 1552-1576.
166. F. Meinardi, S. Ehrenberg, L. Dharmo, F. Carulli, M. Mauri, F. Bruni, R. Simonutti, U. Kortshagen and S. Brovelli, *Nature Photonics*, 2017, **11**, 177-185.
167. S. K. E. Hill, R. Connell, C. Peterson, J. Hollinger, M. A. Hillmyer, U. Kortshagen and V. E. Ferry, *ACS Photonics*, 2018, **6**, 170-180.
168. R. Mazzaro, A. Gradone, S. Angeloni, G. Morselli, P. G. Cozzi, F. Romano, A. Vomiero and P. Ceroni, *ACS Photonics*, 2019, **6**, 2303-2311.
169. S. Ren, C. Shou, S. Jin, G. Chen, S. Han, Z. Chen, X. Chen, S. Yang, Y. Guo and C.-C. Tu, *ACS Photonics*, 2021, **8**, 2392-2399.
170. J. S. Van Der Burgt, D. R. Needell, T. Veecken, A. Polman, E. C. Garnett and H. A. Atwater, *ACS Applied Materials & Interfaces*, 2021, **13**, 40742-40753.
171. Restriction of Hazardous Substances in Electrical and Electronic Equipment (RoHS), https://environment.ec.europa.eu/topics/waste-and-recycling/rohs-directive_en#overview, (2023).
172. K. Y. Cheng, R. Anthony, U. R. Kortshagen and R. J. Holmes, *Nano Letter*, 2011, **11**, 1952-1956.
173. F. Maier-Flaig, J. Rinck, M. Stephan, T. Bocksrocker, M. Bruns, C. Kubel, A. K. Powell, G. A. Ozin and U. Lemmer, *Nano Letter*, 2013, **13**, 475-480.
174. H. Yamada, N. Saitoh, B. Ghosh, Y. Masuda, N. Yoshizawa and N. Shirahata, *The Journal of Physical Chemistry C*, 2020, **124**, 23333-23342.
175. P. Photopoulos and A. G. Nassiopoulou, *Applied Physics Letters*, 2000, **77**, 1816.
176. B. Ghosh, Y. Masuda, Y. Wakayama, Y. Imanaka, J.-i. Inoue, K. Hashi, K. Deguchi, H. Yamada, Y. Sakka, S. Ohki, T. Shimizu and N. Shirahata, *Advanced Functional Materials*, 2014, **24**, 7151-7160.
177. I. T. Cheong, J. Mock, M. Kallergi, E. Groß, A. Meldrum, B. Rieger, M. Becherer and J. G. C. Veinot, *Advanced Optical Materials*, 2022, **11**, 2201834.
178. J. Mock, M. Kallergi, E. Gros, M. Golibrzuch, B. Rieger and M. Becherer, *IEEE Photonics Journal*, 2022, **14**, 1-9.

179. L. Yao, T. Yu, L. Ba, H. Meng, X. Fang, Y. Wang, L. Li, X. Rong, S. Wang, X. Wang, G. Ran, X. Pi and G. Qin, *Journal of Materials Chemistry C*, 2016, **4**, 673-677.
180. B. Ghosh, H. Yamada, S. Chinnathambi, I. N. G. Ozbilgin and N. Shirahata, *Journal of Physical Chemistry Letter*, 2018, **9**, 5400-5407.
181. H. Yamada, J. Watanabe, K. Nemoto, H.-T. Sun and N. Shirahata, *Nanomaterials*, 2022, **12**, 4314.
182. N. Hodgson and H. Weber, in *Optical Resonators*, Springer London, 1997.
183. Z. Yuan, P. C. Wu and Y. C. Chen, *Laser & Photonics Reviews*, 2022, **16**, 2100202.
184. N. Ismail, C. C. Kores, D. Geskus and M. Pollnau, *Optics express*, 2016, **24**, 16366-16389.
185. H. Becker, S. E. Burns, N. Tessler and R. H. Friend, *Journal of Applied Physics*, 1997, **81**, 2825-2829.
186. F. Ma and X. Liu, *Applied Optics*, 2007, **46**, 6247-6250.
187. Y. Fujiwara, H. Nishitani, H. Nakata and T. Ohyama, *Japanese Journal of Applied Physics*, 1992, **31**, L1763.
188. C. L. Curtis, V. V. Doan, G. M. Credo and M. J. Sailor, *Journal of the Electrochemical Society*, 1993, **140**, 3492.
189. V. S.-Y. Lin, K. Motesharei, K.-P. S. Dancil, M. J. Sailor and M. R. Ghadiri, *Science*, 1997, **278**, 840-843.
190. M. J. Sailor and J. R. Link, *Chemical Communications* 2005, **11**, 1375-1383.
191. G. Vincent, *Applied Physics Letters*, 1994, **64**, 2367-2369.
192. L. Pavesi and V. Mulloni, *Journal of Luminescence*, 1998, **80**, 43-52.
193. V. Mulloni and L. Pavesi, *Applied Physics Letters*, 2000, **76**, 2523-2525.
194. F. Duerinckx, I. Kuzma-Filipek, K. Van Nieuwenhuysen, G. Beaucarne and J. Poortmans, *Progress in Photovoltaics: Research and Applications*, 2008, **16**, 399-407.
195. L. Pavesi, *Solid State Communications*, 1996, **97**, 1051-1053.
196. M. Araki, H. Koyama and N. Koshida, *Applied Physics Letters*, 1996, **69**, 2956-2958.
197. D. Amans, S. Callard, A. Gagnaire, J. Joseph, F. Huisken and G. Ledoux, *Journal of Applied Physics*, 2004, **95**, 5010-5013.
198. S. Jaiswal, J. Simpson, S. Withrow, C. White and P. Norris, *Applied Physics A*, 2003, **77**, 57-61.
199. K. Dohnalová, I. Pelant, P. Gilliot, O. Crégut and B. Hönerlage, *Applied Physics Letters*, 2006, **88**, 251105.
200. D.-C. Wang, C. Zhang, P. Zeng, W.-J. Zhou, L. Ma, H.-T. Wang, Z.-Q. Zhou, F. Hu, S.-Y. Zhang, M. Lu and X. Wu, *Science Bulletin*, 2018, **63**, 75-77.
201. P. Zeng, F. Wang, Y. Zhang, W. Zhou, Z. Guo, X. Wu, M. Lu and S. Zhang, *ACS Photonics*, 2021, **8**, 1353-1363.
202. Y.-C. Zhang, Z.-Y. Yu, F.-Y. Ma, X.-Y. Xue, K.-X. Liu, J. Sun, S.-Y. Wang and M. Lu, *Results in Physics*, 2022, **39**, 105734.
203. M. Ajgaonkar, Y. Zhang, H. Grebel and C. White, *Applied Physics Letters*, 1999, **75**, 1532-1534.
204. J. Valenta, J. Linnros, R. Juhasz, J.-L. Rehspringer, F. Huber, C. Hirlimann, S. Cheylan and R. G. Elliman, *Journal of Applied Physics*, 2003, **93**, 4471-4474.
205. A. M. Beltaos and A. Meldrum, *Journal of Luminescence*, 2007, **126**, 607-613.
206. R.-J. Zhang, S.-Y. Seo, A. P. Milenin, M. Zacharias and U. Gösele, *Applied Physics Letters*, 2006, **88**, 153120.

207. J. R. Rodríguez, J. G. C. Veinot, P. Bianucci and A. Meldrum, *Applied Physics Letters*, 2008, **92**, 131119.
208. C. D. Presti, A. Irrera, G. Franzò, I. Crupi, F. Priolo, F. Iacona, G. Di Stefano, A. Piana, D. Sanfilippo and P. G. Fallica, *Applied Physics Letters*, 2006, **88**, 033501.
209. L. Ondič, M. Varga, I. Pelant, J. Valenta, A. Kromka and R. G. Elliman, *Scientific Reports*, 2017, **7**, 5763.
210. J. N. Milgram, J. Wojcik, P. Mascher and A. P. Knights, *Optics Express*, 2007, **15**, 14679.
211. Z.-Y. Yu, Z.-H. Guo, Y.-C. Zhang, X. Zhang, Y. Wang, F.-Y. Ma, Y. Liu, X.-Y. Xue, Q.-Y. Jin, J. Li, J. Sun, S.-Y. Wang, D.-C. Wang and M. Lu, *Results in Physics*, 2022, **34**, 105336.
212. A. Hryciw, J. Laforge, C. Blois, M. Glover and A. Meldrum, *Advanced Materials*, 2005, **17**, 845-849.
213. C.-K. Tseng, M.-C. M. Lee, H.-W. Hung, J.-R. Huang, K.-Y. Lee, J.-M. Shieh and G.-R. Lin, *Journal of Applied Physics*, 2012, **111**, 074512.

Chapter 2

1. R. Rossetti, S. Nakahara and L. E. Brus, *Journal of Chemical Physics*, 1983, **79**, 1086–1088.
2. V. Colvin, M. C. Schlamp and A. P. Alivisatos, *Nature*, 1994, **370**, 354–357.
3. W. C. Chan, *Science*, 1998, **281**, 2016–2018.
4. I. L. Medintz, H. T. Uyeda, E. R. Goldman and H. Mattoussi, *Nature Materials*, 2005, **4**, 435–446.
5. G. Konstantatos, I. Howard, A. Fischer, S. Hoogland, J. Clifford, E. Klem, L. Levina and E. H. Sargent, *Nature*, 2006, **442**, 180–183.
6. K.-Y. Cheng, R. Anthony, U. R. Kortshagen and R. J. Holmes, *Nano Letter*, 2011, **11**, 1952–1956.
7. J. Song, J. Li, X. Li, L. Xu, Y. Dong and H. Zeng, *Advanced Materials*, 2015, **27**, 7162–7167.
8. M. K. Choi, J. Yang, T. Hyeon and D.-H. Kim, *Npj Flexible Electronics*, 2018, **2**, 10.
9. J. M. Pietryga, Y.-S. Park, J. Lim, A. F. Fidler, W. K. Bae, S. Brovelli and V. I. Klimov, *Chemical Reviews*, 2016, **116**, 10513–10622.
10. X. Dai, Y. Deng, X. Peng and Y. Jin, *Advanced Materials*, 2017, **29**, 1607022.
11. A. M. Derfus, W. C. W. Chan and S. N. Bhatia, *Nano Letter*, 2004, **4**, 11–18.
12. R. Hardman, *Environmental Health Perspect.*, 2006, **114**, 165–172.
13. W. Ke and M. G. Kanatzidis, *Nature Communications*, 2019, **10**, 965.
14. X. Li, M. Rui, J. Song, Z. Shen and H. Zeng, *Advanced Functional Materials*, 2015, **25**, 4929–4947.
15. M. V. Kovalenko, L. Manna, A. Cabot, Z. Hens, D. V. Talapin, C. R. Kagan, V. I. Klimov, A. L. Rogach, P. Reiss, D. J. Milliron, P. Guyot-Sionnest, G. Konstantatos, W. J. Parak, T. Hyeon, B. A. Korgel, C. B. Murray and W. Heiss, *ACS Nano*, 2015, **9**, 1012–1057.
16. S. Morozova, M. Alikina, A. Vinogradov and M. Pagliaro, *Frontiers in Chemistry*, 2020, **8**, 191.
17. J. Emsley, *Nature's Building Blocks: An A-Z Guide to the Elements*, Oxford University Press, New York, 2nd edn., 2011.
18. R. J. Walters, G. I. Bourianoff and H. A. Atwater, *Nature Materials*, 2005, **4**, 143–146.
19. M. J. Sailor and E. C. Wu, *Advanced Functional Materials*, 2009, **19**, 3195–3208.

20. C. Zhang, Y. Xu, J. Liu, J. Li, J. Xiang, H. Li, J. Li, Q. Dai, S. Lan and A. E. Miroshnichenko, *Nature Communication*, 2018, **9**, 2964.
21. M. Dasog, G. B. De los Reyes, L. V. Titova, F. A. Hegmann and J. G. C. Veinot, *ACS Nano*, 2014, **8**, 9636–9648.
22. R. J. Clark, M. K. M. Dang and J. G. C. Veinot, *Langmuir*, 2010, **26**, 15657–15664.
23. Z. Yang, C. M. Gonzalez, T. K. Purkait, M. Iqbal, A. Meldrum and J. G. C. Veinot, *Langmuir*, 2015, **31**, 10540–10548.
24. M. H. Mobarok, T. K. Purkait, M. A. Islam, M. Miskolzie and J. G. C. Veinot, *Angewandte Chemie International Edition*, 2017, **56**, 6073–6077.
25. M. A. Islam, T. K. Purkait and J. G. C. Veinot, *Journal of the American Chemical Society*, 2014, **136**, 15130–15133.
26. M. Dasog, K. Bader and J. G. C. Veinot, *Chemistry of Materials*, 2015, **27**, 1153–1156.
27. S. Ivanov, S. Zhuravsky, G. Yukina, V. Tomson, D. Korolev and M. Galagudza, *Materials*, 2012, **5**, 1873–1889.
28. A. G. Cullis and L. T. Canham, *Nature*, 1991, **353**, 335–338.
29. H. Takagi, H. Ogawa, Y. Yamazaki, A. Ishizaki and T. Nakagiri, *Applied Physics Letter*, 1990, **56**, 2379–2380.
30. W. L. Wilson, P. F. Szajowski and L. E. Brus, *Science*, 1993, **262**, 1242–1244.
31. I. Sychugov, R. Juhasz, J. Valenta and J. Linnros, *Physics Review Letter*, 2005, **94**, 087405.
32. M. Dasog, Z. Yang, S. Regli, T. M. Atkins, A. Faramus, M. P. Singh, E. Muthuswamy, S. M. Kauzlarich, R. D. Tilley and J. G. C. Veinot, *ACS Nano*, 2013, **7**, 2676–2685.
33. R. Sinelnikov, M. Dasog, J. Beamish, A. Meldrum and J. G. C. Veinot, *ACS Photonics*, 2017, **4**, 1920–1929.
34. N. Shirahata, J. Nakamura, J. Inoue, B. Ghosh, K. Nemoto, Y. Nemoto, M. Takeguchi, Y. Masuda, M. Tanaka and G. A. Ozin, *Nano Letter*, 2020, **20**, 1491–1498.
35. A. N. Thiessen, L. Zhang, A. O. Oliynyk, H. Yu, K. M. O'Connor, A. Meldrum and J. G. C. Veinot, *Chemistry of Materials*, 2020, **32**, 6838–6846.
36. A. Marinins, Z. Yang, H. Chen, J. Linnros, J. G. C. Veinot, S. Popov and I. Sychugov, *ACS Photonics*, 2016, **3**, 1575–1580.
37. C. M. Hessel, D. Reid, M. G. Panthani, M. R. Rasch, B. W. Goodfellow, J. Wei, H. Fujii, V. Akhavan and B. A. Korgel, *Chemistry of Materials*, 2012, **24**, 393–401.
38. A. Marinins, R. Zandi Shafagh, W. van der Wijngaart, T. Haraldsson, J. Linnros, J. G. C. Veinot, S. Popov and I. Sychugov, *ACS Applied Materials & Interfaces*, 2017, **9**, 30267–30272.
39. L. Canham, *Faraday Discussions*, 2020, **222**, 10–81.
40. D. Jurbergs, E. Rogojina, L. Mangolini and U. Kortshagen, *Applied Physics Letter*, 2006, **88**, 233116.
41. T. A. Pringle, K. I. Hunter, A. Brumberg, K. J. Anderson, J. A. Fagan, S. A. Thomas, R. J. Petersen, M. Sefannaser, Y. Han, S. L. Brown, D. S. Kilin, R. D. Schaller, U. R. Kortshagen, P. R. Boudjouk and E. K. Hobbie, *ACS Nano*, 2020, **14**, 3858–3867.
42. Q. Li, T.-Y. Luo, M. Zhou, H. Abroshan, J. Huang, H. J. Kim, N. L. Rosi, Z. Shao and R. Jin, *ACS Nano*, 2016, **10**, 8385–8393.
43. B. Ghosh, Y. Masuda, Y. Wakayama, Y. Imanaka, J. Inoue, K. Hashi, K. Deguchi, H. Yamada, Y. Sakka, S. Ohki, T. Shimizu and N. Shirahata, *Advanced Functional Materials*, 2014, **24**, 7151–7160.

44. C. M. Gonzalez and J. G. C. Veinot, *Journal of Materials Chemistry C*, 2016, **4**, 4836–4846.
45. M. Locritani, Y. Yu, G. Bergamini, M. Baroncini, J. K. Molloy, B. A. Korgel and P. Ceroni, *Journal of Physical Chemistry Letter*, 2014, **5**, 3325–3329.
46. M. D. Mason, G. M. Credo, K. D. Weston and S. K. Buratto, *Physical Review Letter*, 1998, **80**, 5405–5408.
47. M. L. Mastronardi, E. J. Henderson, D. P. Puzzo and G. A. Ozin, *Advanced Materials*, 2012, **24**, 5890–5898.
48. I. Sychugov, A. Fucikova, F. Pevere, Z. Yang, J. G. C. Veinot and J. Linnros, *ACS Photonics*, 2014, **1**, 998–1005.
49. N. Hodgson and H. Weber, in *Optical Resonators: Fundamentals, Advanced Concepts and Applications*, eds. N. Hodgson and H. Weber, Springer, London, 1997.
50. V. Wood and V. Bulović, *Nano Reviews*, 2010, **1**, 5202.
51. F. Ma and X. Liu, *Applied Optics*, 2007, **46**, 6247.
52. H. Becker, S. E. Burns, N. Tessler and R. H. Friend, *Journal of Applied Physics*, 1997, **81**, 2825–2829.
53. D. Amans, S. Callard, A. Gagnaire, J. Joseph, F. Huisken and G. Ledoux, *Journal of Applied Physics*, 2004, **95**, 5010–5013.
54. A. Hryciw, J. Laforge, C. Blois, M. Glover and A. Meldrum, *Advanced Materials*, 2005, **17**, 845–849.
55. M. A. Islam, M. H. Mobarok, R. Sinelnikov, T. K. Purkait and J. G. C. Veinot, *Langmuir*, 2017, **33**, 8766–8773.
56. M. Dasog, J. Kehrlé, B. Rieger and J. G. C. Veinot, *Angewandte Chemie International Edition*, 2016, **55**, 2322–2339.
57. W. T. Collins, C. L. Frye, Patent US3615272, 1971,
58. C. M. Hessel, E. J. Henderson and J. G. C. Veinot, *Chemistry of Materials* **2006**, **18**, 6139–6146
59. Z. Yang, M. Dasog, A. R. Dobbie, R. Lockwood, Y. Zhi, A. Meldrum and J. G. C. Veinot, *Advanced Functional Materials*, 2014, **24**, 1345–1353.
60. S. K. E. Hill, R. Connell, C. Peterson, J. Hollinger, M. A. Hillmyer, U. Kortshagen and V. E. Ferry, *ACS Photonics*, 2019, **6**, 170–180.
61. M. X. Dung, J.-K. Choi and H.-D. Jeong, *ACS Applied Materials & Interfaces*, 2013, **5**, 2400–2409.
62. J. G. C. Veinot, *Chemical Communications.*, **2006**, 4160–4168.
63. J.-K. Choi, M. X. Dung and H.-D. Jeong, *Materials Chemical and Physics*, 2014, **148**, 463–472.
64. L.-M. Chen, Z. Hong, W. L. Kwan, C.-H. Lu, Y.-F. Lai, B. Lei, C.-P. Liu and Y. Yang, *ACS Nano*, 2010, **4**, 4744–4752.
65. M. Aghajamali, I. T. Cheong and J. G. C. Veinot, *Langmuir*, 2018, **34**, 9418–9423.
66. L. Hou, Q. Hou, Y. Mo, J. Peng and Y. Cao, *Applied Physics Letter*, 2005, **87**, 243504.

Chapter 3

1. R. Rossetti, S. Nakahara and L. E. Brus, *The Journal of Chemical Physics*, 1983, **79**, 1086–1088.
2. W. Ke and M. G. Kanatzidis, *Nature Communications*, 2019, **10**, 965.
3. Q. Xu, I. T. Cheong, L. Meng, J. G. C. Veinot and X. Wang, *ACS Nano*, 2021, **15**, 18429–18436.

4. I. L. Medintz, H. T. Uyeda, E. R. Goldman and H. Mattoussi, *Nature Materials*, 2005, **4**, 435-446.
5. Q.-B. Zhu, B. Li, D.-D. Yang, C. Liu, S. Feng, M.-L. Chen, Y. Sun, Y.-N. Tian, X. Su, X.-M. Wang, S. Qiu, Q.-W. Li, X.-M. Li, H.-B. Zeng, H.-M. Cheng and D.-M. Sun, *Nature Communications*, 2021, **12**, 1798.
7. D. T. Yonemoto, C. M. Papa, C. Mongin and F. N. Castellano, *Journal of the American Chemical Society*, 2020, **142**, 10883-10893.
8. N. Li, X. Chen, J. Wang, X. Liang, L. Ma, X. Jing, D.-L. Chen and Z. Li, *ACS Nano*, 2022, **16**, 3332-3340.
9. Z. Liu, C. H. Lin, B. R. Hyun, C. W. Sher, Z. Lv, B. Luo, F. Jiang, T. Wu, C. H. Ho, H. C. Kuo and J. H. He, *Light: Science & Applications*, 2020, **9**, 83.
10. Y. Shirasaki, G. J. Supran, M. G. Bawendi and V. Bulović, *Nature Photonics*, 2012, **7**, 13-23.
11. X. Dai, Y. Deng, X. Peng and Y. Jin, *Advanced Materials*, 2017, **29**.
12. M. K. Choi, J. Yang, T. Hyeon and D.-H. Kim, *npj Flexible Electronics*, 2018, **2**, 10.
13. Y. Yin, Z. Hu, M. U. Ali, M. Duan, L. Gao, M. Liu, W. Peng, J. Geng, S. Pan, Y. Wu, J. Hou, J. Fan, D. Li, X. Zhang and H. Meng, *Advanced Materials Technologies*, 2020, **5**, 2000251.
14. Y.-H. Won, O. Cho, T. Kim, D.-Y. Chung, T. Kim, H. Chung, H. Jang, J. Lee, D. Kim and E. Jang, *Nature*, 2019, **575**, 634-638.
15. F. P. Garcia de Arquer, D. V. Talapin, V. I. Klimov, Y. Arakawa, M. Bayer and E. H. Sargent, *Science*, 2021, **373**.
16. A. Das and P. T. Snee, *Chemphyschem*, 2016, **17**, 598-617.
17. S. Ivanov, S. Zhuravsky, G. Yukina, V. Tomson, D. Korolev and M. Galagudza, *Materials*, 2012, **5**, 1873-1889.
18. K. Y. Cheng, R. Anthony, U. R. Kortshagen and R. J. Holmes, *Nano Letters*, 2011, **11**, 1952-1956.
19. S. Zhao, X. Liu, X. Pi and D. Yang, *Journal of Semiconductors*, 2018, **39**.
20. B. Ghosh, H. Yamada, S. Chinnathambi, I. N. G. Ozbilgin and N. Shirahata, *Journal of Physical Chemistry Letter*, 2018, **9**, 5400-5407.
21. A. Angi, M. Loch, R. Sinelnikov, J. G. C. Veinot, M. Becherer, P. Lugli and B. Rieger, *Nanoscale*, 2018, **10**, 10337-10342.
22. J. Mock, E. Groß, M. J. Klobereg, B. Rieger and M. Becherer, *Advanced Photonics Research*, 2021, **2**, 2100083.
23. T. Ono, Y. Xu, T. Sakata and K. I. Saitow, *ACS Applied Materials & Interfaces*, 2022, **14**, 1373-1388.
24. J. G. Veinot, *Chemical Communications*, 2006, 4160-4168.
25. S. Milliken, A. N. Thiessen, I. T. Cheong, K. M. O'Connor, Z. Li, R. W. Hooper, C. J. T. Robidillo and J. G. C. Veinot, *Nanoscale*, 2021, **13**, 16379-16404.
26. I. M. Hohlein, A. Angi, R. Sinelnikov, J. G. Veinot and B. Rieger, *Chemistry*, 2015, **21**, 2755-2758.
27. A. Halimaoui, C. Oules, G. Bomchil, A. Bsiesy, F. Gaspard, R. Herino, M. Ligeon and F. Muller, *Applied Physics Letters*, 1991, **59**, 304-306.
28. N. Koshida and H. Koyama, *Applied Physics Letters*, 1992, **60**, 347-349.
29. R. K. Ligman, L. Mangolini, U. R. Kortshagen and S. A. Campbell, *Applied Physics Letters*, 2007, **90**, 061116.

30. P. Photopoulos and A. G. Nassiopoulou, *Applied Physics Letters*, 2000, **77**, 1816.
31. R. J. Walters, G. I. Bourianoff and H. A. Atwater, *Nature Materials*, 2005, **4**, 143-146.
32. D. P. Puzzo, E. J. Henderson, M. G. Helander, Z. Wang, G. A. Ozin and Z. Lu, *Nano Letter*, 2011, **11**, 1585-1590.
33. M. L. Mastronardi, E. J. Henderson, D. P. Puzzo, Y. Chang, Z. B. Wang, M. G. Helander, J. Jeong, N. P. Kherani, Z. Lu and G. A. Ozin, *Small*, 2012, **8**, 3647-3654.
34. F. Maier-Flaig, J. Rinck, M. Stephan, T. Bocksrocker, M. Bruns, C. Kubel, A. K. Powell, G. A. Ozin and U. Lemmer, *Nano Letter*, 2013, **13**, 475-480.
35. X. Liu, S. Zhao, W. Gu, Y. Zhang, X. Qiao, Z. Ni, X. Pi and D. Yang, *ACS Applied Materials & Interfaces*, 2018, **10**, 5959-5966.
36. J. Watanabe, H. Yamada, H.-T. Sun, T. Moronaga, Y. Ishii and N. Shirahata, *ACS Applied Nano Materials*, 2021, **4**, 11651-11660.
37. V. Kveder, M. Badylevich, E. Steinman, A. Izotov, M. Seibt and W. Schröter, *Applied Physics Letters*, 2004, **84**, 2106-2108.
38. F. Maier-Flaig, C. Kubel, J. Rinck, T. Bocksrocker, T. Scherer, R. Prang, A. K. Powell, G. A. Ozin and U. Lemmer, *Nano Letter*, 2013, **13**, 3539-3545.
39. L. Yao, T. Yu, L. Ba, H. Meng, X. Fang, Y. Wang, L. Li, X. Rong, S. Wang, X. Wang, G. Ran, X. Pi and G. Qin, *Journal of Materials Chemistry C*, 2016, **4**, 673-677.
40. S. Terada, H. Ueda, T. Ono and K.-i. Saitow, *ACS Sustainable Chemistry & Engineering*, 2022, **10**, 1765-1776.
41. Y. C. Zhang, Z. Y. Yu, X. Y. Xue, F. L. Wang, S. Li, X. Y. Dai, L. Wu, S. Y. Zhang, S. Y. Wang and M. Lu, *Optic Express*, 2021, **29**, 34126-34134.
42. D. V. Talapin and J. Steckel, *MRS Bulletin*, 2013, **38**, 685-691.
43. I. Sychugov, R. Juhasz, J. Valenta and J. Linnros, *Physics Review Letters*, 2005, **94**, 087405.
44. I. Sychugov, A. Fucikova, F. Pevere, Z. Yang, J. G. C. Veinot and J. Linnros, *ACS Photonics*, 2014, **1**, 998-1005.
45. M. L. Mastronardi, F. Maier-Flaig, D. Faulkner, E. J. Henderson, C. Kubel, U. Lemmer and G. A. Ozin, *Nano Letters*, 2012, **12**, 337-342.
46. M. L. Mastronardi, F. Hennrich, E. J. Henderson, F. Maier-Flaig, C. Blum, J. Reichenbach, U. Lemmer, C. Kubel, D. Wang, M. M. Kappes and G. A. Ozin, *Journal of the American Chemical Society*, 2011, **133**, 11928-11931.
47. N. Hodgson and H. Weber, in *Optical Resonators*, Springer London, 1997.
48. H. Zhu, W. Zhang, and S. F. Yu, *Nanoscale* **2013**, 5 (5), 1797-1802
49. X. Yang, E. Mutlugun, C. Dang, K. Dev, Y. Gao, S. T. Tan, X. W. Sun, and H. V. Demi, *ACS Nano* **2014**, 8 (8), 8224-8231.
50. D. Li, B. Kristal, Y. Wang, J. Feng, Z. Lu, G. Yu, Z. Chen, Y. Li, X. Li, and X. Xu, *ACS Applied Materials & Interfaces* **2019**, 11 (37), 34067-34075.
51. Y. Miao, L. Cheng, W. Zou, L. Gu, J. Zhang, Q. Guo, Q. Peng, M. Xu, Y. He, S. Zhang, Y. Cao, R. Li, N. Wang, W. Huang, and J. Wang, *Light: Science & Applications* **2020**, 9 (1), 89.
52. M. Lu, J. Guo, S. Sun, P. Lu, J. Wu, Y. Wang, S. V. Kershaw, W. W. Yu, A. L. Rogach, and Y. Zhang, *Y. Nano Letters* **2020**, 20 (4), 2829-2836.
53. L. Wang, J. Lin, Y. Lv, B. Zou, J. Zhao, and X. Liu, *ACS Applied Nano Materials* **2020**, 3 (6), 5301-5310.
54. G. Liu, X. Zhou, and S. Chen, *ACS Appl Mater Interfaces* **2016**, 8 (26), 16768-16775.

55. D. Amans, S. Callard, A. Gagnaire, J. Joseph, F. Huisken and G. Ledoux, *Journal of Applied Physics*, 2004, **95**, 5010-5013
56. A. Hryciw, J. Laforge, C. Blois, M. Glover and A. Meldrum, *Advanced Materials*, 2005, **17**, 845-849.
57. P. Zeng, F. Wang, Y. Zhang, W. Zhou, Z. Guo, X. Wu, M. Lu and S. Zhang, *ACS Photonics*, 2021, **8**, 1353-1363.
58. Y.-C. Zhang, Z.-Y. Yu, F.-Y. Ma, X.-Y. Xue, K.-X. Liu, J. Sun, S.-Y. Wang and M. Lu, *Results in Physics*, 2022, **39**, 105734.
59. I. T. Cheong, W. Morrish, W. Sheard, H. Yu, B. Tavares Luppi, L. Milburn, A. Meldrum and J. G. C. Veinot, *ACS Applied Materials & Interfaces*, 2021, **13**, 27149-27158.
60. C. M. Hessel, E. J. Henderson, and J. G. C. Veinot, *Chemistry of Materials* **2006**, *18* (26), 6139-6146.
61. S. L. Anderson, E. J. Luber, B. C. Olsen, and J. M. Buriak, *Chemistry of Materials* **2016**, *28* (17), 5973-5975.
62. Z. Yang, M. Iqbal, A. R. Dobbie, and J. G. C. Veinot, *Journal of the American Chemical Society* **2013**, *135* (46), 17595-17601.
63. M. A. Islam, M. H. Mobarok, R. Sinelnikov, T. K. Purkait, and J. G. C. Veinot, *Langmuir* **2017**, *33* (35), 8766-8773.
64. Y. Xu, S. Terada, Y. Xin, H. Ueda, and K. Saitow, *ACS Applied Nano Materials* **2022**.
65. K.-Y. Cheng, R. Anthony, U. R. Kortshagen and R. J. Holmes, *Nano Letters*, 2010, **10**, 1154-1157.
66. J. Mock, M. Kallergi, E. Gro, M. Golibrzuch, B. Rieger and M. Becherer, *IEEE Photonics Journal*, 2022, **14**, 1-9.
67. F. Ma and X. Liu, *Applied Optics*, 2007, **46**, 6247-6250.
68. D. Hunger, T. Steinmetz, Y. Colombe, C. Deutsch, T. W. Hänsch and J. Reichel, *New Journal of Physics*, 2010, **12**. 065038
69. T. Klaassen, M. P. van Exter and J. P. Woerdman, *Applied Optics*, 2007, **46**, 5210-5215.
70. L. Chen, Z. Qin, and S. Chen, *Small Methods* **2022**, *6* (1), e2101090.
71. E. A. Weiss, *ACS Energy Letters*, 2017, **2**, 1005-1013.
72. M. H. Mobarok, T. K. Purkait, M. A. Islam, M. Miskolzie, and J. G. C. Veinot, *Angewandte Chemie International Edition* **2017**, *56* (22), 6073-6077.
73. J. Chen, Z. Wang, Z. Chen, S. Cong and Z. Zhao, *Nano Letter*, 2020, **20**, 1915-1922
74. Z. Wang, X. Wang, S. Cong, J. Chen, H. Sun, Z. Chen, G. Song, F. Geng, Q. Chen and Z. Zhao, *Nature Communications*, 2020, **11**, 302.
75. Q. Zhang, Q. Jin, A. Mertens, C. Rainer, R. Huber, J. Fessler, G. Hernandez-Sosa, and U. Lemmer, *Advanced Materials*, **2022**, *34* (33), e2201348.

Chapter 4

1. G. Ledoux, J. Gong, F. Huisken, O. Guillois and C. Reynaud, *Applied Physics Letters*, 2002, **80**, 4834-4836.
2. R. J. Clark, M. K. Dang and J. G. Veinot, *Langmuir*, 2010, **26**, 15657-15664.
3. C. M. Hessel, D. Reid, M. G. Panthani, M. R. Rasch, B. W. Goodfellow, J. Wei, H. Fujii, V. Akhavan and B. A. Korgel, *Chemistry of Materials*, 2012, **24**, 393-401.
4. M. Dasog, G. B. De los Reyes, L. V. Titova, F. A. Hegmann and J. G. C. Veinot, *ACS Nano*, 2014, **8**, 9636-9648.

5. S. Ivanov, S. Zhuravsky, G. Yukina, V. Tomson, D. Korolev and M. Galagudza, *Materials*, 2012, **5**, 1873-1889.
6. A. Das and P. T. Snee, *Chemphyschem*, 2016, **17**, 598-617.
7. A. Shiohara, S. Hanada, S. Prabakar, K. Fujioka, T. H. Lim, K. Yamamoto, P. T. Northcote and R. D. Tilley, *Journal of the American Chemical Society*, 2010, **132**, 248-253.
8. National Toxicology Program. Toxicology and carcinogenesis studies of indium phosphide (CAS No. 22398-90-7) in F344/N rats and B6C3F1 mice (inhalation studies). *Natl Toxicol Program Tech Rep Ser.* 2001, 7-340. PMID: 12087422.
9. R. Hardman, *Environmental Health Perspect*, 2006, **114**, 165-172.
10. J. Sobhanan, J. V. Rival, A. Anas, E. Sidharth Shibu, Y. Takano and V. Biju, *Advanced Drug Delivery Reviews*, 2023, **197**, 114830.
11. K. Y. Cheng, R. Anthony, U. R. Kortshagen and R. J. Holmes, *Nano Letter*, 2011, **11**, 1952-1956.
12. B. Ghosh, Y. Masuda, Y. Wakayama, Y. Imanaka, J.-i. Inoue, K. Hashi, K. Deguchi, H. Yamada, Y. Sakka, S. Ohki, T. Shimizu and N. Shirahata, *Advanced Functional Materials*, 2014, **24**, 7151-7160.
13. J. Watanabe, H. Yamada, H.-T. Sun, T. Moronaga, Y. Ishii and N. Shirahata, *ACS Applied Nano Materials*, 2021, **4**, 11651-11660.
14. Y. C. Zhang, Z. Y. Yu, X. Y. Xue, F. L. Wang, S. Li, X. Y. Dai, L. Wu, S. Y. Zhang, S. Y. Wang and M. Lu, *Optic Express*, 2021, **29**, 34126-34134.
15. I. T. Cheong, J. Mock, M. Kallergi, E. Groß, A. Meldrum, B. Rieger, M. Becherer and J. G. C. Veinot, *Advanced Optical Materials*, 2022, **11**, 2201834.
16. F. Meinardi, S. Ehrenberg, L. Dharmo, F. Carulli, M. Mauri, F. Bruni, R. Simonutti, U. Kortshagen and S. Brovelli, *Nature Photonics*, 2017, **11**, 177-185.
17. R. Mazzaro, A. Gradone, S. Angeloni, G. Morselli, P. G. Cozzi, F. Romano, A. Vomiero and P. Ceroni, *ACS Photonics*, 2019, **6**, 2303-2311.
18. S. Han, G. Chen, C. Shou, H. Peng, S. Jin and C.-C. Tu, *ACS Applied Materials & Interfaces*, 2020, **12**, 43771-43777.
19. J. Huang, J. Zhou, E. Jungstedt, A. Samanta, J. Linnros, L. A. Berglund and I. Sychugov, *ACS Photonics*, 2022, **9**, 2499-2509.
20. T. Lin, X. Liu, B. Zhou, Z. Zhan, A. N. Cartwright and M. T. Swihart, *Advanced Functional Materials*, 2014, **24**, 6016-6022.
21. M. Dutta, L. Thirugnanam, P. V. Trinh and N. Fukata, *ACS Nano*, 2015, **9**, 6891-6899.
22. E. J. Henderson, A. J. Shuhendler, P. Prasad, V. Baumann, F. Maier-Flaig, D. O. Faulkner, U. Lemmer, X. Y. Wu and G. A. Ozin, *Small*, 2011, **7**, 2507-2516.
23. C. J. T. Robidillo, M. A. Islam, M. Aghajamali, A. Faramus, R. Sinelnikov, X. Zhang, J. Boekhoven and J. G. C. Veinot, *Langmuir*, 2018, **34**, 6556-6569.
24. Z. F. Li and E. Ruckenstein, *Nano Letters*, 2004, **4**, 1463-1467.
25. D. Yang, Z. Cui, Z. Wen, Z. Piao, H. He, X. Wei, L. Wang, S. Mei, W. Zhang and R. Guo, *ACS Materials Letters*, 2023, **5**, 985-1008.
26. Z. Kang, C. H. A. Tsang, N.-B. Wong, Z. Zhang and S.-T. Lee, *Journal of the American Chemical Society*, 2007, **129**, 12090-12091.
27. T. Kojima, H. Sugimoto and M. Fujii, *The Journal of Physical Chemistry C*, 2018, **122**, 1874-1880.
28. M. Iqbal, T. K. Purkait, G. G. Goss, J. R. Bolton, M. Gamal El-Din and J. G. Veinot, *ACS Nano*, 2016, **10**, 5405-5412.

29. W. L. Wilson, P. Szajowski and L. Brus, *Science*, 1993, **262**, 1242-1244.
30. T. van Buuren, L. N. Dinh, L. L. Chase, W. J. Siekhaus and L. J. Terminello, *Physical Review Letters*, 1998, **80**, 3803-3806.
31. J. D. Holmes, K. J. Ziegler, R. C. Doty, L. E. Pell, K. P. Johnston and B. A. Korgel, *Journal of the American Chemical Society*, 2001, **123**, 3743-3748.
32. D. C. Hannah, J. Yang, P. Podsiadlo, M. K. Y. Chan, A. Demortière, D. J. Gosztola, V. B. Prakapenka, G. C. Schatz, U. Kortshagen and R. D. Schaller, *Nano Letters*, 2012, **12**, 4200-4205.
33. N. Shirahata, J. Nakamura, J. I. Inoue, B. Ghosh, K. Nemoto, Y. Nemoto, M. Takeguchi, Y. Masuda, M. Tanaka and G. A. Ozin, *Nano Letters*, 2020, **20**, 1491-1498.
34. D. S. English, L. E. Pell, Z. Yu, P. F. Barbara and B. A. Korgel, *Nano Letters*, 2002, **2**, 681-685.
35. M. Zacharias, J. Heitmann, R. Scholz, U. Kahler, M. Schmidt and J. Bläsing, *Applied Physics Letters*, 2002, **80**, 661-663.
36. J. G. Veinot, *Chemical Communications*, 2006, 4160-4168.
37. S. Godefroo, M. Hayne, M. Jivanescu, A. Stesmans, M. Zacharias, O. I. Lebedev, G. Van Tendeloo and V. V. Moshchalkov, *Nature Nanotechnology*, 2008, **3**, 174-178.
38. W. Sun, C. Qian, X. Cui, L. Wang, M. Wei, G. Casillas, A. S. Helmy and G. A. Ozin, *Nanoscale*, 2016, **8**, 3678-3684.
39. Y. Yu, G. Fan, A. Fermi, R. Mazzaro, V. Morandi, P. Ceroni, D.-M. Smilgies and B. A. Korgel, *The Journal of Physical Chemistry C*, 2017, **121**, 23240-23248.
40. J. Zhou, J. Huang, H. Chen, A. Samanta, J. Linnros, Z. Yang and I. Sychugov, *The Journal of Physical Chemistry Letters*, 2021, **12**, 8909-8916.
41. L. Mangolini, E. Thimsen and U. Kortshagen, *Nano Letters*, 2005, **5**, 655-659.
42. A. Gupta, M. T. Swihart and H. Wiggers, *Advanced Functional Materials*, 2009, **19**, 696-703.
43. Z. Li and U. R. Kortshagen, *Chemistry of Materials*, 2019, **31**, 8451-8458.
44. Y. Ding, R. Yamada, R. Gresback, S. Zhou, X. Pi and T. Nozaki, *Journal of Physics D: Applied Physics*, 2014, **47**, 485202.
45. T. A. Pringle, K. I. Hunter, A. Brumberg, K. J. Anderson, J. A. Fagan, S. A. Thomas, R. J. Petersen, M. Sefannaser, Y. Han, S. L. Brown, D. S. Kilin, R. D. Schaller, U. R. Kortshagen, P. R. Boudjouk and E. K. Hobbie, *ACS Nano*, 2020, **14**, 3858-3867.
46. T. Orii, M. Hirasawa and T. Seto, *Applied Physics Letters*, 2003, **83**, 3395-3397.
47. T. Nakamura, Z. Yuan, K. Watanabe and S. Adachi, *Applied Physics Letters*, 2016, **108**.
48. A. V. Kabashin, A. Singh, M. T. Swihart, I. N. Zvestovskaya and P. N. Prasad, *ACS Nano*, 2019, **13**, 9841-9867.
49. M. Dasog, Z. Yang, S. Regli, T. M. Atkins, A. Faramus, M. P. Singh, E. Muthuswamy, S. M. Kauzlarich, R. D. Tilley and J. G. Veinot, *ACS Nano*, 2013, **7**, 2676-2685.
50. M. Dasog, K. Bader and J. G. C. Veinot, *Chemistry of Materials*, 2015, **27**, 1153-1156.
51. R. Sinelnikov, M. Dasog, J. Beamish, A. Meldrum and J. G. C. Veinot, *ACS Photonics*, 2017, **4**, 1920-1929.
52. I. Sychugov, A. Fucikova, F. Pevero, Z. Yang, J. G. C. Veinot and J. Linnros, *ACS Photonics*, 2014, **1**, 998-1005.
53. A. Fucikova, I. Sychugov and J. Linnros, *Faraday Discussions*, 2020, **222**, 135-148.
54. E. Cartier, J. H. Stathis and D. A. Buchanan, *Applied Physics Letters*, 1993, **63**, 1510-1512.

55. M. Rosso-Vasic, E. Spruijt, B. van Lagen, L. De Cola and H. Zuilhof, *Small*, 2008, **4**, 1835-1841.
56. K. Sato, N. Fukata, K. Hirakuri, M. Murakami, T. Shimizu and Y. Yamauchi, *Chemistry: An Asian Journal*, 2010, **5**, 50-55.
57. J. Yang, R. Liptak, D. Rowe, J. Wu, J. Casey, D. Witker, S. A. Campbell and U. Kortshagen, *Applied Surface Science*, 2014, **323**, 54-58.
58. J. J. Wu and U. R. Kortshagen, *RSC Advances*, 2015, **5**, 103822-103828.
59. A. Marinins, R. Zandi Shafagh, W. van der Wijngaart, T. Haraldsson, J. Linnros, J. G. C. Veinot, S. Popov and I. Sychugov, *ACS Applied Materials & Interfaces*, 2017, **9**, 30267-30272.
60. D. Kajiya and K. I. Saitow, *RSC Advances*, 2018, **8**, 41299-41307.
61. K. Fujimoto, T. Hayakawa, Y. Xu, N. Jingu and K.-i. Saitow, *ACS Sustainable Chemistry & Engineering*, 2022, **10**, 14451-14463.
62. K. Q. Loh, H. P. Andaraarachchi, V. E. Ferry and U. R. Kortshagen, *ACS Applied Nano Materials*, 2023, **6**, 6444-6453.
63. X. Li, Y. He and M. T. Swihart, *Langmuir*, 2004, **20**, 4720-4727.
64. Z. Yang, C. M. Gonzalez, T. K. Purkait, M. Iqbal, A. Meldrum and J. G. Veinot, *Langmuir*, 2015, **31**, 10540-10548.
65. F. A. Reboredo and G. Galli, *The Journal of Physical Chemistry B*, 2005, **109**, 1072-1078.
66. O. Wolf, M. Dasog, Z. Yang, I. Balberg, J. G. C. Veinot and O. Millo, *Nano Letters*, 2013, **13**, 2516-2521.
67. D. L. Staebler and C. R. Wronski, *Applied Physics Letters*, 1977, **31**, 292-294.
68. H. Plagwitz, B. Terheiden and R. Brendel, *Journal of Applied Physics*, 2008, **103**, 094506.
69. R. Anthony and U. Kortshagen, *Physical Review B*, 2009, **80**.
70. A. N. Thiessen, M. Ha, R. W. Hooper, H. Yu, A. O. Oliynyk, J. G. C. Veinot and V. K. Michaelis, *Chemistry of Materials*, 2019, **31**, 678-688.
71. A. N. Thiessen, L. Zhang, A. O. Oliynyk, H. Yu, K. M. O'Connor, A. Meldrum and J. G. C. Veinot, *Chemistry of Materials*, 2020, **32**, 6838-6846.
72. R. A. Street, *Advances in Physics*, 2006, **30**, 593-676.
73. G. D. Cody, T. Tiedje, B. Abeles, B. Brooks and Y. Goldstein, *Physical Review Letters*, 1981, **47**, 1480-1483.
74. W. Bludau, A. Onton and W. Heinke, *Journal of Applied Physics*, 2003, **45**, 1846-1848.
75. I. T. Cheong, W. Morrish, W. Sheard, H. Yu, B. Tavares Luppi, L. Milburn, A. Meldrum and J. G. C. Veinot, *ACS Applied Materials & Interfaces*, 2021, **13**, 27149-27158.
76. C. M. Hessel, E. J. Henderson and J. G. Veinot, *Chemistry of Materials*, 2006, **18**, 6139-6146.
77. A. F. van Driel, I. S. Nikolaev, P. Vergeer, P. Lodahl, D. Vanmaekelbergh and W. L. Vos, *Physical Review B*, 2007, **75**, 035329.
78. J. I. Langford and A. J. C. Wilson, *Journal of Applied Crystallography*, 1978, **11**, 102-113.
79. P. Yogi, M. Tanwar, S. K. Saxena, S. Mishra, D. K. Pathak, A. Chaudhary, P. R. Sagdeo and R. Kumar, *Analytical Chemistry*, 2018, **90**, 8123-8129.
80. B. P. Falcão, J. P. Leitão, M. R. Soares, L. Ricardo, H. Águas, R. Martins and R. N. Pereira, *Physical Review Applied*, 2019, **11**, 024054.
81. D. A. Kislitsyn, J. M. Mills, S. K. Chiu, B. N. Taber, J. D. Barnes, C. F. Gervasi, A. M. Goforth and G. V. Nazin, *Journal of Physical Chemistry Letters*, 2018, **9**, 710-716.
82. L. Canham, *Faraday Discussions*, 2020, **222**, 10-81.

83. M. L. Mastronardi, F. Maier-Flaig, D. Faulkner, E. J. Henderson, C. Kubel, U. Lemmer and G. A. Ozin, *Nano Letters*, 2012, **12**, 337-342.
84. M. Nolan, M. Legesse and G. Fagas, *Physical Chemistry Chemical Physics*, 2012, **14**, 15173-15179.
85. X. D. Pi, L. Mangolini, S. A. Campbell and U. Kortshagen, *Physical Review B*, 2007, **75**, 085423.
86. X. Liu, Y. Zhang, T. Yu, X. Qiao, R. Gresback, X. Pi and D. Yang, *Particle & Particle Systems Characterization*, 2016, **33**, 44-52.
87. T. L. Cocker, V. Jelic, M. Gupta, S. J. Molesky, J. A. J. Burgess, G. D. L. Reyes, L. V. Titova, Y. Y. Tsui, M. R. Freeman and F. A. Hegmann, *Nature Photonics*, 2013, **7**, 620-625.
88. T. M. Atkins, A. Thibert, D. S. Larsen, S. Dey, N. D. Browning and S. M. Kauzlarich, *Journal of the American Chemical Society*, 2011, **133**, 20664-20667.
89. P. Gupta, V. L. Colvin and S. M. George, *Phys Rev B Condens Matter*, 1988, **37**, 8234-8243.
90. P. Martín, J. F. Fernández and C. R. Sánchez, *physica status solidi (a)*, 2000, **182**, 255-260.
91. B. N. Jariwala, N. J. Kramer, M. C. Petcu, D. C. Bobela, M. C. M. v. d. Sanden, P. Stradins, C. V. Ciobanu and S. Agarwal, *The Journal of Physical Chemistry C*, 2011, **115**, 20375-20379.
92. R. Walsh, *Accounts of Chemical Research*, 1981, **14**, 246-252.
93. R. T. Sanderson, *Journal of the American Chemical Society*, 1983, **105**, 2259-2261.
94. T. M. Hafshejani, J. Wohlgemuth and P. Thissen, *The Journal of Physical Chemistry C*, 2021, **125**, 19811-19820.
95. Y. Shu, U. R. Kortshagen, B. G. Levine and R. J. Anthony, *The Journal of Physical Chemistry C*, 2015, **119**, 26683-26691.
96. Y. Q. Wang, R. Smirani and G. G. Ross, *Nano Letters*, 2004, **4**, 2041-2045.
97. G. Hadjisavvas, I. N. Remediakis and P. C. Kelires, *Physical Review B*, 2006, **74**, 165419.
98. H. F. Wilson and A. S. Barnard, *The Journal of Physical Chemistry C*, 2014, **118**, 2580-2586.
99. S. M. Gates, R. R. Kunz and C. M. Greenlief, *Surface Science*, 1989, **207**, 364-384.
100. M. Suemitsu, H. Nakazawa and N. Miyamoto, *Surface science*, 1996, **357**, 555-559.
101. A. M. Žak, *Nano Letters*, 2022, **22**, 9219-9226.
102. M. P. Hanrahan, E. L. Fought, T. L. Windus, L. M. Wheeler, N. C. Anderson, N. R. Neale and A. J. Rossini, *Chemistry of Materials*, 2017, **29**, 10339-10351.
103. R. N. Pereira, D. J. Rowe, R. J. Anthony and U. Kortshagen, *Physical Review B*, 2012, **86**, 085449.
104. N. Bushlanova, V. Baturin, S. Lepeshkin and Y. Uspenskii, *Nanoscale*, 2021, **13**, 19181-19189.

Chapter 5

1. S. Pramanik, S. K. E. Hill, B. Zhi, N. V. Hudson-Smith, J. J. Wu, J. N. White, E. A. McIntire, V. S. S. K. Kondeti, A. L. Lee, P. J. Bruggeman, U. R. Kortshagen and C. L. Haynes, *Environmental Science: Nano*, 2018, **5**, 1890-1901.

2. F. Maier-Flaig, J. Rinck, M. Stephan, T. Bocksrocker, M. Bruns, C. Kubel, A. K. Powell, G. A. Ozin and U. Lemmer, *Nano Letters*, 2013, **13**, 475-480.
3. F. Meinardi, S. Ehrenberg, L. Dharmo, F. Carulli, M. Mauri, F. Bruni, R. Simonutti, U. Kortshagen and S. Brovelli, *Nature Photonics*, 2017, **11**, 177-185.
4. Z.-Y. Yu, Z.-H. Guo, Y.-C. Zhang, X. Zhang, Y. Wang, F.-Y. Ma, Y. Liu, X.-Y. Xue, Q.-Y. Jin, J. Li, J. Sun, S.-Y. Wang, D.-C. Wang and M. Lu, *Results in Physics*, 2022, **34**, 105336.
5. H.-J. Song, B. G. Jeong, J. Lim, D. C. Lee, W. K. Bae and V. I. Klimov, *Nano Letters*, 2018, **18**, 395-404.
6. K. Gardner, M. Aghajamali, S. Vagin, J. Pille, W. Morrish, J. G. C. Veinot, B. Rieger and A. Meldrum, *Advanced Functional Materials*, 2018, **28**, 1802759.
7. C. Park, J. Na, M. Han and E. Kim, *ACS Nano*, 2017, **11**, 6977-6984.
8. F. Romano, Y. Yu, B. A. Korgel, G. Bergamini and P. Ceroni, in *Photoactive Semiconductor Nanocrystal Quantum Dots: Fundamentals and Applications*, ed. A. Credi, Springer International Publishing, 2017.
9. M. Dasog, G. B. De los Reyes, L. V. Titova, F. A. Hegmann and J. G. C. Veinot, *ACS Nano*, 2014, **8**, 9636-9648.
10. A. Angi, R. Sinelnikov, A. Meldrum, J. G. Veinot, I. Balberg, D. Azulay, O. Millo and B. Rieger, *Nanoscale*, 2016, **8**, 7849-7853.
11. M. Dasog, J. Kehrlé, B. Rieger and J. G. Veinot, *Angewandte Chemie International Edition*, 2016, **55**, 2322-2339.
12. T. Ishizone and R. Goseki, in *Encyclopedia of Polymeric Nanomaterials*, eds. S. Kobayashi and K. Müllen, Springer Berlin Heidelberg, Berlin, Heidelberg, 2015.
13. K. Ratkanthwar, J. Zhao, H. Zhang, N. Hadjichristidis and J. Mays, in *Anionic Polymerization: Principles, Practice, Strength, Consequences and Applications*, eds. N. Hadjichristidis and A. Hirao, Springer Japan, Tokyo, 2015.
14. M. P. Hanrahan, E. L. Fought, T. L. Windus, L. M. Wheeler, N. C. Anderson, N. R. Neale and A. J. Rossini, *Chemistry of Materials*, 2017, **29**, 10339-10351.
15. A. N. Thiessen, M. Ha, R. W. Hooper, H. Yu, A. O. Oliynyk, J. G. C. Veinot and V. K. Michaelis, *Chemistry of Materials*, 2019, **31**, 678-688.
16. D. A. Kislitsyn, J. M. Mills, S. K. Chiu, B. N. Taber, J. D. Barnes, C. F. Gervasi, A. M. Goforth and G. V. Nazin, *Journal of Physical Chemistry Letters*, 2018, **9**, 710-716.
17. V. I. Klimov, C. J. Schwarz, D. W. McBranch and C. W. White, *Applied Physics Letters*, 1998, **73**, 2603-2605.
18. J. Z. Zhang, *The Journal of Physical Chemistry B*, 2000, **104**, 7239-7253.
19. M. R. Bergren, P. K. B. Palomaki, N. R. Neale, T. E. Furtak and M. C. Beard, *ACS Nano*, 2016, **10**, 2316-2323.
20. I. Sychugov, A. Fucikova, F. Peveré, Z. Yang, J. G. C. Veinot and J. Linnros, *ACS Photonics*, 2014, **1**, 998-1005.
21. B. G. Lee, D. Hiller, J.-W. Luo, O. E. Semonin, M. C. Beard, M. Zacharias and P. Stradins, *Advanced Functional Materials*, 2012, **22**, 3223-3232.
22. Y. Su, C. Wang, Z. Hong and W. Sun, *Frontiers in Chemistry*, 2021, **9**, 721454.
23. E. J. Henderson, J. A. Kelly and J. G. C. Veinot, *Chemistry of Materials*, 2009, **21**, 5426-5434.
24. S. Terada, Y. Xin and K.-i. Saitow, *Chemistry of Materials*, 2020, **32**, 8382-8392.
25. C. M. Hessel, E. J. Henderson and J. G. C. Veinot, *The Journal of Physical Chemistry C*, 2007, **111**, 6956-6961.

26. B. Garrido Fernandez, M. López, C. García, A. Pérez-Rodríguez, J. R. Morante, C. Bonafos, M. Carrada and A. Claverie, *Journal of Applied Physics*, 2002, **91**, 798-807.
27. T. Lopez and L. Mangolini, *Nanoscale*, 2014, **6**, 1286-1294.
28. S. Niesar, R. N. Pereira, A. R. Stegner, N. Erhard, M. Hoeb, A. Baumer, H. Wiggers, M. S. Brandt and M. Stutzmann, *Advanced Functional Materials*, 2012, **22**, 1190-1198.
29. M. K. Weldon, K. T. Queeney, A. B. Gurevich, B. B. Stefanov, Y. J. Chabal and K. Raghavachari, *The Journal of Chemical Physics*, 2000, **113**, 2440-2446.
30. D. Neiner and S. M. Kauzlarich, *Chemistry of Materials*, 2010, **22**, 487-493.
31. J. Holm and J. T. Roberts, *Journal of the American Chemical Society*, 2007, **129**, 2496-2503.
32. T. Hawa and M. R. Zachariah, *The Journal of Physical Chemistry C*, 2008, **112**, 14796-14800.
33. A. S. Barnard and H. F. Wilson, *The Journal of Physical Chemistry C*, 2015, **119**, 7969-7977.
34. H. F. Wilson, L. McKenzie-Sell and A. S. Barnard, *Journal of Materials Chemistry C*, 2014, **2**, 9451-9456.

Appendices

Appendix A: Cavity Analyses

Resonant Wavelength Equation in a Fabry-Pérot Cavity

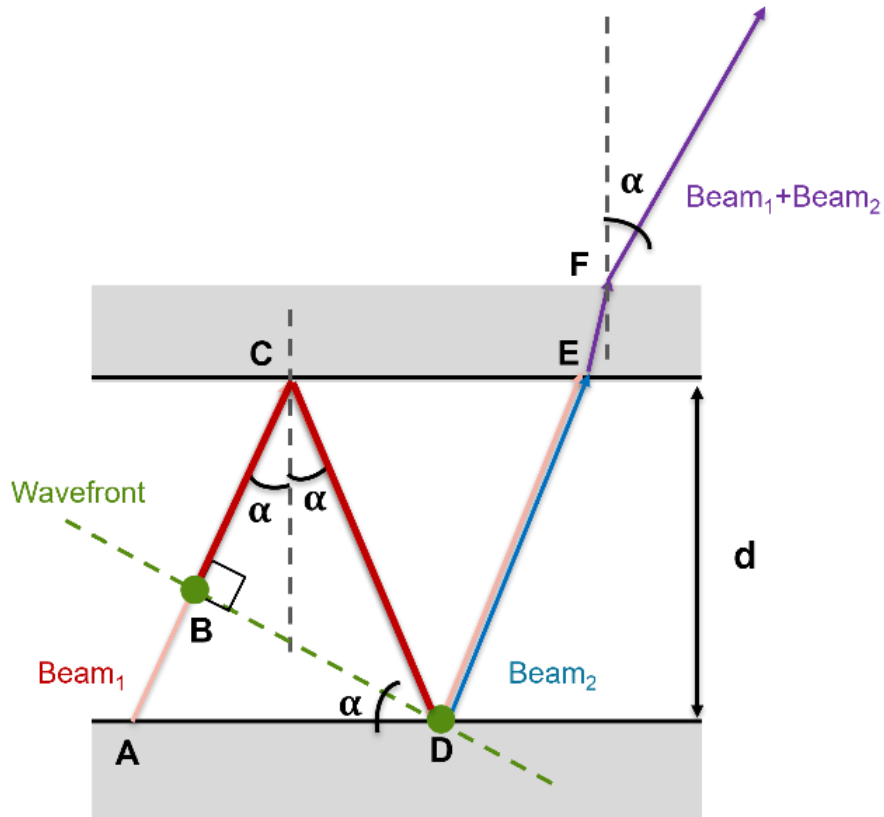


Figure A.1. Interference of Beam₁ (pink) and Beam₂ (blue) within a Fabry-Pérot cavity. The bold red lines (BC and CD) are the the optical pathlength difference between the two beams.

A simple two-beam interference in a Fabry-Pérot cavity is depicted in Figure A.1. At here, Beam₁ is emitted at Point A at an angle (α) and is reflected by the two mirrors (Points C and D). When Beam₁ is reflected from Point D, it interferes with another emission, Beam₂. The resonant emission (Beam₁+Beam₂) then is transmitted out of the cavity from the top mirror at Point E.

In vacuum, the condition of constructive interference is based on the requirement that the optical pathlength difference (Δl) of the two beams traveling between the mirrors must be an integer (m) multiple of the photon wavelength (λ):

$$\Delta l = m\lambda \quad (A1)$$

As the wavefront of the two beams – the points where the light waves are in phase – is tilted, the pathlength difference is the summation of BC and CD as bolded in the figure. Using trigonometry, we find BC and CD:

$$\Delta l = BC + CD \quad (\text{A2})$$

$$CD = \frac{d}{\cos(\alpha)} \quad (\text{A3})$$

$$BC = \left(\frac{d}{\cos(\alpha)} \right) \cos(2\alpha) \quad (\text{A4})$$

where d is the physical distance between the two mirrors and $\cos(2\alpha) = 2\cos^2(\alpha) - 1$. By substituting Equations A3 and A4 into A2, the pathlength difference is obtained:

$$\Delta l = \frac{2d\cos^2(\alpha) - d}{\cos(\alpha)} + \frac{d}{\cos(\alpha)} \quad (\text{A5})$$

$$\Delta l = 2d\cos(\alpha) \quad (\text{A6})$$

In combination of Equations A1 and A6, the resonant wavelength is therefore:

$$2d\cos(\alpha) = m\lambda \quad (\text{A7})$$

If the cavity is filled with a medium of refractive index (η), the photon wavelength in the medium is related to vacuum wavelength by $\frac{\lambda}{\eta}$. By substituting this into Equation A7, we will obtain the expression for the resonant wavelength (λ_m) in the Fabry-Perot cavity equation:

$$2\eta d\cos(\alpha) = m\lambda_m \quad (\text{A8})$$

Phase changes, or penetration depth, arised from the metal mirrors ($L_{pen,\alpha}$) should also be accounted for the optical pathlength; details can be found in Chapter 2.

Full Width Half Maximum

Full-width-half-maximum (FWHM) is the bandwidth at the half-maximum of a peak.

While the FWHM ($\Delta\lambda$) of the resonance mode can be determined graphically, the wavelength interval can be converted into frequency ($\Delta\nu$) by:

$$\Delta\nu = \frac{c}{\lambda^2} \Delta\lambda \quad (\text{A9})$$

where c is the speed of light and λ is the center wavelength.

Free Spectral Range Calculation

Free spectral range (FSR) is the spacing in wavelength or frequency between two successive modes, where in wavelength interval (λ_{FSR}) is calculated by

$$\lambda_{FSR} = \lambda_{m+1} - \lambda_m \quad (\text{A10})$$

where λ_m is the wavelength of mode in consideration and λ_{m+1} is the wavelength of $m+1$ mode.

To convert the wavelength interval into the frequency interval ν_{FSR} ,

$$\nu_{FSR} = \frac{c}{\lambda_{FSR}} \quad (\text{A111})$$

Quality Factor Calculation

Quality factor (Q) is a dimensionless parameter that describes how energy dissipated in the resonator. A high Q indicates slower damping, where the oscillator is more stable and resonate at a smaller range of frequencies (i.e., narrower bandwidth). Thus, Q can be defined as the ratio of a resonator's centre wavelength to its bandwidth:

$$Q = \frac{\lambda}{\Delta\lambda} \quad (\text{A12})$$

Finesse Calculation

Finesse (F) is a measure of how narrow the resonant peak is in relation to its frequency distance:

$$F = \frac{\nu_{FSR}}{\Delta\nu} \quad (\text{A13})$$

Appendix B: Surface Coverage Calculation of SiQDs

The surface coverage from TGA weight loss was calculated following previous study from our group: ¹

$$\% \text{ Coverage} = \frac{\% \text{ Experimental weight loss}}{\% \text{ Theoretical weight loss}} \cdot 100 \quad (\text{B1})$$

At here, the % Theoretical weight loss is obtained from the following equation:

$$\% \text{ Theoretical weight loss} = \frac{\text{Ligands theoretical weight}}{\text{Ligands and SiQDs theoretical weight}} \cdot 100 \quad (\text{B2})$$

$$\text{Ligands theoretical weight} = \frac{N_L \cdot M_L}{N_A} \cdot 100 \quad (\text{B3})$$

$$\text{SiQDs theoretical weight} = \frac{N_{Si} \cdot M_{Si}}{N_A} \cdot 100 \quad (\text{B4})$$

where N_L is the total number of ligands on the QD surface, N_{Si} is the total number of Si atoms per QDs, M_i is the molar mass of the ligand or Si, and N_A is Avogadro number.

N_{Si} is calculated considering Si has a diamond unit cell containing 8 atoms and a volume of 0.164 nm³. As the spherical SiQDs are 2.78 nm in diameter according to the TEM image (Figure 3.3a), a SiQD has a volume of 11 nm³ that is composed of 69 unit cells with 552 Si atoms in it.

N_L is determined from the surface area of a SiQD and bonding sites on the surface as shown by Xu *et al.*: ² Since SiQD is approximately a spherical particle, its surface area, S , was calculated from $S = 4\pi (d/2)^2$. The average number of bonding sites, N , is calculated by multiplying the surface area, the number density of Si atoms on each plane, and the number of bonding sites per Si atom as shown in the following equation:

$$N = \frac{(N_{111} + N_{100} + N_{110})}{3} = 1S\rho_{111} + 2S\rho_{100} + 1S\rho_{110} \quad (\text{B5})$$

where N_i are the number of bonding sites and ρ_i are surface number density of Si atom on each (111), (100), and (110) crystal plane.

$$\rho_{111} = 2 \text{ atoms} / \frac{1}{2}(\sqrt{2} \cdot 0.547 \text{ nm}) \left(\sqrt{\frac{3}{2}} \cdot 0.547 \text{ nm}\right) = 7.72 \text{ atoms/nm}^2$$

$$\rho_{100} = 2 \text{ atoms} / (0.547 \text{ nm})^2 = 6.68 \text{ atoms/nm}^2$$

$$\rho_{110} = 4 \text{ atoms} / (0.547 \text{ nm} * \sqrt{2} \cdot 0.547 \text{ nm}) = 9.45 \text{ atoms/nm}^2$$

The coefficients of 1, 2, and 1 correspond to -Si-H₁, =Si-H₂, and -Si-H₁ bonding sites on each crystal plane. This results 247 bonding sites on a SiQD with a diameter of 2.78nm.

Appendix C: LED External Quantum Efficiency Calculation

The EQE limited by the internal quantum efficiency (IQE) and the outcoupling efficiency (η_{out}),³

$$EQE = IQE \cdot \eta_{out} \quad (C1)$$

where this can be calculated directly by dividing the number of photons into the free space (N_{photon}) by the number of electrons injected into the LED ($N_{electron}$),

$$EQE = \frac{N_{photon}}{N_{electron}} \quad (C2)$$

At here, Equation C3 was adopted into an integral to fit the measurement setup as shown by Mock et al. :⁴

$$EQE = \frac{A \cdot e}{h \cdot c \cdot I} \int_0^{\infty} E_{e,\lambda} \cdot \lambda \, d\lambda \quad (C3)$$

where A is the LED area ($3 \times 3 \text{ mm}^2$), e is the elementary charge, h is the Planck's constant, c is the speed of light, I is the injected current, $E_{e,\lambda}$ is the spectral irradiance at the specific wavelength λ .

References:

1. Islam, M. A.; Mobarok, M. H.; Sinelnikov, R.; Purkait, T. K.; Veinot, J. G. C. Phosphorus Pentachloride Initiated Functionalization of Silicon Nanocrystals. *Langmuir* **2017**, *33* (35), 8766-8773. DOI: 10.1021/acs.langmuir.7b00518.
2. Xu, Y.; Terada, S.; Xin, Y.; Ueda, H.; Saitow, K.-i. Ligand Effects on Photoluminescence and Electroluminescence of Silicon Quantum Dots for Light-Emitting Diodes. *ACS Applied Nano Materials* **2022**. DOI: 10.1021/acsanm.2c00811.
3. Schubert, E. F. *Light-Emitting Diodes*; Cambridge University Press, 2006. DOI: DOI: 10.1017/CBO9780511790546.
4. Mock, J.; Groß, E.; Kloberg, M. J.; Rieger, B.; Becherer, M. Surface Engineering of Silicon Quantum Dots: Does the Ligand Length Impact the Optoelectronic Properties of Light-Emitting Diodes? *Advanced Photonics Research* **2021**, *2* (9). DOI: 10.1002/adpr.202100083.